CORRIGENDA

p.24 Eq. 1.65 should read

$$E = \frac{\hbar^2}{2I_1} J(J+1) + \tfrac{1}{2}\hbar^2 \left(\frac{1}{I_3} - \frac{1}{I_1}\right) K^2$$

p.56 Eq. 2.21 should read

$$\mathcal{Q}_{M\lambda\mu}(\varepsilon,w) := - \frac{i\mu}{\lambda \sinh w} \mathcal{Q}_{E\lambda\mu}(\varepsilon,w)$$

Eq. 2.26 should read

$$\nu_\lambda = \begin{cases} 1 & \text{target excitation} \\ (-)^\lambda & \text{projectile excitation} \end{cases}$$

p.65 Add to caption to fig. 2.3:

"Curves for other ζ values can be obtained using $\Pi(\theta,\xi,\zeta) = -\Pi(\theta,\xi,1-\zeta)$."

p.75, line 1. Replace "gdr" with "giant resonance"

p.76, line 5. Delete "dipole"

p.83, line 19. Replace "seem" with "seen"

p.89 Eq. 2.95 should read

$$\varphi_{[V]} = -32.65\ Z_t^{7/5}$$

p.95 Eq. 2.109 should read

$$E_{D[MeV]} = 47.9\ A^{-0.234}$$

p.103 Delete comma after eq.2.124

p.105, line 26. Replace "r_c" with "d_c"

p.106, line 27. Replace "p^2" with "p^4"

p.108, Eq.2.138 should read

$$\xi_r = \xi_c \sqrt{1 - 0.002147\ E_{[MeV]}/A_{p[u]}}$$

p.119, line 13. Replace "tantalum" with "lead"

p.176, line 7. Replace "Q_{2+} = 93 e fm^2" with "Q_{2+} = -15 e fm^2".

p.181, table 4.9, entry 4. Replace "projectile" with "target"

p.206, line 8. Replace "Verlovich" with "Berlovich"

REORIENTATION-EFFECT MEASUREMENTS ON ^{18}O, ^{24}Mg AND ^{198}Hg

Matthew Peter Fewell

A thesis submitted to
The Australian National University
for the degree of
Doctor of Philosophy

October 1978

Preface

This thesis describes measurements of the quadrupole moments of the first-excited states of ^{18}O, ^{24}Mg and ^{198}Hg. The experiments made use of the facilities of the Department of Nuclear Physics, A.N.U.

The projectile excitation measurements were suggested by Dr. D.C. Kean and the measurements on ^{198}Hg by Dr. M.T. Esat. The technique for the manufacture of mercury targets was developed by Drs. Kean and Esat. They also designed the apparatus for detecting backscattered particles. The apparatus for detecting particles scattered through 90° was designed by myself from a suggestion by Dr. Kean and with the assistance of Mr. W.C. O'Hare. I was assisted in the collection of experimental data by Professor S. Hinds and Drs. A.M. Baxter, M.T. Esat, D.C. Kean, A.M.R. Joye, R.H. Spear and T.H. Zabel. The analysis of the data was performed by myself. For this purpose I modified a spectrum fitting program originally written by Dr. Joye and a least squares fitting program written by Dr. Kean. I also substantially re-wrote the de Boer-Winther Coulomb excitation computer program to include magnetic and mixed-multipole excitations and to include the electric multipole-electric multipole interaction.

Some of the work described in this thesis is also reported in the following papers:

"The quadrupole moment of the first excited state of ^{18}O", M.P. Fewell, D.C. Kean, R.H. Spear and A.M. Baxter. *J. Phys. (Lond.)* G3 (1977), L23.

"Energy calibration of the A.N.U. 14 UD pelletron accelerator", R.H. Spear, D.C. Kean, M.T. Esat, A.M.R. Joye and M.P. Fewell. *Nucl. Instr. Meth.* 147 (1977), 455.

"The quadrupole moment of the first excited state of ^{198}Hg", M.T. Esat, D.C. Kean, R.H. Spear, M.P. Fewell and A.M. Baxter. *Phys. Lett.* 72B (1977), 49.

"Systematics of Coulomb-nuclear interference: implications for reliable measurements of the reorientation effect", R.H. Spear, T.H. Zabel, D.C. Kean, A.M.R. Joye, A.M. Baxter, M.P. Fewell and S. Hinds. *Phys. Lett.* 76B (1978), 49.

"The static quadrupole moment of the first excited state of ^{24}Mg", M.P. Fewell, S. Hinds, D.C. Kean and T.H. Zabel. Submitted to *Nucl. Phys.*

"Electric moments of the first excited state of ^{18}O", M.P. Fewell, A.M. Baxter, D.C. Kean, R.H. Spear and T.H. Zabel. Submitted to *Nucl. Phys.*

I wish to thank my supervisor, Dr. A.M. Baxter, for his encouragement, criticism and quiet enthusiasm. The eight years during which I have worked under him, first as an undergraduate and then as a doctoral student, have been most enjoyable. In a sense Dr. Baxter has not been my only supervisor — it is one of the great advantages of nuclear physics that it tends to be pursued by groups of workers and Professor Hinds, Dr. Kean and Dr. Spear have all played unofficial (with the exception of Professor Hinds who supervised me during Dr. Baxter's absence on study leave) but most stimulating parts in my supervision. This includes offering much helpful criticism on the draft of this thesis.

I also wish to thank Professor Hinds for giving me the opportunity to work in the Department of Physics and Professor J.O. Newton for allowing me to use the facilities of the Department of Nuclear Physics.

In this thesis, I have used a circumflex, ^, to denote a unit vector and an asterisk to denote complex conjugation. The symbols := and =: are used to mean "equals by definition", where the quantity being defined is on the same side of the equation as the colon. The S.I. system of units is used where this does not do too severe an injury to convention; in particular, all equations involving electromagnetic quantities are written in their S.I. form. Operators are given no special distinguishing mark, but attention is drawn to them in the text. The convention of Alder and Winther [Al75, p.316] is used for reduced matrix elements. Further comments on the conventions used can be found in the appendix.

No part of this thesis has been submitted for a degree at any other University.

M.P. Fewell

Abstract

The quadrupole moments of the first-excited states of ^{18}O, ^{24}Mg and ^{198}Hg have been measured using the reorientation effect in Coulomb excitation. The excitation probabilities were measured by resolving the elastically and inelastically scattered projectiles with silicon surface-barrier detectors. Contrary to some previously published measurements on ^{18}O and ^{24}Mg, the current results are in agreement with theoretical predictions. The results for ^{198}Hg are also in agreement with two other, as yet unpublished, measurements.

The theory used in the analysis of these experiments is examined in detail. It is found that uncertainty in the treatment of relativistic effects can be significant in some cases. Further work on the relativistic theory of Coulomb excitation is desirable.

Table of Contents

PREFACE ii
ABSTRACT iv
LIST OF FIGURES ix
LIST OF TABLES xiii

CHAPTER 1. INTRODUCTION 1

1.1 THE SHAPE OF A NUCLEUS 3
1.1.1 The Deformation of a Uniform Sphere 3
1.1.2 The Multipole Moments of a Quantal Object 9
1.1.3 N-Body Quadrupole Moments 11
1.1.4 Some Limitations 15

1.2 THEORETICAL PREDICTIONS 16
1.2.1 The Harmonic Vibrational Model 17
1.2.2 Anharmonic Effects 20
1.2.3 The Rigid Rotational Model 23
1.2.4 The Rotation-Vibration Model 27
1.2.5 The Shell Model 31
1.2.6 Microscopic Models 34
1.2.7 Summary 35

1.3 METHODS OF MEASURING EXCITED-STATE QUADRUPOLE MOMENTS 36
1.3.1 Measurements Using Crystals 36
1.3.2 X-Rays from Exotic Atoms 39
1.3.3 Inelastic Scattering Other than Coulomb Excitation 40
1.3.4 Coulomb Excitation 41

CHAPTER 2. THEORY OF ELECTROMAGNETIC EXCITATION 50

2.1 NON-RELATIVISTIC SEMICLASSICAL THEORY 51
2.1.1 Range of Validity 51
2.1.2 Outline 52
2.1.3 Perturbation Treatment 57
2.1.4 Summary 64

2.2 THE EFFECTS OF SOME NUCLEAR PARAMETERS WHICH ARE EITHER GENERALLY IGNORED OR ARE DIFFICULT TO ESTIMATE 66

2.2.1 Magnetic Dipole and Electric Hexadecapole Reorientation 66

2.2.2 Interference Involving Electric Hexadecapole Moments 71

2.2.3 The Effect of the Giant Dipole Resonance 73

2.2.4 The Structure of the Exciting Nucleus 80

2.3 CORRECTIONS FOR THE SEMICLASSICAL APPROXIMATION 85

2.3.1 Symmetrization 86

2.3.2 Residual Corrections 87

2.4 LONG-RANGE DEVIATIONS FROM THE COULOMB POTENTIAL 88

2.4.1 Method of Treatment 88

2.4.2 Electron Screening 89

2.4.3 Vacuum Polarization 91

2.4.4 Nuclear Polarization 93

2.5 THE NUCLEAR FORCE 95

2.5.1 Inelastic Scattering 95

2.5.2 Nucleon Tunnelling 97

2.6 RELATIVISTIC CORRECTIONS 99

2.6.1 The Relativistic Kepler Problem 100

2.6.2 Kinematics 101

2.6.3 Orbit Dynamics 104

2.6.4 Modifications to the Perturbation Theory 106

CHAPTER 3. EXPERIMENTAL METHOD AND RESULTS 109

3.1 INTRODUCTION 110

3.1.1 The Number and Precision of Measurements 110

3.1.2 Experimental Strategy 112

3.1.3 A Reorienteer's Checklist 114

3.2 GENERAL 117

3.2.1 Beam Handling 117

3.2.2 Accelerator Calibration 118

3.2.3 Scattering Chamber Geometry 119

3.2.4 Targets 125

3.2.5 Detectors and Electronics 129

3.3 ^{198}Hg DATA 130
3.3.1 ^{16}O and ^{12}C Data 131
3.3.2 ^{4}He Data 136
3.3.3 Checks for Contaminant Peaks 140
3.3.4 Safe Bombarding Energies 141
3.4 ^{24}Mg DATA 143
3.4.1 Backscattering Data 143
3.4.2 90° Data 145
3.4.3 Checks for Contaminant Peaks 147
3.4.4 Safe Bombarding Energies 149
3.5 ^{18}O DATA 149
3.5.1 Backscattering and 90° Data 149
3.5.2 Checks for Contaminant Peaks 152
3.5.3 Safe Bombarding Energies 156
3.6 SUMMARY OF EXPERIMENTAL RESULTS 158
3.6.1 Maximum Safe Bombarding Energies 158
3.6.2 Tabulation of Measured Excitation Probabilities 160

CHAPTER 4. EXTRACTION OF QUADRUPOLE MOMENTS 164
4.1 LEAST-SQUARES EQUATIONS 165
4.2 ^{198}Hg 167
4.2.1 Higher-State Matrix Elements 167
4.2.2 Other Corrections 171
4.3 ^{24}Mg 173
4.3.1 Higher-State Matrix Elements 173
4.3.2 Other Corrections 176
4.4 ^{18}O 177
4.4.1 Higher-State Matrix Elements 177
4.4.2 Other Corrections 180

CHAPTER 5. CONCLUSION 183
5.1 COMPARISON WITH PREVIOUS WORK 184
5.1.1 ^{198}Hg 184
5.1.2 ^{24}Mg 188

5.1.3 ^{18}O 191

5.2 NUCLEAR SHAPES 195

5.2.1 The Nuclei ^{198}Hg, ^{24}Mg and ^{18}O 195

5.2.2 Systematics in the Mass Ranges $186 \leqslant A \leqslant 208$ and $16 \leqslant A \leqslant 40$ 199

5.3 CONCLUSION 202

APPENDIX 203

REFERENCES 205

List of Figures

Fig.		
1.1	Four shapes all having $Q_0^{E2} = 0$	16
1.2	The spectrum of ^{198}Hg as predicted by the harmonic vibrational model	20
1.3	The dependence of the relative spacings of the lowest energy levels predicted by the asymmetric rigid rotational model on the asymmetry angle γ	26
1.4	Energy levels of the rotation-vibration model	29
1.5	Energy levels of the shell model	32
1.6	The explanation of the reorientation effect as a dynamic hyperfine splitting	42
1.7	A spectrum of 60 MeV ^{17}O ions backscattered from ^{208}Pb	46
1.8	A spectrum of 120 MeV ^{32}S ions backscattered from ^{208}Pb	48
2.1	The function $R^2_{E2}(\Theta,\xi)$	59
2.2	The function $R^2_{M1}(\Theta,\xi)$	60
2.3	The function $\Pi^{E2E2}_{E2}(180°,\xi,\zeta)$	65
2.4	The function $\Pi^{E2E2}_{E2}(\Theta,\xi,1)$	66
2.5	Monopole-multipole excitation mechanisms	67
2.6	Reorientation-effect excitation mechanisms	68
2.7	The function $\Pi^{E2M1}_{E2}(\Theta,\xi,1)$	68
2.8	The function $\Pi^{E2E4}_{E2}(\Theta,\xi,1)$	69
2.9	The function $\Pi^{E2M1}_{E2}(\Theta,\xi,1)/\Pi^{E2E2}_{E2}(\Theta,\xi,1)$	70
2.10	The function $\Pi^{E2E4}_{E2}(\Theta,\xi,1)/\Pi^{E2E2}_{E2}(\Theta,\xi,1)$	71
2.11	The function $\Pi^{E4E2}_{E2}(180°,\xi,\zeta)$	73
2.12	The function $\Pi^{E4E2}_{E2}(180°,\xi,\zeta)/\Pi^{E2E2}_{E2}(\Theta,\xi,1)$	74
2.13	Excitation via the giant dipole resonance	76
2.14	The function $\Delta^{11}_{E2}(\Theta,\xi)$	77

Fig.

2.15 Multipole-multipole excitation mechanisms 82

2.16 The function $\Xi^{E2}_{E2}(180°,\xi_1,\xi_2,50)$ 84

2.17 The function $\Xi^{E3}_{E2}(180°,\xi_1,\xi_2,50)$ 84

2.18 The function $\Xi^{E3}_{E2}(\theta,\xi_1,0.8,50)$ 85

2.19 Polarization processes 93

3.1 The magnet constant of the analysing magnet of the ANU 14 UD Pelletron accelerator 119

3.2 The apparatus for detecting backscattered particles 120

3.3 A schematic diagram of the apparatus for detecting particles scattered through ±90° 122

3.4 The apparatus for detecting particles scattered through ±90° 124

3.5 A photograph of the scattering chamber assembled to perform projectile-excitation measurements 126

3.6 The apparatus for the preparation of Hg targets 128

3.7 The response of an ORTEC "F" series detector to 80 MeV monoenergetic ^{28}Si ions 131

3.8 Spectra of 64 MeV and 67 MeV ^{16}O ions backscattered from ^{198}Hg 132

3.9 Uncertainty in peak unfolding in the ^{198}Hg data 134

3.10 Spectra of 65 MeV ^{16}O ions backscattered from ^{208}Pb and ^{198}Hg 134

3.11 Spectra of 43 MeV and 45 MeV ^{12}C ions backscattered from ^{198}Hg 136

3.12 Spectra of 46 MeV ^{12}C ions backscattered from ^{208}Pb and ^{198}Hg 137

3.13 A spectrum of 14.1 MeV ^{4}He ions backscattered from ^{198}Hg 138

3.14 A spectrum of 15.8 MeV ^{4}He ions backscattered from ^{198}Hg 138

3.15 A spectrum of 15.3 MeV ^{4}He ions backscattered from a $^{208}PbCl_2$ target 139

3.16 A spectrum of 69 MeV ^{16}O ions backscattered from ^{198}Hg 141

Fig.

3.17 The Coulomb barrier for the backscattering of ^{4}He, ^{12}C and ^{16}O ions from ^{198}Hg 142

3.18 A spectrum of 55 MeV ^{24}Mg ions backscattered from ^{208}Pb 143

3.19 Spectra of 80 MeV and 90 MeV ^{24}Mg ions backscattered from ^{208}Pb 144

3.20 Uncertainty in peak unfolding in the ^{24}Mg data 145

3.21 A spectrum of 81.8 MeV ^{24}Mg ions scattered through 30° from ^{208}Pb 146

3.22 Spectra of 85 MeV and 100 MeV ^{24}Mg ions scattered through 90° from ^{208}Pb 146

3.23 A spectrum of 55 MeV ^{24}Mg ions backscattered from ^{208}Pb 147

3.24 A spectrum of 100 MeV ^{24}Mg ions backscattered from ^{208}Pb 148

3.25 The Coulomb barrier for the scattering of ^{24}Mg ions through 90° and 172° from ^{208}Pb 149

3.26 Spectra of ^{18}O ions of various energies scattered through 90° and ~ 173° from ^{208}Pb 151

3.27 Spectra of ^{16}O and ^{18}O ions scattered through 90° and 174° from ^{208}Pb 153

3.28 A spectrum of 40 MeV ^{18}O ions backscattered from ^{208}Pb 154

3.29 The response of an ORTEC "F" series silicon surface-barrier detector to monoenergetic ^{18}O ions 155

3.30 The Coulomb barrier for the scattering of ^{18}O ions through 90° and 173° from ^{208}Pb 156

3.31 A comparison of the Coulomb-nuclear interference anomalies in the backscattering of ^{16}O from ^{198}Hg, ^{16}O from ^{204}Pb, and ^{18}O from ^{208}Pb 159

4.1 The low-lying energy levels of ^{198}Hg 168

4.2 A spectrum of 17.0 MeV ^{4}He ions backscattered from ^{198}Hg 168

4.3 The determination of some matrix elements involving the 4_1^+ state of ^{198}Hg 170

4.4 The variation of P_{exp}/F with ρ for ^{198}Hg 173

4.5 The low-lying energy levels of ^{24}Mg 174

4.6 The variation of P_{exp}/F with ρ for ^{24}Mg 178

Fig.

4.7 The low-lying energy levels of ^{18}O 179

4.8 The variation of P_{exp}/F with ρ for ^{18}O 182

5.1 Values of the shape parameters B and Γ of the ground states of some even-even nuclei in the mass range $186 \leqslant A \leqslant 206$ 201

5.2 Values of the shape parameters B and Γ of the ground states of some even-even nuclei in the mass range $18 \leqslant A \leqslant 40$ 201

List of Tables

1.1	The relationship between "multipole moments" and "spectroscopic multipole moments"	10
2.1	The effects of magnetic dipole and electric hexadecapole reorientation	70
3.1	The isotopic composition of the ^{198}Hg and ^{208}Pb targets	127
3.2	Probabilities of exciting the first-excited state of ^{198}Hg by the backscattering of ^{16}O, ^{12}C and ^{4}He	161
3.3	Probabilities of exciting the first-excited state of ^{24}Mg by scattering from ^{208}Pb through 90° and 172°	162
3.4	Probabilities of exciting the first-excited state of ^{18}O by scattering from ^{208}Pb through 90° and 172°	163
4.1	Sources of uncertainty in the ^{198}Hg experiment	170
4.2	Corrections to the ^{198}Hg analysis	171
4.3	Matrix elements used in the analysis of the ^{24}Mg data	175
4.4	Sources of uncertainty in the ^{24}Mg experiment	175
4.5	Corrections to the ^{24}Mg analysis	176
4.6	Values of β_2, β_4, $\langle r^2 \rangle$ and $\langle r^4 \rangle$ derived from the inelastic scattering of protons, ^{4}He and electrons	177
4.7	Matrix elements used in the analysis of the ^{18}O data	180
4.8	Sources of uncertainty in the ^{18}O experiment	180
4.9	Corrections to the ^{18}O analysis	181
5.1	Results of previous and present measurements of Q_{2^+} and $B(E2;0^+ \rightarrow 2^+)$ of ^{198}Hg	185
5.2	A comparison of the theoretical predictions of Q_{2^+} and $B(E2;0^+ \rightarrow 2^+)$ of ^{198}Hg with experiment	186
5.3	Results of present and previous measurements of Q_{2^+} and $B(E2;0^+ \rightarrow 2^+)$ of ^{24}Mg	189
5.4	A comparison of the theoretical predictions of Q_{2^+} and $B(E2;0^+ \rightarrow 2^+)$ of ^{24}Mg with experiment	191

5.5 Results of previous and present measurements of Q_{2^+} and $B(E2;0^+ \rightarrow 2^+)$ of ^{18}O 193

5.6 A comparison of the theoretical predictions of Q_{2^+}, $B(E2;0^+ \rightarrow 2^+)$ and sgn p_3 of ^{18}O with experiment 196

5.7 Excited states included in the determination of the n-body quadrupole moments of the ground and first-excited states of ^{198}Hg, ^{24}Mg and ^{18}O 196

5.8 Values of the 2-body and 3-body quadrupole moments of the ground and first-excited states of ^{198}Hg, ^{24}Mg and ^{18}O 197

5.9 Shape parameters for the ground and first-excited states of ^{198}Hg, ^{24}Mg and ^{18}O 198

5.10 Values of the 2-body and 3-body quadrupole moments of the ground states of some even-even nuclei in the mass range $184 \leqslant A \leqslant 206$ 199

5.11 Values of the 2-body and 3-body quadrupole moments of the ground states of some even-even nuclei in the mass range $18 \leqslant A \leqslant 40$ 200

Chapter 1

INTRODUCTION

Shape is a fundamental consideration in the description of any object. In the case of the atomic nucleus, one might seek information about its shape after questions of its charge, mass and average dimensions have been answered. But while charge and mass can be measured directly, shape can only be inferred indirectly, for example, from electric multipole measurements. The first section of this chapter outlines two methods which are often used to relate shape and multipole moments.

Irrespective of what they may say about shape, nuclear models give predictions of multipole moments and the verification of these predictions provides another motivation for the measurement of multipole moments. The predictions of some of the simpler nuclear models are outlined in the second section of this chapter. Here and subsequently, emphasis is placed on the electric quadrupole moment of the first excited state of a nucleus as this is, apart from the ground state moments, the only static electric moment of a nucleus which is readily measurable with current techniques. The third section of this chapter describes some of these techniques.

Subsequent chapters describe the measurement of the quadrupole moments of the first excited states of the nuclei ^{18}O, ^{24}Mg and ^{198}Hg using the reorientation effect in Coulomb excitation. The second chapter presents the theory of Coulomb excitation, the third an account of the measurement of the Coulomb excitation probabilities of the various levels under consideration and the fourth discusses the inference of the quadrupole moments from excitation probabilities. The final chapter relates these quadrupole moments to other measurements and to theoretical values and attempts to draw some conclusions about the shapes of these nuclei.

1.1 THE SHAPE OF A NUCLEUS

1.1.1 The Deformation of a Uniform Sphere

Some feel for the multipole moments of a charged distribution of matter can be gained by considering the moments of a deformed uniform distribution of zero diffuseness, that is, a distribution whose charge density is given by

$$\rho(r,\theta,\phi) = \begin{cases} \rho_0 & r \leqslant R(\theta,\phi) \\ 0 & r > R(\theta,\phi) \end{cases} . \qquad (1.1)$$

A general expression for $R(\theta,\phi)$ which is in common use is [Bo75a, for a summary of some other expressions see Lo70, Yo72]

$$R(\theta,\phi) =: R_0 \sum_{\lambda\mu} \alpha_{\lambda\mu} Y^*_{\lambda\mu}(\theta,\phi) , \qquad (1.2)$$

where $Y_{\lambda\mu}(\theta,\phi)$ are spherical harmonics, defined for example by Rose [Ro57], and the $\alpha_{\lambda\mu}$ are deformation parameters. To ensure that $R(\theta,\phi)$ is real, $\alpha_{\lambda\mu}$ must satisfy

$$\alpha_{\lambda -\mu} = (-)^{\mu} \alpha^*_{\lambda\mu} \qquad (1.3)$$

and to ensure that $R(\theta,\phi)$ is invariant under rotations, $\alpha_{\lambda\mu}$ must transform as a spherical tensor [Ro57] of rank λ. If the origin of coordinates is taken to coincide with the centre of charge, then the parameters $\alpha_{1\mu}$ must be related to the other deformation parameters by [Ei75]

$$\alpha_{1\mu} = -\sqrt{\frac{3}{16\pi}} \sum_{\lambda\nu\lambda'\nu'} \sqrt{(2\lambda+1)(2\lambda'+1)}\, C(\lambda\lambda' 1;000) C(\lambda\lambda' 1;\nu\nu'\mu)\, \alpha_{\lambda\nu}\alpha_{\lambda'\nu'} , \qquad (1.4)$$

where $C(\lambda\lambda' L;\mu m M)$ is a Clebsch-Gordan coefficient [Ro57].

The electric multipole moments of this distribution are defined by

$$Q_0^{E\lambda} := \int \rho(r,\theta,\phi)\, r^{\lambda}\, Y_{\lambda 0}(\theta,\phi)\, \underset{\sim}{dr} , \qquad (1.5)$$

where the subscript "0" on $Q_0^{E\lambda}$ indicates that the axes in eq. 1.5 are

the same as those in eq. 1.2. This is often referred to as the intrinsic frame. The result of inserting eq. 1.1 into eq. 1.5 is

$$Q_0^{E\lambda} = \frac{\rho_0 R_0^{\lambda+3}}{\lambda+3} \alpha_{00}^{\lambda+3} \int Y_{\lambda 0}(\Omega) \sum_{n=0}^{\lambda+3} \frac{(\lambda+3)!}{(\lambda+3-n)!n!} \left(\frac{1}{\alpha_{00}} \sum_{\substack{l \geq 1 \\ m}} \alpha_{lm} Y_{lm}^*(\Omega) \right)^n d\Omega . \tag{1.6}$$

In particular, the $\lambda = 0$ moment is given by

$$Q_0^{E0} = \frac{2\sqrt{\pi}}{3} \rho_0 R_0^3 \left(\alpha_{00}^3 + \frac{3\alpha_{00}}{4\pi} \sum_{\lambda\mu} |\alpha_{\lambda\mu}|^2 \right.$$

$$+ (4\pi)^{-\frac{3}{2}} \sum_{\substack{\lambda\lambda'\lambda'' \\ \mu\mu'\mu''}} \alpha_{\lambda\mu} \alpha^*_{\lambda'\mu'} \alpha^*_{\lambda''\mu''} \sqrt{\frac{(2\lambda'+1)(2\lambda''+1)}{2\lambda+1}}$$

$$\left. \times C(\lambda'\lambda''\lambda;000) C(\lambda'\lambda''\lambda;\mu'\mu''\mu) \right) . \tag{1.7}$$

For a spherical distribution, eq. 1.7 reduces to

$$Q_0^{E0} = \frac{\alpha_{00}^3}{\sqrt{4\pi}} \frac{4}{3} \pi \rho_0 R_0^3 \tag{1.8}$$

and α_{00} is taken to be unity for this case. One therefore interprets R_0 in the general case as an average radius, and adjusts α_{00} so that eq. 1.7 reduces to eq. 1.8 in general. It is usual to suppose that $\alpha_{\lambda\mu}$ are all small compared with unity so that

$$\alpha_{00} = 1 - \frac{1}{4\pi} \sum_{\lambda\mu} |\alpha_{\lambda\mu}|^2 - \frac{1}{3} (4\pi)^{-\frac{3}{2}} \sum_{\substack{\lambda\lambda'\lambda'' \\ \mu\mu'\mu''}} \sqrt{\frac{(2\lambda'+1)(2\lambda''+1)}{2\lambda+1}}$$

$$\times C(\lambda'\lambda''\lambda;000) C(\lambda'\lambda''\lambda;\mu'\mu''\mu) \alpha_{\lambda\mu} \alpha^*_{\lambda'\mu'} \alpha^*_{\lambda''\mu''} + O(\alpha_{\lambda\mu}^4) \tag{1.9}$$

and

$$Q_0^{E\lambda} = \rho_0 R_0^{\lambda+3} \left(\frac{2\sqrt{\pi}}{\lambda+3} \alpha_{00}^3 \delta_{\lambda 0} + \alpha_{\lambda 0} + \frac{\lambda+2}{4\pi} \alpha_{\lambda 0} \sum_{lm} |\alpha_{lm}|^2 \right.$$

$$\left. + \frac{\lambda+2}{4\sqrt{\pi}} \sum_{ll'm} \sqrt{\frac{(2l+1)(2l'+1)}{2\lambda+1}} C(ll'\lambda;000) C(ll'\lambda;m-m0) \alpha_{lm} \alpha_{l'-m} \right.$$

$$+\frac{(\lambda+2)(\lambda+1)}{24\pi}\sum_{\substack{\ell\ell'\ell''L\\ mm'm''}}'\sqrt{\frac{(2\ell+1)(2\ell'+1)(2\ell''+1)}{2\lambda+1}}\,C(\ell'\ell''L;m'm''-M)$$

$$\times\, C(\ell L\lambda;M-M0)C(\ell'\ell''L;000)C(\ell L\lambda;000)\;\alpha_{\ell m}\alpha_{\ell' m'}\alpha_{\ell'' m''}+O(\alpha^4_{\lambda\mu})\Big]\,, \tag{1.10}$$

where δ_{ab} is the Kronecker delta. At this point, one of two simplifying assumptions are made. These are either axial symmetry with all the odd-λ deformation parameters equal to zero, or $\lambda = 2$ deformations only. These two assumptions are considered in turn.

When assuming axial symmetry, it is conventional to take the intrinsic z axis as the symmetry axis, so that

$$\alpha_{\lambda\mu} =: \beta_\lambda\,\delta_{\mu 0}\,. \tag{1.11}$$

Also, if $\beta_\lambda = 0$ for odd values of λ, then all of the $\alpha_{l\mu}$ are zero (eq. 1.4) and the resultant shape is such that $\rho(r,\theta,\phi) = \rho(r,\pi-\theta,\pi+\phi)$, that is, it has good parity. In this case, the quadrupole moment is given by[†]

$$\begin{aligned} Q_0^{E2} = \rho_0 R_0^5[&\beta_2 + 0.3604\;\beta_2^2 + 0.9672\;\beta_2\beta_4 + 0.3277\;\beta_4^2 \\ &+ 0.9543\;\beta_4\beta_6 + 0.3211\;\beta_6^2 + \ldots + 0.0227\;\beta_2^3 + 0.4992\;\beta_2^2\beta_4 \\ &+ 0.7171\;\beta_2\beta_4^2 + 0.1920\;\beta_4^3 + \ldots] \end{aligned} \tag{1.12}$$

and the hexadecapole moment by

$$\begin{aligned} Q_0^{E4} = \rho_0 R_0^7[&\beta_4 + 0.7254\;\beta_2^2 + 0.9831\;\beta_2\beta_4 + 1.4314\;\beta_2\beta_6 \\ &+ 0.4109\;\beta_4^2 + 0.8535\;\beta_4\beta_6 + 1.4066\;\beta_4\beta_8 + 0.3801\;\beta_6^2 + \ldots \\ &+ 0.4160\;\beta_2^3 + 1.6559\;\beta_2^2\beta_4 + 1.4398\;\beta_2\beta_4^2 + 0.4036\;\beta_4^3 + \ldots]\,. \end{aligned} \tag{1.13}$$

[†] It may be noted that some of the coefficients of the third order terms in this and in the following equation do not agree with those of Mackintosh [Ma77]. This is partly due to the assumption $\alpha_{00} = 1$ which is made in [Ma77], but not all of the discrepancies can be ascribed to this cause. The origin of the other discrepancies is not known.

Consideration of eq. 1.12 reveals two points which are worth emphasizing:

(a) Changing β_2 to $-\beta_2$ does not change Q_0^{E2} to $-Q_0^{E2}$, even if all of the other β_λ are zero. The magnitude of Q_0^{E2} is always slightly less for an oblate shape ($\beta_2 < 0$) than for a prolate shape ($\beta_2 > 0$) with the same value of $|\beta_2|$ due to the terms in even powers of β_2.

(b) There are many values of the β_λ other than all β_λ equal to zero for which $Q_0^{E2} = 0$. Thus Q_0^{E2} equal to zero does not necessarily imply a spherical shape.

There are two assumptions inherent in the way in which eqs. 1.12 and 1.13 have been written. The first, that $\beta_\lambda^n > \beta_\lambda^{n+1}$, is reasonable for small deformations, but the second, namely $\beta_\lambda > \beta_{\lambda+1}$ is not as obvious. It is difficult to test this by appeal to experimental result, as this assumption is invariably a starting point in the inference of the values of β_λ from experimental results. Even if this second assumption is true, there are problems in computing higher order moments. For example, in eq. 1.13, it is not obvious that $\beta_4 > \beta_2^2$, so that it really is necessary to take these expressions to at least third order. Some "realistic" examples for which eq. 1.13 converges poorly are given by Mackintosh [Ma77].

Let us now consider the other assumption often used in the application of eq. 1.10, that is, $\lambda = 2$ only but all values of μ allowed. This shape has three mutually perpendicular planes of reflection symmetry, the intersections of which define three principal axes [Bo75a]. It is conventional to take the intrinsic z axis along the longest principal axis, and the intrinsic x axis along the shortest. This results in

$$\alpha_{20} =: \beta \cos\gamma , \qquad \alpha_{2\pm1} = 0 , \qquad \alpha_{2\pm2} =: \frac{1}{\sqrt{2}} \beta \sin\gamma ,$$

$$\beta \geqslant 0 , \qquad 0 \leqslant \gamma \leqslant \frac{\pi}{3} . \tag{1.14}$$

Values of the new parameters β and γ outside the above ranges correspond to other choices of the intrinsic coordinate system [Ei75].

To third order in β,

$$\alpha_{00} = 1 - \frac{\beta^2}{4\pi} + \frac{1}{84\pi}\sqrt{\frac{5}{\pi}}\,\beta^3 \cos\gamma\,(4\cos^2\gamma - 3) \qquad (1.15)$$

and

$$Q_0^{E\lambda} = \rho_0 R_0^{\lambda+3}\Big(\beta\cos\gamma\;\delta_{\lambda 2} + \frac{5}{4\sqrt{\pi}}\,\frac{\lambda+2}{\sqrt{2\lambda+1}}\,C(22\lambda;000)\;\beta^2\{C(22\lambda;000)\cos^2\gamma + C(22\lambda;2\text{-}20)\sin^2\gamma\} - \frac{\lambda+2}{4\pi}\,\delta_{\lambda 2}\,\beta^3\cos\gamma + \frac{5\sqrt{5}}{24\pi}\,\frac{(\lambda+2)(\lambda+1)}{\sqrt{2\lambda+1}} \times \beta^3\cos\gamma \sum_{l} C(22l;000)C(2l\lambda;000)\{C(22l;000)C(2l\lambda;000)\cos^2\gamma \times [2C(22l;202)C(2l\lambda;2\text{-}20) + C(22l;2\text{-}20)C(2l\lambda;000)]\sin^2\gamma\} + O(\beta^4)\Big). \qquad (1.16)$$

Explicit expressions for the quadrupole and hexadecapole moments are

$$Q_0^{E2} = \rho_0 R_0^5[\beta\cos\gamma + 0.3604\;\beta^2\cos 2\gamma + 0.3183\;\beta^3\cos\gamma(1.0715\cos^2\gamma + 0.3043\sin^2\gamma - 1)] \qquad (1.17)$$

and

$$Q_0^{E4} = \rho_0 R_0^7[0.7254\;\beta^2(\cos^2\gamma + 0.1667\sin^2\gamma) + 0.4160\;\beta^3\cos\gamma \times (\cos^2\gamma + 0.7943\sin^2\gamma)]. \qquad (1.18)$$

The following points arise from eqs. 1.14 to 1.18:

(a) These shapes are not ellipsoids. To obtain an ellipsoid of given eccentricities, an expansion involving all even orders of spherical harmonics is required [Lo70].

(b) While eqs. 1.17 and 1.18 reduce to eqs. 1.12 and 1.13 for $\gamma = 0$, they are clearly different for $\gamma = \pi/3$, the upper limit of γ in the conventional representation. Inspection of eqs. 1.17 and 1.18 shows that $\gamma = \pi$ produces equations which correspond to the oblate case of eqs. 1.12 and 1.13. The difficulty can be resolved by writing out the expression for $R(\theta,\phi)$ in detail. This shows $\gamma = \pi/3$ and $\gamma = \pi$ in fact correspond to the same axially symmetric oblate shape but

with different orientations. The shape with $\gamma = \pi$ has the z axis as the symmetry axis whereas the symmetry axis is the y axis for $\gamma = \pi/3$. For the purpose of determining multipole moments then, the conventional choice for the range of γ would seem to be inappropriate. A more symmetric choice is $\gamma = 0$, $\pi/3 < \gamma < 2\pi/3$, $\gamma = \pi$. This ensures that the z axis is the symmetry axis when one exists, and takes the z axis as the axis of intermediate length and the x axis as the long axis in the triaxial cases.

(c) There are values of β and γ with $\beta \neq 0$ for which $Q_0^{E2} = 0$. The value of γ is clearly not $\pi/2$ (because of the terms in $\cos 2\gamma$ and $\sin^2 \gamma$) but differs from $\pi/2$ by an amount which depends on β.

The discussion above emphasizes the point that, even after a considerable number of assumptions (uniform density, zero diffuseness, small deformations, axial symmetry or just quadrupole deformations), ambiguities in the determination of shape parameters from a quadrupole moment still occur. The reason for this is clear. The description of a shape requires a large number of parameters and we have, in general, just one experimental result in the quadrupole moment. After a discussion similar to the above, Mackintosh [Ma77] comments that series expansions "... tend to lose their point once deformations beyond the quadrupole are taken seriously, as they must be". It seems to me that this statement gains most of its force from the current lack of knowledge of hexadecapole and higher order electric moments. Once reliable values of these moments become available, the series expansions method may prove to be more useful.

Until that time, it seems necessary to look for another approach. One other may be to express the radius in terms of functions other than spherical harmonics. It may be possible to find a set of functions whose properties are such that the coefficient of one term in the equation corresponding to eq. 1.12 or eq. 1.17 is much larger than the coefficients of all of the other terms. Then the value of Q_0^{E2} would be largely determined by that one parameter. If, in addition, one had some expectation, based perhaps on a nuclear model,

that the parameter which dominated the expression for Q_0^{E2} was also reasonably significant in the expression for $R(\theta,\phi)$, then one could obtain a better idea of nuclear shapes from quadrupole moments than is possible at present.

1.1.2 The Multipole Moments of a Quantal Object

The multipole moments of a quantum mechanical charge and current distribution are defined by

$$Q_J^{\sigma\lambda} := \langle \upsilon JM{=}J | M(\sigma\lambda,0) | \upsilon JM{=}J \rangle , \tag{1.19}$$

where σ is either "E" to denote "electric" or "M" to denote "magnetic", υ are whatever other quantum numbers are necessary and the multipole moment operators $M(\sigma\lambda,\mu)$ are [A175]

$$M(E\lambda,\mu) = \int \rho(\underset{\sim}{r})\ r^{\lambda}\ Y_{\lambda\mu}(\hat{\underset{\sim}{r}})\ \underset{\sim\sim}{dr} \tag{1.20}$$

and

$$M(M\lambda,\mu) = \frac{1}{\lambda+1} \int r^{\lambda}\ \underset{\sim}{j}(\underset{\sim}{r}) \cdot (\underset{\sim}{r} \times \underset{\sim}{\nabla})\ Y_{\lambda\mu}(\hat{\underset{\sim}{r}})\ \underset{\sim\sim}{dr} , \tag{1.21}$$

$\rho(\underset{\sim}{r})$ and $\underset{\sim}{j}(\underset{\sim}{r})$ being the charge and current densities respectively and $\underset{\sim}{\nabla}$ the vector differential operator. Since nuclear states have definite parity, it follows from eqs. 1.19 - 1.21 that $Q_J^{E\lambda}$ is zero if λ is odd and $Q_J^{M\lambda}$ is zero if λ is even.

To compare the moments $Q_J^{E\lambda}$ with the moments defined in subsection 1.1.1, the state vector $|\upsilon JM\rangle$ is separated into a part describing the orientation of the intrinsic (i.e. body fixed) coordinate system and a part which is referred to that intrinsic system thus [Bo69]

$$|\upsilon JM\rangle = \sqrt{\frac{2J+1}{8\pi^2}}\ \mathcal{D}^J_{MK}(\phi,\theta,\psi)\ |\upsilon\rangle . \tag{1.22}$$

Here $\mathcal{D}^J_{MK}(\phi,\theta,\psi)$ is a rotation matrix element [defined in Bo69] and ϕ, θ, ψ are the Euler angles specifying the orientation of the intrinsic system with respect to the space fixed system. The quantum numbers M and K are the projection of the angular momentum on the space fixed

and intrinsic z axes respectively. The electric multipole operator is also written in terms of an operator $M_{int}(E\lambda,\mu)$ which is referred to the intrinsic system

$$M(E\lambda,\mu) = \sum_{\nu} M_{int}(E\lambda,\nu)\ \mathcal{D}^{\lambda}_{\mu\nu}(\phi,\theta,\psi)\ . \tag{1.23}$$

Insertion of these equations into eq. 1.19 yields

$$Q^{E\lambda}_{J} = C(J\lambda J;J0J)C(J\lambda J;K0K)\ Q^{E\lambda}_{0}\ , \tag{1.24}$$

where

$$Q^{E\lambda}_{0} = \langle \upsilon | M_{int}(E\lambda,0) | \upsilon \rangle \tag{1.25}$$

are the quantum mechanical analogues of the electric moments defined in the previous subsection. Eq. 1.24 is only valid if K is a good quantum number. This is not always so. In the general case, it is necessary to perform a weighted sum over K [Bo75a].

There are many different definitions of the multipole moments in the literature. In the remainder of this thesis, I shall refer to the $Q^{E\lambda}_{0}$ as "intrinsic multipole moments" and $Q^{\sigma\lambda}_{J}$ as "spectroscopic multipole moments". I shall also use quantities, referred to simply as "multipole moments", which are related to the $Q^{\sigma\lambda}_{J}$ as shown in table 1.1. These relations seem to be the ones in general use.

Table 1.1

The relationship between "multipole moments" and "spectroscopic multipole moments".

	Multipole Moment	Spectroscopic Multipole Moment
Dipole	μ_{J^π}	$= \frac{1}{c}\sqrt{\frac{4\pi}{3}}\ Q^{M1}_{J}$
Quadrupole	Q_{J^π}	$= \sqrt{\frac{16\pi}{5}}\ Q^{E2}_{J}$
Hexadecapole	H_{J^π}	$= \sqrt{\frac{16\pi}{9}}\ Q^{E4}_{J}$

From eq. 1.24 it can be seen that, no matter what the value of Q^{E2}_{0}, Q^{E2}_{J} is always zero for $J = 0$ or $J = \frac{1}{2}$.

1.1.3 N-body Quadrupole Moments

So-called "n-body quadrupole moments" were introduced by Kumar [Ku72, Ku75a] in an attempt to find "... a method which does not require the assumption of a specific nuclear model for determining some quantities which measure the intrinsic nuclear quadrupole moments" [Ku72]. They have also been discussed by Cline *et al.* [Cl72, Cl73].

So that the n-body quadrupole moments will not be constrained to be zero for certain J-values, Kumar defined his n-body quadrupole moment operator to be the following rank-zero tensor:

$$M(E2;n) := [[...[M(E2) \times M(E2)]_{\ell_1} \times ... \times M(E2)]_{\ell_{n-3}} \times M(E2)]_2 \cdot M(E2) . \tag{1.26}$$

The notations used here for the products of spherical tensor operators are

$$[M(\sigma_1\lambda_1) \times N(\sigma_2\lambda_2)]_{\ell m} := \sum_{\mu} C(\lambda_1\lambda_2\ell;\mu m-\mu m)\ M(\sigma_1\lambda_1,\mu)M(\sigma_2\lambda_2,m-\mu) \tag{1.27}$$

and

$$M(\sigma_1\lambda)\cdot N(\sigma_2\lambda) := (-)^{\lambda}\sqrt{2\lambda+1}\ [M(\sigma_1\lambda) \times N(\sigma_2\lambda)]_0 , \tag{1.28}$$

where the projection quantum numbers are often suppressed as in eq. 1.28. The expectation values of the operators defined in eq. 1.26 are evaluated by inserting as many complete sets as are necessary to obtain products of the expectation values of $M(E2,\mu)$.[†] For example, for the state m,

$$\begin{aligned} Q^{E2(2)}_{J_m} &:= \langle \upsilon_{m\,m\,m}\, J\, M_m | M(E2)\cdot M(E2) | \upsilon_{m\,m\,m}\, J\, M_m \rangle \\ &= \sum_{z\mu} |\langle \upsilon_{m\,m\,m}\, J\, M_m | M(E2,\mu) | \upsilon_{z\,z\,z}\, J\, M_z \rangle|^2 . \end{aligned} \tag{1.29}$$

[†] The following derivation is given in detail as it overcomes a difficulty in Kumar's derivation. Kumar's conclusions are all correct, but clearly his eq. 8 [Ku72] has a zero in the denominator if his I_s (my J) equals zero or one-half. The resolution of the problem is that his $Q_s{}^S$ is also zero under these conditions, and the zeros "cancel", as my derivation shows.

The matrix element is zero if the triangle relation $\Delta(J_m\ J_z 2)$ does not hold. For other cases, eq. 1.29 can be simplified by use of the Wigner-Eckart theorem [Bo69]

$$\langle \upsilon_2 J_2 M_2 | M(\sigma\lambda,\mu) | \upsilon_1 J_1 M_1 \rangle = (2J_2+1)^{-\frac{1}{2}}\, C(J_1 \lambda J_2; M_1 \mu M_2) \times \langle \upsilon_2 J_2 \| M(\sigma\lambda) \| \upsilon_1 J_1 \rangle \qquad (1.30)$$

to give

$$Q^{E2(2)}_{J_m} = (2J_m+1)^{-1} \sum_z (-)^{J_z - J_m} |\langle \upsilon_m J_m \| M(E2) \| \upsilon_z J_z \rangle|^2 . \qquad (1.31)$$

Similarly,

$$Q^{E2(3)}_{J_m} = \sqrt{5}\ (2J_m+1)^{-1} \sum_{zz'} W(22J_m J_z; 2J_{z'}) \langle \upsilon_m J_m \| M(E2) \| \upsilon_{z'} J_{z'} \rangle \times \langle \upsilon_{z'} J_{z'} \| M(E2) \| \upsilon_z J_z \rangle \langle \upsilon_z J_z \| M(E2) \| \upsilon_m J_m \rangle , \qquad (1.32)$$

where W(abcd;ef) is a Racah coefficient [Ro57]. The sums in these equations include the state m as well as all other states connected to it by E2 matrix elements. They exclude, however, any state for which the triangle relation $\Delta(J_m\ J_z 2)$ does not hold.

Kumar relates the $Q^{E2(n)}_{J_m}$ to the shape of the nucleus by considering the moments of an equivalent ellipsoid. These are written as [Ku75a]

$$Q^{E2,\mu}_{(e)} := \int \rho_e(\underset{\sim}{r})\ r^2\ Y_{2\mu}(\hat{\underset{\sim}{r}})\ d\underset{\sim}{r} , \qquad (1.33)$$

where (e) indicates that we are considering the ellipsoidal charge distribution $\rho_e(\underset{\sim}{r})$. The reflection symmetry of the system leads to

$$Q^{E2,0}_{(e)} =: Q^{E2}_{(e)} \cos\Gamma$$

$$Q^{E2,\pm1}_{(e)} = 0$$

$$Q^{E2\pm2}_{(e)} =: 2^{-\frac{1}{2}} Q^{E2}_{(e)} \sin\Gamma \qquad (1.34)$$

which defines the quantities $Q^{E2}_{(e)}$ and Γ. The parameter B is defined as the ratio of the quadrupole moment to the mean square radius:

$$B := Q^{E2}_{(e)} \Big/ \int \rho(\underset{\sim}{r})\, r^2\, \underset{\sim}{dr}\,. \tag{1.35}$$

By replacing the expectation values of $M(E2,\mu)$ in eqs. 1.31 and 1.32 with $Q^{E2,\mu}_{(e)}$ and ignoring the sum over states, one obtains

$$Q^{E2}_{(e)} = \sqrt{Q^{E2\,(2)}_{J}} \tag{1.36}$$

and

$$\cos 3\Gamma = -\sqrt{\frac{7}{2}}\, Q^{E2\,(3)}_{J} \left(Q^{E2\,(2)}_{J}\right)^{-\frac{3}{2}}. \tag{1.37}$$

Thus Γ can be determined if the 2-body and 3-body quadrupole moments are known. Kumar shows that, for a uniformly charged ellipsoid of total charge Z, B is the real solution of

$$\left(\sqrt{\frac{5}{4\pi}}\, B\right)^3 \left[\frac{216\, Z^3 R_0^6}{125\left(Q^{E2}_{(e)}\right)^3} \left(\frac{5}{16\pi}\right)^{\frac{3}{2}} - 2\cos 3\Gamma\right] + \frac{15B^2}{4\pi} - 1 = 0\,, \tag{1.38}$$

where R_0 is the radius of the sphere with the same volume as the ellipsoid.

The parameters B,Γ are not the same as the parameters β,γ of the previous subsection. The deformation described by B,Γ is ellipsodal, whereas that described by β,γ has the $(1 + Y_{2\mu})$ shape. The two sets of parameters approach one another in the limit $\beta \to 0$ [Ro78].

The procedure for determining the shape of the nucleus in state m consists of using experimentally determined reduced matrix elements to compute the 2- and 3-body quadrupole moments (eqs. 1.31 and 1.32) and then determining B and Γ through eqs. 1.36 - 1.38. If this method is to be used, one must have some idea of how the results will be affected by "missing strength", that is, terms in eqs. 1.31 and 1.32 whose values are not known due to incomplete experimental data. This question has been investigated at some length by Kumar [Ku75a] and Cline and Flaum [Cl72]. The general conclusions are:

(a) the more collective a nucleus, the more the strength will be concentrated among a few states.

(b) the number of states which must be considered increases rapidly with the order n of the n-body moment.

(c) sufficient experimental evidence is probably available for many nuclei to determine $Q_J^{E2(2)}$ and $Q_J^{E2(3)}$ reasonably reliably.

For these reasons, I have not considered n-body moments with $n > 3$, although some of these can be related to the softness of the nucleus to β and γ vibrations [Ku75a]. For similar reasons, I have confined my attention to n-body quadrupole moments only. The formalism could be applied to any other multipolarity (E4 would be an interesting case) but there are not yet sufficient experimental data to make it worthwhile.

One practical problem in the evaluation of the n-body moments with $n > 2$ is that, in general, only the absolute values of non-diagonal matrix elements are known from experiment. This is because these matrix elements are derived from partial decay widths which are proportional to the squares of the matrix elements. Thus, in general, the relative phases of the terms in the expressions for $Q_J^{E2(n)}$ are not known. This restricts the applicability of the method to those levels which are only connected to a few other levels so that the sums contain only a small number of terms.

In summary, we may enquire as to the extent that Kumar's aim, quoted at the beginning of this subsection, has been fulfilled. It is certainly true that the n-body moments $Q_J^{E2(n)}$ are defined in a way which is model independent and which permits them, in principle, to be determined from experimental data. However, in order to interpret the values of $Q_J^{E2(n)}$ in terms of a shape, a model must be introduced. Kumar chooses to use an ellipsoid. It would be very interesting to know by how much the inferred shape would be altered if other choices were made. The big advantage of the n-body moment method is that, by using the dynamic moments of a state, one can determine both B and Γ. The analysis of the previous subsection, which used static moments

only, could only give a relationship between β and γ (unless the E4 moment is known).

1.1.4 Some Limitations

Having described two methods of extracting nuclear shapes from multipole moment measurements, it may be worthwhile to list some of the problems with the philosophy of this procedure. Some which come to mind are:

(a) Electric multipole moments mainly provide information about the distribution of protons in the nucleus, they say little about neutron distributions.

(b) Since the electric 2^{λ}-pole moment operator contains the factor r^{λ}, its expectation value gets its largest contribution near the nuclear surface and so, while it may be useful in outlining the shape of the surface, its value is relatively insensitive to the details of the nuclear interior. It could be argued that this is only a problem if "shape" is interpreted to mean "density distribution of nuclear matter" rather than "outline of nuclear surface". One is, however, forced by the diffuseness of the nuclear surface to adopt the former interpretation. That is, the nuclear surface can only be defined by a statement involving the nuclear density distribution.

(c) It is rarely possible to measure any other than the quadrupole moment and there are very many shapes which can have the same quadrupole moment, as fig. 1.1 illustrates. This is partly a practical difficulty — experimental values of higher multipolarity moments are not yet available — but it may also be a limitation in principle. This is because, for reasons analogous to those which require a state with $J < 1$ to have a zero quadrupole moment regardless of its intrinsic shape, a state must have $J \geqslant 2$ if it is to have a non-zero hexadecapole moment. Generalizing the argument, one finds that states with $J = 0$ have all multipole moments

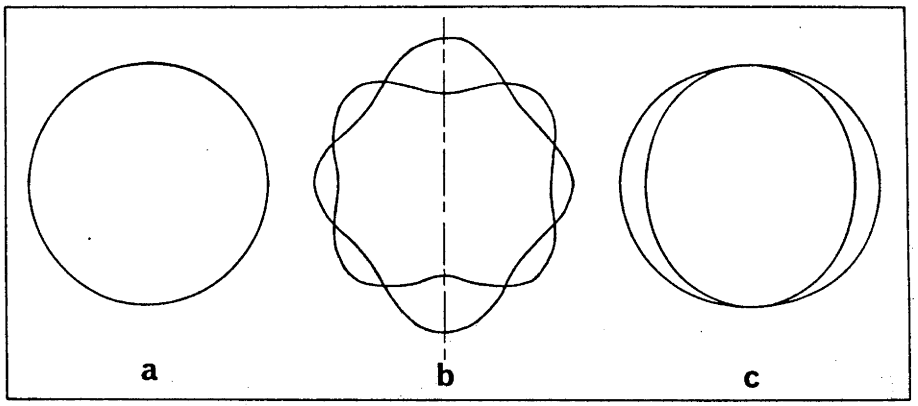

Fig. 1.1: Four shapes all having $Q_0^{E2} = 0$: (a) a sphere, (b) two axially symmetric shapes, (c) a "triaxial" shape. The outer curve in part (c) is the cross section in the xz plane and the inner curve is the cross section in the yz plane.

zero, those with $J = 1$ can only have non-zero E2 moments, those with $J = 2$ only non-zero E2 and E4 moments and so on. Thus the amount of available information about the shape of a nucleus in a given state is restricted by the angular momentum of that state. In the limit of $J = 0$, no model-independent information is available.

1.2 THEORETICAL PREDICTIONS

In this section the results of some models of the structure of low-lying states of even-even nuclei will be presented. Emphasis will be placed on predictions of the properties, and in particular, of the quadrupole moment of the first excited state. The literature is very extensive and some representative references will be given in the appropriate places. The first few subsections are devoted to the simplest phenomenological models. These yield many simple predictions which seem to be fairly accurate for some nuclei. Later subsections give very brief descriptions of some of the more complex models. It is usually true that the more complex the model, the fewer general predictions can be made. One must then rely on the availability of calculations appropriate to the particular nucleus in question to test these models.

1.2.1 The Harmonic Vibrational Model

The Hamiltonian of this system is [Bo75a, Ei75]

$$H = \sum_{\lambda} \frac{1}{2B_\lambda} \pi_\lambda \cdot \pi_\lambda + \frac{1}{2} C_\lambda \alpha_\lambda \cdot \alpha_\lambda \,, \tag{1.39}$$

where $\pi_{\lambda\mu}$ are the momenta conjugate with the deformations $\alpha_{\lambda\mu}$ which are the operator analogues of the deformations defined in subsection 1.1.1. The inertia parameters B_λ and stiffness parameters C_λ can either be empirically determined, or can be calculated by making further assumptions about the nucleus. The subscript λ labels the multipolarity of the vibration; $\lambda = 2$, the quadrupole vibration, is the lowest order vibration.

The Hamiltonian (eq. 1.39) can be cast in a form involving creation and annihilation operators. The resulting eigenstates are labelled by the number of phonons N_λ of multipolarity λ, the total angular momentum J, its projection M on the z axis and whatever other quantum numbers υ which are needed. I will denote the state vectors by $|\upsilon N_2 N_3 \ldots JM\rangle$. The energy levels of the harmonic oscillator are [Da68]

$$E = \sum_{\lambda} (N_\lambda + \lambda + \tfrac{1}{2}) \hbar \sqrt{C_\lambda / B_\lambda} \,. \tag{1.40}$$

This equation seems to imply that the energy of the vacuum state, that is, the state with $N_\lambda = 0$ for all λ, is infinite since $\sqrt{C_\lambda/B_\lambda}$ increases with increasing λ in any realistic model. One might infer therefore, that there is an upper limit on the possible values of λ. A shape of multipolarity λ can be pictured as λ protrusions from a sphere. It has been argued that each protrusion must contain a particle so that an upper limit on λ is given by the number of fundamental particles in the nucleus.

One phonon states have angular momenta $J = \lambda$ and two phonon states are degenerate multiplets with $J = 0,2,4,\ldots,2\lambda$ if the phonons are identical and $J = |\lambda_1-\lambda_2|, |\lambda_1-\lambda_2|+1, \ldots \lambda_1+\lambda_2$ otherwise. The values of J for a level of three identical phonons are given by Davidson [Da68]. Bohr and Mottelson [Bo75a] give general methods for determining these

J values. The parity of the levels is even unless the state contains an odd number of odd multipolarity phonons.

In order to determine the relative energies of the levels, it is necessary to have relations between the value of B_λ and C_λ for various λ. These are often derived by assuming that the vibrational motion of the nucleus can be described as the flow of an inviscid incompressible fluid of constant mass density. One then obtains [Ei75]

$$B_\lambda = 3AR_0^2/4\pi\lambda \tag{1.41}$$

and

$$C_\lambda = (\lambda-1)\left((\lambda+2)\ R_0^2\sigma - \frac{3Z^2e^2}{8\pi^2\varepsilon_0(2\lambda+1)R_0}\right), \tag{1.42}$$

where R_0 is the mean radius, σ the surface tension, Z the atomic number and A the mass of the nucleus. It follows that the first excited state is the $N_\lambda = \delta_{\lambda 2}$ state.

It is commonly stated [e.g. Bo75a, Ku75] that, in this model, matrix elements of the electric multipole operator $M(E\ell,\mu)$ between states $|\upsilon N_2 \ldots JM\rangle$ and $|\upsilon' N_2' \ldots J'M'\rangle$ are zero unless the rule

$$N_\lambda - N_\lambda' = \pm\delta_{\lambda\ell} \tag{1.43}$$

holds. This rule implies that all electric multipole moments are zero. Eisenberg and Greiner [Ei75] show that this is correct to first order only. They demonstrate that, for a nucleus with a shape and density given by eqs. 1.1 and 1.2, the electric multipole operators expressed in terms of the collective coordinates $\alpha_{\lambda\mu}$ have the form

$$M_{coll}(E\lambda,\mu) = \frac{3eZR_0}{4\pi}\left(\alpha_{\lambda\mu} + \frac{\lambda+2}{4\sqrt{\pi}}\sum_{\substack{\lambda_1\lambda_2\\ \nu_1\nu_2}}\sqrt{\frac{(2\lambda_1+1)(2\lambda_2+1)}{2\lambda+1}}\right.$$
$$\left.\times\, C(\lambda_1\lambda_2\lambda;000)C(\lambda_1\lambda_2\lambda;\nu_1-\nu_2\mu)\ \alpha_{\lambda_1\nu_1}\alpha_{\lambda_2\nu_2} + O(\alpha_{\lambda\mu}^3)\right) \tag{1.44}$$

analogous with eq. 1.10 for the classical multipole moments of this charge distribution. The selection rule of eq. 1.43 applies only to the matrix elements of the first term of eq. 1.44. In particular, the quadrupole moment of the first excited state (the $N_\lambda = \delta_{\lambda 2}$ state) is

given to second order by [Ei75]

$$Q_{2^+} = -\frac{6}{7\pi} ZeR_0^2\hbar(B_2C_2)^{-\frac{1}{2}} . \qquad (1.45)$$

There will also be non-zero values of matrix elements for transitions which do not obey eq. 1.43, but these will be small compared to those which do obey eq. 1.43 as they arise from higher order terms in eq. 1.44.

The reduced transition probability $B(\sigma\lambda;J_i \to J_f)$ is defined by

$$B(\sigma\lambda;J_i \to J_f) := (2J_i+1)^{-1} \left| \langle J_f \| M(\sigma\lambda) \| J_i \rangle \right|^2 , \qquad (1.46)$$

where σ is either E or M. For the first excited state, this model predicts

$$B(E2;0^+ \to 2^+) = \frac{45}{32\pi^2} Z^2e^2R_0^4\hbar(B_2C_2)^{-\frac{1}{2}} \qquad (1.47)$$

to lowest order in the electric quadrupole operator. The applicability of this model to real nuclei is often judged by comparing both the energy level predictions of eq. 1.40 and the prediction

$$B(E2;J^+ \to 2^+)/B(E2;2^+ \to 0^+) = 2 \qquad (1.48)$$

(J^+ being any of the "2 phonon" levels) with experimental values.

The lower part of a vibrational energy spectrum is shown in fig. 1.2. The parameters $Z = 80$, $A = 198$, $R_0 = 1.25\ A^{1/3}$ fm and $\sigma = 17$ MeV fm^{-2} were used to generate the relative spacings of the levels (see eqs. 1.41 and 1.42). This value of the surface tension σ is consistent with the semi-empirical mass formula [Bo69]. The transitions shown in fig. 1.2 are all those for which eq. 1.43 holds.

A quantity which will be required in the analysis of the experiments and which is not readily available from other experimental data (see ch. 4) is the sign of the product

$$p_3 := \langle 2_1^+ \| M(E2) \| 0^+ \rangle \langle 2_2^+ \| M(E2) \| 0^+ \rangle \langle 2_2^+ \| M(E2) \| 2_1^+ \rangle . \qquad (1.49)$$

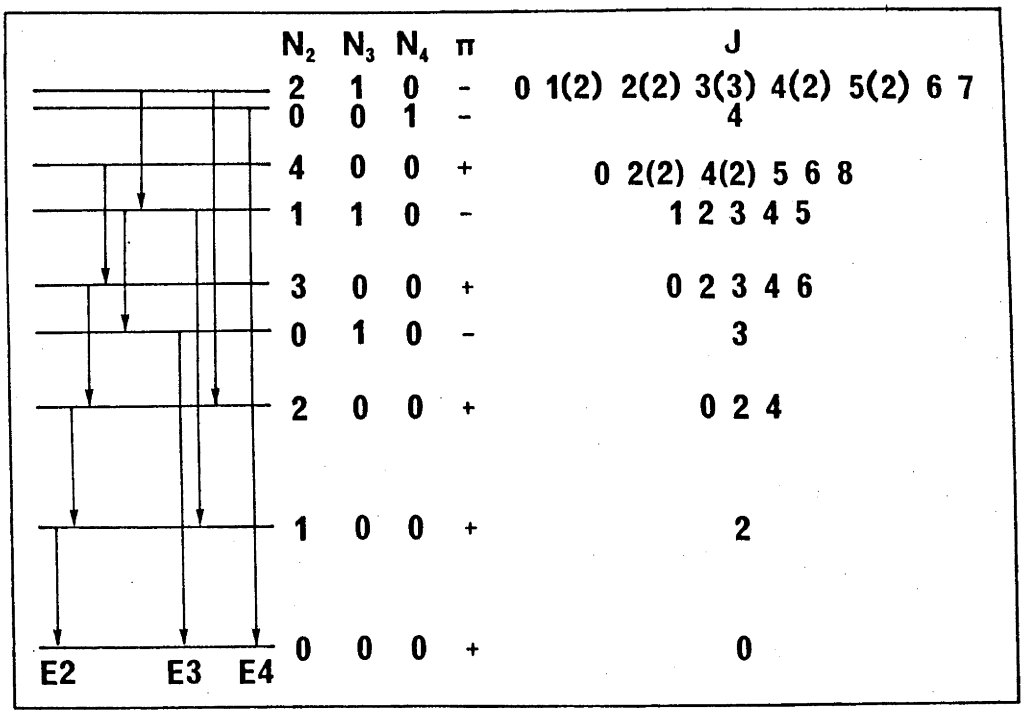

Fig. 1.2: The lower part of the energy spectrum of ^{198}Hg as predicted by the harmonic vibrational model with inviscid irrotational flow. Alongside each degenerate multiplet of levels is shown the number of quadrupole, octupole and hexadecapole phonons for that multiplet, the parity and the various J-values of the levels in the multiplet. The numbers in brackets show the number of times a J-value occurs where this differs from one. Also shown are the strongest E2, E3 and E4 transitions predicted.

However, to make the result independent of the phase convention used for the wave functions and multipole operators, it is more usual to quote the sign of the product

$$p_4 := p_3 \langle 2_1^+ \| M(E2) \| 2_1^+ \rangle . \tag{1.50}$$

This model predicts

$$p_4 > 0 . \tag{1.51}$$

1.2.2 Anharmonic Effects

The general Hamiltonian for quadrupole vibrations about a spherical equilibrium shape can be written

$$H = T(\pi_2, \alpha_2) + V(\alpha_2) , \tag{1.52}$$

where α_2, π_2 are quadrupole deformation operators and the conjugate momenta. The kinetic energy operator T and the potential energy operator V are given by

$$T(\pi_2, \alpha_2) = \frac{1}{2B_2} \pi_2 \cdot \pi_2 + \frac{1}{2B_2'} [\pi_2 \times \alpha_2]_2 \cdot \pi_2 + \ldots \tag{1.53}$$

and

$$V(\alpha_2) = \tfrac{1}{2}C_2 \alpha_2 \cdot \alpha_2 + \tfrac{1}{2}C_2' [\alpha_2 \times \alpha_2]_2 \cdot \alpha_2 + \tfrac{1}{2}C_2'' [\alpha_2 \times \alpha_2] \cdot [\alpha_2 \times \alpha_2] + \ldots . \tag{1.54}$$

These equations are the most general possible if the Hamiltonian is to be invariant under rotation, spatial inversion and time reversal [Ei75].

The first terms of each of eqs. 1.53 and 1.54 give the Hamiltonian for the quadrupole harmonic oscillator. One should note that the general Hamiltonian for all multipolarities of vibrations cannot be obtained by merely replacing the "2"s by "λ"s in eqs. 1.52 - 1.54 and summing over λ. Cross terms such as $[\alpha_3 \times \alpha_3]_2 \cdot \alpha_2$ must also be considered.

The anharmonic terms are usually invoked to explain the following empirical facts:—

(a) the quadrupole moment of the first excited state of "vibrational" nuclei (e.g. the even-mass cadmium isotopes) is $\sim$ 10 times the value given by eq. 1.45.

(b) the energies of multiphonon states depend on J as well as N_λ.

(c) $\Delta N_2 = 2$ electromagnetic transitions are stronger than is expected.

An indication of how anharmonicities can explain these effects is obtained by considering the second term in eq. 1.54 and assuming that the effect of the anharmonicity is sufficiently small for perturbation theory to be used. Since the perturbing potential is a spherical tensor of rank zero and is a product of three creation or annihilation

operators, the state which was described as $|\upsilon N_2 JM\rangle$ in the harmonic approximation will be mixed with small amounts of $|\upsilon N_2 \pm 1 JM\rangle$ and $|\upsilon N_2 \pm 3 JM\rangle$. Thus the ground state is

$$|0_1^+\rangle = |000\rangle + \frac{1}{2}\frac{C_2'}{C_2}\sqrt{\frac{1}{3}\hbar(B_2C_2)^{-\frac{1}{2}}}\,|300\rangle + O(C_2'^2) \qquad (1.55)$$

and the first excited state is

$$|2_1^+M\rangle = |12M\rangle + \frac{3}{2}\frac{C_2'}{C_2}\sqrt{\hbar(B_2C_2)^{-\frac{1}{2}}}\,|22M\rangle$$
$$+ \text{terms involving } N_2 = 4 \text{ states} + O(C_2'^2)\,. \qquad (1.56)$$

The admixture of the $N_2 = 2$ eigenstate in the first excited state permits the first order term of the electric quadrupole operator to have a non-zero expectation value, so that the spectroscopic quadrupole moment of the first excited state is, to first order in C_2',

$$Q^{E2}_{2_1^+} = \frac{9}{2\pi} Ze\hbar R_0^2 (7B_2C_2)^{-\frac{1}{2}}\frac{C_2'}{C_2}\,. \qquad (1.57)$$

It has been estimated [Sp77a] that a first excited state containing $\sim 5\%$ of the two phonon eigenstate is sufficient to account for the measured values of $Q^{E2}_{2^+}$ in the even cadmium isotopes.

Clearly the second excited 2^+ state will contain a corresponding admixture of $|12M\rangle$ and so will have a "first order" decay to the ground state, thus explaining point (c) above. The explanation of the splitting of the multiphonon multiplets is less clear. The change of energy due to the second term of eq. 1.54 is, to lowest order, quadratic in C_2', while that due to the third term is linear in C_2''. Which of these is the larger clearly depends on the relative magnitudes of the two stiffness parameters.

Other results of interest are that, to first order, $B(E2; 0_1^+ \to 2_1^+)$ is still given by eq. 1.47 but [Ku69]

$$p_4 < 0\,. \qquad (1.58)$$

1.2.3 The Rigid Rotational Model

The Hamiltonian for a non-spherical rigid body rotating about its centre of mass is [Ei75]

$$H = \sum_k \tfrac{1}{2} L_k^2 / I_k \,, \tag{1.59}$$

where k numbers the principal axes of the intrinsic (body-fixed) system, L_k are the components of the angular momentum operator and I_k are the principal moments of inertia.

The simplest case is that of axial symmetry and it is usual to take the 3 axis as the symmetry axis, so that $I_1 = I_2 \neq I_3$. Since the 3 axis is a symmetry axis, the angular momentum cannot have a component in that direction. The eigenstates are then identified by the total angular momentum J and its projection M on the space-fixed z axis. The energies of these eigenstates are given by

$$E = \tfrac{1}{2}\hbar^2 J(J+1)/I_1 \,. \tag{1.60}$$

Because of the invariance of the Hamiltonian (1.59) under reflections in the intrinsic 1-2 plane, only even values of J are allowed [Bo75a].

To compute reduced transition probabilities, the eigenstates and multipole operators are written in terms of the intrinsic axes and the Euler angles which relate the intrinsic and space-fixed systems (eqs. 1.22 and 1.23). In particular, the spectroscopic quadrupole moments are related to the intrinsic quadrupole moment Q_0^{E2} by eq. 1.24 (with K = 0) and the reduced transition probabilities are given by

$$B(E2; J_i \rightarrow J_f) = [C(J_i 2 J_f; 000)\ Q_0^{E2}]^2 \,. \tag{1.61}$$

If the nucleus is taken to have a Y_{20} deformation only, then [Da68]

$$I_1 = 3B_2\beta_2^2 \,, \tag{1.62}$$

where B_2 is an inertia parameter (eq. 1.39). Using eq. 1.10, and writing $4/3\ \pi\rho_0 R_0^3 = Ze$, one finds for J = 2

$$Q_{2^+}^{E2} = -\frac{6ZeR_0^2}{28\pi}\beta_2\left(1 + \frac{2}{7}\sqrt{\frac{5}{\pi}}\beta_2 + \ldots\right). \qquad (1.63)$$

Since there is no second 2^+ state in this model, the product p_4 of eq. 1.50 is not defined.

The relaxation of the requirement of axial symmetry allows the angular momentum to have a projection K on the intrinsic 3 axis. However, this projection is no longer a good quantum number as the Hamiltonian does not commute with L_3. The eigenstates can be labelled by J_n and M where J and M are the usual angular momentum quantum numbers, and n counts the number of states of that particular J from the ground state. The eigenstates are then [Ei75]

$$|J_nM\rangle = \sum_k A_{JKn}(\gamma)\ |JKM\rangle, \qquad (1.64)$$

where $|JKM\rangle$ are eigenfunctions of that part of the Hamiltonian which is diagonal in L_3. The parameters $A_{JKn}(\gamma)$ depend on the asymmetry angle γ (eq. 1.14) and are tabulated in refs. Da59 and Ei75.

For $\gamma < 15°$, the states of eq. 1.64 are dominated by one value of K [Da59]. In the limit of axial symmetry (i.e. $\gamma \to 0$) the energies of the levels are given by [Da68]

$$E = \frac{\hbar}{2I_1}J(J+1) + \tfrac{1}{2}\hbar\left(\frac{1}{I_3} - \frac{1}{I_1}\right)K^2 \qquad (1.65)$$

and the moment of inertia I_1 about the intrinsic 1 axis approaches the value given by eq. 1.62. Also, the moment of inertia I_3 about the intrinsic 3 axis, given by [Da68]

$$I_3 = 4B_2\beta_2^2\sin^2\gamma, \qquad (1.66)$$

approaches zero. Clearly then, the energies of the levels are functions of γ and this can be used to determine γ for a given nucleus. For example, the energies of the two J = 2 states are [Da58]

$$E = \frac{9\hbar^2}{4B_2\beta^2}\sin^{-2}3\gamma\left(1 \pm \sqrt{1 - \frac{8}{9}\sin^2 3\gamma}\right) \qquad (1.67)$$

and that of the J = 3 state is

$$E = \frac{9\hbar^2}{2B_2\beta^2} \sin^{-2} 3\gamma . \tag{1.68}$$

A table of level energies for many levels has been computed by Moore and White [Mo60] and fig. 1.3 shows some of these energies. One simple result of this model, which allows its applicability to be readily tested, is the existence of certain identities between various excitation energies. Two of these are [Ei75]

$$\begin{aligned} E(2_1) + E(2_2) &= E(3_1) , \\ 4E(2_2) + E(2_2) &= E(5_1) . \end{aligned} \tag{1.69}$$

The spectroscopic moment of the first excited state of a non-axial rigid rotor is given by [Da58]

$$Q^{E2}_{2^+} = - Q^{E2}_0 \frac{6}{7} \cos 3\gamma (9 - 8 \sin^2 3\gamma)^{-\frac{1}{2}} \tag{1.70}$$

which reduces to eq. 1.24 for $\gamma\big|_{\text{mod } \pi/3} = 0$ (and hence $K = 0$). The expressions for reduced transition probabilities are also functions of γ. Some of these are [Da58]

$$\begin{aligned} B(E2;2_n \rightarrow 0) &= \tfrac{1}{2}(Q^{E2}_0)^2 \left(1 \pm \frac{3 - 2 \sin^2 3\gamma}{\sqrt{9 - 8 \sin^2 3\gamma}} \right) \\ &\qquad (+ \text{ sign for } n = 1, - \text{ sign for } n = 2) , \\ B(E2;2_2 \rightarrow 2_1) &= \frac{10}{7} (Q^{E2}_0)^2 \frac{\sin^2 3\gamma}{9 - 8 \sin^2 3\gamma} . \end{aligned} \tag{1.71}$$

It is concluded [Da59] that E2 transitions between levels in this model fall into three categories:

(a) Transitions between members of the "ground state band" (i.e. those levels which remain when $\gamma = 0$) and transitions between members of the "anomalous band". These are strong transitions.

(b) Transitions between members of the two bands which have the same J values. The reduced transition probabilities for these transitions are zero for $\gamma = 0$ and rise to values of the order of those of group (a) for $\gamma = 30°$.

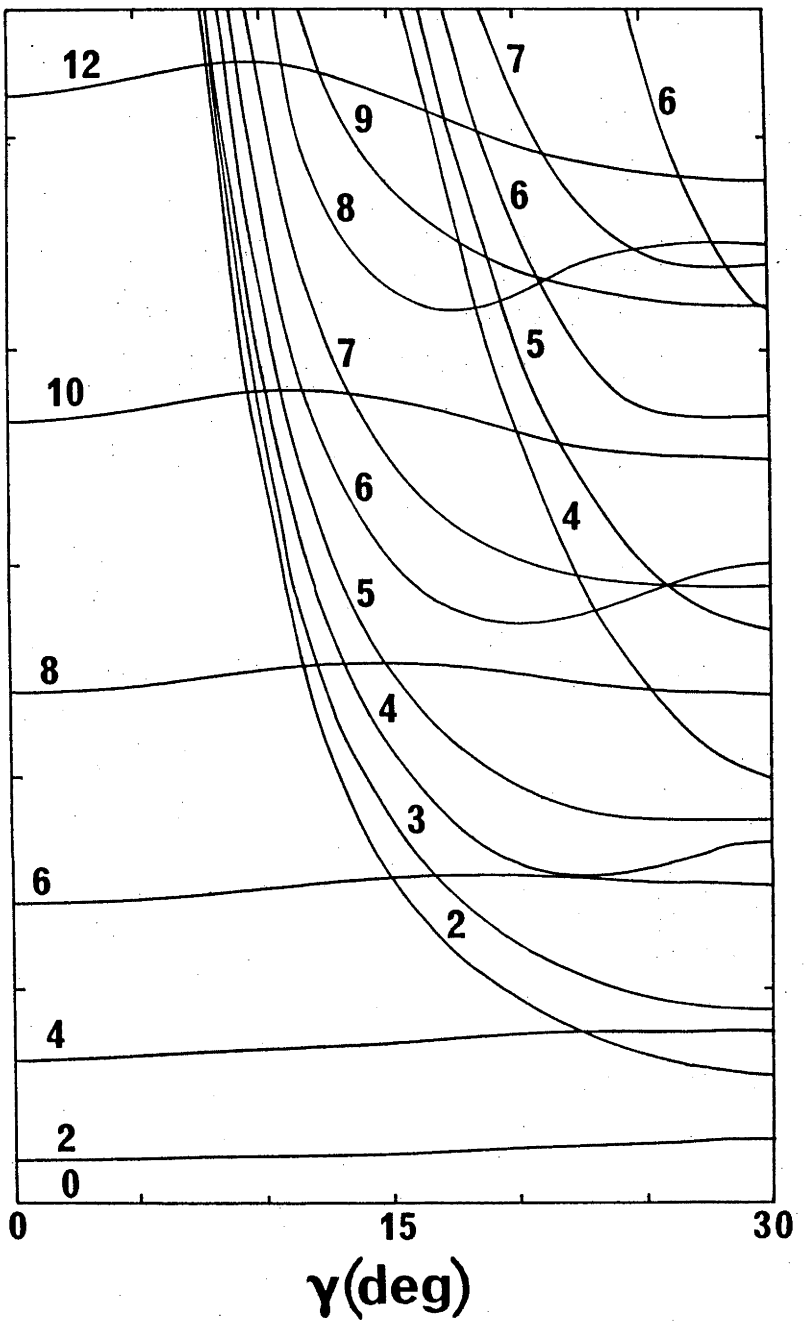

Fig. 1.3: The dependence of the relative spacings of the lowest energy levels predicted by the asymmetric rigid rotational model on the asymmetry angle γ. The levels are labelled by their angular momenta. The scale on the y axis is in units of the excitation energy of the first $J = 2$ state at $\gamma = 0$.

(c) Other transitions which are possible under angular momentum selection rules. These have zero reduced transition probabilities for $\gamma = 0$ and $\gamma = 30°$ and small values in between. An exception is the transition $3_1^+ \rightarrow 4_1^+$ which behaves as if it belongs to group (b).

In this model [Is69]

$$p_4 < 0 . \tag{1.72}$$

1.2.4 The Rotation-Vibration Model

Many nuclei have level schemes which appear to consist of rotational bands, but with relatively low-lying excited 0^+ states. Such level schemes can be produced by considering vibrations about a non-spherical equilibrium. Two such models have been described [Fa65, Da60]. Both consider harmonic quadrupole vibrations about equilibrium values β_0, γ_0 of the deformation parameters (eq. 1.14) thus

$$V(\beta,\gamma) = \tfrac{1}{2}C_\beta(\beta - \beta_0)^2 + \tfrac{1}{2}C_\gamma(\gamma - \gamma_0)^2 . \tag{1.73}$$

In one model, the equilibrium deformation is assumed to be axially symmetric ($\gamma_0 = 0$), while the other model considers β vibrations only ($C_\gamma = \infty$).

The Hamiltonian for the rotations and vibrations of a system with a non-spherical but axially symmetric equilibrium shape may be written

$$H = H_r + H_v + H_{rv} , \tag{1.74}$$

where explicit forms for each part are given by Eisenberg and Greiner [Ei75]. The first two parts are diagonal in L_3 and can be easily solved. The coupling Hamiltonian H_{rv} may be treated, for low angular momenta at least, as a small perturbation [Ei75].

Eigenstates of the Hamiltonian $H_r + H_v$ are described as $|n_\beta n_\gamma KJM\rangle$ where n_β and n_γ are the number of quadrupole phonons for β and γ vibrations respectively, J and M are the usual angular momentum quantum numbers and K is the projection of the angular momentum on the

intrinsic 3 axis. The energies of these eigenstates are given by [Ei75]

$$E = E_r[J(J+1) - K^2] + E_\beta(n_\beta + \tfrac{1}{2}) + E_\gamma(\tfrac{1}{2}|K| + 2n_\gamma + 1) , \qquad (1.75)$$

where the characteristic energies E_r, E_β and E_γ are given by

$$E_r = \frac{\hbar}{6B_2\beta_0^2}, \qquad E_\beta = \hbar\sqrt{\frac{C_\beta}{B_2}}, \qquad E_\gamma = \hbar\sqrt{\frac{C_\gamma}{B_2}}. \qquad (1.76)$$

Because of various symmetries of the Hamiltonian, K is restricted to even integers only, and J is also restricted to even integers if $K=0$. In addition, all states have even parity.

The states are arranged into bands identified by n_β, n_γ and K. Quadrupole moments and reduced transition probabilities between states within a band are [Ei75]

$$Q^{E2}_{J^+} = C(J2J;J0J)C(J2J;K0K)\ Q^{E2}_0$$

$$B(E2;J_i \to J_f) = \left(C(J_i 2J_f;K0K)\ Q^{E2}_0\right)^2 , \qquad (1.77)$$

where Q^{E2}_0 is given by eq. 1.25. For transitions between bands, ratios of the characteristic energies enter into the expression for the B(E2). For example [Ei75]

$$B(E2;100J_i \to 000J_f) = \frac{3E_r}{E_\beta}\left(C(J_i 2J_f;000)\ Q^{E2}_0\right)^2$$

$$B(E2;002J_i \to 000J_f) = \frac{6E_r}{E_\gamma}\left(C(J_i 2J_f;022)\ Q^{E2}_0\right)^2 , \qquad (1.78)$$

where the quantum numbers are given in the order $n_\beta n_\gamma KJ$. Generally E_r is considerably smaller than either of the other two characteristic energies so that the cross-band transitions are weaker than the in-band transitions. A schematic diagram of the energy levels predicted by this approximation is shown in fig. 1.4.

So far, the coupling term H_{rv} has been ignored. For low values of J, it can be treated as a perturbation, the effect of which is to

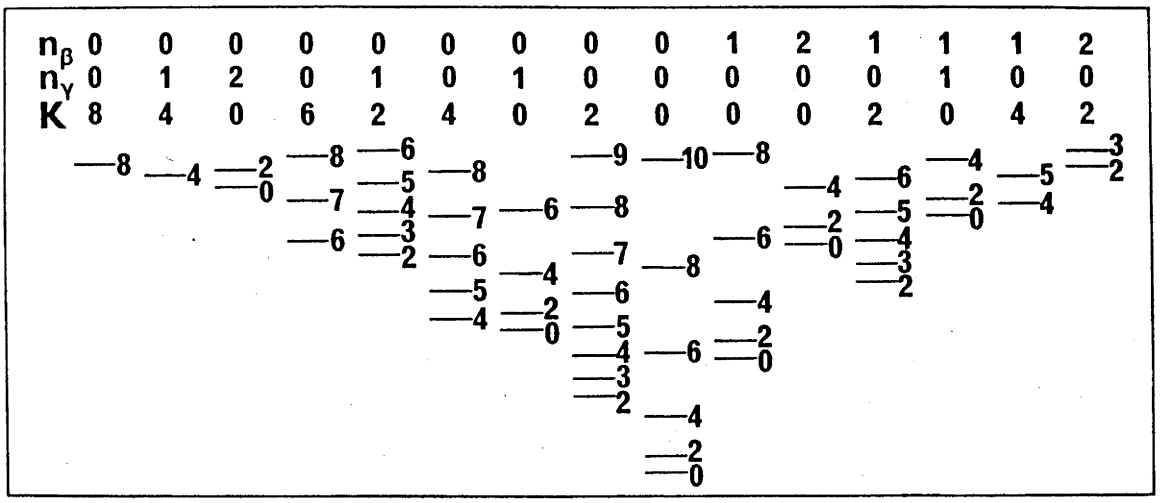

Fig. 1.4: The lower part of the energy spectrum predicted by the rotation-vibration model in the limit of no rotation-vibration interaction for the case $E_\beta = 40\ E_r$, $E_\gamma = 25\ E_r$. The levels are labelled by the angular momenta and are separated into bands according to their quantum numbers n_β, n_γ and K. From left to right are shown eight gamma bands, the ground-state band, two beta bands and four mixed bands.

mix states with the same J and M and with either $K = \pm 2$ or with $K = 0$. In particular, we are interested in the ground-state band which will mainly be the $|000JM\rangle$ states but which will contain admixtures of the $|100JM\rangle$ and $|002JM\rangle$ states. There will also be other components but these two are the largest since they are the closest in energy to the state $|000JM\rangle$. The energy levels of the ground-state band are now given by [Ei75]

$$E_{gs} = J(J+1)\ E_r[1 + 3E_r/E_\beta + 6E_r/E_\gamma + 8E_r^2/E_\gamma(E_\gamma - 4E_r)]$$

$$- J^2(J+1)^2\ E_r[4E_r^2/E_\gamma(E_\gamma - 4E_r) + 12E_r^2/E_\beta^2]\ . \qquad (1.79)$$

The electric quadrupole moment and reduced transition probability of the first excited state are

$$Q_{2^+}^{E2} = -\frac{6ZeR_0^2}{28\pi}\beta_2\left(1 + \frac{2}{7}\sqrt{\frac{5}{\pi}}\beta_2(1 + 3E_r/E_\beta - 6E_r/E_\gamma)\right.$$

$$\left. + \frac{72E_r^2}{E_\beta^2}\left(1 + \frac{4}{7}\sqrt{\frac{5}{\pi}}\beta_2\right) - \frac{48E_r^2}{E_\gamma(E_\gamma - 4E_r)}\left(1 - \frac{4}{7}\sqrt{\frac{5}{\pi}}\beta_2\right)\right) \qquad (1.80)$$

and

$$B(E2;0^+ \to 2^+) = \frac{9Z^2e^2R_0^4}{80\pi^2}\beta_2^2\left[1 + \frac{2}{7}\sqrt{\frac{5}{\pi}}\beta_2\left(1 + \frac{3E_r}{E_\beta} - \frac{6E_r}{E_\gamma}\right) + \frac{42E_r^2}{E_\beta^2}\left(1 + \frac{4}{7}\sqrt{\frac{5}{\pi}}\beta_2\right) + \frac{24\sqrt{2}\,E_r^2}{E_\gamma(E_\gamma - 4E_r)}\left(1 - \frac{4}{7}\sqrt{\frac{5}{\pi}}\beta_2\right)\right]^2 . \quad (1.81)$$

It is now not so simple to determine the characteristic energies from the energy spectrum. The $J = 0$ member of the first β band still has an excitation energy E_β, but E_γ and E_r must be determined from eq. 1.79 and the energy of the lowest $(J = 2)$ member of the first γ band, which is [Ei75]

$$E = E_\gamma + 2E_r\left[1 + 12\frac{E_r}{E_\gamma} + 3\frac{E_r}{E_\beta} + 48\frac{E_r^2}{E_\gamma(E_\gamma - 4E_r)} + 1296\frac{E_r^3}{E_\beta E_\gamma(E_\gamma - E_\beta - 4E_r)}\right] . \quad (1.82)$$

The sign of the product p_4 of eq. 1.50 is given in this model by [Ku69]

$$\operatorname{sgn} p_4 = \begin{cases} +1 & \text{if the } 2_2^+ \text{ state is in the first } \beta \text{ band} \\ -1 & \text{if the } 2_2^+ \text{ state is in the first } \gamma \text{ band} . \end{cases} \quad (1.83)$$

It may be noted that this model does not give any account of levels with negative parity. This can be rectified by allowing octupole as well as quadrupole vibrations [Da68]. However, the first excited states of even-even nuclei all have positive parity, and since the various model Hamiltonians do not mix states of opposite parity, these refinements do not affect predictions of the quadrupole moments of first excited states.

The alternative form of the rotation-vibration model considers β vibrations about a non-axial equilibrium deformation. As in the case of the rigid model, K is not a good quantum number except in the limit of $\gamma_0\big|_{\text{mod } \pi/3} \to 0$. If we write $E(J_n,\gamma_0)$ for the rigid-rotor energies graphed in fig. 1.3, then the level energies in this model are [Da60]

$$E = E_\beta(\nu+\tfrac{1}{2})\sqrt{1+\frac{4E(J_n,\gamma_0)}{C_\beta\beta_0^2 r^4}}+\frac{4}{r^2}E(J_n,\gamma_0)+\frac{C_\beta\beta_0^2}{2}(r-1)^2, \tag{1.84}$$

where E_β, C_β, β_0 and γ_0 are as defined in eqs. 1.73 and 1.76 and r is the root of the equation

$$r^3(r-1) = \frac{2E(J_n,\gamma_0)}{C_\beta\beta_0^2} \tag{1.85}$$

which is greater than unity. The quantum number ν is not, in general, an integer. Eq. 1.84 corresponds to a complicated combination of vibrational and rotational motion.

Unfortunately, expressions for quadrupole moments do not seem to be available for this model.

1.2.5 The Shell Model

The models described above have treated the nucleus as if it consisted of a lump of continuous matter. This could only be reasonable if the nucleus contains a large number of nucleons. The other extreme is to consider the behaviour of a few "valence" nucleons in the potential produced by all of the other nucleons. A potential of the form

$$V = \tfrac{1}{2}M\omega^2r^2 - C\underset{\sim}{l}\cdot\underset{\sim}{s} - D\underset{\sim}{l}\cdot\underset{\sim}{l} \tag{1.86}$$

can, for a suitable choice of the parameters ω, C and D, reproduce observed shell structure [Ma55]. The first term in eq. 1.86 is a harmonic oscillator potential with a characteristic frequency ω, the second term provides spin-orbit coupling in such a way that the state of higher total angular momentum ($j = l+\frac{1}{2}$) is the more bound, and the third term makes the potential more like a square well for high orbital angular momenta. A typical level scheme is shown in fig. 1.5. The levels can be labelled by the number N of harmonic oscillator quanta, and the orbital angular momentum l and the total angular momentum j. However, the notation given on the right of fig. 1.5 is more conventional. It might be expected that nuclei which have one

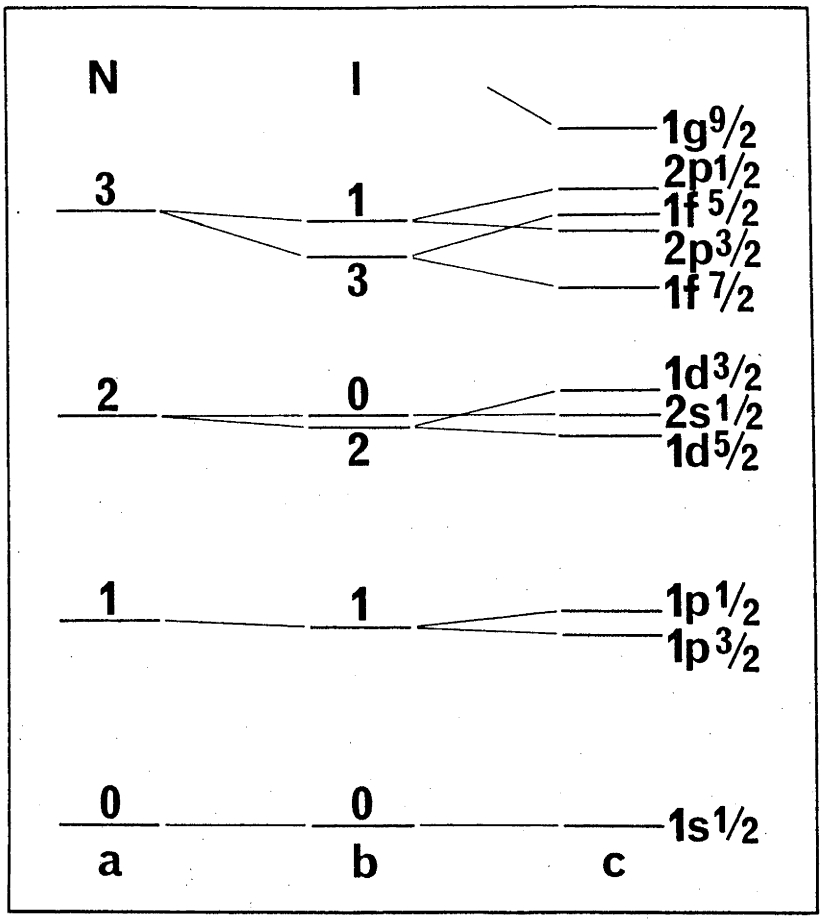

Fig. 1.5: Part of a typical energy spectrum predicted by the shell model. Shown are (a) the harmonic oscillator levels labelled by the number of oscillator quanta, (b) the splitting caused by the addition of the $\underset{\sim}{l}\cdot\underset{\sim}{l}$ term, the levels being labelled by their l-values, (c) the final spectrum after the addition of the $\underset{\sim}{l}\cdot\underset{\sim}{s}$ term, the levels being labelled with the conventional notation.

particle outside of a doubly-closed core might have a level scheme something like fig. 1.5 but starting, of course, after the appropriate closed shell. However, there will also be states corresponding to the excitation of particles out of the core. For levels which are due to a single proton, the shell model predicts a value of the quadrupole moment equal to [Ei75]

$$Q_j = -e \langle r^2 \rangle (2j-1)(2j+2)^{-1} . \qquad (1.87)$$

For an odd neutron level, the corresponding expression, due to a

"recoil effect", is

$$Q = -Ze \langle r^2 \rangle (A-1)^{-2} (2j-1)(2j+2)^{-1} . \qquad (1.88)$$

In these expressions, $\langle r^2 \rangle$ is the mean square radius of the particle's orbit, which is given by

$$\langle r^2 \rangle = \frac{3}{5} R_0^2 \qquad (1.89)$$

for a uniform charge distribution.

For the case of nuclei with many particles outside of a closed shell, it is necessary to postulate how they interact. The assumption of pairing gives results in reasonable agreement with the properties of ground states. That is, it is assumed that the protons or neutrons outside of the closed shell pair off to states of zero total angular momentum. The residual interaction which causes this pairing seems to increase in strength with the j-value of the particles [Ei75]. A simple expression for the quadrupole moment of the ground state can only be obtained when all protons outside of a closed shell have the same j-value. Neglecting recoil effects, it is

$$Q = [1 - (2n-2)(2j-1)^{-1}] Q_j , \qquad (1.90)$$

where n is the number of valence protons.

For excited states, it is necessary to be more quantitative about the residual interaction between the valence particles, and it is here that the shell model begins to become very complex. In general, one must consider not only the valence particles, but also the effect of excitations from the core. This produces vast numbers of combinations of single particle states for relatively modest numbers of nucleons, and a selection of what seem to be the most important ones must be made in order to render the calculations tractable. For example, in calculations of the structure of ^{18}O, which consists of two "valence" neutrons outside of an ^{16}O core, excitation of the neutrons out of the 2s-1d shell is usually not considered. Indeed, one recent calculation [La76] ignored states with more than one particle in the $1d_{3/2}$ level. As well as differing in the number of basis states considered,

different shell model calculations will usually differ in the model parameters used and may also differ in the number and type of core excitations considered. The model parameters are empirically determined constants which define

(a) the spacings of the various single particle levels. This is equivalent to choosing values of ω, C, D in eq. 1.86, but it is usual to quote the spacings directly.

(b) the residual interaction between the various valence nucleons.

It is clear that some nuclei may display both single particle (or few particle) and collective behaviour. Models combining these two types of behaviour are most often applied to odd-mass non-spherical nuclei but the particle-vibration coupling model is also extensively used for heavy even mass nuclei such as ^{198}Hg. It is common in these calculations to consider only two valence nucleons (or nucleon holes).

1.2.6 Microscopic Models

All of the models previously described have expressed the nuclear Hamiltonian in terms of a variety of parameters (B_2, I, E_β, ω, C, etc.) which are chosen to fit experimental data. It seems reasonable to attempt to formulate theories which compute the values of these parameters "from first principles". A severe problem is that the nature of the nucleon-nucleon interaction is not well understood. In practice then, microscopic calculations reduce the number of parameters but do not completely eliminate them.

A very widely used method is the Hartree-Fock method or the related Hartree-Fock-Bogoliubov method. These are types of variational methods which, by varying a trial wave function, seek to minimize the energy eigenvalue of the Hamiltonian. The results of these calculations are often presented as a contour plot of the "potential-energy surface" of the nucleus as a function of the deformation parameters β and γ. From these plots, the equilibrium values β_0 and γ_0 and stiffness parameters C_β and C_γ can be obtained

for use in the rotation-vibration model. The Hartree-Fock method has a very extensive literature [see Ma77 for some references].

Another method of generating potential-energy surfaces is the boson expansion technique which has been most recently described by Kishimoto and Tamura [Ki72, Ki76]. This method starts with a Hamiltonian written in terms of fermion creation and annihilation operators and expresses it in terms of boson operators which create and annihilate pairs of fermions. This gives the Hamiltonian in the form of eqs. 1.52 - 1.54 but with the stiffness and inertia parameters defined in terms of the single-particle orbit energies and the matrix elements of the particle-hole and pairing interactions. This method generates spectra which are qualitatively like those of the rotation-vibration model.

1.2.7 Summary

In this section, the predictions of the phenomenological models have been discussed in some detail (subsections 1.2.1 - 1.2.4) while relatively little has been said about "serious" nuclear models. This is due to the impossibility of extracting general expressions for, say, quadrupole moments from the more complex shell model and microscopic models. However, in many cases the results of microscopic calculations are qualitatively similar to one or other of the phenomenological models. The simple models then, convey the idea of the broad range of behaviour exhibited by nuclei.

As an example of this range of behaviour, it is seen that predictions of quadrupole moments range from near zero (single particle shell model and harmonic vibrational model) to large values (rotational model). This makes measurements of quadrupole moments a useful test of the validity of the various models. Of course, measurements of excitation energies and transition probabilities (i.e. lifetimes) are also useful in this respect, but the quadrupole moment has, along with other multipole moments, the characteristic that its value is determined by the state vector of just one nuclear state and is thus a particularly direct way of testing predictions of that state vector.

1.3 METHODS OF MEASURING EXCITED-STATE QUADRUPOLE MOMENTS

Basically, quadrupole moments are determined by measuring the interaction of the quadrupole moment with an electric field gradient. The energy of a non-spherical charge distribution in an electric field gradient varies with the orientation of the distribution relative to the field gradient. For an axially symmetric charge distribution in a uniform field gradient, the difference in energy between the orientations with the symmetry axis parallel to and perpendicular to the field gradient is [Bo68]

$$\Delta E = \frac{1}{4} Q_0^{E2} \frac{d^2\varphi}{dz^2}, \tag{1.91}$$

where Q_0^{E2} is the quadrupole moment of the distribution and $d^2\varphi/dz^2$ the uniform electric field gradient. Quantum mechanically, the expectation value of the energy of the interaction between Q_0^{E2} and the second derivatives of the electric potential is of the same order of magnitude as that given by eq. 1.91 provided that the angular momentum of the level is neither zero nor one-half [Bo75].

The highest electric field gradients which can currently be produced between sets of electrodes are of the order of $10^{18}\ V m^{-2}$ [Bo68], which gives an energy splitting ΔE of the order of 10^{-11} eV for a quadrupole moment of 100 e fm^2. This interaction energy is far too small to be measured. The methods of quadrupole moment measurement can therefore be conveniently classified according to the method used to generate the electric field gradient. This is done in the following subsections, where the discussion is confined to methods of measuring the quadrupole moments of excited states. Measurements on ground states using various effects of the hyperfine interaction with the atomic electrons are a separate study in themselves.

1.3.1 Measurements Using Crystals

Electric field gradients at the lattice sites of non-cubic crystals are often as high as $10^{22}\ V m^{-2}$ [Gr73]. This produces

splittings of gamma decay lines of the order of 10^{-7} eV and there are several ways of detecting such energy shifts, as discussed by Bodenstedt [Bo75]. Two of these are outlined below.

(i) Mössbauer-effect measurements

A single non-cubic crystal which contains the nucleus under investigation is manufactured. The field gradient in this crystal splits the magnetic substates of the nucleus. A second crystal which contains a gamma emitting radionuclide is also prepared. The energy of these gamma rays must be very close to the excitation energy of the level under consideration. In practice, this means that one must use the nucleus that one is studying as a gamma source. For example, in an experiment to measure the quadrupole moment of the first excited state of ^{129}I [Ha64], the hyperfine splitting was obtained by using a crystal of KIO_3 enriched in ^{129}I while the gamma rays were obtained from the decay of $^{129}Te^{m}$ in a ZnTe crystal. As is usually the case in these experiments, the crystal which contained the gamma source is cubic so that the gamma rays are "unsplit". The two crystals, source and absorber, are cooled to promote recoilless emission and absorption and set in relative motion in order to compensate for the energy difference between the unsplit source and the split energy levels of the absorber with the Doppler effect. Resonant absorption then occurs. The experiment consists of measuring the relative velocities of the two crystals for which resonant absorption is observed. This measures the hyperfine splitting of the energy levels directly. To determine the quadrupole moment however, one must know the field gradient at the site of the absorbing nucleus and calculations of field gradients in crystals are not very reliable. In the case of the experiment on ^{129}I, the ground state also has a non-zero hyperfine splitting, so that the quantity measured was the ratio of quadrupole moments of the ground and first excited states. In nuclei where the ground state J-value is less than one, some other method of calibrating the field gradient, for example, by making a measurement on another isotope, must be found.

This rather direct and elegant method has two severe limitations which restrict its applicability. These are:—

(a) The condition for a high proportion of recoilless emissions and absorptions of gamma rays is roughly that the momentum of the gamma ray should not be large compared with momentum uncertainty of the absorbing or emitting nucleus [Bo62]. By confining the nucleus in a crystal cooled to low temperatures, the position uncertainty of a nucleus can be reduced to about 0.01 of the dimension of the crystal lattice or ~ 1 pm. This limits these measurements to excited states whose excitation energies are ~ 100 keV or less.

(b) A suitable source of gamma rays must be found. In practice, this means that only nuclei which are gamma emitting daughters of moderately long-lived radio nuclides can be studied.

(ii) Spin-rotation measurements

A method which is used when Mössbauer spectroscopy is impractical is the observation of the rotation of the nuclear spin due to the interaction of the quadrupole moment with the field gradient of the crystal. The rotation frequency ω_0 is of the order

$$\hbar\omega_0 \sim Q_J \frac{d^2\varphi}{dz^2}. \qquad (1.92)$$

For substate splittings ~ 10^{-7} eV, the period of the spin rotation is ~ 1 nsec. Thus this method can only be used for nuclear levels whose lifetimes are comparable with or longer than ~ 10 psec. The spin rotation of the daughter of a radioactive nucleus located in a non-cubic crystal is usually detected by observing the perturbation of a gamma-gamma angular correlation. This method has the disadvantage that only the sign of Q_J can be determined if the nuclei are unpolarized. Polarization may be achieved by, for example, the measurement of beta-gamma angular correlations [Ra73].

These spin rotation measurements all suffer from the problem of calibrating the electric field gradient at the site of the nucleus. In spite of considerable efforts towards the reliable calculation of

field gradients in crystals [e.g. Ni78], it is common practice either for the product $Q_J \, d^2\varphi/dz^2$ to be quoted as the result of these experiments or for the experiment to be carried out on nuclei of known Q_J with a view to determining $d^2\varphi/dz^2$.

1.3.2 X-rays from Exotic Atoms

The hyperfine interaction between atomic electrons and the quadrupole moment of the nucleus has long been used to infer quadrupole moments of ground states. With exotic atoms, that is, atoms with an orbital particle which is not an electron, it becomes possible to obtain quadrupole moments of excited states. This is because exotic particles, being more massive than electrons, are more tightly bound. In many cases their transition energies are comparable with nuclear excitation energies, allowing a sort of inverse internal conversion to take place; the exotic atom decays by exciting the nucleus.

Most work to date has been done with muonic atoms. The muons have orbits which are ~ 0.005 times the dimensions and ~ 200 times the binding energies of the corresponding electron orbits. After the capture of a muon, the muonic atom decays until the muon is in the 1s state (or, rarely, the 2s state) [An74]. This decay, being electromagnetic, is much faster than the decay of the muon itself, which occurs, in low atomic-number atoms, by conversion to an electron ($\tau \sim 2.2$ μsec) and, in high atomic-number atoms, by capture by a nuclear proton ($\tau \sim 80$ nsec) [De69]. This difference in the μ^- decay mode emphasizes that, even in the 1s state, the muon does not have an appreciable overlap with the nucleus for light nuclei. In moderately heavy nuclei, the 1s and 2p states have a significant nuclear overlap while only in the heaviest nuclei does the 3d state appreciably penetrate the nucleus [De69, Po78]. Clearly, the muonic atom technique is only useful in the determination of excited state quadrupole moments of heavy nuclei which have excited states at relatively low excitation energies.

The analysis of muonic-X-ray data is somewhat model dependent in

that nuclear models must be used to calculate both the extent of polarization of the nucleus by the muon and the electric field gradients acting on the muon when it penetrates the nucleus. It is claimed that this model dependence can be reduced below 5% in those cases where penetration of the nucleus by the muon is relatively high [Po78].

In passing, it might be mentioned that pionic atoms have also been used to measure the quadrupole moments of ground states. Because pions interact strongly as well as electromagnetically, the pion and nucleus never get very close. In a recent experiment on ^{181}Ta [Be78], the 5g→4f transition was the lowest one observed. The interesting point is that the strong interaction between the pion and the nucleus is sensitive not only to the proton distribution, but to the neutron distribution as well. Thus a mass quadrupole moment can be inferred. This is one of the very few experimental methods available for doing this. It has been suggested [Sc72] that kaonic atoms might be even better for such a measurement but neither experimental nor theoretical techniques are yet precise enough to provide useful results [An74].

1.3.3 Inelastic Scattering Other than Coulomb Excitation

The methods considered in this subsection are electron scattering and nuclear scattering at energies above the Coulomb barrier. These two methods share the feature that the analysis requires the assumption of a nuclear model.

(i) Inelastic electron scattering

The electron interacts electromagnetically with the nucleus but, because it penetrates into the nucleus, a nuclear model must be used to determine the field gradients inside the nucleus. The results obtained will therefore depend on the model used.

(ii) Inelastic nuclear scattering

The most commonly used particles are protons, neutrons, deuterons and alpha particles although recently ^{3}He and heavier ions have also been used. The data, which consist of angular distributions of the inelastically scattered projectiles, are usually fitted using a deformed optical potential. The deformations considered vary, sometimes β_2 deformations only are used, in other cases β,γ or β_2,β_4 are taken as adjustable parameters. Clearly the values obtained will depend on the parameters chosen. Having obtained a set of parameters for the deformed optical potential, one must then interpret them in terms of the deformations of the nuclei involved. There are a number of prescriptions for doing this which may give substantially different deformations. After considering the analysis of some inelastic ^{4}He scattering data from ^{20}Ne and ^{24}Mg, Mackintosh and Tassie [Ma74] remark

> "The contradictory results of table 1 (which contains values of β_2 and β_4 for ^{20}Ne and ^{24}Mg obtained by three different procedures) remind us that *none* of these reactions can be said to be understood."

The best that can currently be expected from inelastic nuclear scattering then, is an order of magnitude estimate of the nuclear shape.

1.3.4 Coulomb Excitation

"The reorientation effect in Coulomb excitation" is widely used to measure excited-state quadrupole moments. The nucleus under examination is excited by bombardment with a second nucleus and the bombarding energy is kept sufficiently low for the interaction to be predominantly electromagnetic. The reorientation effect can be understood by reference to fig. 1.6. The upper part of this figure shows the minimum energy orientation of a spheroidal nucleus relative to a spherical nucleus. If the states of the spheroidal nucleus have $K=0$, then the substates with lowest energy are those with $|M|=J$ for prolate nuclei (fig. 1.6a) and $M=0$ for oblate nuclei (fig. 1.6b). The shifts of the substates from the unperturbed value are

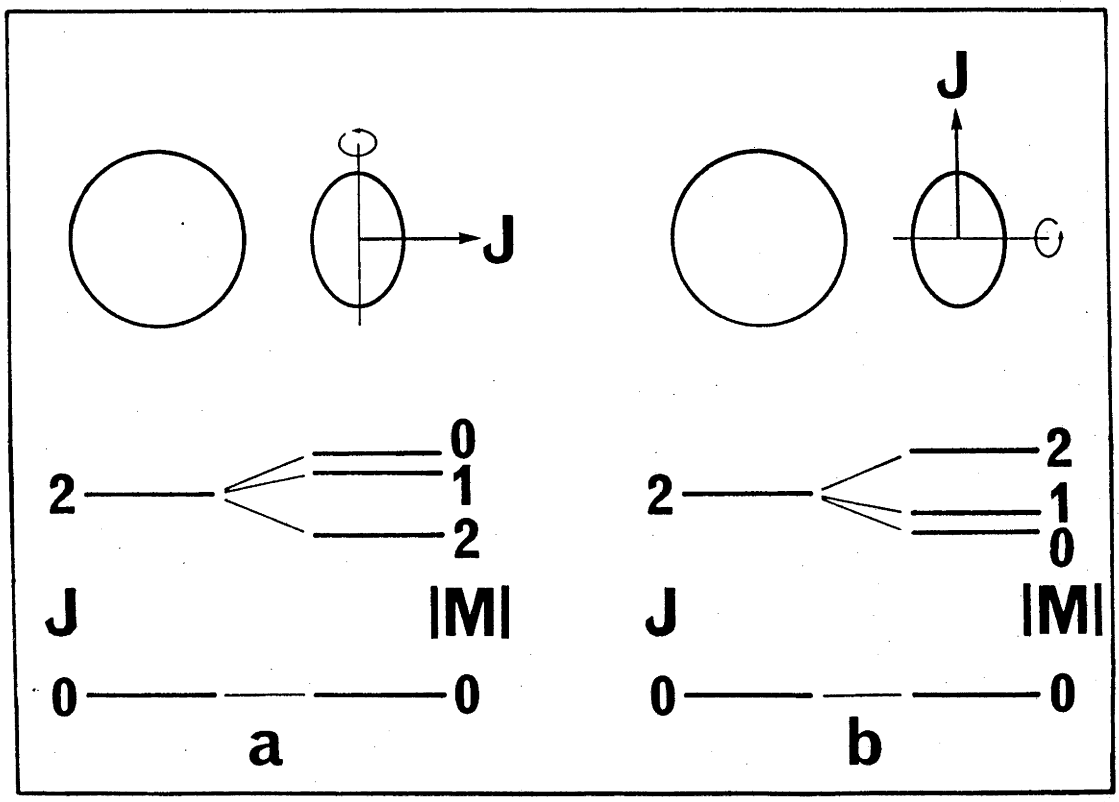

Fig. 1.6: The explanation of the reorientation effect as a dynamic hyperfine splitting. Part (a) is for a prolate nucleus and part (b) for an oblate nucleus. The top part of the figure shows schematically the lowest-energy orientation of a deformed nucleus relative to a spherical one. The lower part shows the resulting hyperfine splitting of a $J = 2$ state.

proportional to $3M^2 - J(J+1)$ [Bo75]. The shifts for the case of a $J = 2$ excited state are shown in the lower part of fig. 1.6. If attention is restricted to scattering through 180°, then only the $M = 0$ substate can be populated. Since the Coulomb excitation probability falls rapidly with increasing excitation energy (subsection 2.1.3), it is clear that, for the J-values in fig. 1.6, the effect of the quadrupole moment of a prolate nucleus is to reduce the Coulomb excitation probability of the excited state, while the reverse is true for an oblate nucleus. A little thought reveals that the opposite would occur if the ground state had $J = 2$ and the excited state $J = 0$. The effect can be substantial; at closest approach in the backscattering of 90 MeV ^{24}Mg from ^{208}Pb, the $M = 0$ substate of the 1.37 MeV first excited state of ^{24}Mg is raised some 400 keV [Ha74].

The effect of the quadrupole moment is strongest in scattering through 180° because at other scattering angles substates other than that with $M = 0$ can be populated and because for a given bombarding energy, the two nuclei approach most closely in 180° scattering.

It is clear that, as well as affecting the total excitation probability, the transient hyperfine splitting also affects the relative population of the projection substates and hence the angular distribution of the de-excitation gamma rays. A number of distinct experimental techniques have been developed to exploit these effects. These are considered in detail below.

(i) Reorientation precession

If attention is restricted to one particular scattering angle, then the excited nuclei are, in general, partially polarized causing a perturbation of the angular distribution of the de-excitation gamma rays. This perturbation takes the form of a precession plus an attenuation [Gr73]. Because the collision time is short, the amount of precession is small, typically $\lesssim 1°$ [Gr73]. One way of detecting this is to place particle detectors at ±90° and to compare the coincidence rates between each of these detectors and a gamma ray detector. Alternatively, two gamma ray detectors and one particle detector can be used [Bo68]. A problem with this sort of measurement is the attenuation of the gamma ray angular distribution, known as "deorientation", which may occur if the excited nucleus recoils into vacuum. This attenuation is due to the strong magnetic field produced by unpaired atomic electrons. In order to correct for this effect, one must know both the fraction of recoil nuclei which are accompanied by, in particular, a single 1s or 2s electron and the magnetic field at the nucleus due to these electrons. These difficulties combined with the smallness of the effect sought usually result in experimental results with relatively large uncertainties.

(ii) Gamma-ray angular distribution

This method determines the quadrupole moment by its effect on the angular distribution of the de-excitation gamma ray. Scattered particles are not detected. The same problems that affect reorientation precession measurements also arise here. Olsen *et al.* [0174] present details on the analysis of this type of experiment. It has the advantage that the value of Q_{2+} obtained is insensitive to the value assumed for the reduced transition probability. However, the effect sought is again very small.

(iii) Gamma-ray lineshapes

This method uses the Doppler shift of the de-excitation gamma rays. To date, its use has been restricted to light nuclei, targets of which are bombarded with projectiles of greater mass, the de-excitation gamma rays being detected at 0°. The reorientation effect is such that the ratio of the cross section for backward projectile scattering (in the centre of mass frame) to the cross section for scattering with $\Theta < 90°$ is enhanced if $Q_J > 0$ and reduced if $Q_J < 0$. This variation is reflected in the angular distribution of the excited target recoils and hence in the details of the Doppler-broadened gamma-ray lineshape which is seen at 0°. This technique has been discussed by Schwalm *et al.* [Sc72a]. It also has the advantage that it is insensitive to the value of the reduced excitation probability. However, deorientation must again be taken into account and the effects sought are almost as small as those in the reorientation-precession and gamma-ray-angular-distribution techniques, so that the results still have relatively large uncertainties.

(iv) Gamma-ray yields

In principle, the quadrupole moment of a state could be measured simply by measuring the yield of gamma rays from a thick target. Such methods have been used [e.g. Pe69] but they require that, among other things, the gamma ray detector be calibrated absolutely to sufficient

accuracy and the beam-current integration system be sufficiently reliable. These problems can be avoided if one is prepared to restrict oneself to relative measurements of quadrupole moments. In this case, beam current integration is not required and only the relative efficiency of the gamma-ray detector is needed. The big advantage of this technique is that, by using a thick target of natural composition, information on many nuclei can be obtained with relatively small amounts of accelerator time. However, this must be weighed against the problem of unfolding relatively complex gamma-ray spectra. These difficulties are discussed by Maynard *et al.* [Ma77b] in a report of some recent work on isotopes of Ru, Pd and Cd using this method.

(v) Particle-gamma coincidence yields

This, perhaps the most popular of the techniques, aims to infer the value of the quadrupole moment from its effect on the inelastic scattering cross section. No attempt is made to resolve the elastically and inelastically scattered particles with the particle detector but rather the detection of a coincident gamma ray of the right energy is used to identify an event as inelastic. Being a coincidence experiment, this method is less affected by gamma-ray backgrounds, or target contaminants. However, deorientation may again be a problem, particularly in experiments to measure the excitation of the projectile.

(vi) Particle singles

The most direct method of measuring quadrupole moments using Coulomb excitation is to use particle detectors with sufficient resolution to resolve the elastically and inelastically scattered particles thus dispensing with the need to detect gamma rays and greatly simplifying the experimental arrangement. This simplification is the main advantage of this method and was the reason why we chose it to make the measurements described in later chapters. The main disadvantage of this method is that, being a singles experiment, it is

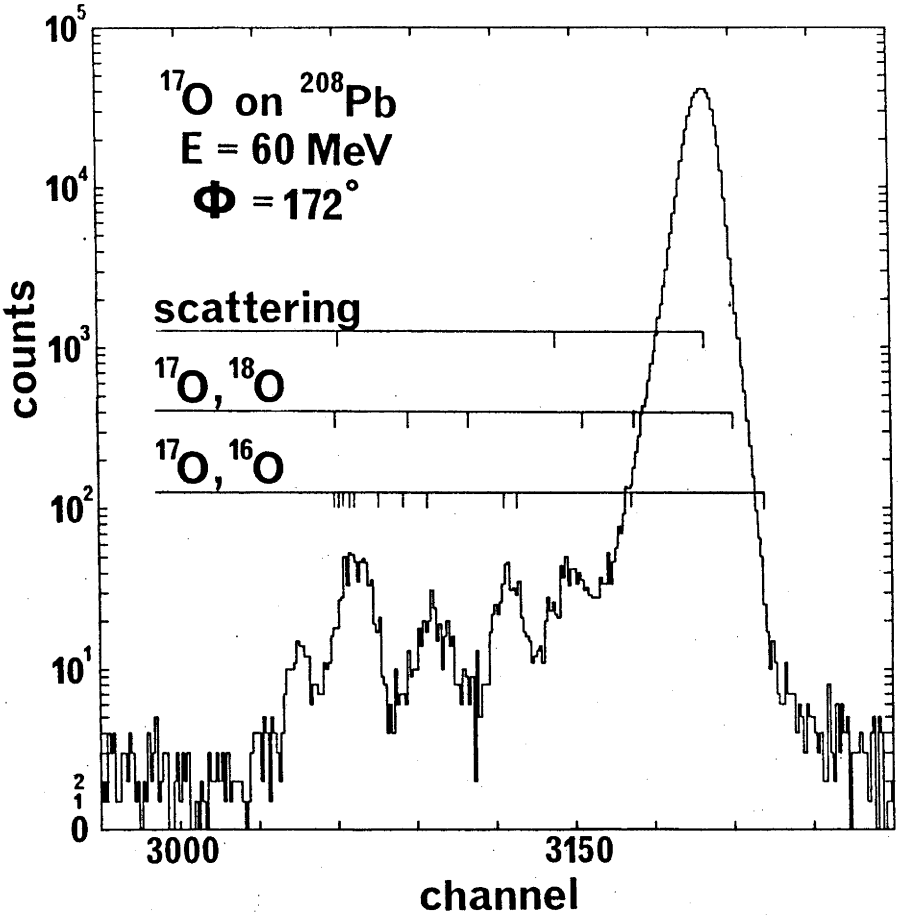

Fig. 1.7: A spectrum of 60 MeV ^{17}O ions backscattered from ^{208}Pb. The positions of peaks due to elastic and inelastic scattering and to the reactions ^{208}Pb(^{17}O,^{16}O)^{209}Pb and ^{208}Pb(^{17}O,^{18}O)^{207}Pb are shown.

sensitive to background effects such as target contaminants and nuclear reactions. For example, fig. 1.7 shows a spectrum of 60 MeV ^{17}O ions backscattered from a ^{208}Pb target. The presence of single nucleon transfer peaks makes this spectrum useless for the determination of the quadrupole moment of the ground state of ^{17}O.

Both magnetic spectrometers and silicon surface-barrier detectors have been used to detect the scattered particles. So far as solid angle is concerned, surface-barrier detectors are better for scattering angles near 180° where annular detectors may be used. For other scattering angles, magnets will have larger solid angles if their design includes kinematic compensation. For $\Phi = 90°$, there is

considerable advantage, as is shown in subsection 3.2.3, in having two detectors, one on each side of the target. As there are very few laboratories with two magnetic spectrometers attached to the one scattering chamber, it may be desirable to sacrifice the solid angle and use surface-barrier detectors for $\Phi = 90°$.

The other consideration in making a choice between magnets and surface-barrier detectors is the one of lineshape and resolution. Fig. 1.8 shows a spectrum of 120 MeV ^{32}S ions backscattered from a ^{208}Pb target and detected by an annular surface-barrier detector. The elastic peak has a low-energy exponential tail which is substantial even in the region of the inelastic peak due to the excitation of the projectile. Also, the projectile-excitation and target-excitation peaks are not resolved. This spectrum is probably not good enough to be used to determine Q_{2^+} of ^{32}S. For ^{32}S and heavier projectiles then, magnets appear to be required. The main problem with a magnet is that all of the particles of a given scattered energy do not appear in one peak, but are split according to their atomic charge states. One must therefore, either determine the relative charge state distributions of the elastically and inelastically scattered particles or know the variation of effective solid angle along the focal plane to sufficient accuracy to enable one to sum the yields of the different charge states.

(vii) Other methods

The six techniques used above are not the only possible ways of exploiting the reorientation effect in Coulomb excitation, but they are the most commonly used ones. Two others which have come to my notice are described below.

Andreyev *et al.* [An70] measured the value of Q_{2^+} in ^{114}Cd with a cyclotron using basically the particle-gamma coincidence yield method. Cyclotrons have the difficulty of poorer energy stability than electrostatic accelerators and also of a pulsed beam which increases the proportion of random coincidences. These problems were overcome by simultaneously bombarding ^{114}Cd targets with $^{4}He^{+}$ and $^{12}C^{3+}$ ions.

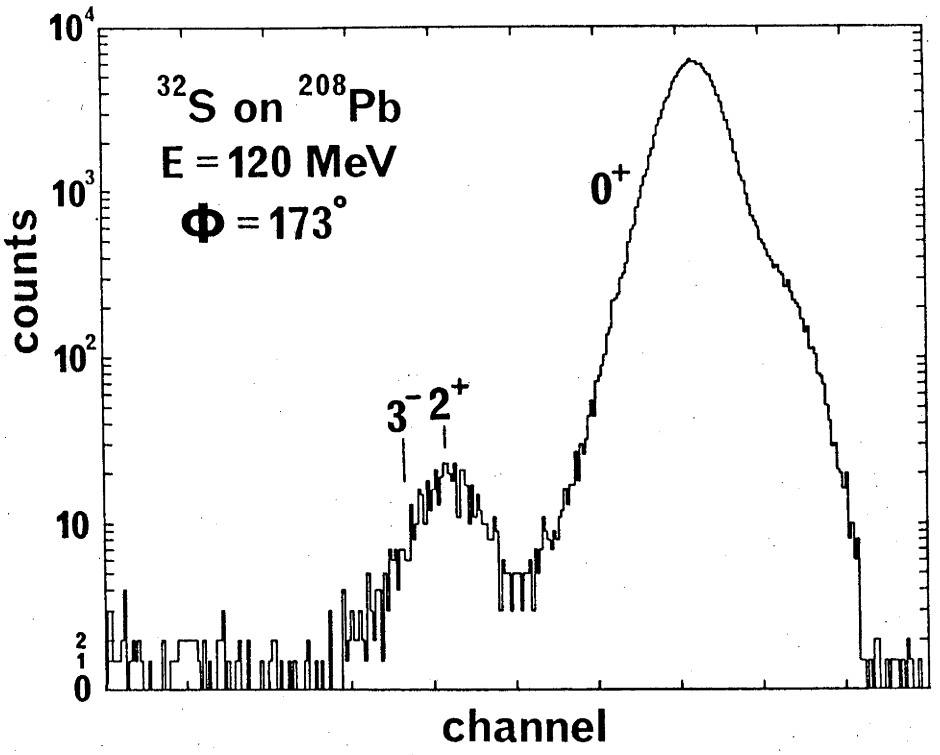

Fig. 1.8: A spectrum of 120 MeV ^{32}S ions backscattered from ^{208}Pb and detected by an annular silicon surface-barrier detector. The peaks are due to elastic scattering (0^+) and to excitation of the first excited states of ^{32}S (2^+) and ^{208}Pb (3^-). The target excitation peak is approximately 0.1 times the area of the projectile excitation peak. The shoulder on the high-energy side of the elastic-scattering peak is a detector artifact (see subsection 3.3.1).

The elastically and inelastically scattered ^{4}He were resolved by the particle detector thus providing a measurement of the real-to-random coincidence ratio. Details may be found in the above reference.

Vitoux *et al.* [Vi71] used a variant of the particle singles technique to measure the quadrupole moment of ^{24}Mg. They bombarded a ^{24}Mg target with ^{16}O projectiles. This combination gives scattered energies which vary rapidly with scattering angle. In order to obtain reasonable resolution and solid angle, they used a surface-barrier detector and a position-sensitive detector to detect the scattered ^{16}O projectiles and the ^{24}Mg recoils in coincidence. Experimental details can be found in ref. Ha71.

(viii) Summary

We have chosen the particle singles method because of its relative directness and simplicity. Surface-barrier detectors were chosen firstly because of the solid angle available with annular detectors and secondly because of the advantage of having two detectors at $\Phi = 90°$ (subsection 3.2.3). By avoiding the detection of gamma rays, certain potential sources of systematic errors are eliminated, but others are introduced. A case might perhaps be made for the superiority of the particle-gamma coincidence yields and particle singles methods over the others, but it is difficult to choose between these two. An exception is the case of nuclei with $40 \lesssim A \lesssim 100$. The problems of either accelerating and detecting these nuclei or making impurity-free targets containing them give the particle-gamma coincidence yields method a distinct advantage. Apart from this mass region, it seems wise to consider all of these techniques as being complementary. The measurement of a given quadrupole moment ought to be carried out using more than one method in order to assist in the detection of unsuspected systematic errors.

Chapter 2

THEORY OF ELECTROMAGNETIC EXCITATION

A theory of the excitation of one nucleus by the electromagnetic field of a second nucleus in relative motion with it was first given by Ter-Martirosyan [Te52]. It has subsequently been amplified in many articles, notably in the seminal review paper by Alder, Bohr, Huus, Mottelson and Winther [Al56] and in the recent comprehensive monograph by Alder and Winther [Al75]. The approach used is primarily that of non-relativistic, semiclassical perturbation theory. The adjectives non-relativistic, semiclassical and perturbation each indicate an approximation for which a correction may be needed before the theory is of use in the interpretation of experimental data. Although it happens that many such corrections are required, the non-relativistic semiclassical perturbation approach deserves exposition here as it provides a useful set of concepts with which to view the process of electromagnetic nuclear excitation.

In the first section of this chapter, the main conclusions of the non-relativistic semiclassical perturbation treatment are outlined. Subsequent sections examine the effects of the various approximations.

2.1 NON-RELATIVISTIC SEMICLASSICAL THEORY

2.1.1 Range of Validity

A non-relativistic calculation might be expected to differ from a relativistic one in terms of the order of $(v/c)^2$, where v is the projectile's speed and c the speed of light. For the case of a nucleus of energy E and mass A,

$$(v/c)^2 = 0.00215\ E_{[MeV]}/A_{[u]} \,. \qquad (2.1)$$

For the projectiles and energies used in this work, $(v/c)^2 \lesssim 0.009$.

The term "semiclassical" implies that the projectile can be considered to follow the usual hyperbolic orbit of a point charge in a

repulsive electric field. There are two aspects to this [A175, p.301]. The first is generally expressed through the Sommerfeld parameter $\eta := a/\lambda\!\!\!^{-}$ where a is half of the distance of closest approach in a head-on collision and $\lambda\!\!\!^{-}$ is the wavelength of the projectile. If

$$\eta = \frac{Z_p Z_t e^2}{4\pi\varepsilon_0 \hbar u} \gg 1 , \tag{2.2}$$

then the wave packet of the projectile is localized and it makes sense to talk of an orbit. The second aspect concerns the excitation energy, ΔE, absorbed in exciting either the target or projectile or both. Since we do not know at which point on the orbit the energy is transferred, we must have

$$\Delta E/E \ll 1 \tag{2.3}$$

so that the orbit is not greatly affected by the loss of kinetic energy. This loss is then neglected (see, however, section 2.3). Under the experimental situations in this work $\eta \gtrsim 40$ for heavy ion scattering and $\eta \sim 12$ for ^{4}He scattering. In both cases $\Delta E/E \lesssim 0.03$.

2.1.2 Outline

Schrödinger's equation (which is non-relativistic) for the system of two nuclei can be written

$$\frac{\partial \Psi}{\partial t} = -\frac{i}{\hbar}\,[H_0 + V(t)]\,\Psi , \tag{2.4}$$

where H_0 is the Hamiltonian of the two nuclei at an infinite separation, and V(t) is the interaction between the nuclei at finite distances. It is assumed that the nuclei always remain sufficiently distant from one another that the nuclear force between them can be ignored. This ensures that V(t) is electromagnetic only. Non-relativistically

$$V(t) = \frac{1}{4\pi}\iint \frac{\rho(\underset{\sim}{r}_p)\rho(\underset{\sim}{r}_t)/\varepsilon_0 - \mu_0\, \underset{\sim}{j}(\underset{\sim}{r}_p)\cdot\underset{\sim}{j}(\underset{\sim}{r}_t)}{|\underset{\sim}{r}_p - \underset{\sim}{r}_t|}\, \underset{\sim}{dr}_p\, \underset{\sim}{dr}_t , \tag{2.5}$$

where $\rho(\underset{\sim}{r})$ and $\underset{\sim}{j}(\underset{\sim}{r})$ are charge and current densities and the subscripts p and t refer to the projectile and target. The neglect of the nuclear force requires that $|\underset{\sim}{r}_p - \underset{\sim}{r}_t|$ be large for all points $\underset{\sim}{r}_p$ and $\underset{\sim}{r}_t$, so the nuclei certainly never overlap, and V(t) can therefore be broken into three parts [Ca50, Al75, p.297]

$$V(t) \;=:\; V_{EE} + V_{MM} + V_{EM} \,. \tag{2.6}$$

In terms of the electric and magnetic multipole moments

$$M(E\lambda,\mu) \;:=\; \int \rho(\underset{\sim}{r})\; r^{\lambda}\; Y_{\lambda\mu}(\hat{\underset{\sim}{r}})\; \underset{\sim\sim}{dr} \tag{2.7}$$

and

$$M(M\lambda,\mu) \;:=\; -(\lambda+1)^{-1} \int r^{\lambda}\; \underset{\sim}{j}(\underset{\sim}{r})\cdot(\underset{\sim}{r}\times\underset{\sim}{\nabla})\; Y_{\lambda\mu}(\hat{\underset{\sim}{r}})\; \underset{\sim\sim}{dr} \tag{2.8}$$

which are measured with respect to the centre of mass of the appropriate nuclei,

$$V_{EE} = \frac{1}{\varepsilon_0} \sum_{\substack{\lambda_p\mu_p \\ \lambda_t\mu_t}} (-)^{\mu}\, b_{\lambda_p\lambda_t}\, r^{-\lambda_p-\lambda_t-1}\, M_p(E\lambda_p,-\mu_p) M_t(E\lambda_t,-\mu_t)$$

$$\times\, C(\lambda_p\lambda_t\lambda_p{+}\lambda_t;\mu_p\mu_t\mu)\; Y_{\lambda_p+\lambda_t\mu}(\hat{\underset{\sim}{r}}) \,, \tag{2.9}$$

$$V_{MM} = \mu_0 \sum_{\substack{\lambda_p\mu_p \\ \lambda_t\mu_t}} (-)^{\mu}\, b_{\lambda_p\lambda_t}\, r^{-\lambda_p-\lambda_t-1}\, M_p(M\lambda_p,-\mu_p) M_t(M\lambda_t,-\mu_t)$$

$$\times\, C(\lambda_p\lambda_t\lambda_p{+}\lambda_t;\mu_p\mu_t\mu)\; Y_{\lambda_p+\lambda_t\mu}(\hat{\underset{\sim}{r}}) \tag{2.10}$$

and

$$V_{EM} = \mu_0 \sum_{\substack{\lambda_p\mu_p \\ \lambda_t\mu_t}} (-)^{\mu}\, b_{\lambda_p\lambda_t}\, r^{-\lambda_p-\lambda_t-1} \left[M(E\lambda_p,-\mu_p)M(M\lambda_t,-\mu_t)\right.$$

$$\left. - M(M\lambda_p,-\mu_p)M(E\lambda_t,-\mu_t)\right] \dot{\underset{\sim}{r}}\cdot \Bigg((\lambda_p{+}\lambda_t)^{-1}\; C(\lambda_p\lambda_t\lambda_p{+}\lambda_t;\mu_p\mu_t\mu)$$

$$(\underset{\sim}{r}\times\underset{\sim}{\nabla})\; Y_{\lambda_p+\lambda_t\mu}(\underset{\sim}{r}) \;-\; i \sqrt{\frac{\lambda_p(2\lambda_p{+}2\lambda_t{+}1)}{\lambda_t(\lambda_p{+}\lambda_t)(2\lambda_p{+}2\lambda_t{-}1)}}$$

$$C(\lambda_p\lambda_t\lambda_p{+}\lambda_t{-}1;\mu_p\mu_t\mu)\; \underset{\sim}{Y}_{\lambda_p+\lambda_t\lambda_p+\lambda_t-1\mu}(\hat{\underset{\sim}{r}}) \Bigg) \,. \tag{2.11}$$

In these equations, $\underset{\sim}{r}$ is the position vector of the centre of mass of the projectile with respect to that of the target, the coefficient

$$b_{\lambda_p \lambda_t} := (-)^{\lambda_p} \sqrt{\frac{4\pi(2\lambda_p+2\lambda_t)!}{(2\lambda_p+2\lambda_t+1)(2\lambda_p+1)!(2\lambda_t+1)!}} \tag{2.12}$$

and $\underset{\sim}{Y}_{jlm}(\hat{\underset{\sim}{r}})$ is a vector spherical harmonic as defined by, for example, de Shalit and Talmi [Sh63]. The sums over λ_p and λ_t range over all non-negative values, though only V_{EE} has a non-zero term for $\lambda_p = \lambda_t = 0$. The term involving $\underset{\sim}{Y}_{jlm}(\hat{\underset{\sim}{r}})$ in V_{EM} is zero if either $\lambda_p = 0$ or $\lambda_t = 0$, as are all the terms of V_{MM}.

It is now assumed that only one of the target or projectile has structure, and that the other is a point charge with no magnetic moment. Henceforth subscript 1 will refer to the structureless exciting nucleus and subscript 2 to the excited nucleus; that is, $\lambda_1 = 0$. Therefore $V_{MM} = 0$ and, replacing the summation indices λ_2, μ_2 by λ, μ,

$$V_{EE} = \frac{Z_1 e}{\varepsilon_0} \sum_{\lambda\mu} (-)^{\mu+\lambda_p} (2\lambda+1)^{-1} M_2(E\lambda,-\mu)\, r^{-\lambda-1}\, Y_{\lambda\mu}(\hat{\underset{\sim}{r}}) \tag{2.13}$$

and

$$V_{EM} = Z_1 e \mu_0 \sum_{\lambda\mu} (-)^{\mu+\lambda_p} (2\lambda^2+\lambda)^{-1} M_2(M\lambda,-\mu)\, r^{-\lambda-1}\, \dot{\underset{\sim}{r}} \cdot (\underset{\sim}{r} \times \underset{\sim}{\nabla})\, Y_{\lambda\mu}(\hat{\underset{\sim}{r}}) \,. \tag{2.14}$$

The semiclassical approximation is now applied. The projectile is assumed to follow the hyperbolic orbit which is obtained from the assumption that both particles are structureless charges. The state vector of the system is written

$$\Psi = |0\rangle_1 \sum_n a_n(t)\, |n\rangle_2 \,, \tag{2.15}$$

where $|0\rangle_1$ is the unperturbed state vector of the structureless exciting nucleus, $a_n(t)$ are coefficients and $|n\rangle_2$ are the unperturbed state vectors of the excited nucleus in state n. It is sometimes convenient to explicitly sum over the magnetic substates of the energy levels. In order to distinguish whether a particular sum is over all states, including substates, or only over energy levels, the symbols k,l,m,n are used to label all states while the symbols o,f,z are used

to label energy levels. Inserting eq. 2.15 into Schrödinger's equation gives

$$\frac{da_n(t)}{dt} = -\frac{i}{\hbar}\sum_m \langle n|\ V_{EE}+V_{EM}-\frac{Z_1Z_2e^2}{4\pi\varepsilon_0 r}\ |m\rangle \exp\left((E_n-E_m)\ \frac{it}{\hbar}\right)\ a_m(t)\ , \tag{2.16}$$

where E_n and E_m are the energies of substates n and m. The subscript "2" has been dropped from the state vectors and the Coulomb potential has been subtracted from V_{EE} as its action is to determine the orbit and not to cause excitation. The initial conditions for this coupled set of differential equations are

$$a_n(-\infty) = \delta_{n\ell}\ , \tag{2.17}$$

the state ℓ being the state of the excited nucleus before the interaction.

The hyperbolic orbit of the projectile in the Coulomb field of the target can be written in terms of the parameter w as [La69, p.38]

$$x = 0\ ,\quad y = a\sqrt{\varepsilon^2-1}\ \sinh w\ ,\quad z = a(\cosh w+\varepsilon)\ ,$$

$$t = a(\varepsilon\sinh w+w)/u\ , \tag{2.18}$$

where $\varepsilon=\operatorname{cosec}(\Theta/2)$ is the eccentricity of an orbit associated with the centre of mass scattering angle Θ,

$$a := \frac{Z_pZ_te^2}{4\pi\varepsilon_0 m_0u^2}\ , \tag{2.19}$$

u is the initial speed of the projectile in the laboratory frame and m_0 is the reduced mass of the target and projectile. The differential equations (eq. 2.16) are then written in terms of three characteristic functions:—

(a) the collision functions

$$Q_{E\lambda\mu}(\varepsilon,w) := i^{|\mu|}\ \frac{(2\lambda-1)!!}{2(\lambda-1)!}\sqrt{\frac{(\lambda-|\mu|)!}{(\lambda+|\mu|)!}}\ \frac{P_\lambda^{|\mu|}\left(\dfrac{\cosh w+\varepsilon}{\cosh w+1}\right)}{(\varepsilon\cosh w+1)^{\lambda}} \tag{2.20}$$

$$\mathcal{Q}_{M\lambda\mu}(\varepsilon,w) \;:=\; -\frac{i}{\lambda \sinh w}\,\mathcal{Q}_{E\lambda\mu}(\varepsilon,w)\;, \tag{2.21}$$

where $P_\lambda^\mu(x)$ is an associated Legendre polynomial defined as in ref. Ab73.

(b) the strength of the interaction

$$\chi^{E\lambda}_{mn} \;:=\; \frac{Z_1 e}{\sqrt{\pi\varepsilon_0}\hbar u}\,\frac{(\lambda-1)!}{(2\lambda+1)!!}\,\frac{\langle n\|M(E\lambda)\|m\rangle}{a^\lambda\sqrt{2J_m+1}} \tag{2.22}$$

$$\chi^{M\lambda}_{mn} \;:=\; \frac{Z_1 e\mu_0}{\sqrt{\pi}\hbar}\,\frac{(\lambda-1)!}{(2\lambda+1)!!}\,\frac{\langle n\|M(M\lambda)\|m\rangle}{a^\lambda\sqrt{2J_m+1}}\,. \tag{2.23}$$

(c) the adiabaticity

$$\xi_{mn} \;:=\; a(E_n - E_m)/\hbar u\,. \tag{2.24}$$

With these definitions, the coupled equations become

$$\frac{da_n(w)}{dw} \;=\; -i\sum_{m\sigma\lambda\mu}\nu_\lambda\sqrt{\frac{(2\lambda+1)(2J_m+1)}{2J_n+1}}\,C(J_m\lambda J_n;M_m-\mu M_n)$$

$$\times\,\chi^{\sigma\lambda}_{mn}\,\mathcal{Q}_{\sigma\lambda\mu}(\varepsilon,w)\,\exp[i\xi_{mn}(\varepsilon\sinh w + w)]\;a_m(w)\;, \tag{2.25}$$

where

$$\nu_\lambda \begin{cases} 1 & \text{target excitation} \\ (-)^\lambda & \text{projectile excitation} \end{cases} \tag{2.26}$$

and σ ranges over the values "E" and "M".

Solving these equations with the initial conditions of eq. 2.17 produces solutions which will be denoted $a_{n,l}(w)$. If the ground state of the excited nucleus is unpolarized, then there are $2J_0+1$ equally populated initial states, so that the excitation probability, P_f, of energy level f is

$$P_f \;=\; \frac{1}{2J_0+1}\sum_{n,l}\left|a_{n,l}(\infty)\right|^2\,, \tag{2.27}$$

where l runs over all substates of the ground state o, and n over all

substates of the final level f. It may be noted that, as a consequence of the reflection symmetry possessed by the system, $|a_{n,\ell}| = |a_{m,k}|$ if $M_n = -M_m$ and $M_k = -M_\ell$ [A175, p.48]. Finally, the cross section for the scattering of the projectile accompanied by the excitation of state f is

$$d\sigma_f = \tfrac{1}{4} P_f a^2 \operatorname{cosec}^4(\Theta/2) . \qquad (2.28)$$

There are three approaches commonly used to integrate eq. 2.25. If $\xi_{mn} \ll 1$, then an approach based on S matrix theory allows $a_n(\infty)$ to be written as a series in powers of ξ_{mn}. This approach is valid for all values of $\chi_{mn}^{\sigma\lambda}$ [A175, p.178] and is sometimes used to describe the excitation of rotational nuclei, which have states of relatively low excitation energy. This method is not suitable for the analysis of the experiments described here, since we have $0.2 < \xi < 1.2$. A second method of approximation valid for all ξ can be applied when $\chi_{mn} \ll 1$. This is the perturbation approach which is described in the next section. It produces a power series in χ_{mn} for $a_n(\infty)$. Finally, eq. 2.25 may be integrated numerically. A computer program to do this for the case of E2 excitations was first described by A. Winther and J. de Boer [Wi65], and has subsequently been extended to include electric and magnetic excitations of any multipolarity. It is this program which was used in the analysis to be described later.

2.1.3 Perturbation Theory

The solution of eq. 2.25 using first order perturbation theory is obtained by replacing $a_m(w)$ with $\delta_{m\ell}$. This assumes that, at any time, the dominant term in the expression for $da_n(w)/dw$ is that involving the ground state. In other words, it is assumed that the excited state populations are always small compared with the ground state population. The result of applying this approximation is

$$a_{n,\ell}(\infty) = -i \sqrt{\frac{2J_\ell+1}{2J_n+1}} \sum_{\sigma\lambda\mu} \nu_\lambda \sqrt{2\lambda+1}\, C(J_\ell \lambda J_n; M_\ell - \mu M_n)\, \chi_{\ell n}^{\sigma\lambda}\, R_{\sigma\lambda\mu}(\Theta, \xi_{\ell n}) , \qquad (2.29)$$

where the orbit integrals $R_{\sigma\lambda|\mu}$ are defined by

$$R_{\sigma\lambda\mu}(\Theta,\xi) \;:=\; \int_{-\infty}^{\infty} Q_{\sigma\lambda\mu}(\varepsilon,w)\ \exp[i\xi(\varepsilon\sinh w + w)]\ dw\,. \quad (2.30)$$

By computing $R^{*}_{\sigma\lambda\mu}(\Theta,\xi)$ it can be seen that $R_{\sigma\lambda\mu}$ is real, so that the amplitudes $a_{n,\ell}(\infty)$ are purely imaginary. Using the orthogonality properties of the Clebsch-Gordan coefficients and the conservation of parity, the excitation probability is found to be

$$P_f \;=\; \sum_{\sigma\lambda} \left|\chi^{\sigma\lambda}_{of}\right|^2\ R^2_{\sigma\lambda}(\Theta,\xi_{of})\,, \quad (2.31)$$

where the subscript "o" indicates the ground state and

$$R^2_{\sigma\lambda}(\Theta,\xi) \;:=\; \sum_{\mu} \left|R_{\sigma\lambda\mu}(\Theta,\xi)\right|^2\,. \quad (2.32)$$

Some of the properties of the squared orbit integrals $R^2_{\sigma\lambda}$ are:—

(a)
$$R^2_{E\lambda}(\Theta,\xi) \;\leqslant\; R^2_{E\lambda}(\pi,0) \;=\; 1$$

$$R^2_{M\lambda}(\pi,0) \;=\; 0\,. \quad (2.33)$$

The maximum values of $R^2_{M\lambda}(\Theta,\xi)$ are for $\Theta \sim 90°$, $\xi = 0$ where $R^2_{M\lambda}(\Theta,\xi)$ is of order 0.01.

(b) given two multipolarities L and ℓ, $R^2_{EL}(\Theta,\xi)$ and $R^2_{E\ell}(\Theta,\xi)$ are of similar magnitude for low ξ values and backscattering. If $L > \ell$ then $R^2_{EL}(\Theta,\xi)$ falls more rapidly than $R^2_{E\ell}(\Theta,\xi)$ as $\Theta \to 0$ but less rapidly as ξ is increased.

(c) as $\xi\ \mathrm{cosec}(\Theta/2) \to \infty$ [A175, p.339]

$$R^2_{E\lambda}(\Theta,\xi) \to \xi^{2\lambda-1}\ \sin(\Theta/2)\ \exp[-2\xi\ \mathrm{cosec}(\Theta/2)]$$

$$R^2_{M\lambda}(\Theta,\xi) \to \xi^{2\lambda}\ \exp[-2\xi\ \mathrm{cosec}(\Theta/2)]\,. \quad (2.34)$$

Values of $R^2_{\sigma\lambda}(\Theta,\xi)$ are given by Alder and Winther [A156a, A175] for E1-E4 and M1,M2 transitions. The E2 and M1 functions are graphed in figs. 2.1 and 2.2.

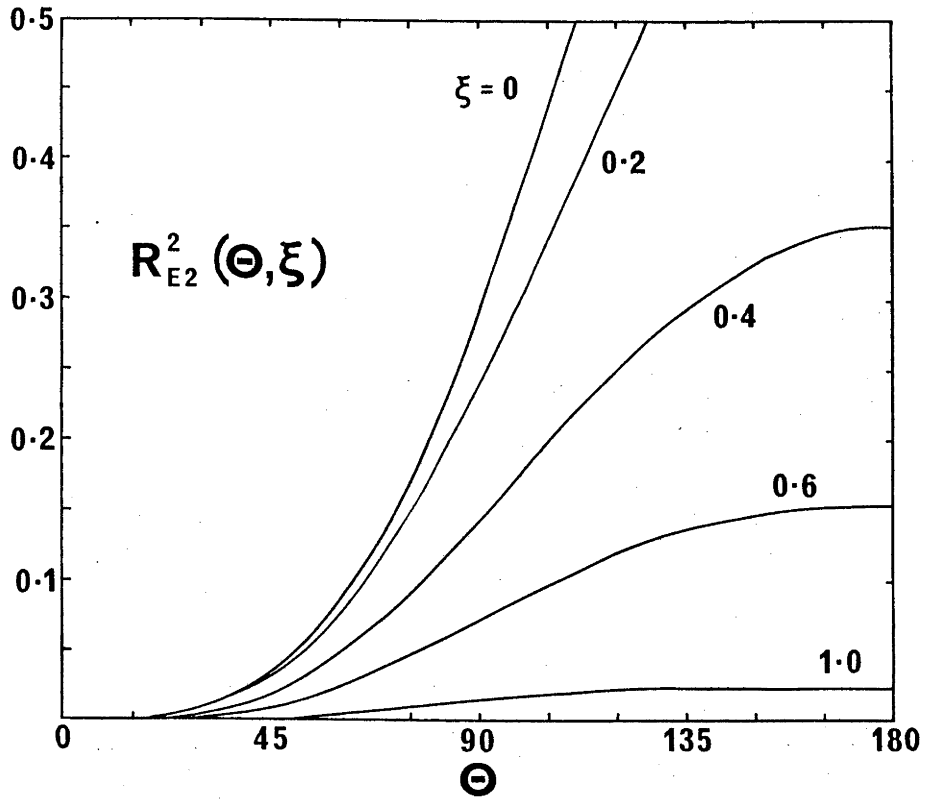

Fig. 2.1: The variation of the squared orbit integral $R^2_{E2}(\Theta,\xi)$ (eq. 2.32) with scattering angle and adiabaticity.

Thus, on the basis of the properties of the orbit integrals, the largest excitation probabilities occur in the electric excitations of low lying energy levels (since $\xi_{of} \propto E_f$) by backscattered projectiles. This statement must be qualified by consideration of the magnitudes of the strength functions $\chi^{\sigma\lambda}_{of}$. One notes that:—

(a) $\chi^{\sigma\lambda}_{of} \propto Z_1 Z_p^{-\lambda} Z_t^{-\lambda}$ so that, for the same ξ, λ and Θ, the excitation probability of the projectile is (Z_t/Z_p) times that of the target.

(b) $\chi^{\sigma\lambda}_{of} \propto (\lambda-1)!/(2\lambda+1)!!$ so that low multipolarity excitations are favoured.

(c) $\chi^{M\lambda}_{of} \sim \chi^{E\lambda}_{of}$ u/c so that electric transitions are favoured.

(d) $\chi^{E\lambda}_{of} \propto E^{\lambda-\frac{1}{2}}$ favouring transitions at high bombarding energy.

(e) $$\left|\chi^{\sigma\lambda}_{of}\right|^2 \propto B(\sigma\lambda;o\rightarrow f) \,. \qquad (2.35)$$

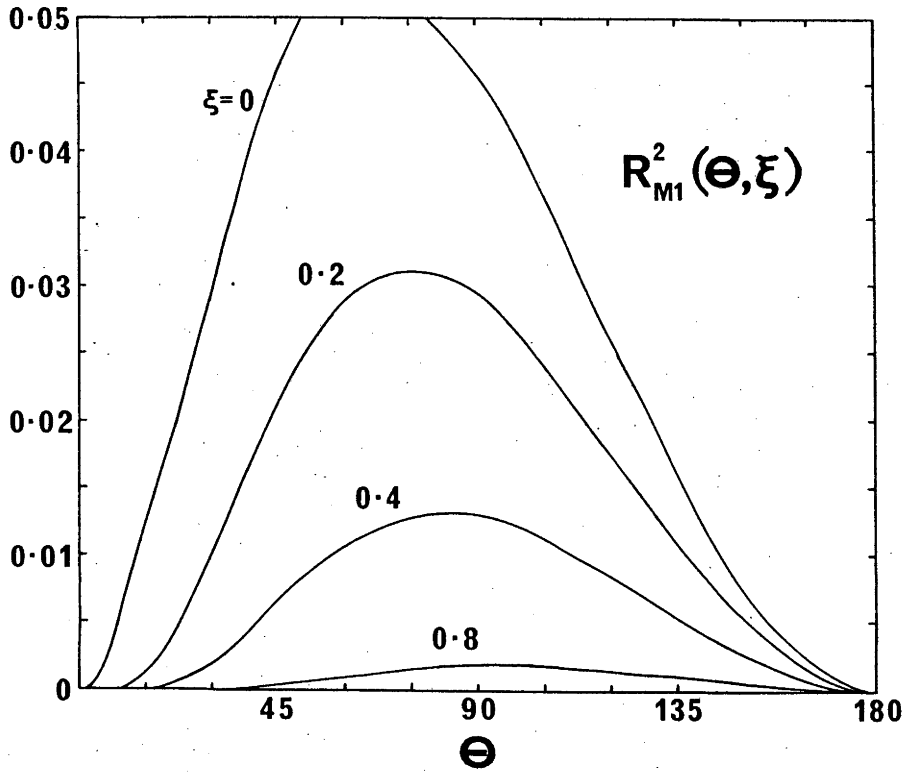

Fig. 2.2: The variation of the squared orbit integral $R^2_{M1}(\Theta,\xi)$ (eq. 2.32) with scattering angle and adiabaticity.

The reduced transition probabilities $B(\sigma\lambda;o\rightarrow f)$ (see eq. 1.46) are the only nuclear properties which influence the excitation probability in first order perturbation theory. To discover how the nuclear quadrupole moment affects the excitation, it is necessary to go to second order perturbation theory.

In the second order theory, the amplitudes $a_m(w)$ in eq. 2.25 are replaced by their first-order estimates at any particular w. One obtains [A175, p.122]

$$a_{n,l} = a^{(1)}_{n,l} + a^{(2)}_{n,l}, \tag{2.36}$$

where $a^{(1)}_{n,l}$ is the first order solution given by eq. 2.29 and

$$a^{(2)}_{n,\ell} = -\hbar^{-2} \sum_m \int_{-\infty}^{\infty} \langle n| \; V_{EE}(t) + V_{EM}(t) - \frac{Z_p Z_t e^2}{4\pi\varepsilon_0 r(t)} \; |m\rangle$$

$$\times \exp[i(E_n - E_m)t/\hbar] \int_{-\infty}^{t} \langle m| \; V_{EE}(t') + V_{EM}(t') - \frac{Z_p Z_t e^2}{4\pi\varepsilon_0 r(t')} \; |\ell\rangle$$

$$\times \exp[i(E_m - E_\ell)t'/\hbar] \; dt'dt \, . \qquad (2.37)$$

As usual, m labels all of the projection substates of the nucleus. Insertion of the multipole expansions for V_{EE} and V_{EM} gives, with the use of a step function,

$$a^{(2)}_{n,\ell} = -\tfrac{1}{2}\sqrt{\frac{2J_\ell+1}{2J_n+1}} \sum_{\substack{m\sigma\lambda\mu \\ \sigma'\lambda'\mu'}} \nu_{\lambda+\lambda'} \sqrt{(2\lambda+1)(2\lambda'+1)} \; \chi^{\sigma\lambda}_{\ell m} \chi^{\sigma'\lambda'}_{mn}$$

$$\times C(J_\ell \lambda J_m; M_\ell - \mu M_m) C(J_m \lambda' J_n; M_m - \mu' M_n)$$

$$\times \left[R_{\sigma\lambda\mu}(\Theta, \xi_{\ell m}) R_{\sigma'\lambda'\mu'}(\Theta, \xi_{mn}) + \frac{i}{\pi} \int_{-\infty}^{\infty} R_{\sigma\lambda\mu}(\Theta, \xi_{\ell m} + \xi) \right.$$

$$\left. \times R_{\sigma'\lambda'\mu'}(\Theta, \xi_{mn} - \xi) \; \frac{d\xi}{\xi} \right] , \qquad (2.38)$$

where the parameters σ and σ' range independently over "E" and "M". It is convenient to write the products of the spherical tensors $R_{\sigma\lambda\mu}$ as sums by defining

$$R_{(\sigma\lambda\sigma'\lambda')k\kappa}(\Theta, \xi, \xi') = (-)^{\lambda+\lambda'+k} \sum_{\mu\mu'} C(\lambda\lambda' k; \mu\mu'\kappa)$$

$$\times R_{\sigma\lambda\mu}(\Theta, \xi) R_{\sigma'\lambda'\mu'}(\Theta, \xi') \qquad (2.39)$$

and

$$G_{(\sigma\lambda\sigma'\lambda')k\kappa}(\Theta, \xi, \xi') = \frac{(-)^{\lambda+\lambda'+k}}{\pi} \sum_{\mu\mu'} C(\lambda\lambda' k; \mu\mu'\kappa)$$

$$\times \int_{-\infty}^{\infty} R_{\sigma\lambda\mu}(\Theta, \xi + t) R_{\sigma'\lambda'\mu'}(\Theta, \xi' - t) \; \frac{dt}{t} \, . \qquad (2.40)$$

The sum over the magnetic substates of the intermediate levels z is

also performed to give

$$a^{(2)}_{n,\ell} = -\tfrac{1}{2}\sqrt{\frac{2J_\ell+1}{2J_n+1}} \sum_{\substack{z\sigma\lambda\sigma'\lambda' \\ k\kappa}} \nu_{\lambda+\lambda'} \sqrt{(2\lambda+1)(2\lambda'+1)(2k+1)(2J_z+1)}\ \chi^{\sigma\lambda\ \sigma'\lambda'}_{\ell z}\chi_{zn}$$

$$\times W(J_\ell \lambda J_n \lambda'; J_z k) C(J_\ell k J_n; M_\ell - \kappa M_n)$$

$$\times \left[R_{(\sigma\lambda\sigma'\lambda')k\kappa}(\Theta, \xi_{\ell z}, \xi_{zn}) + iG_{(\sigma\lambda\sigma'\lambda')k\kappa}(\Theta, \xi_{\ell z}, \xi_{zn})\right] . \qquad (2.41)$$

This equation is similar in form to eq. 2.29 which gives the first order amplitude. However, $a^{(2)}_{n,\ell}$ has both real and imaginary parts while $a^{(1)}_{n,\ell}$ is purely imaginary.

The excitation probability is found by inserting eq. 2.41 into eq. 2.27. To display the various terms most clearly, one usually writes

$$P_f =: P_f^{(1,1)} + P_f^{(1,2)} + P_f^{(2,2)} , \qquad (2.42)$$

the superscripts in brackets indicating the order of the amplitudes contained in that term. The term $P_f^{(1,1)}$ is the same as the first order estimate (eq. 2.31) and the second order term is

$$P_f^{(1,2)} = \sum_{\substack{z\sigma\lambda\sigma'\lambda' \\ \sigma''\lambda''}} \nu_{\lambda+\lambda'+\lambda''} \sqrt{(2\lambda+1)(2\lambda'+1)(2J_z+1)}\ W(J_o \lambda J_f \lambda'; J_z \lambda'')$$

$$\times \chi^{\sigma\lambda\ \sigma'\lambda'}_{oz}\chi^{\sigma''\lambda''}_{zf}\chi_{of} \sum_\mu R_{\sigma''\lambda''\mu}(\Theta, \xi_{of}) G_{(\sigma\lambda\sigma'\lambda')\lambda''\mu}(\Theta, \xi_{oz}, \xi_{zf}) . \qquad (2.43)$$

The term $P_f^{(2,2)}$ contains a product of four strength functions and so is of the same order as the term $P_f^{(1,3)}$ which would be obtained if the expression for $a_{n,\ell}(w)$ were computed to third order [Ma65].

In principle, all nuclear states with both χ_{oz} and χ_{zf} non-zero must be considered in computing $P_f^{(1,2)}$ although, in practice, $P_f^{(1,2)}$ is dominated by a few terms only. The terms in $P_f^{(1,2)}$ with $z = o$ and $z = f$ are of particular interest as they involve the quadrupole moments (table 1.1) of the ground state and the excited state respectively.

The appearance of these terms is known as the "reorientation effect".

For illustrative purposes, let us consider electric quadrupole excitations involving just the intermediate level. Then

$$P_f = \left|\chi_{of}^{E2}\right|^2 R_{E2}^2(\theta,\xi_{of}) \left(1 + y_{E2}^{E2E2}\, \Pi_{E2}^{E2E2}(\theta,\xi_{of}\zeta_{ozf})\right), \qquad (2.44)$$

where the new parameter ζ_{ozf} is defined by

$$\zeta_{ozf} := \xi_{oz}/\xi_{of} \qquad (2.45)$$

and the other functions are

$$y_{\sigma''\lambda''}^{\sigma\lambda\sigma'\lambda'} = \sqrt{(2\lambda''+1)(2J_z+1)}\; W(J_o\lambda J_f\lambda';J_z\lambda'')\; \chi_{oz}^{\sigma\lambda}\chi_{zf}^{\sigma'\lambda'}/\chi_{of}^{\sigma''\lambda''} \qquad (2.46)$$

and

$$\Pi_{\sigma''\lambda''}^{\sigma\lambda\sigma'\lambda'}(\theta,\xi,\zeta) := \nu_{\lambda+\lambda'+\lambda''} \sqrt{\frac{(2\lambda+1)(2\lambda'+1)}{2\lambda''+1}} \sum_{\mu} R_{\sigma''\lambda''\mu}(\theta,\xi) \times G_{(\sigma\lambda\sigma'\lambda')\lambda''\mu}(\theta,\zeta\xi,\xi-\zeta\xi)\; [R_{\sigma''\lambda''}^2(\theta,\xi)]^{-1}. \qquad (2.47)$$

For the reorientation effect, $\zeta_{ozf} = 0$ or $\zeta_{ozf} = 1$ and one of the strength functions in the numerator of the expression for y_{E2}^{E2E2} is χ_{of}^{E2} while the other is

$$\chi^{E2} = \sqrt{\frac{(2J+3)(J+1)}{5J(2J-1)}}\; \frac{Z_1 e}{12\pi\varepsilon_0\hbar u a^2}\; Q_{J^\pi}, \qquad (2.48)$$

Q, J and π referring to either the ground or excited state. The sensitivity ρ of P_f to the quadrupole moment is given by the coefficients of Q_{J^π}. For the excitation of a $J = 2$ state from a $J = 0$ ground state,

$$\rho = \frac{Z_1 e}{12\pi\varepsilon_0\hbar u a^2} \sqrt{\frac{7}{10}}\; \Pi_{E2}^{E2E2}(\theta,\xi,1)$$

or

$$\rho_{[e^{-1}\ fm^{-2}]} = 0.08472\; \frac{Z_1}{Z_p^2 Z_t^2}\; \frac{\sqrt{A_{p[u]}\ E^3_{[MeV]}}}{(1 + A_p/A_t)^2}\; \Pi_{E2}^{E2E2}(\theta,\xi,1). \qquad (2.49)$$

The appearance of Z_1, the atomic number of the exciting nucleus, in the numerator shows that ρ is larger by a factor of Z_t/Z_p for projectile excitation than for target excitation.

The effects of other nuclear levels on the excitation probability of the level in question is given by the particular ζ value concerned. It is interesting to note that $\Pi_{E2}^{E2E2}(\Theta,\xi,\frac{1}{2}) = 0$. That is, a level of exactly half the excitation energy of another level has no effect (to second order, there will be a third order effect) on the excitation of that other level.

The functions $\Pi_{E2}^{E2E2}(180°,\xi,\zeta)$ and $\Pi_{E2}^{E2E2}(\Theta,\xi,1)$ are shown in figs. 2.3 and 2.4.

2.1.4 Summary

The processes which occur in electromagnetic excitation may be visualized, from the viewpoint of perturbation theory, in a manner displayed in fig. 2.5. In this figure, each half arrow represents a probability amplitude. First order terms consist of the product of two amplitudes, second order terms of three amplitudes and so on. Since each amplitude contains a strength function χ, the first order term can be considered to be of order χ^2, the second order terms of order χ^3, etc. In the experiments described below, $\chi \sim 0.1$.

Another feature of the nuclei studied below is that they all have $J = 0$ ground states, so the only reorientation effects involved are due to the static moments of the excited state. To analyse the data obtained, one writes

$$P_f = F\, B(E2;o \rightarrow f)[1 + \rho Q_{J^\pi_f}] . \qquad (2.50)$$

Rather than compute ρ and F using perturbation theory, a computer program which integrates eq. 2.25 directly is used. This allows for the effect of third and higher order terms. Because of the lack of information concerning reduced transition probabilities of high-lying states, and because of limitations on computer space, it is usual to include only the first few levels of a nucleus in the calculation.

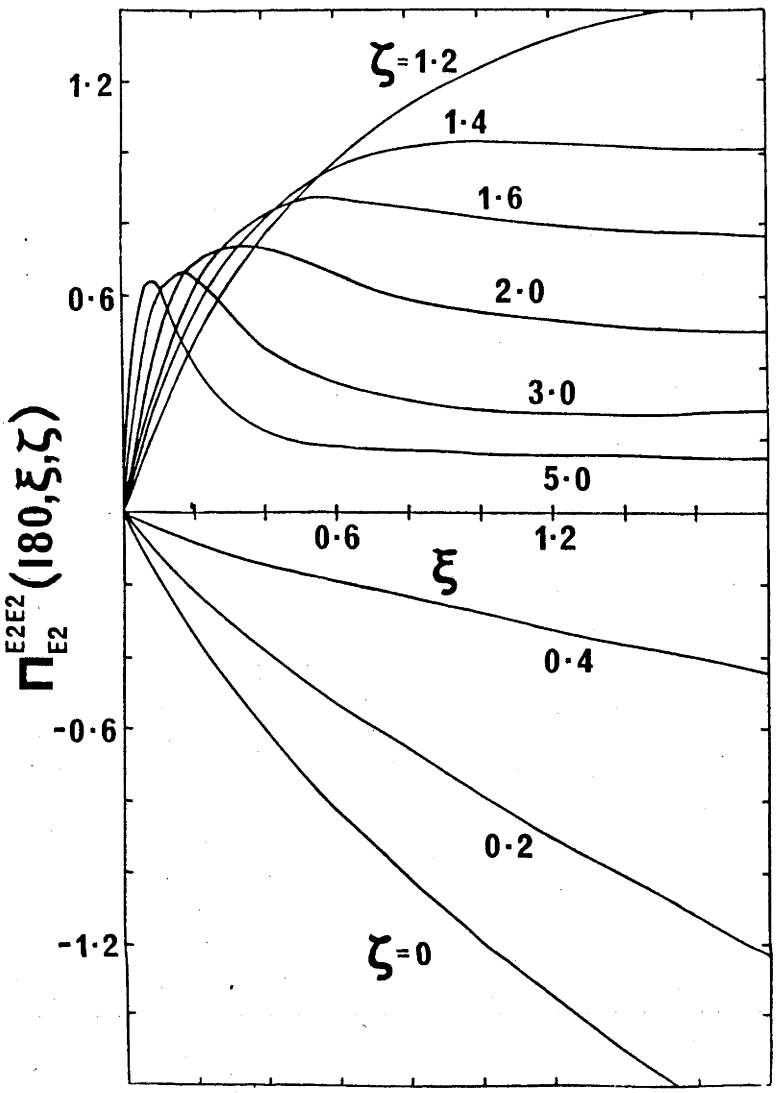

Fig. 2.3: The variation of the function $\Pi_{E2}^{E2E2}(\theta,\xi,\zeta)$ (eq. 2.47) with adiabaticity and adiabaticity ratio for $\theta = 180°$.

This procedure obtains some justification, at least for $\xi \gtrsim 0.1$ in the decrease of $\Pi_{E2}^{E2E2}(\theta,\xi,\zeta)$ with increasing ζ (fig. 2.3). One important difficulty with this restriction on the nuclear levels considered concerns the effect of the giant dipole resonance which has relatively large values of χ. This will be considered in subsection 2.2.3.

Since the reorientation effect, that is, the product ρQ in eq. 2.50, is of the order of 0.1, the excitation probabilities must be computed to better than 1% to ensure that the experimental data are correctly interpreted. Thus various sources of error, stemming from

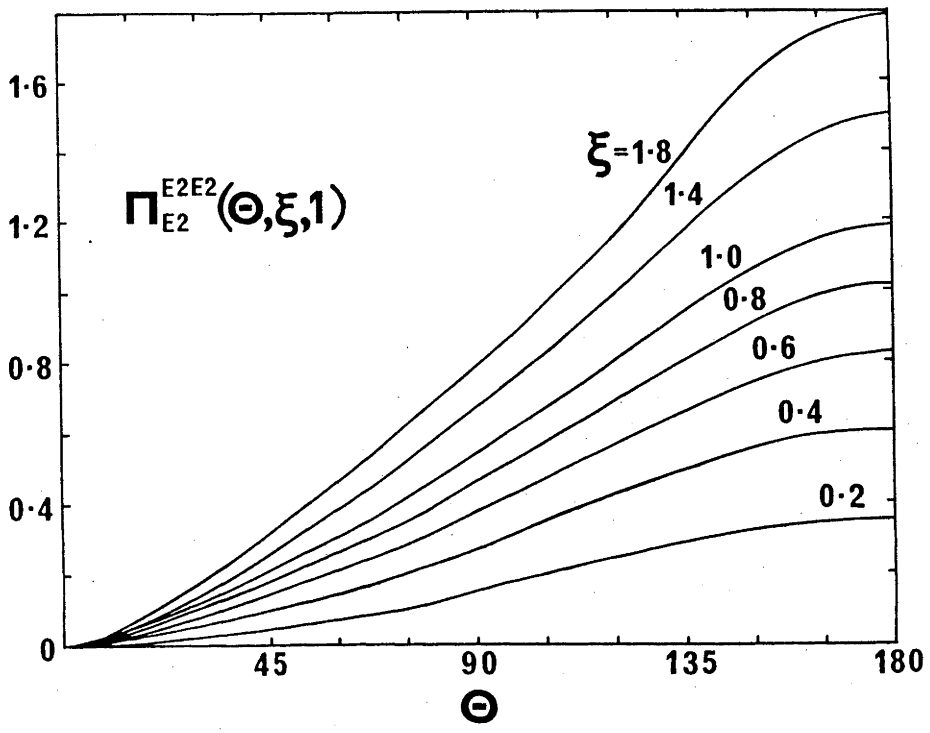

Fig. 2.4: The variation of the function $\Pi_{E2}^{E2E2}(\Theta,\xi,\zeta)$ (eq. 2.47) with scattering angle and adiabaticity for $\zeta = 1$.

omissions in the above analysis, must be considered and, if their magnitudes warrant it, corrected for. This is done in the remaining sections of this chapter.

2.2 THE EFFECTS OF SOME NUCLEAR PARAMETERS WHICH ARE EITHER GENERALLY IGNORED OR ARE DIFFICULT TO ESTIMATE

2.2.1 Magnetic Dipole and Electric Hexadecapole Reorientation

The M1 and E4 moments are, respectively, the lowest order static magnetic and the next lowest order static electric moment which a nucleus may possess. Their effects on P_f may be determined in a manner analogous to that of the electric quadrupole moment. Thus

$$P_f = |\chi_{of}^{E2}|^2 R_{E2}^2(\Theta,\xi_{of}) \left(1 + y_{E2}^{E2\sigma\lambda}\, \Pi_{E2}^{E2\sigma\lambda}(\Theta,\xi_{of},\zeta_{ozf})\right) \qquad (2.51)$$

is the excitation probability of a level being populated in the manner

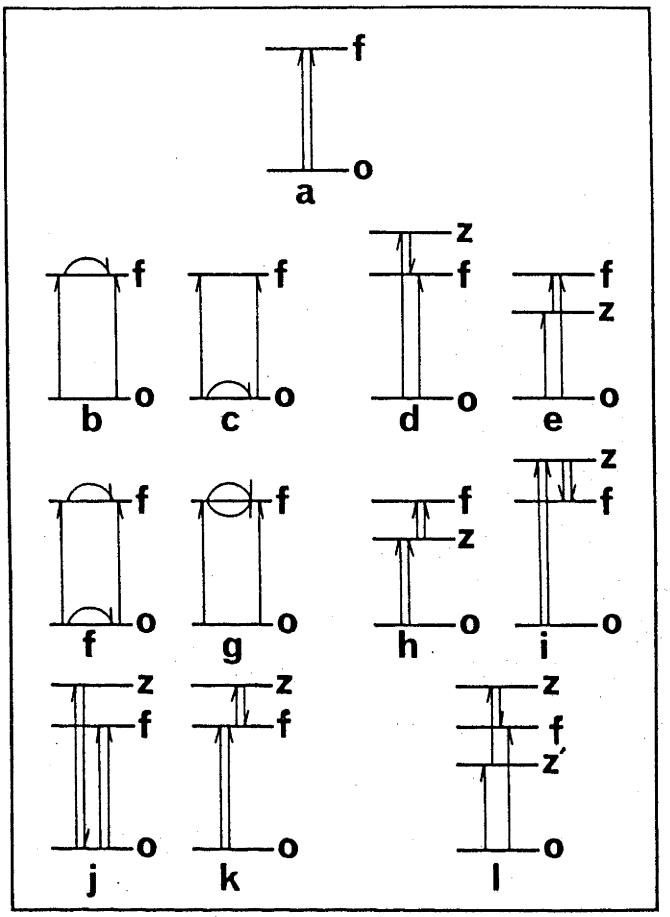

Fig. 2.5: Some mechanisms for the excitation of a state f from a state o. Each half arrow represents a first-order probability amplitude. Shown are the first order term (a), the second order terms (b-e), and some third order terms (f-$\mathcal{l}$). Terms b and c are reorientation effects, d and e interference effects, f and g double reorientation effects, k and i two-step excitations, j and k depopulation effects and $\mathcal{l}$ is the general third order term.

shown in fig. 2.6. The reorientation effect again corresponds to $\zeta_{ozf} = 1$ and the functions $\Pi_{E2}^{E2M1}(\theta,\xi,1)$ and $\Pi_{E2}^{E2E4}(\theta,\xi,1)$ are shown in figs. 2.7 and 2.8. The relative importance of M1 and E4 reorientation is best seen by considering the ratios $y_{E2}^{E2\sigma\lambda}\ \Pi_{E2}^{E2\sigma\lambda} \Big/ y_{E2}^{E2E2}\ \Pi_{E2}^{E2E2}$. The ratios of the y's are, for the case of a $J = 0$ ground state and a $J = 2$ excited state of a projectile,

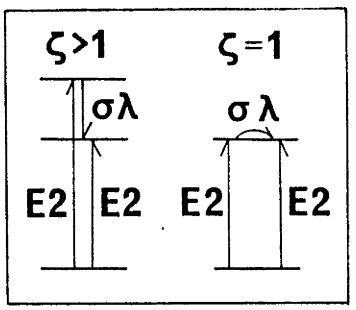

Fig. 2.6: The second order excitation mechanism considered in eq. 2.51.

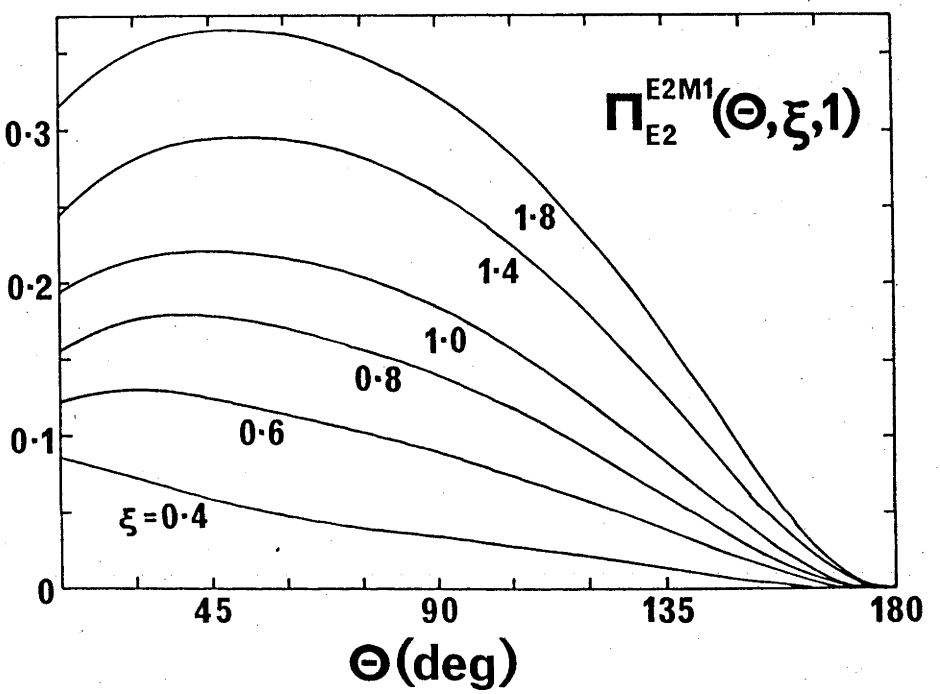

Fig. 2.7: The variation of the function $\Pi_{E2}^{E2M1}(\Theta,\xi,\zeta)$ (eq. 2.47) with scattering angle and adiabaticity for $\zeta = 1$ and for projectile excitation.

$$y_{E2}^{E2M1} \Big/ y_{E2}^{E2E2} = 6\sqrt{\frac{3}{7}}\frac{ua}{c}\mu_{2^+}/Q_{2^+}$$

$$= 0.01478\, Z_p Z_t (1 + A_p/A_t)(A_p E_{[MeV]})^{-\frac{1}{2}} \frac{\mu_{2^+}[\mu_N/c]}{Q_{2^+}[e\ fm^2]} \qquad (2.52)$$

and

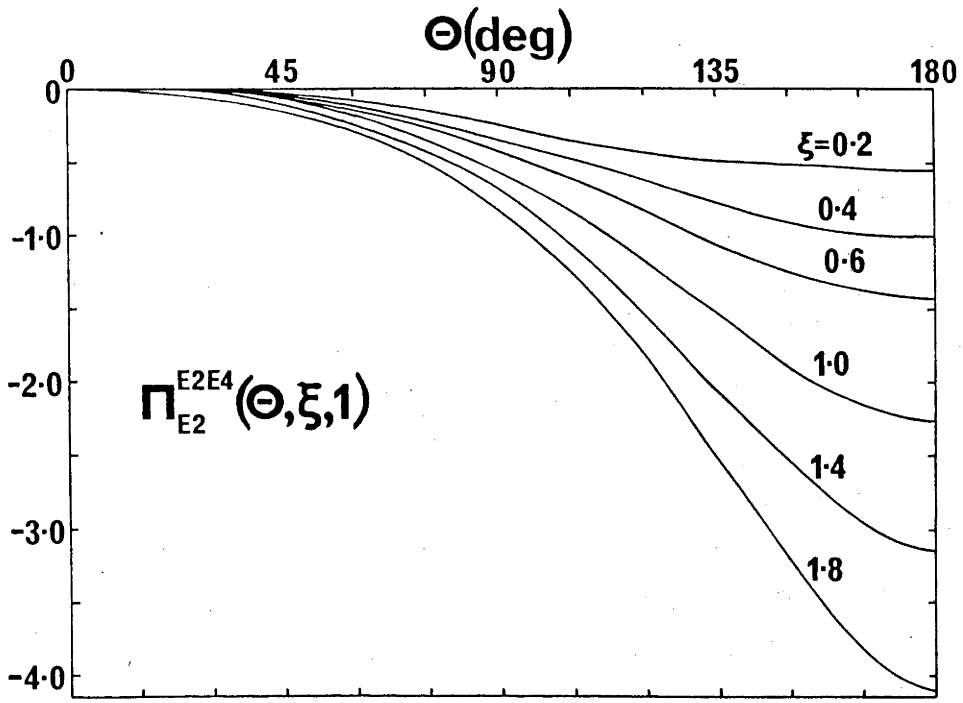

Fig. 2.8: The variation of the function $\Pi_{E2}^{E2E4}(\Theta,\xi,\zeta)$ (eq. 2.47) with scattering angle and adiabaticity for $\zeta = 1$.

$$y_{E2}^{E2E4} \Big/ y_{E2}^{E2E2} = \frac{36H_{2^+}}{35\dot{a}^2 Q_{2^+}}$$

$$= 1.984\, Z_p^{-2} Z_t^{-2} E^2_{[MeV]} (1 + A_p/A_t)^{-2} \frac{H_{2^+}[e\ fm^4]}{Q_{2^+}[e\ fm^2]}, \quad (2.53)$$

where the magnetic dipole moment μ_{2^+} is measured in the conventional units of the nuclear magneton $\mu_N = e\hbar/2m_p$ divided by the velocity of light. Plots of the ratios of the Π's are shown in figs. 2.9 and 2.10. These show that magnetic dipole reorientation vanishes at $\Theta = 180°$ while electric hexadecapole reorientation is largest at that angle. The values of the Π's and y's which apply to the present experiments are shown in table 2.1. It is seen that the effect of μ_{2^+} or H_{2^+} may be as much as 10% of the effect of Q_{2^+} if $\mu_{2^+[\mu_N/c]} \sim Q_{2^+[e\ fm^2]}$ or $H_{2^+[e\ fm^4]} \sim 3Q_{2^+[e\ fm^2]}$.

As the magnetic dipole moments of the first excited states of many nuclei have been measured, the correction for μ_{2^+} can readily be

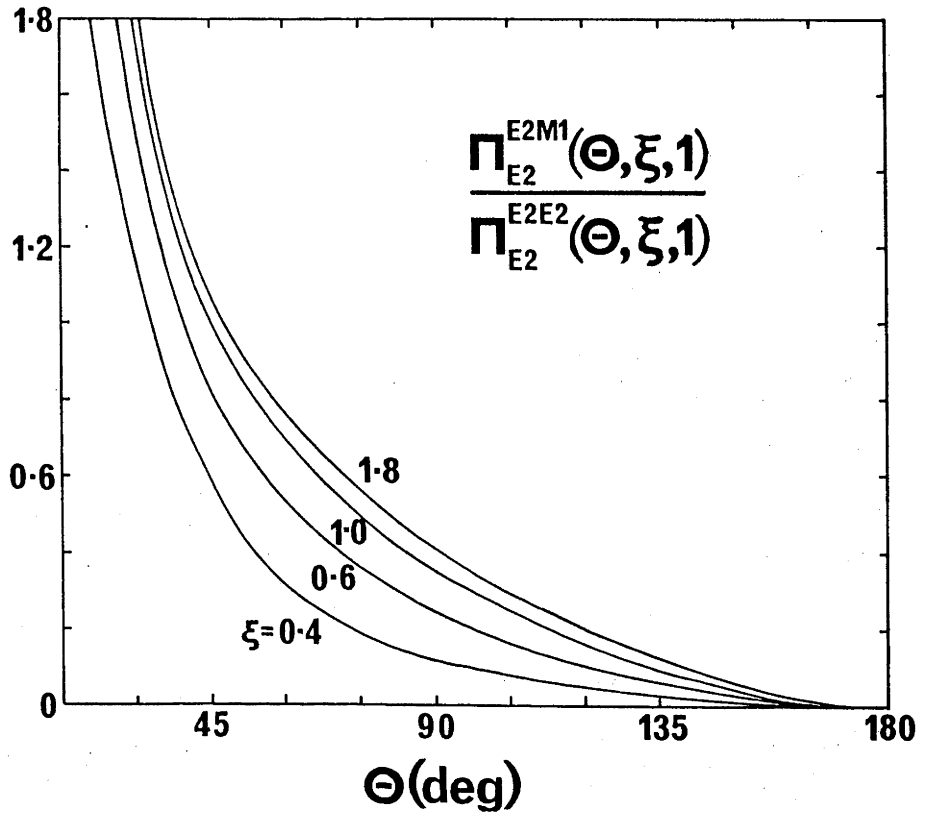

Fig. 2.9: The relative variations of the functions $\Pi_{E2}^{E2M1}(\theta,\xi,\zeta)$ and $\Pi_{E2}^{E2E2}(\theta,\xi,\zeta)$ (eq. 2.47) with scattering angle and adiabaticity for $\zeta = 1$ and for projectile excitation.

Table 2.1

The effects of magnetic dipole and electric hexadecapole reorientation in the present experiments

Conditions	16 MeV ^{4}He on ^{198}Hg, $\Theta = 180°$	60 MeV ^{18}O on ^{208}Pb, $\Theta = 180°$	60 MeV ^{18}O on ^{208}Pb, $\Theta = 95°$
$\Pi_{E2}^{E2M1} / \Pi_{E2}^{E2E2}$	0	0	0.3
$y_{E2}^{E2M1} / y_{E2}^{E2E2}$	0.30 μ_2+/Q_2+	0.32 μ_2+/Q_2+	0.32 μ_2+/Q_2+
$\Pi_{E2}^{E2E4} / \Pi_{E2}^{E2E2}$	-1.6	-1.9	-1.3
$y_{E2}^{E2E4} / y_{E2}^{E2E2}$	0.019 H_2+/Q_2+	0.014 H_2+/Q_2+	0.014 H_2+/Q_2+

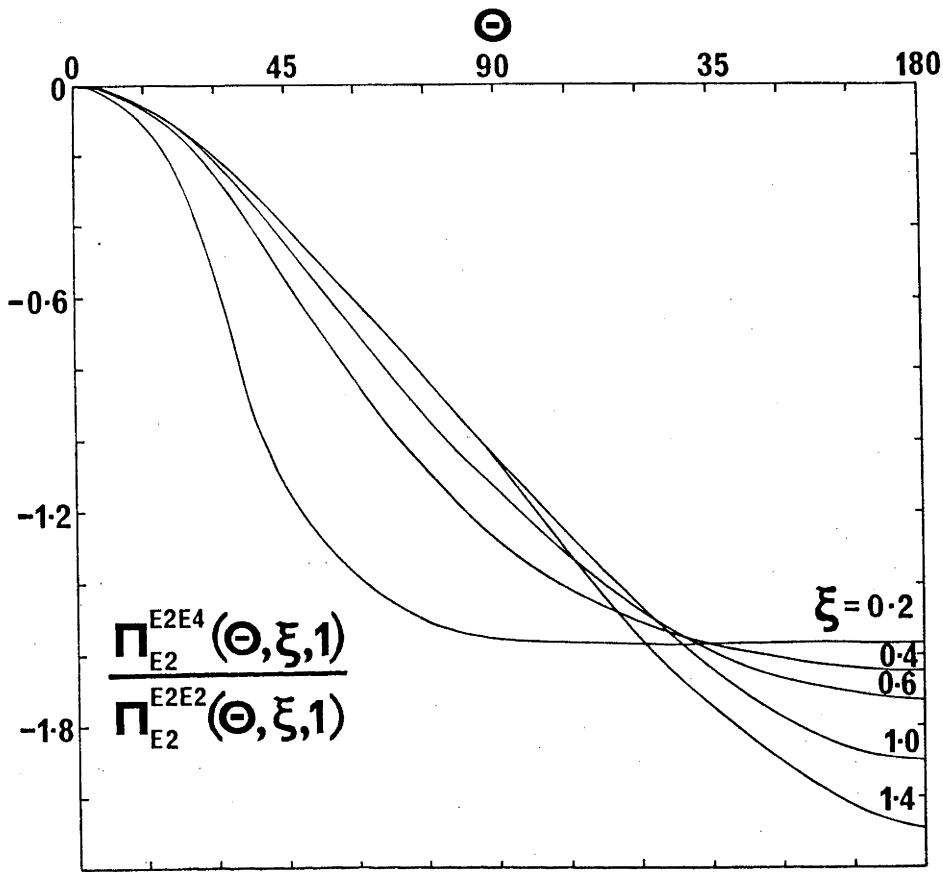

Fig. 2.10: The relative variations of the functions $\Pi_{E2}^{E2E4}(\Theta,\xi,\zeta)$ and $\Pi_{E2}^{E2E2}(\Theta,\xi,\zeta)$ (eq. 2.47) with scattering angle and adiabaticity for $\zeta = 1$.

made. In general, its magnitude is too small compared with that of Q_{2+} to have a significant effect in 90° scattering. As fig. 2.9 shows, care must be exercised at scattering angles further forward than 90°.

The effect of the E4 static moment is more difficult to determine since its magnitude is generally not known. Estimates of its size are made in later sections for each of the nuclei considered.

2.2.2 Interference Involving Electric Hexadecapole Moments

By "interference" is meant terms identified as such in fig. 2.5. In even-even nuclei, it is usually found that the most important of the interference terms involve E2 matrix elements connecting the

ground state and first excited state with the second $J^\pi = 2^+$ state. Where the lifetime and gamma-ray branching ratio of the 2_2^+ state and the mixing ratio of the $2_2^+ \rightarrow 2_1^+$ transition are known, the interference of the 2_2^+ state can, apart from an ambiguity in the signs of the matrix elements, be allowed for.

The problem addressed in this section is the effect of the first excited $J^\pi = 4^+$ state when it is at a relatively low excitation energy and connected by a relatively large E2 moment to the first excited state. Such a situation occurs in collective nuclei. The effect on the excitation probability is given, analogously with eq. 2.51, as the product of

$$\Pi_{E2}^{E4E2}(\Theta,\xi_{of},\zeta_{ozf}) = -\Pi_{E2}^{E2E4}(\Theta,\xi_{of},1-\zeta_{ozf}) \qquad (2.54)$$

and

$$y_{E2}^{E4E2} = \chi_{oz}^{E4}\chi_{zf}^{E2}\Big/\chi_{of}^{E2}$$

$$= 0.008794\ Z_1 Z_p^{-4} Z_t^{-4} (A_p E^7_{[MeV]})^{\frac{1}{2}}\ (1+A_p/A_t)^{-4}$$

$$\times \frac{\langle 4^+\|M(E4)\|0^+\rangle_{[e\ fm^4]}\langle 2^+\|M(E2)\|4^+\rangle_{[e\ fm^2]}}{\langle 2^+\|M(E2)\|0^+\rangle_{[e\ fm^2]}}\ . \qquad (2.55)$$

Unfortunately, the E4 matrix element is often not known. This is because the probability for the radiative decay of a level decreases more rapidly with increasing multipolarity than does the probability for the Coulomb excitation of that level. Thus the E4 branch of the gamma decay of the 4^+ level may be undetectable although the corresponding excitation is significant.

The importance of the effect of the 4^+ state can be gauged from the ratio of its interference to the reorientation effect, that is, from the product of the ratios

$$Y_{E2}^{E4E2} \Big/ Y_{E2}^{E2E2} = \frac{8}{63}\sqrt{\frac{2\pi}{35}}\,\frac{1}{a^2}\,\frac{\langle 4^+\|M(E4)\|0^+\rangle\langle 2^+\|M(E2)\|4^+\rangle}{Q_2+\langle 2^+\|M(E2)\|0^+\rangle}$$

$$= 0.1038\; Z_p^{-2} Z_t^{-2} (1 + A_p/A_t)^{-2}\; E^2_{[MeV]}$$

$$\frac{\langle 4^+\|M(E4)\|0^+\rangle_{[e\ fm^4]}\langle 2^+\|M(E2)\|4^+\rangle_{[e\ fm^2]}}{Q_{2^+[e\ fm^2]}\langle 2^+\|M(E2)\|0^+\rangle_{[e\ fm^2]}} \qquad (2.56)$$

and $\Pi_{E2}^{E4E2}(\Theta,\xi_{of},\zeta_{ozf}) \Big/ \Pi_{E2}^{E2E2}(\Theta,\xi_{of},1)$. The function $\Pi_{E2}^{E4E2}(180°,\xi,\zeta)$ is plotted in fig. 2.11 and the ratio of the Π's in fig. 2.12. From fig. 2.12, eq. 2.56 and the experimental conditions in table 2.1, this interference term may be 10% of the reorientation effect if

$$B(E4;0^+\to 4^+)_{[e^2fm^8]} \sim 6000\,\frac{B(E2;0^+\to 2^+)_{[e^2fm^4]}\,(Q_{2^+[e\ fm^2]})^2}{B(E2;2^+\to 4^+)_{[e^2fm^4]}} \qquad (2.57)$$

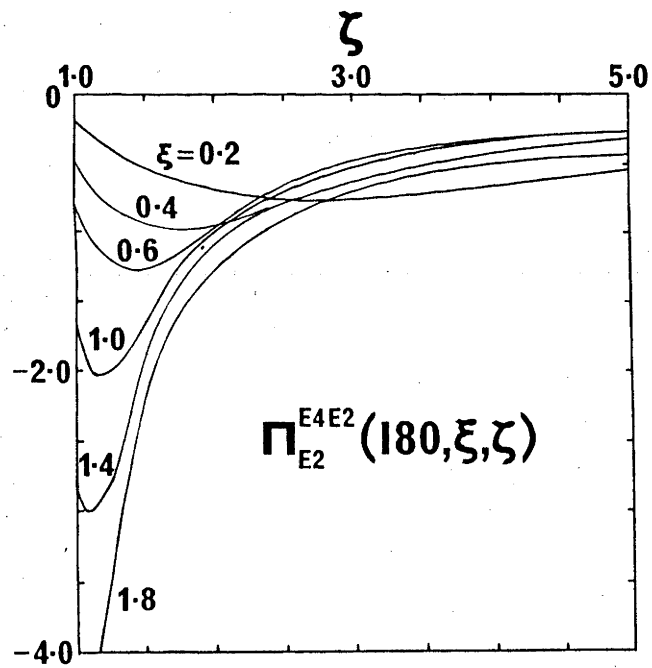

Fig. 2.11: The variation of the function $\Pi_{E2}^{E4E2}(\Theta,\xi,\zeta)$ with adiabaticity and adiabaticity ratio for $\Theta = 180°$.

2.2.3 The Effect of the Giant Dipole Resonance

The giant dipole resonance (gdr) consist of a collection of

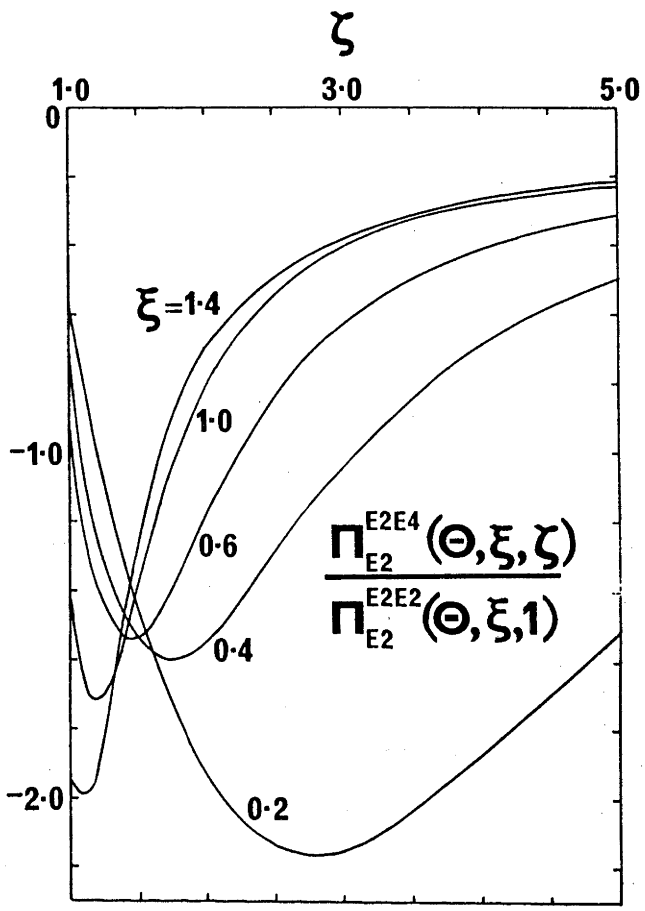

Fig. 2.12: The relative variations of the functions $\Pi_{E2}^{E4E2}(\Theta,\xi,\zeta)$ and $\Pi_{E2}^{E2E2}(\Theta,\xi,1)$ with adiabaticity and adiabaticity ratio for $\Theta = 180°$.

states at relatively high excitation energy which are connected to the ground state by relatively large electric dipole strengths. Not enough is known about the individual states in the gdr, nor is there a computer large enough, to include the gdr in detail in a numerical integration of eq. 2.25. However, use can be made of the high excitation energy of the gdr to determine its effect on the excitation of low lying states. Eq. 2.16 is split into two coupled equations which can be formally solved [A175, p.37] to give

$$i\hbar \frac{da_n(t)}{dt} = \sum_m \langle n|V(t) + V_{pol}(t)|m\rangle \exp[i(E_n - E_m)t/\hbar]\, a_m(t) , \quad (2.58)$$

where

$$\langle n|V_{pol}(t)|m\rangle = -\sum_z (E_z - E_m)^{-1} \langle n|V(t)|z\rangle \langle z|V(t)|m\rangle , \quad (2.59)$$

z labelling states in the gdr. The validity of eq. 2.59 depends on $E_z >> E_m$ [A175, p.37].

If we restrict our attention to V_{EE}, then, after a parameterization of the orbit as in subsection 2.1.2, eq. 2.58 becomes

$$\frac{da_n(w)}{dw} = -i \sum_{m\lambda\mu} \nu_\lambda \sqrt{\frac{(2\lambda+1)(2J_m+1)}{2J_n+1}}\, C(J_m \lambda J_n; M_m - \mu M_n)$$

$$\times \left(\left(\chi_{mn}^{E\lambda} - \sum_{\lambda'\lambda''} (\varepsilon \cosh w + 1)^{\lambda-\lambda'-\lambda''-1}\, S_{mn}^{(\lambda'\lambda'')\lambda} \right) \varrho_{E\lambda\mu}(\varepsilon, w) \right.$$

$$\left. + \chi_{mn}^{M\lambda}\, \varrho_{M\lambda\mu}(\varepsilon, w) \right) \exp[i\xi_{mn}(\varepsilon \sinh w + w)]\; a_m(w) \,, \qquad (2.60)$$

where

$$S_{mn}^{(\lambda'\lambda'')\lambda} := \frac{Z_1^2 e^2}{2\pi\varepsilon_0^2 \hbar u} \frac{(\lambda-1)!}{(2\lambda-1)!!} \frac{C(\lambda'\lambda''\lambda; 000)\, W(J_m \lambda' J_n \lambda''; J_z \lambda)}{\sqrt{(2\lambda'+1)(2\lambda''+1)(2J_m+1)}\; a^{\lambda'+\lambda''+1}}$$

$$\times \sum_z (E_z - E_m)^{-1} \langle J_n \| M(E\lambda'') \| J_z \rangle \langle J_z \| M(E\lambda') \| J_m \rangle \qquad (2.61)$$

is a strength function analogous to $\chi_{mn}^{E\lambda}$. It is seen that $\lambda+\lambda'+\lambda''$ must be even for $S_{mn}^{(\lambda'\lambda'')\lambda}$ to be non-zero. The multipolarities are identified in fig. 2.13. The solution of eq. 2.60 using first order perturbation theory gives the excitation probability of an excited state f as

$$P_f = \sum_{\lambda\mu} \left| \chi_{of}^{E\lambda} R_{E\lambda\mu}(\Theta, \xi_{of}) - \sum_{\lambda'\lambda''} S_{of}^{(\lambda'\lambda'')\lambda} R_{E\lambda\mu}^{(\lambda'\lambda'')}(\Theta, \xi_{of}) \right|^2$$

$$+ \sum_\lambda \left| \chi_{of}^{M\lambda} \right|^2 R_{M\lambda}^2(\Theta, \xi_{of}) \,, \qquad (2.62)$$

where

$$R_{E\lambda\mu}^{(\lambda'\lambda'')}(\Theta, \xi) = \int_{-\infty}^{\infty} \varrho_{E\lambda\mu}(\varepsilon, w)\, (\varepsilon \cosh w + 1)^{\lambda-\lambda'-\lambda''-1}$$

$$\times \exp[i\xi(\varepsilon \sinh w + w)]\; dw \,. \qquad (2.63)$$

In the case of the excitation of a 2^+ excited state of an even-even nucleus, eq. 2.62 becomes

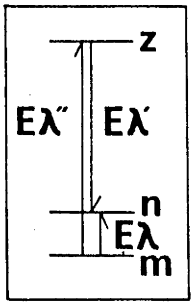

Fig. 2.13: Multipolarities involved in the second order excitation of a level n from a level m via a high-lying level z.

$$P_f = |\chi^{E2}_{of}|^2 \, R^2_{E2}(\Theta,\xi_{of}) \left(1 - \Delta^{11}_{E2}(\Theta,\xi_{of}) \, S^{(11)2}_{of} \Big/ \chi^{E2}_{of}\right) , \qquad (2.64)$$

where

$$\Delta^{\lambda'\lambda''}_{E\lambda}(\Theta,\xi) := 2 \sum_{\mu} R^{(\lambda'\lambda'')}_{E\lambda\mu}(\Theta,\xi) R_{E\lambda\mu}(\Theta,\xi) / R^2_{E\lambda}(\Theta,\xi) , \qquad (2.65)$$

if it is supposed that:—

(a) the gdr is the only important giant dipole resonance,

(b) E3 matrix elements between the gdr and the 2^+ state can be neglected,

(c) $\chi^{E2}_{of} >> S^{(11)2}_{of}$ so that the term in $\left(S^{(11)2}_{of}\right)^2$ can be neglected.

Values of $\Delta^{11}_{E2}(\Theta,\xi)$ are shown in fig. 2.14. In the experimental analysis described in chapter 4, assumptions (a) and (b) above are made, but assumption (c) is avoided by integrating eq. 2.60 numerically.

It remains to estimate the quantity $S^{(11)2}_{of}$, the problem being the sum over the gdr states z which appears in eq. 2.61. This problem is commonly divided into two parts by writing

$$\sum_z E_z^{-1} \langle 2^+ \| M(E1) \| z \rangle \langle z \| M(E1) \| 0^+ \rangle =: \eta_0 \sum_z E_z^{-1} |\langle z \| M(E1) \| 0^+ \rangle|^2 \qquad (2.66)$$

and separately estimating η_0 and the new sum over the gdr states z. This new sum can be related to the polarization tensor α_{ij} which is defined by

$$d_i =: \sum_j \alpha_{ij} \, \mathcal{E}_j , \qquad (2.67)$$

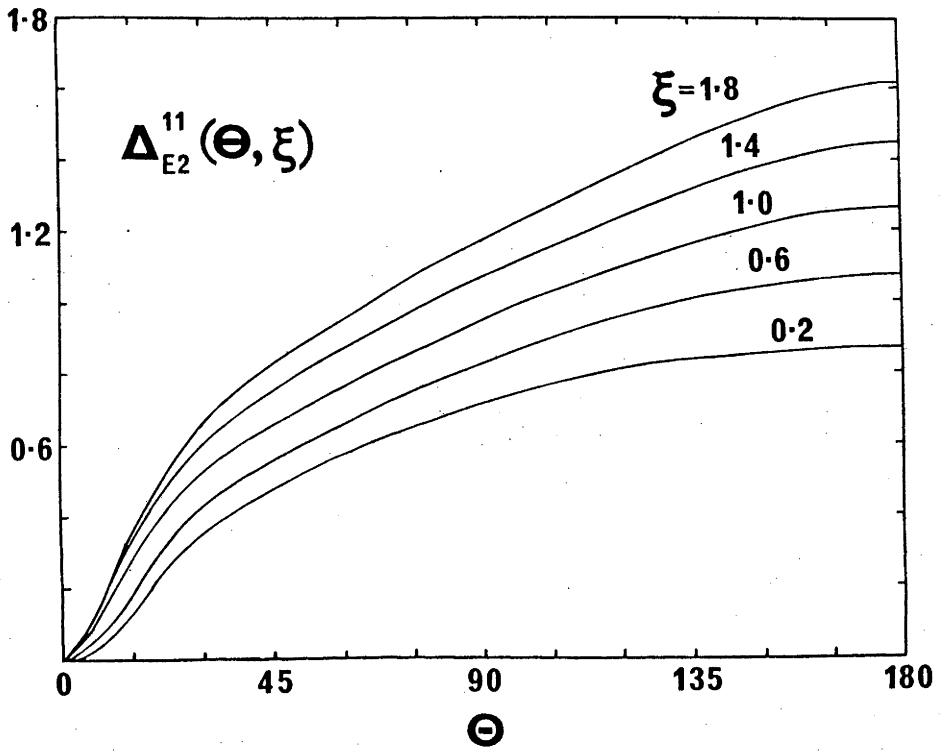

Fig. 2.14: The variation of the function $\Delta^{11}_{E2}(\Theta,\xi)$ (eq. 2.65) with scattering angle and adiabaticity.

$\underset{\sim}{d}$ being the dipole moment induced in the nucleus by the electric field $\underset{\sim}{\mathcal{E}}$. If $\underset{\sim}{\mathcal{E}}$ is treated as a perturbation to the nuclear potential, then second order perturbation theory shows that α_{ij} is a dyadic given, for a nucleus in the state f, by [Me70, p.422]

$$\alpha_{ij}(f) = e^2 \sum_{z\neq f} (E_z - E_f)^{-1} [\langle f|r_i|z\rangle\langle z|r_j|f\rangle + \langle z|r_i|f\rangle\langle f|r_j|z\rangle] . \tag{2.68}$$

Transformation of eq. 2.68 to a spherical basis results in

$$\alpha_{\mu\nu}(f) = \frac{4\pi}{3}\delta_{\mu\nu} \sum_{z\neq f} (-)^{J_f - J_z + \mu} (E_z - E_f)^{-1} (2J_z+1)^{-1} |\langle z\|M(E1)\|f\rangle|^2$$

$$\times [C^2(J_f 1 J_z; M_f \mu M_f+\mu) + C^2(J_f 1 J_z; M_f -\mu M_f -\mu)] \tag{2.69}$$

thus showing that $\alpha_{\mu\nu}$ is diagonal and consists of two parts only; $\alpha_{11} = \alpha_{-1-1} \neq \alpha_{00}$ in general. However, for a $J=0$ state, all three non-zero components are equal:

$$\alpha_{\mu\nu}(J=0) = \frac{8\pi}{9}\,\delta_{\mu\nu}\sum_{z}(E_z - E_o)^{-1}\left|\langle z\|M(E1)\|0^+\rangle\right|^2 . \qquad (2.70)$$

Eq. 2.70 relates the sum on the right hand side of eq. 2.66 to the polarizability $\alpha := \alpha_{\mu\mu}(J=0)$ which can be related to the quantity

$$\sigma_{-2} := \int \sigma(E)\, E^{-2}\, dE , \qquad (2.71)$$

($\sigma(E)$ being the total photonuclear cross section) by the expression [Le57]

$$\alpha = \frac{2\varepsilon_0}{\pi}\,\hbar c\,\sigma_{-2} . \qquad (2.72)$$

A two-fluid model was used by Migdal [Mi45, reported in Le57] to compute α and hence infer a value of σ_{-2}. He obtained $\sigma_{-2} \propto A^{5/3}$ with a constant of proportionality which did not agree with experimental values. Agreement with experiment is obtained by adopting [Le57]

$$\sigma_{-2} = 3.5\ k\ A^{5/3}\ \mu b\ MeV^{-1} . \qquad (2.73)$$

The parameter k is introduced here to allow for deviations of particular nuclei from the general trend. It is to be determined experimentally. Thus, provided σ_{-2} is known, the sum over z in eq. 2.66 can be determined. If σ_{-2} is not known, and the nucleus concerned has $A \gtrsim 50$ [Ha73], then eq. 2.73 may be used with $k = 1$.

For the determination of η_0 (eq. 2.66) one must rely wholly on nuclear models as there are no experimental data which can be used to construct a semiempirical equation similar to eq. 2.73. Estimates have been made using the rigid rotational model [Mc64] and the dynamic collective model [Do67, Ne67] giving values in the range $0.1 \leqslant \eta_0 \leqslant 0.3$. It may be noted that these models predict $\eta_0 > 0$ so that, from eq. 2.64, the effect of the polarization is to reduce the excitation probability.

A different approach has been suggested by Alder and Winther [Al75, p.340]. They identify the polarization potential V_{pol} in eq. 2.58 with the vector product $\underset{\sim}{d}\cdot\underset{\approx}{\mathcal{E}}$ and they assume that the polarization tensor in the intrinsic frame is diagonal and proportional to the

square of the radius vector. This gives

$$V_{pol} = -\alpha \frac{Z_1^2 e^2}{32\pi^2 \varepsilon_0^2 r^4} \left[1 + \frac{8\pi}{3 Z_2^2 e R_2^2} \sum_{\mu} M(E2,\mu)\ Y^*_{2\mu}(\hat{\underset{\sim}{\xi}}) \right] , \qquad (2.74)$$

where r is the distance between the exciting nucleus (charge Z_1) and the excited nucleus (charge Z_2, average radius R_2, average polarizability α). It has been assumed that the nucleus being excited has an intrinsic quadrupole deformation and that the vibrational-model relationship between the deformation parameters $\alpha_{2\mu}$ and $M(E2,\mu)$ applies. The similarity of the second term of eq. 2.74 to the expression for the electric quadrupole potential $V_{EE}(\lambda = 2)$ (eq. 2.13) leads Alder and Winther to propose that

$$\begin{aligned} V_{pol} &= - \frac{5 Z_1 \alpha}{12\pi\varepsilon_0 Z_2 R_2^2 r} V_{EE}(\lambda = 2) \\ &= - 0.005625\ Z_2^{-2} A_2 k E_{[MeV]}\ (\varepsilon \cosh w + 1)^{-1}\ V_{EE}(\lambda = 2) . \end{aligned} \qquad (2.75)$$

Eqs. 2.18, 2.72 and 2.73 and the expression $R_2 = 1.2\ A_2^{1/3}$ fm have been used to obtain the last line of eq. 2.75. These equations imply [Ha73]

$$\eta_0 = \frac{4\sqrt{\pi}}{3} \frac{\langle 0^+ \| M(E2) \| 2^+ \rangle}{ZeR^2} . \qquad (2.76)$$

For ^{198}Hg, ^{24}Mg and ^{18}O, this gives $\eta_0 = 0.06$, 0.32 and 0.18 respectively.

Due to the ease with which eq. 2.75 can be incorporated into the de Boer-Winther computer program, it has become customary to use Alder and Winther's formalism for estimating the effect of the gdr on the excitation of the first excited state of even-even nuclei. I follow that practice here, but I observe that the values of η_0 given by eq. 2.76 can differ from the range $0.1 \lesssim \eta_0 \lesssim 0.3$ predicted by the rotational and dynamic collective models. It therefore seems reasonable to adopt an error of ± 0.1 in η_0. This gives a considerable uncertainty to the estimate of the effect of the gdr and has, in general, a larger effect than the uncertainty in the parameter k.

2.2.4 The Structure of the Exciting Nucleus

In the analysis of section 2.1, it was assumed that only the excited nucleus has structure and that the exciting nucleus acts as a point charge. This analysis can readily be extended to allow for the structure of both target and projectile. If the discussion is restricted to the electric multipole-electric multipole interaction V_{EE} (eq. 2.9) only, then the analogue of eq. 2.25 is

$$\frac{da_{n_p n_t}(w)}{dw} = -\frac{i}{2\eta} \sum_{\substack{m_p m_t \lambda_p \\ \lambda_t \mu_p \mu_t}} (-)^{\lambda_p} \lambda_p \lambda_t d_{\lambda_p \lambda_t} \sqrt{\frac{(2J_{m_p}+1)(2J_{m_t}+1)}{(2J_{n_p}+1)(2J_{n_t}+1)}} \chi^{E\lambda_p}_{m_p n_p} \chi^{E\lambda_t}_{m_t n_t}$$

$$\times C(J_{m_p} \lambda_p J_{n_p}; M_{m_p} -\mu_p M_{n_p}) C(J_{m_t} \lambda_t J_{n_t}; M_{m_t} -\mu_t M_{n_t}) C(\lambda_p \lambda_t \lambda_p+\lambda_t; \mu_p \mu_t \mu)$$

$$\times Q_{E\lambda_p+\lambda_t \mu}(\varepsilon, w) \exp[i(\xi_{m_p n_p} + \xi_{m_t n_t})(\varepsilon \sinh w + w)] \, a_{m_p m_t}(w) , \qquad (2.77)$$

where $a_{n_p n_t}(w)$ is the amplitude for scattering to the projectile's state n_p and the target's state n_t, Q, χ and ξ are defined by eqs. 2.20 - 2.24, η by eq. 2.2, ε and w by eq. 2.18 and $d_{\lambda_p \lambda_t}$ by

$$d_{\lambda_p \lambda_t} = \begin{cases} 0 & (\lambda_p = \lambda_t = 0) \\ \sqrt{\dfrac{(\lambda_p+\lambda_t)(2\lambda_p+1)!(2\lambda_t+1)!}{2(2\lambda_p+2\lambda_t-1)!}} \left(\dfrac{(\lambda_p+\lambda_t-1)!}{\lambda_p!\lambda_t!} \right)^2 & \text{(otherwise)} . \end{cases} \qquad (2.78)$$

For the case of one multipolarity being zero, the equation

$$\tfrac{1}{2}\lambda \, \chi^{E\lambda}_{mn} = \eta \, \delta_{mn} \qquad (\lambda = 0) \qquad (2.79)$$

is adopted [A175, p.117] as this then causes eq. 2.77 to reduce to eq. 2.25. Consideration of eq. 2.22 shows that eq. 2.79 is reasonable.

The application of perturbation theory to eq. 2.77 gives the following first and second order expressions for the excitation probability of the state f_p of the projectile accompanied by excitation of state f_t of the target:

$$P^{(1,1)}_{f_p f_t} = \frac{1}{4\eta^2} \sum_{\lambda_p \lambda_t} \left(\lambda_p \lambda_t d_{\lambda_p \lambda_t} \chi^{E\lambda_p}_{o_p f_p} \chi^{E\lambda_t}_{o_t f_t} \right)^2 R^2_{E\lambda_p + \lambda_t}(\theta, \xi_{o_p f_p} + \xi_{o_t f_t}) \tag{2.80}$$

and

$$\begin{aligned} P^{(1,2)}_{f_p f_t} = \frac{1}{8\eta^2} \sum_{\substack{z_p \lambda_p \lambda'_p \lambda''_p \\ z_t \lambda_t \lambda'_t \lambda''_t}} (-)^{\lambda_p + \lambda'_p + \lambda''_p} \lambda_p \lambda'_p \lambda''_p \lambda_t \lambda'_t \lambda''_t d_{\lambda_p \lambda_t} d_{\lambda'_p \lambda'_t} d_{\lambda''_p \lambda''_t} \\ \times \chi^{E\lambda_p}_{o_p z_p} \chi^{E\lambda'_p}_{z_p f_p} \chi^{E\lambda''_p}_{o_p f_p} \chi^{E\lambda_t}_{o_t z_t} \chi^{E\lambda'_t}_{z_t f_t} \chi^{E\lambda''_t}_{o_t f_t} \sqrt{(2J_{z_p}+1)(2J_{z_t}+1)(2\lambda_p+1)} \\ \times \sqrt{(2\lambda'_p+1)(2\lambda''_p+1)(2\lambda_t+1)(2\lambda'_t+1)(2\lambda''_t+1)(2\lambda_p+2\lambda_t+1)(2\lambda'_p+2\lambda'_t+1)} \\ \times X(\lambda_p \lambda_t \lambda_p + \lambda_t; \lambda'_p \lambda'_t \lambda'_p + \lambda'_t; \lambda''_p \lambda''_t \lambda''_p + \lambda''_t) W(J_{o_p} \lambda_p J_{f_p} \lambda'_p; J_{z_p} \lambda''_p) \\ \times W(J_{o_t} \lambda_t J_{f_t} \lambda'_t; J_{z_t} \lambda''_t) \sum_{\mu} R_{E\lambda''_p + \lambda''_t \mu}(\theta, \xi_{o_p f_p} + \xi_{o_t f_t}) \\ \times G_{(E\lambda_p + \lambda_t E\lambda'_p + \lambda'_t)\lambda''_p + \lambda''_t \mu}(\theta, \xi_{o_p z_p} + \xi_{o_t z_t}, \xi_{z_p f_p} + \xi_{z_t f_t}) , \end{aligned} \tag{2.81}$$

where X(abc;def;ghi) is a Fano (or X) coefficient [Ro57]. Some of the terms of eqs. 2.80 and 2.81 are shown diagrammatically in fig. 2.15. The general first order term is fig. 2.15c and the general second order term is fig. 2.15j. The other terms were obtained (except for fig. 2.15b) by setting some of the multipolarities to zero. There are some restrictions on which λ's can be set to zero without causing the resulting term to itself be zero. In the first order case, the coefficient $d_{\lambda_p \lambda_t}$ permits only one of the pair (λ_p, λ_t) to be zero. In the second order case, one is similarly limited to not more than one of each of the pairs (λ_p, λ_t), (λ'_p, λ'_t) and $(\lambda''_p, \lambda''_t)$ being zero. In addition, the Racah coefficients forbid that two of either of the triads $(\lambda_p, \lambda'_p, \lambda''_p)$ and $(\lambda_t, \lambda'_t, \lambda''_t)$ be zero; it must be none, one or all three. All of the diagrams in fig. 2.15 obey these rules and comparison with the monopole-multipole diagrams of fig. 2.5 highlight some interesting differences, viz.:—

(a) Each order (in the perturbation theory sense) contains terms

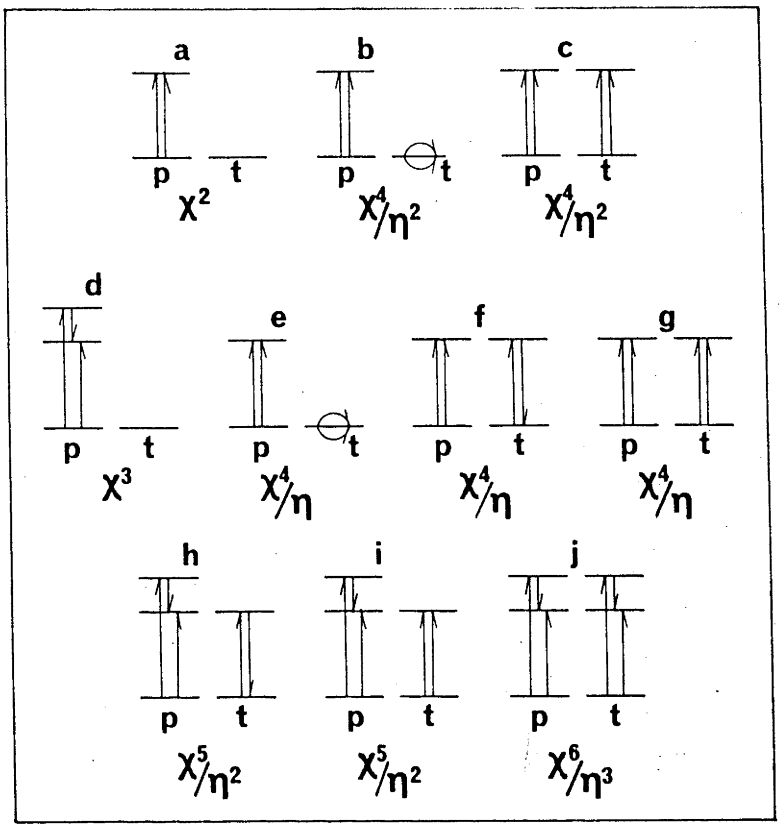

Fig. 2.15: Some first (a-c) and second (d-j) order excitation mechanisms for multipole-multipole excitation. The letters "p" and "t" stand for "projectile" and "target". The approximate magnitude of each term is indicated below each diagram. Terms a and d are the general first and second order monopole-multipole projectile excitation terms and terms c and j are the general first and second order multipole-multipole excitation terms.

whose magnitudes are very different. For example, of the three first order terms shown in fig. 2.15, term a is of order χ^2 while terms b and c are of order χ^4/η^2. The approximate magnitudes implied can be gauged by recalling that $\eta \sim 50$ for heavy ion scattering and that $\chi \ll 1$ is a condition for the validity of perturbation theory. In the experimental situations below, $\chi \sim 0.1$. Similarly, the second order terms range in magnitude from χ^3 to χ^6/η^3.

(b) Certain excitation mechanisms occur more than once in the perturbation expansion, which does not happen in the monopole-multipole case. For example, figs. 2.15b and 2.15e

refer to the same process. Further, the magnitude of the second order term is η times larger than the magnitude of the first order term! It is clear however that a given process cannot recur indefinitely as higher and higher orders of perturbation theory are considered. For example, the process of figs. 2.15b,e cannot occur in a fourth order term since fourth order diagrams must contain between five and ten half-arrows. It may, however, occur in a third order term which will be a further η times larger than the second order term.

It follows from point (b) above that one cannot estimate multipole-multipole effects from first, or even second order perturbation theory alone. Since the development of the third order theory is algebraically daunting and third order orbit integrals are not readily available, the approach of numerically integrating eq. 2.77 was adopted. This produces a large number of functions which might be discussed, but I shall concentrate on those which are important for the analysis of the current experiment. Referring to fig. 2.15 again, it is seem that figs. 2.15c,g,i and j all leave both nuclei excited and will thus be distinguished from the other processes by the energy of the scattered projectile. Also, since all nuclei considered have $J = 0$ ground states, figs. 2.15b and e are zero. Of the remaining terms, fig. 2.15f is the most interesting. The magnitude of this process can be determined by writing, analogously with eq. 2.44,

$$P_{f_2} = \left|\chi^{E\lambda_2}_{o_2 f_2}\right|^2 R^2_{E\lambda_2}(\theta,\xi_{o_2 f_2}) \left(1 + \left|\chi^{E\lambda_1}_{o_1 f_1}\right|^2 \Xi^{E\lambda_1}_{E\lambda_2}(\theta,\xi_{o_1 f_1},\xi_{o_2 f_2},\eta)\right), \tag{2.82}$$

where the subscript 2 refers, as in subsection 2.1.1, to the excited nucleus and subscript 1 to the exciting nucleus, which is no longer structureless, but suffers a virtual excitation or polarization. Graphs of $\Xi^{E2}_{E2}(180°,\xi_1,\xi_2,50)$, $\Xi^{E3}_{E2}(180°,\xi_1,\xi_2,50)$ and $\Xi^{E3}_{E2}(\theta,\xi_1,0.8,50)$ are shown in figs. 2.16 - 2.18.

Of the experiments described below, the ones most likely to be affected by the polarization of the exciting nucleus are the

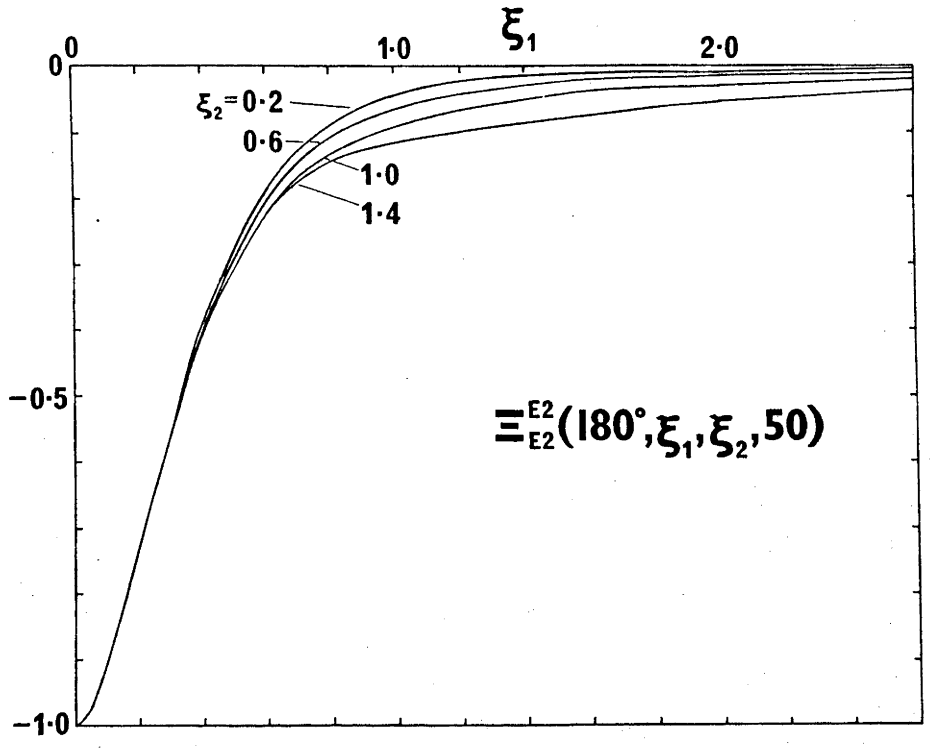

Fig. 2.16: The variation of the function $\Xi^{E2}_{E2}(\Theta,\xi_1,\xi_2,\eta)$ (eq. 2.82) with the adiabaticity ξ_1 of the polarized nucleus and the adiabaticity ξ_2 of the excited nucleus for $\Theta = 180°$ and $\eta = 50$.

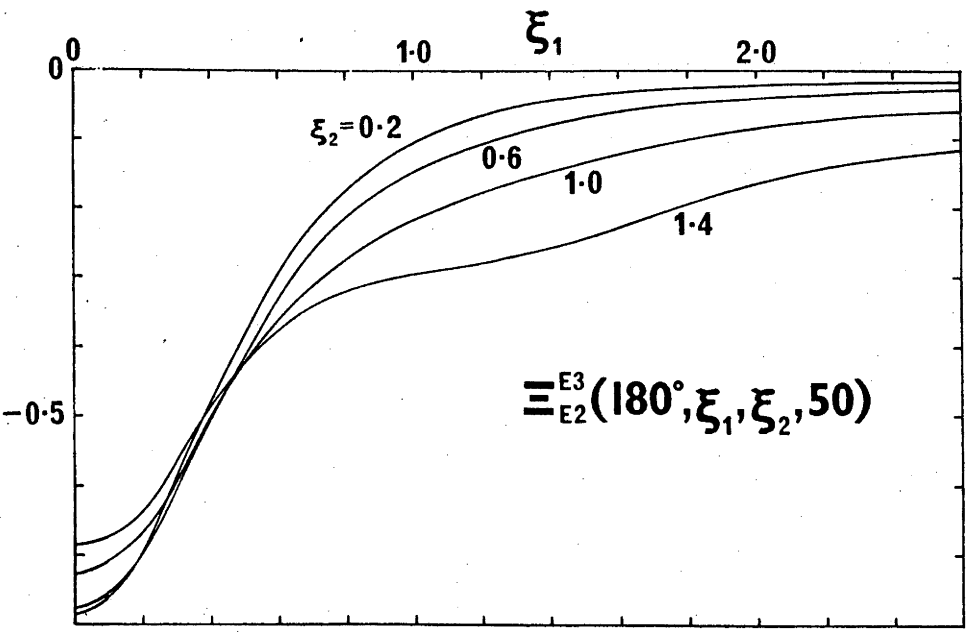

Fig. 2.17: The variation of the function $\Xi^{E3}_{E2}(\Theta,\xi_1,\xi_1,\eta)$ (eq. 2.82) with the adiabaticity ξ_1 of the polarized nucleus and the adiabaticity ξ_2 of the excited nucleus for $\Theta = 180°$ and $\eta = 50$.

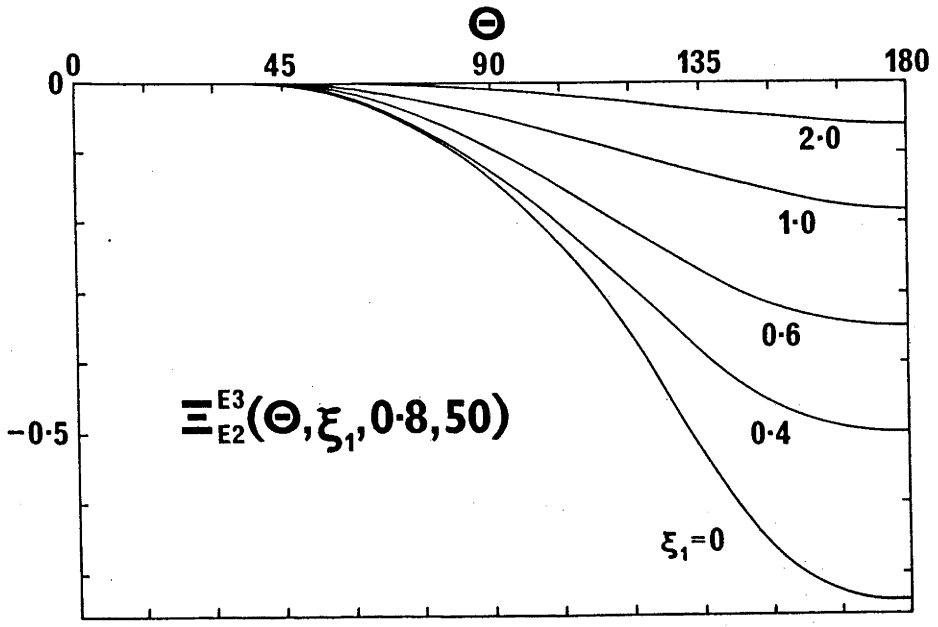

Fig. 2.18: The variation of the function $\Xi^{E3}_{E2}(\Theta,\xi_1,\xi_2,\eta)$ (eq. 2.82) with scattering angle Θ and the adiabaticity ξ_1 of the polarized nucleus for $\xi_2 = 0.8$ and $\eta = 50$.

excitation of ^{198}Hg by ^{12}C and the excitation of ^{18}O and ^{24}Mg by ^{208}Pb. For the bombarding energies used, the $J^\pi = 2^+$ first excited state of ^{12}C has $\xi_1 = 2.3$ and $\chi^{E2}_{of} = 0.25$ rendering the change in excitation probability of the first excited state of ^{198}Hg ($\xi_2 = 0.2$) negligible compared with the 5% reorientation effect. For the case of excitation of projectiles by ^{208}Pb, $\xi_1 = 1.3$ and $\chi^{E3}_{of} = 0.12$. The effect on the projectile's excitation probability is small compared with the reorientation effect of ~ 30%, but is taken into account in the analysis of these data.

2.3 CORRECTIONS FOR THE SEMICLASSICAL APPROXIMATION

A considerable amount of work has been carried out on the fully quantum mechanical theory of electromagnetic excitation [see Al56, Br59, Sm68, Al69, Al72, Al75, Ro77, Al77]. A computer program based on this theory is also available [Ro74]. It might therefore be wondered why the semiclassical theory was chosen for our analysis.

The answer is that the more localized the projectile, that is, the larger the value of the Sommerfeld parameter η (eq. 2.2), the more partial waves are needed in the quantum mechanical calculation. This places an upper limit of ~ 30 on the values of η which can be handled by the computer program [Ro74]. Thus most cases involving the scattering of heavy ions must be analysed using the semiclassical theory, which corresponds to infinite η, with subsequent corrections for the finiteness of the Sommerfeld parameter. This section presents the methods by which such corrections are made.

2.3.1 Symmetrization

The principle of detailed balance requires the cross section for an inelastic scattering process to have the form [Wi65]

$$\frac{d\sigma}{d\Omega} = \frac{v_f}{v_i} f(v_i,v_f) , \tag{2.83}$$

where v_i and v_f are the initial and final projectile velocities and $f(v_i,v_f)$ is a function which is unchanged by the interchange of v_i and v_f. A WKB treatment of the quantal theory [Al69, Al75] suggests that a reasonable way to "symmetrize" the expressions of subsections 2.1.2 and 2.1.3 is to replace eqs. 2.19, 2.22 - 2.24 and 2.27 with

$$\tilde{a}_{mn} := \frac{Z_p Z_t e^2}{4\pi\varepsilon_0 m_0 v_m v_n} \tag{2.84}$$

$$\tilde{\chi}^{\sigma\lambda}_{mn} = \frac{Z_1 e}{\sqrt{\pi}\hbar} \frac{(\lambda-1)!}{(2\lambda+1)!!} \frac{\langle n\|M(\sigma\lambda)\|m\rangle}{\tilde{a}^{\lambda}_{mn}\sqrt{2J_m+1}} \begin{cases} \varepsilon_0^{-1}(v_m v_n)^{-\frac{1}{2}} & (\sigma = E) \\ \mu_0 & (\sigma = M) \end{cases} \tag{2.85}$$

$$\tilde{\xi}_{mn} = \frac{Z_p Z_t e^2}{4\pi\varepsilon_0\hbar}\left(\frac{1}{v_m} - \frac{1}{v_n}\right) \tag{2.86}$$

and

$$d\sigma_f = \frac{1}{4}\frac{v_f}{u} P_f \tilde{a}^2_{of} \operatorname{cosec}^4(\Theta_f/2) \tag{2.87}$$

respectively and to use the appropriate symmetrized quantities in eq.

2.25. In eqs. 2.83 - 2.87, v_n is given by

$$v_n = \sqrt{2[E - (1 + A_p/A_t)E_n]/A_p} \tag{2.88}$$

and Θ_f is the centre of mass scattering angle corresponding to inelastic scattering to the state f. A problem arises in the choice of Θ_f. If a different value of Θ is used for each level, as is suggested by eq. 2.87, then one is integrating eq. 2.25 along different paths for each state with the result that $\sum_f P_f$ is no longer unity [Wi65]. In order to preserve unitarity, a particular state f is nominated as the state of interest, and eq. 2.25, properly symmetrized, is integrated to obtain $d\sigma_f$. Thus the integration must be done separately for each state of interest.

The multipole-multipole calculation (subsection 2.2.4) must also be symmetrized. This is done by using

$$v_{n_p n_t} = \sqrt{2[E - (1 + A_p/A_t)(E_{n_p} + E_{n_t})}} \tag{2.89}$$

$$\tilde{a}_{m_p m_t n_p n_t} = a v_{oo}^2 / v_{n_p n_t} v_{m_p m_t} \tag{2.90}$$

$$\tilde{\chi}^{E\lambda_p E\lambda_t}_{m_p m_t n_p n_t} = (v_{m_p m_t} v_{n_p n_t} / v_{oo}^2)^{\lambda_p + \lambda_t - 1} \chi^{E\lambda_p}_{m_p n_p} \chi^{E\lambda_t}_{m_t n_t} \tag{2.91}$$

and

$$\tilde{\xi}_{m_p m_t n_p n_t} = \frac{Z_p Z_t e^2}{4\pi\epsilon_0 \hbar} \left(\frac{1}{v_{n_p n_t}} - \frac{1}{v_{m_p m_t}} \right) . \tag{2.92}$$

2.3.2 Residual Corrections

The symmetrization procedure of the previous subsection does not completely correct for the finiteness of the Sommerfeld parameter. The residual corrections, commonly known as quantal corrections, are considered in refs. Sm68 and Al72 where it is shown that corrections to the functions F and ρ (eq. 2.50) are of the order η^{-2} and η^{-1} respectively. Alder *et al.* [Al72] give tables of these functions

(among others) for various values of Θ, ξ and ζ and for $\eta = 4,8,\infty$. The results of the integration of the symmetrized semiclassical equations are corrected by interpolation in these tables. For heavy ion scattering, $\eta \sim 50$ giving a correction to F of less than 0.02% and to ρ of $\sim$ 7%. For ^{4}He scattering, $\eta \sim 10$ which gives a correction to F of $\sim$ 0.2% and to ρ of $\sim$ 25%.

2.4 LONG RANGE DEVIATIONS FROM THE COULOMB POTENTIAL

For various reasons the potential energy between the two colliding nuclei is not given strictly by eq. 2.5. In this section other sources of potential energy are considered, but the nuclear force is specifically ignored — it is considered separately in the following section.

2.4.1 Method of Treatment

Following the philosophy of the semiclassical theory, one can identify two ways in which additional potentials will affect the excitation probability. They will cause the orbit to be different from that given by eq. 2.18, thus altering the values of the orbit integrals, and they may have non-zero matrix elements between nuclear states, thus modifying the strength functions $\chi^{\sigma\lambda}$ (eqs. 2.22 and 2.23). It is conventional to ignore this second effect, the justification being that the additional potential energies are very small compared with the Coulomb energy, even at closest approach in backscattering. In addition, the modifications to the orbit are treated approximately with the same justification.

The correction consists of determining the value of the additional potential energy at closest approach and subtracting that value from the beam energy [Al75, p.292]. This retains the hyperbolic shape of the orbit, but gives the correct distance of closest approach which is where the Coulomb interaction is the strongest. Thus the bombarding energy E is replaced in all of the above equations by an effective bombarding energy $\breve{E}$ given by [Al75, p.293]

$$\check{E} = E - \tfrac{1}{2}(1 + A_p/A_t)(1 + \sin\,\theta/2)\;\Delta V(d)\;, \qquad (2.93)$$

where $\Delta V(d)$ is the increase in the potential energy over the Coulomb value at the distance of closest approach d, which is given by

$$d = a(1 + \mathrm{cosec}\;\theta/2)\;. \qquad (2.94)$$

2.4.2 Electron Screening

From a consideration of the Hartree model of the atom and experimental atomic binding energies, Foldy [Fo51] concluded that the electrostatic potential at the nucleus due to the orbital electrons is given to a good approximation by

$$\varphi_{[e^{-1}\ eV]} = -32.65\ Z_t^{7/5}\;. \qquad (2.95)$$

If the collision occurs so rapidly that the electrons of the target nucleus have no time to adjust to the presence of the highly stripped projectile, then eq. 2.95 multiplied by Z_p gives the required electron screening potential. If, on the other hand, the collision is so slow that the electrons are able to adjust to the presence of the projectile, then some of the projectile's energy goes into tighter binding of the orbital electrons. It has been estimated that the energy so lost, the "adiabatic correction", is equal to $22.85\ Z_p^2 Z_t^{2/5}$ eV [Se52]. For ^{24}Mg on ^{208}Pb this is $\sim$ 20 keV. Thomas [Th54] has suggested a procedure for deciding what fraction of the adiabatic correction should be applied in the case of alpha decay. A suitable adaptation of his approach for heavy ion scattering might be to include a fraction f of the adiabatic correction which is equal to the fraction of orbital electrons having velocities higher than the projectile's asymptotic velocity. The idea is that those electrons which are moving faster than the projectile are able to adjust to its presence. It is reasonable to use the projectile's asymptotic velocity since the radius of maximum charge density of the 1s electrons in Pb is $\sim$ 1 pm and the potential energy of an O and a Pb nucleus separated by this distance is $\sim$ 1 MeV or $\sim$ 2% of the bombarding energy. As mentioned in subsection 2.1.1, we have

projectile speeds ~ 0.1 c. The speed of orbital electrons is often taken to be [Th54]

$$v_{e[c]} = \alpha_F \frac{Z - s}{n^*}$$

$$= 0.00730 \frac{Z - s}{n^*}, \qquad (2.96)$$

where n^* is the effective principal quantum number, s the shielding constant [Sl30] and α_F the fine structure constant. A calculation of s and n^* shows that all those electrons in Pb outside of the 4p shell have velocities less than 0.1 c, that is, f = 0.44. Similarly, f = 0.45 for Hg.

From the above discussion, the additional potential due to electronic screening is taken to be[†]

$$\Delta V_{es} = -32.65\, Z_p Z_t^{7/5} + 22.85\, f Z_p^2 Z_t^{2/5}. \qquad (2.97)$$

For ^{24}Mg on ^{208}Pb, ΔV_{es} = -180 keV or ~ 0.2% of the bombarding energy.

Several authors [e.g. Ra72, Ra76, Mu76] have noted the existence of a "molecular potential" due to the nonlinearity of the binding energy of the orbital electrons as a function of the nuclear charge. This potential energy is defined as the total electron binding energy when the target and projectile are in close proximity minus the total binding energies of the target and projectile atoms when separated. It has been graphed for the system Br + Br and U + U as a function of the internuclear separation by Müller and Greiner [Mu76]. The U + U molecular potential energy is 6 MeV or ~ 0.8% of the Coulomb energy when the surfaces of the two nuclei are touching. An extrapolation from the graphs of ref. Mu76 suggests that the corresponding figures

---

[†] It may be noted that eq. 2.97 differs slightly from the generally adopted expression [Sa69]

$$\Delta V_{es} = -32.65\, Z_p Z_t^{7/5} + 40\, Z_p Z_t^{2/5}. \qquad (2.98)$$

It is not clear to me how eq. 2.98 was obtained, but I suspect that it was from an incorrect generalization of a formula correctly quoted by Perlman and Rasmussen [Pe57] in the context of alpha decay.

for Br + Br are ~ 300 keV and ~ 0.2%. These calculations assume that the collision is adiabatic and that both the colliding atoms have their full complement of electrons [Ra72]. In addition, the mutual shielding of the electrons is neglected [Mu76, Ra76].

In the analysis below, molecular potentials are ignored. The reasons for this are:

(a) the ratio of the molecular to Coulomb potentials at closest approach is less for Br + Br than for U + U. Although none of the references above give the dependence of the molecular potential on the two atomic numbers involved, they leave the impression that the molecular potential is negligible for collisions involving light ions.

(b) each of the three approximations mentioned above contributes to an overestimation of the molecular potential present in the collision of a fast, highly stripped ion such as O^{6+} or Mg^{7+} with an atom. Thus, even if there were potentials available for e.g. O + Pb, they may not be useful in our experimental situation.

In support of this neglect of the molecular potential, it may be noted that Rafelski [Ra76], in his calculation of the effect of various small potentials on elastic scattering cross sections, ignores the molecular potential when considering the $^{16}O + ^{208}Pb$ system.

2.4.3 Vacuum Polarization

It is well known that the Coulomb potential is only an approximate description of the potential betwen two charges. For distances of separation less than the reduced Compton wavelength $\lambda\!\!\!^{-}_e$ of the electron ($\lambda\!\!\!^{-}_e = 386$ fm), the correction to the Coulomb potential is approximated by [Li74, p.427][†]

[†] Eq. 2.99 is different from that given by Alder and Winther [Al75] whose source is unclear. It differs also from that given by Blomqvist [Bl72], but is the same as is quoted by Huang [Hu76]. Eq. 2.99 is adopted since it is explicitly derived by Lifshitz and Pitaevskiĭ [Li74] and Huang [Hu76].

$$\Delta V_{vp}(r) = \frac{Z_p Z_t e^2}{4\pi\varepsilon_0 r} \frac{2\alpha_F}{3\pi} \left(ln \frac{\lambda\!\!\!^{-}_e}{r} - \gamma_E - \frac{5}{6} \right) , \qquad (2.99)$$

where α_F is the fine structure constant and γ_E is Euler's constant. Inserting the constants, one obtains

$$\Delta V_{vp}(r)_{[keV]} = 2.33 \frac{Z_p Z_t}{r_{[fm]}} \left(ln \frac{386}{r_{[fm]}} - 1.411 \right) . \qquad (2.100)$$

For the backscattering of 100 MeV ^{24}Mg from ^{208}Pb, $\Delta V_{vp} = 250$ keV at closest approach.

There are many approximations in the derivation of eq. 2.99. Firstly, the terms in square brackets are only the first in a series expansion. The next largest term is $3\pi r/4\lambda\!\!\!^{-}_e$ [Bl72, Hu76] which, for the experimental conditions given above, contributes ~ 13 keV and so is negligible. The derivation of eq. 2.99 also ignored the finite size of the nucleus and vacuum polarization terms of order higher than the first. The magnitude of all the errors so introduced is less than the 13 keV neglected above [Bl72]. Finally, eq. 2.99 considers the effect of virtual electron-positron pairs only. All other elementary particles could also produced a similar effect. The particle with the next largest reduced Compton wavelength is the muon, for which $\lambda\!\!\!^{-}_\mu = 1.87$ fm. This is smaller than typical distances of closest approach (~ 15 fm), so eq. 2.99 cannot be applied by simply replacing $\lambda\!\!\!^{-}_\mu$ for $\lambda\!\!\!^{-}_e$. The large-distance approximation to the vacuum polarization potential is [Li74, p.427, Hu76]

$$\Delta V_{vp}(r) = \frac{Z_p Z_t e^2}{4\pi\varepsilon_0 r} \frac{\alpha_F}{4\sqrt{\pi}} \left(\frac{\lambda\!\!\!^{-}}{r} \right)^{3/2} \exp\left(- \frac{2r}{\lambda\!\!\!^{-}} \right) . \qquad (2.101)$$

For the above experimental conditions, the contribution due to virtual muon-antimuon pairs is therefore 2.7 meV, that is, utterly negligible. Effects from other elementary particles, which have even smaller values of $\lambda\!\!\!^{-}$, will be still less. Thus eq. 2.99 is taken as the vacuum polarization potential.

2.4.4 Nuclear Polarization

The effect considered here is not a new potential, but the polarization of the two nuclei due to each other's Coulomb potential. This effect can be thought of as arising from the processes shown in fig. 2.19. It is clear that the non-diagonal matrix elements of these polarization potentials have been considered in the discussion in sections 2.1 and 2.2 (see figs. 2.5 and 2.15). The diagonal matrix elements represent an attractive correction to the Coulomb potential which varies as $r^{-2(\lambda_p+\lambda_t+1)}$ [Be71] where λ_p and λ_t are the multipolarities shown in fig. 2.19. The largest term might be expected to come from the first two diagrams of fig. 2.19 with $\lambda_p = 1$ and $\lambda_t = 1$, that is, from the separate dipole polarization of the two nuclei. This potential is given by [Be71, Ba77]

$$\Delta V_{np}^{(1)}(r) = -\frac{e^2}{32\pi^2\varepsilon_0^2 r^4}\left(\alpha_p Z_t^2 + \alpha_t Z_p^2\right), \qquad (2.102)$$

where α_p and α_t are respectively the projectile and target polarizabilities. If one uses the estimate of eq. 2.73 with $k = 1$ and eq. 2.72, then

$$\Delta V_{np}^{(1)}(r)_{[keV]} = -\frac{2.52}{r^4_{[fm]}}\left(A_p^{5/3} Z_t^2 + A_t^{5/3} Z_p^2\right) \qquad (2.103)$$

which equals -97 keV at closest approach in the backscattering of 100 MeV ^{24}Mg from ^{208}Pb.

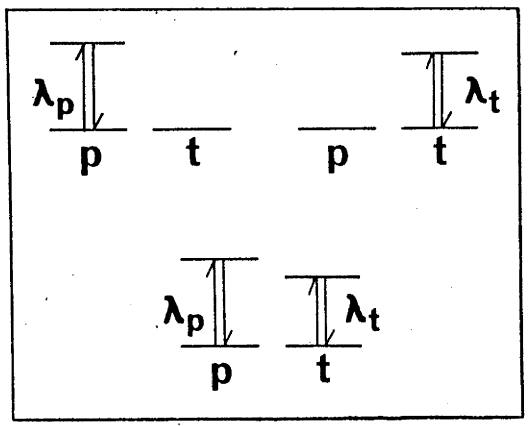

Fig. 2.19: Three processes which modify the orbit of the projectile but which do not cause excitation. The upper part shows the virtual excitation of a level of either the projectile (p) or the target (t) and the lower part shows the mutual virtual excitation of both nuclei.

Terms proportional to r^{-6} arise if both gdr's are simultaneously involved or if one nucleus suffers a quadrupole polarization. These terms have been considered by Beck and Kleber [Be71] who show that they are given by

$$\Delta V_{np}^{(2)} = -\frac{3\alpha_p\alpha_t}{32\pi^2\varepsilon_0^2 r^6}\left(\frac{1}{E_{Dp}}+\frac{1}{E_{Dt}}\right)^{-1} - \frac{e^2}{32\pi^2\varepsilon_0^2 r^6}\left(\alpha_p^{(2)} Z_t^2 + \alpha_t^{(2)} Z_p^2\right), \quad (2.104)$$

where the first term is due to dipole-dipole polarization and the second to the separate quadrupole polarizations of the projectile and the target. The symbols E_{Dp} and E_{Dt} stand for the peak energies of the projectile's and target's gdr's respectively and $\alpha^{(2)}$ is the quadrupole polarizability which is defined by

$$\alpha^{(2)} := \frac{8\pi}{5}\sum_z \frac{|\langle z|M(E2,0)|o\rangle|^2}{E_z}. \quad (2.105)$$

To estimate this quantity, Beck and Kleber treat the first excited 2^+ state separately and estimate the remaining E2 strength using the energy-weighted and non-energy-weighted sum rules which are given by

$$\begin{aligned} S_{EW}(\lambda) &= \frac{3Ze^2\hbar^2}{8\pi m_n}\lambda R^{2\lambda-2} \\ S_{NEW}(\lambda) &= \frac{3Ze^2}{4\pi}\frac{R^{2\lambda}}{(2\lambda+3)}. \end{aligned} \quad (2.106)$$

In eq. 2.106, R is the nuclear radius, which is taken to be

$$R_{[fm]} = 1.25\ \sqrt[3]{A}, \quad (2.107)$$

and m_n is the mass of the nucleon. The quadrupole polarizability is estimated by

$$\alpha^{(2)} = \frac{8\pi}{5}\left(\frac{B(E2;2^+\to 0^+)}{E_{2^+}} + \frac{\{S_{NEW} - B(E2;2^+\to 0^+)\}^2}{S_{EW} - E_{2^+}\,B(E2;2^+\to 0^+)}\right) \quad (2.108)$$

except that the second term is dropped if the first 2^+ state exhausts the non-energy-weighted sum rule. Using eqs. 2.104, 2.106 - 2.108 and the empirical result [Be75]

$$E_D = 47.9\ A^{-0.234} \tag{2.109}$$

one obtains

$$\Delta V_{np}^{(2)}(r)_{[keV]} = -\frac{1}{r^6}\left(\frac{0.880(A_pA_t)^{5/3}}{\left(A_p^{0.234}+A_t^{0.234}\right)} + 1037\left(Z_t^2\alpha_{p[e^2\ fm^4\ MeV^{-1}]}^{(2)} + Z_p^2\alpha_{t[e^2\ fm^4\ MeV^{-1}]}^{(2)}\right)\right) \tag{2.110}$$

with

$$\alpha_{[e^2\ fm^4\ MeV^{-1}]}^{(2)} = 5.027\left(\frac{B(E2;2^+\rightarrow 0^+)_{[e^2\ fm^4]}}{E_{2^+[MeV]}} + \frac{\left\{0.0833\,Z\,A^{4/3} - B(E2;2^+\rightarrow 0^+)_{[e^2\ fm^4]}\right\}^2}{15.5\,Z\,A^{2/3} - E_{2^+[MeV]}\ B(E2;2^+\rightarrow 0^+)_{[e^2\ fm^4]}}\right). \tag{2.111}$$

At closest approach in the backscattering of 100 MeV ^{24}Mg from ^{208}Pb, $\Delta V_{np}^{(1)} + \Delta V_{np}^{(2)}$ equals -240 keV.

2.5 THE NUCLEAR FORCE

2.5.1 Inelastic Scattering

Since the strong interaction is much stronger than the electromagnetic interaction, it might be wondered if it is possible to do Coulomb excitation at all. The answer, as is well known, lies in the short range of the nuclear force. If the colliding nuclei are kept well apart, then the influence of the nuclear force is undetectable. The minimum tolerable separation can be experimentally determined for any pair of nuclei by observing the oft-described phenomenon of Coulomb-nuclear interference, which arises as follows. The first-order-perturbation-theory excitation amplitude is imaginary for a real potential and vice-versa. If the nuclear potential is considered to have a real and imaginary part, then the excitation amplitude from the real part will be opposite in sign to the Coulomb excitation amplitude because the nuclear force is attractive while the Coulomb force is repulsive. Due to the short range of the nuclear force, the

excitation probability, which is the square of the modulus of the amplitude, is dominated by the Coulomb amplitude at low bombarding energies. As the bombarding energy is raised and the nuclei are forced closer together, the contribution of the nuclear amplitude increases. This causes the excitation probability to fall below the purely Coulomb value because of the phase difference mentioned above. If the nuclear potential were purely real then one might expect that the excitation probability would fall to zero at that value of the bombarding energy for which the Coulomb and nuclear amplitudes have equal magnitude. The excitation probability never, in fact, becomes zero because

(a) the nuclear potential has an imaginary part.

(b) the equality of the Coulomb and nuclear amplitudes occurs at slightly different bombarding energies for different projection substates of the excited state.

(c) the above arguments are based on first order perturbation theory. Clearly, if the first order amplitude goes to zero, then the second order amplitude, which has both real and imaginary parts, becomes significant.

At yet higher bombarding energies, the excitation probability rapidly rises above the Coulomb value due to the strength of the nuclear force.

This suggests that there are three regions of bombarding energy in which measurements may be made. The region above the Coulomb nuclear interference region is attractive because of the relatively high excitation probabilities. Of course this is nuclear, not Coulomb, excitation and is the basis of the sorts of measurements mentioned in subsection 1.3.3 (ii). Unfortunately our current lack of knowledge of the strong interaction makes the unambiguous interpretation of these data impossible. The other extreme is to work at energies below the Coulomb-nuclear interference region where, as might be apparent from the previous sections of this chapter, the excitation mechanism is well known. The price which one pays is that the excitation probabilities are much smaller in this region than in the "nuclear" region. This makes the experiments longer and more difficult, but not impossible. It is this second course which is followed in this work.

Some discussion of the third region of bombarding energies is warranted. This region consists of those energies where the excitation is still predominantly Coulomb, but the effect of the nuclear force is significant. A group at the University of Rochester recently claimed to be able to apply empirical corrections to a Coulomb-excitation analysis of data obtained in this region to account for the effect of the nuclear force [Vo77]. They used their method on a measurement of Q_{2^+} in ^{18}O. The main problem is to obtain sufficient data for the empirical corrections to be reliable. In their treatment of the available data, the Rochester group assumed, on the basis of the behaviour of other target-projectile combinations, that the error in the inferred value of Q_{2^+} of ^{18}O due to the effect of the nuclear force depends only on the bombarding energy of the ^{18}O projectile and is, in particular, independent of the target species and of the scattering angle. These assumptions are highly questionable — evidence will be presented in chapter 3 to show that the supposed independence of scattering angle is not even approximately correct.

It seems to me that, considering the currently available knowledge of the nature of the nuclear force, it is unwise to rely on estimates of its effect when its short range compared with the Coulomb force allows one to avoid the problem altogether by choosing bombarding energies where it is negligible. This is provided, of course, that the excitation probability is adequate at these low energies. For example, it is not currently possible to measure the quadrupole moment of the first excited state of ^{12}C by Coulomb excitation.

2.5.2 Nucleon Tunnelling

As well as causing inelastic scattering, the nuclear force may cause the transfer of particles between the target and projectile. There are two ways in which this may affect Coulomb excitation measurements.

Firstly, a reaction product may be mistaken for an inelastically scattered projectile due to a similarity in energy. This clearly can

only happen if the Q value of the reaction is greater than minus the excitation energy of the excited state of interest. We use three lines of argument to suggest that data are unaffected by transfer reactions. The first consists of an examination of the experimental spectra to see if there is any evidence for reaction products of any energy. This argument is based on the unlikelihood of all reaction products having the same energy as the elastically or inelastically scattered projectiles. A second argument consists of examining the intensity of whatever reaction products are observed as a function of bombarding energy. It invariably occurs in the experiments below that reaction products are not observed at the energies below the Coulomb-nuclear interference region. So this argument depends on observing the reactions at higher bombarding energies and extrapolating the energy dependence of the intensity of the reactions down to the energies of interest. The third argument is based on the theoretical work of Buttle and Goldfarb [Bu71]. Their calculations suggest that, for sub-Coulomb transfer, the cross section for neutron transfer is at a maximum for a Q value of zero, that of proton pickup by the projectile for a Q value of E/Z, where E is the bombarding energy and Z is the projectile's atomic number, and that of proton stripping for a Q value of -E/Z.

The second way in which nucleon tunnelling may affect Coulomb excitation measurements is if a sequence of reactions occur whose net result is to leave one of the original nuclei in an excited state. These processes are in effect inelastic scattering but they are certainly not Coulomb in origin. To be more specific, let me adapt fig. 2.5 to this discussion. If the state z is considered to represent the system after a transfer reaction has taken place, then fig. 2.5i may be interpreted as describing a double transfer, the second reaction ($z \rightarrow f$) reconstituting the original nuclei but leaving one of them in an excited state. If such processes occur, then an interference process, represented by fig. 2.5d will also occur. I shall refer to this interference process as "virtual tunnelling" to distinguish it from double tunnelling.

I am not aware of calculations of the magnitude of either double

or virtual tunnelling effects, but it seems reasonable to suppose that the probability of a double tunnelling event is of the order of the square of the probability of a single tunnelling event. Thus if the arguments above have led to the conclusion that the effects of nucleon transfer are negligible, then so will be the effects of double tunnelling. Note however that here all transfer reactions, no matter what their Q values, must be considered.

By examining fig. 2.5d, one might suppose that the probability of a virtual tunnelling event is of the order of the product of the probability of a single tunnelling event and the square root of the first order Coulomb excitation probability. If this were so, then arguments against nucleon transfer would also rule out virtual transfer. However, because the process is virtual, it does not have to conserve energy, momentum, etc., in the intermediate state. This means that the estimate above may only be a lower limit. On the other hand, the Coulomb and tunnelling amplitudes are probably not in phase, so that there may be some interference which would reduce the magnitude of the virtual tunnelling process. It must be admitted that this uncertainty in the magnitude of transfer process is a deficiency in the analysis of Coulomb excitation experiments. From the lack of consideration given to the problem in the literature — few experimental papers even mention virtual transfer (or double transfer for that matter) — there would seem to be little concern about this deficiency. It is certainly easy to imagine that, at the large internuclear separations involved, virtual transfer is negligible. However, the history of reorientation-effect measurements contains many examples of initially neglected processes which were later shown to be important. Nevertheless, I shall take the negligibility of transfer reactions as implying the negligibility of virtual transfer in the analysis below.

2.6 RELATIVISTIC CORRECTIONS

It was mentioned in subsection 2.1.1 that projectiles with velocities ~ 0.1 c were used in the experiments described in Chapter 3. Since excitation probabilities are often measured with uncertainties

as low as 1% and relativistic effects might be expected to be of the order of v^2/c^2, it is not clear that a non-relativistic theory is sufficiently accurate for the analysis of the experimental data. A relativistic semiclassical theory of electromagnetic excitation for the case of a stationary target nucleus and a projectile whose trajectory is a straight line has been described [Wi78]. This theory is useful for ultrarelativistic conditions and for large impact parameters ($\Theta \sim 0$). I am not aware of the existence of a relativistic theory of electromagnetic excitation which is generally applicable, nor do I present one in this section. Rather the difficulties in constructing such a theory are pointed out, and some suggestions for ways of approximating relativistic effects are offered.

2.6.1 The Relativistic Kepler Problem

The first step in the construction of a relativistic semiclassical theory of electromagnetic excitation is the determination of the orbits traced out by the projectile and target. The starting point is the Lagrangian for the motion of two charged particles. Unfortunately, a relativistically correct Lagrangian cannot be constructed without a theory of the field produced by the particles [La75, p.165]. However, it is possible to obtain a Lagrangian which is correct to order v^2/c^2 and this is sufficient for our case. That Lagrangian is [La75, p.168]

$$\mathcal{L} = \tfrac{1}{2}(A_1 v_1^2 + A_2 v_2^2) - \frac{Z_1 Z_2 e^2}{4\pi\varepsilon_0 r_{12}} + \frac{1}{8c^2}(A_1 v_1^4 + A_2 v_2^4) + \frac{Z_1 Z_2 e^2}{8\pi\varepsilon_0 c^2 r_{12}} [\underset{\sim}{v}_1 \cdot \underset{\sim}{v}_2 + (\underset{\sim}{v}_1 \cdot \hat{\underset{\sim}{r}}_{12})(\underset{\sim}{v}_2 \cdot \hat{\underset{\sim}{r}}_{12})] . \qquad (2.112)$$

The next step in the classical calculation of the orbit is to convert to the centre-of-mass frame and to observe that, in this frame of reference, the problem is the same as that of one particle of mass $A_1 A_2/(A_1 + A_2)$ moving in an external fixed Coulomb field [La69, p.29]. In relativistic kinematics, the position of the centre of mass is given by [La75, pp.42,169]

$$\underset{\sim}{r}_r = \left(\left(E_1 + \frac{Z_1 Z_2 e^2}{8\pi\varepsilon_0 r_{12}}\right)\underset{\sim}{r}_1 + \left(E_2 + \frac{Z_1 Z_2 e^2}{8\pi\varepsilon_0 r_{12}}\right)\underset{\sim}{r}_2\right) \Big/ \left(E_1 + E_2 + \frac{Z_1 Z_2 e^2}{4\pi\varepsilon_0 r_{12}}\right) , \tag{2.113}$$

where E_1 and E_2 are the total energies of the two particles. The terms involving the charges of particles arise because of the necessity of including the energy of the field produced by the particles in the expression. Thus the transformation to the centre-of-mass frame is not a simple problem, nor does it result in the reduction of the problem to an equivalent one-body one. This can be seen from the expression for the Hamiltonian in the centre-of-mass frame, which is [La75, p.169]

$$H = \tfrac{1}{2}\left(\frac{1}{A_1} + \frac{1}{A_2}\right)p^2 + \frac{Z_1 Z_2 e^2}{4\pi\varepsilon_0 r} - \frac{1}{8c^2}\left(\frac{1}{A_1^3} + \frac{1}{A_2^3}\right)p^4$$

$$+ \frac{Z_1 Z_2 e^2}{8\pi\varepsilon_0 c^2 A_1 A_2 r}\left[p^2 + (\underset{\sim}{p}\cdot\hat{\underset{\sim}{r}})^2\right] , \tag{2.114}$$

where $\underset{\sim}{r} = \underset{\sim}{r}_2 - \underset{\sim}{r}_1$ and $\underset{\sim}{p} = \underset{\sim}{p}_2 = -\underset{\sim}{p}_1$ is the three-momentum of particle 2. It is clear that no single definition of an effective mass will make eq. 2.114 identical to a Hamiltonian for one particle.

The effort involved in a detailed treatment of eq. 2.114 seems to me to be much larger than is warranted by the expected magnitude of the effects. I therefore propose the following approximate corrections.

2.6.2 Kinematics

There are two aspects of the transformation from the laboratory frame to the centre-of-mass frame which deserve attention. The first is the energy associated with the motion of the centre of mass. For a projectile of mass A_p incident with asymptotic velocity u on an initially stationary target of mass A_t, the classical expression for the energy of the centre of mass is

$$E_c = \tfrac{1}{2} A_p^2 u^2/(A_p + A_t) . \tag{2.115}$$

Relativistically, the velocity of the centre of mass is [La75, pp.42,

168]

$$\underset{\sim}{V}_r = \frac{E_p \underset{\sim}{u} + \int \underset{\sim}{S}\,\underset{\sim}{dr}}{E_p + E_t + \int W\,\underset{\sim}{dr}}, \tag{2.116}$$

where E_p and E_t are the total energies of the projectile and target, and $\underset{\sim}{S}$ is the Poynting vector and W the energy density of the field between the projectile and the target. These are given by the usual expressions [Lo70a, p.464]

$$\underset{\sim}{S} = \underset{\sim}{\mathcal{E}} \times \underset{\sim}{\mathcal{H}} \tag{2.117}$$

and

$$W = \tfrac{1}{2}\varepsilon_0 \mathcal{E}^2 + \tfrac{1}{2}\mu_0 \mathcal{H}^2 . \tag{2.118}$$

The integrals over S and W account for the momentum and energy of the field between the particles. However, since the projectile and target are initially separated, $\int \mathcal{E}^2\,\underset{\sim}{dr}$ is initially zero [La75, p.169] and, since

$$\underset{\sim}{\mathcal{H}} = \varepsilon_0\, \underset{\sim}{v} \times \underset{\sim}{\mathcal{E}} , \tag{2.119}$$

the integrals of S and W are also initially zero. But $\underset{\sim}{V}$ is a constant, and so

$$\underset{\sim}{V}_r = \underset{\sim}{V}_c \left[1 + \tfrac{1}{2}A_t/(A_p + A_t)\, \frac{u^2}{c^2} + O\left(\frac{u^4}{c^4}\right)\right] . \tag{2.120}$$

The kinetic energy of the centre of mass is

$$\begin{aligned} E_r &= (A_p + A_t)\, c^2 [(1 - V_r^2/c^2)^{-\frac{1}{2}} - 1] \\ &= E_c \left[1 + \frac{3A_p^2 + 4A_pA_t + 4A_t^2}{4(A_p + A_t)^2}\, \frac{u^2}{c^2} + O\left(\frac{u^4}{c^4}\right)\right] . \end{aligned} \tag{2.121}$$

Thus there is in fact more energy associated with the motion of the centre of mass than is predicted by the classical theory. This could be corrected for by subtracting the amount

$$\frac{3A_p^2 + 4A_pA_t + 4A_t^2}{2(A_p + A_t)^3}\, \frac{E^2}{c^2} \tag{2.122}$$

from the energy E of the projectile so that, after a classical lab-to-centre-of-mass transformation, the projectile has the correct (to order u^2/c^2) energy. For 100 MeV ^{24}Mg on ^{208}Pb, $u/c = 0.095$ and the change to the bombarding energy is -84 keV.

The second kinematical problem is the centre-of-mass scattering angle. The various Coulomb excitation functions graphed in sections 2.1 and 2.2 are strong functions of angle away from $\Theta = 180°$ so one should investigate by how much the actual centre-of-mass scattering angle differs from the semiclassical prediction. The scattering angle Θ in the centre-of-mass frame can be expressed in terms of the laboratory scattering angle Φ, the asymptotic velocity v of the scattered projectile and the velocity V of the centre of mass. Using the Galilean transformation, one finds

$$\cos \Theta_c = (\cos \Phi - \omega)(1 - 2\omega \cos \Phi + \omega^2)^{-\frac{1}{2}} , \tag{2.123}$$

where

$$\omega := V_c/v_c , \tag{2.124}$$

is the velocity ratio predicted by classical mechanics. Similarly, the Lorentz transformation gives

$$\cos \Theta_r = \left(\cos \Phi - \frac{V_r}{v_r}\right)\left(1 - 2 \cos \Phi \frac{V_r}{v_r} + \frac{V_r^2}{v_r^2} - \sin^2 \Phi \frac{V_r^2}{c^2}\right)^{-\frac{1}{2}} . \tag{2.125}$$

The fact that V_r and v_r differ from V_c and v_c in general has been indicated. The relationship between V_c and V_r is given by eq. 2.120; that between v_r and v_c can be found by some manipulation of the general formula for the energy of the scattered projectile [see e.g. Ma68, p.140]. The result is

$$\cos \Theta_r = \cos \Theta_c + \frac{u^2}{c^2}\left(\frac{A_p}{2(A_p + A_t)} \sin^2 \Phi \cos \Theta_c - \omega K(1-\omega) \cos \Theta_c + \omega K \sqrt{1 - 2\omega \cos \Phi + \omega^2} + O\left(\frac{E_x}{E}\right)\right) \Big/ (1 - 2\omega \cos \Phi + \omega^2) + O\left(\frac{u^4}{c^4}\right) . \tag{2.126}$$

In deriving the correction term, it has been assumed that, if the

collision is inelastic, then the excitation energy E_x is small compared with the projectile's incident energy E. The parameter κ is given by

$$\kappa = \frac{A_p A_t - A_t^2 + 2A_p^2 \sin^2 \Phi}{2(A_p + A_t)^2} + \frac{3A_t^3 + 8A_p A_t^2 + 3A_p^2 A_t + A_p^3 \cos \Phi (1 + \sin^2 \Phi)}{(A_p + A_t)^2 \sqrt{A_t^2 - A_p^2 \sin^2 \Phi}} . \tag{2.127}$$

It will be observed that the correction term is zero if $\Phi = 0$ or $\Phi = 180°$, which agrees with one's expectations. Away from these two angles, the relativistic correction may be thought of as a slight reduction in the centre-of-mass scattering angle, that is

$$\cos \Theta_r = \cos(\Theta_c - \Delta\Theta) . \tag{2.128}$$

For the scattering of 100 MeV ^{24}Mg through 90° by ^{208}Pb, $\Delta\Theta = 0.08°$ which, as will be shown in subsection 3.2.3, is 1/4 of the uncertainty in experimentally determining the scattering angle at 90°. The relativistic correction to the scattering angle was therefore neglected in the analysis presented in chapter 4.

2.6.3 Orbit Dynamics

The considerations of the previous subsection give corrections which allow one to perform a classical laboratory-to-centre-of-mass transformation and retain the right energy and scattering angle. Having done this, one must consider the accuracy of the classical prediction of the orbit of the projectile referred to the centre-of-mass frame. An approach in the spirit of section 2.4 is adopted. That is, the classical trajectory is used but the bombarding energy is adjusted to give the right distance of closest approach.

Classically, the distance of closest approach in the scattering of a particle of mass A_p, charge $Z_p e$ and asymptotic speed u through an angle Θ from an infinitely heavy target of charge $Z_t e$ is given by [La69, p.38]

$$d_c = \frac{Z_p Z_t e^2}{4\pi\varepsilon_0 A_p u^2} [\mathrm{cosec}(\Theta/2) + 1]$$

$$=: a[\mathrm{cosec}(\Theta/2) + 1] , \qquad (2.129)$$

where, in order to obtain this, the relationship

$$L = a u A_p \cot(\Theta/2) \qquad (2.130)$$

between the angular momentum L and the scattering angle was required.

The difficulties with the relativistic Kepler problem were outlined in subsection 2.6.1. If, however, the target is considered to have infinite mass, then the problem is tractable. For $\Theta = 180°$, it is easy to show that the relativistic distance of closest approach is given by

$$d_r = d_c\left(1 - \frac{3}{4}\frac{u^2}{c^2} + O\left(\frac{u^4}{c^4}\right)\right) \qquad (2.131)$$

and, from the equations of motion given by Landau and Lifshitz [La75, p.94], eq. 2.131 is also true at the scattering angle where $L = a A_p u^2/c$. This scattering angle is $\Theta = \pi - 2u/c$ or $\Theta = 168.5°$ for $u/c = 0.1$. The general expression for d_r is very difficult to obtain because the relativistically correct version of eq. 2.130 is, for $L > au^2 A_p/c$, [La75, p.94]

$$\tfrac{1}{2}(\pi-\Theta) = \sqrt{1 - \frac{a^2A_p^2u^4}{L^2c^2}}\ \arccos\left(E_p a A_p \frac{u^2}{c} (L^2E_p^2c^2 - L^2A_p^2c^6 + a^2A_p^4c^2u^4)^{-\frac{1}{2}}\right) \qquad (2.132)$$

which cannot be readily inverted to obtain L in terms of Θ. However, for $\Theta \lesssim 60°$, expansions can be made which show that the correction to d is $\sim -0.89\ u^2/c^2$ for $\Theta = 60°$ and $\sim -0.64\ u^2/c^2$ for $\Theta = 30°$. In view of the difficulty of determining d_r in general, I shall adopt eq. 2.131. It should be noted that

(a) eq. 2.131 is only approximate except at the scattering angles $\Theta = 180°$ and $\Theta = \pi - 2u/c$.

(b) A_t is not infinite and the general expression for r_c contains the reduced mass in place of A_p. This procedure is

adopted in applying eq. 2.131, but this is not relativistically correct. One might suppose, however, that any error introduced would be of order $A_p u^2/A_t c^2$ ($\lesssim 0.1\%$ for all of the experimental situations considered below) and so should not be significant.

Eq. 2.131 requires that the bombarding energy be increased to produce the correct distance of closest approach. This increase is $\sim \frac{1}{2} A_t/A_p$ times the decrease in bombarding energy suggested in subsection 2.6.2. The total correction to the bombarding energy to allow for relativistic effects is therefore

$$\Delta E = \left(\frac{3}{4A_p} - \frac{3A_p^2 + 4A_p A_t + 4A_t^2}{2(A_p + A_t)^3} \right) \frac{E^2}{c^2} \qquad (2.133)$$

whence

$$\Delta E_{[keV]} = 1.07 \left(\frac{3}{4A_p} - \frac{3A_p^2 + 4A_p A_t + 4A_t^2}{2(A_p + A_t)^3} \right) E^2_{[MeV]} . \qquad (2.134)$$

In eq. 2.134 the masses are in unified mass units. For 100 MeV ^{24}Mg on ^{208}Pb, $\Delta E = 250$ keV.

2.6.4 Modifications to the Perturbation Theory

Having obtained relativistic corrections to the orbit of the projectile, the problem of corrections to the perturbation potential (eq. 2.5) should be considered. Inspection of the relativistic Hamiltonian (eq. 2.114) suggests the replacement of the classical perturbation potential $V_c(t)$ by

$$V_r(t) = V_c(t)\,(1 + [p^2 + (\underset{\sim}{p}\cdot\hat{\underset{\sim}{r}})^2]/2A_p A_t c^2) . \qquad (2.135)$$

However, at the point of closest approach $\underset{\sim}{p}\cdot\hat{\underset{\sim}{r}} = 0$ and p has its smallest value; being zero for a head-on collision. As most of the excitation takes place near closest approach, the correction of eq. 2.135 would seem to be negligible. For a similar reason the term involving p^2 would also seem to have a negligible effect on the excitation. Thus no corrections were applied to the classical

perturbation potential.

A correction must, however, be applied to the perturbation formalism to account for retardation. For the restricted dynamical situation considered by them, Winther and Alder [Wi78] have found that, for low velocities, the main effect is a correction to the adiabaticity parameter ξ (eqs. 2.24, 2.86 and 2.92). The relativistically correct adiabaticity parameter ξ_r is given by

$$\xi_r = \xi_c \sqrt{1 - u^2/c^2} , \qquad (2.136)$$

where ξ_c is the classical expression for the adiabaticity. Eq. 2.136 gives a change of -0.5% in ξ for $u/c = 0.1$. For an E2 excitation with $\Theta = 180°$ and $\xi_c = 1$, this change in ξ increases the excitation probability by about 3% (for $\xi_c = 0.4$, the increase is $\sim$ 0.8%). This is by far the largest relativistic effect identified. It can be understood by remembering that the electric field $\underset{\sim}{\mathcal{E}}$ of a charge Ze moving with velocity $\underset{\sim}{u}$ is given by [La75, p.92]

$$\underset{\sim}{\mathcal{E}} = \frac{Ze}{4\pi\varepsilon_0 r^3} \left(1 - \frac{u^2}{c^2}\right)\left(1 - \frac{u^2}{c^2}\sin^2\theta\right)^{-3/2} \underset{\sim}{r} , \qquad (2.137)$$

where $\underset{\sim}{r}$ is the position vector of the field point relative to the charge and θ is the angle between $\underset{\sim}{u}$ and $\underset{\sim}{r}$. Thus, as the velocity of charge increases, the field in the direction perpendicular to $\underset{\sim}{u}$ increases and the field parallel to $\underset{\sim}{u}$ decreases. Now the adiabaticity can be thought of as the product of the collision time ($\sim$ a/u) and the nuclear frequency characteristic for the excitation of state f ($\sim E_f/\hbar$). The effect of the relativistic correction to the electric field of the projectile is to shorten the effective collision time since the electric field at the position of the target nucleus builds up and dies away faster than r^{-2}, where r is the projectile-target separation.

It would therefore seem reasonable that eq. 2.136 should apply in general, and not just for the special case considered in ref. Wi78. It may be noted that eq. 2.136 is not the only relativistic correction derived in ref. Wi78, but the other corrections are probably quite specific to the dynamical situation chosen in that reference. They

also have a much smaller effect at low velocities than that of eq. 2.136. It is clear that there is still considerable doubt as to the exact magnitude of relativistic corrections to the standard theory of Coulomb excitation. For the purpose of data analysis, a conservative course is therefore followed. The corrections suggested in eqs. 2.133 and 2.136 are both applied, but an uncertainty equal to the magnitude of the correction is also adopted. In applying the correction to ξ, the velocity u is interpreted as the asymptotic velocity of the projectile. That is, for a bombarding energy E, eq. 2.136 is

$$\xi_r = \xi_c(1 - 0.002147\ E_{[MeV]}/A_{p[u]}) . \qquad (2.138)$$

Chapter 3

EXPERIMENTAL METHOD AND RESULTS

This chapter contains a description of experiments to measure the excitation probabilities of the first excited states of ^{198}Hg, ^{18}O and ^{24}Mg by the method of resolving elastically and inelastically scattered projectiles with silicon surface-barrier detectors. The experiment on ^{198}Hg consisted of exciting ^{198}Hg targets with various projectiles and the other experiments involved projectile excitation by ^{208}Pb targets.

The account of the experiments is prefaced in the first section of this chapter by some general remarks on this type of experiment. The second section contains those points which are common to all three experiments and the remaining sections treat each experiment in detail and summarize the results.

3.1 INTRODUCTION

3.1.1 The Number and Precision of Measurements

In principle, the measurement of the excitation probability of an excited state of a nucleus under just one set of conditions will suffice to determine the quadrupole moment of the excited state. However, this would depend on knowing, amongst other things, the reduced transition probability of the excited state sufficiently accurately. For example, in the excitation of the first excited state of ^{198}Hg by backscattered ^{16}O projectiles, the effect of the quadrupole moment is to change the excitation probability by $\sim$ 7%. For projectile excitation of ^{18}O and ^{24}Mg by ^{208}Pb, the corresponding figures are $\sim$ 12% and $\sim$ 30%. It is clear from eq. 2.50 that these values are upper limits on the uncertainty which can be tolerated in the value of the reduced transition probability. In general, reduced transition probabilities are not known to sufficient accuracy and one is therefore obliged to measure excitation probabilities under at least two different sets of conditions where the effects of the

quadrupole moment (i.e. the magnitude of the sensitivity ρ in eq. 2.50) are dissimilar. Then both Q_{J^π} and $B(\sigma\lambda)$ can be determined.

The question of the precision to which the excitation probabilities should be determined is a complex one. The magnitude of the reorientation effect in ^{198}Hg suggests that ±1% may be an appropriate level of precision. It is certainly not the case that an arbitrary increase in the precision of measurement will result in a corresponding decrease in the uncertainty of the determination of the quadrupole moment. In the case of ^{198}Hg, one limiting factor is the uncertainty in the matrix elements connecting the ground state and the first excited state with higher excited states. It turns out that, until other experiments are performed to reduce this uncertainty, there is no point in measuring excitation probabilities to much better than ±1% (see section 4.2).

Thus one factor which influences the desired precision is the precision to which other quantities required in the analysis of the data are known. In other cases, for example ^{18}O and ^{208}Pb [Jo77a], the degree of precision which might otherwise be desirable cannot be reached because of experimental limitations. Our technique is such that the ±1% level cannot, except in very favourable circumstances, be reached for excitation probabilities less than about 10^{-3} for heavy ion scattering and about 10^{-4} for ^{4}He scattering.

There is one other quite important consideration involved in deciding the precision to which measurements should be made and this is well illustrated by the case of ^{198}Hg. A result of the current measurements on ^{198}Hg is a value of the reduced transition probability which, neglecting relativistic corrections, has an uncertainty of ±0.6% (section 4.2). When informed of this result, people often exclaim that they do not believe B(E2) measurements to better than a few per cent and proceed to air various examples, the even mass cadmium isotopes being prime ones [Es76a], of wide discrepancies between different B(E2) measurements. In essence then, there is no point in performing high precision measurements if one subsequently obtains quantities with unbelievably small errors. What is believable and what is not often tends to be subjective, with people being unable

to completely justify their prejudices. It seems reasonable that I should state my views on the believability of these measurements and this I do in the following paragraph.

It seems to me, and I believe that the remainder of this chapter demonstrates, that the excitation probabilities of the various nuclei under the conditions stated have been accurately measured and that the uncertainties quoted in subsection 3.6.2 give the ranges of values which have a two-thirds probability of containing the true value. The inference of B(E2) and Q_{2^+} values from these excitation probabilities is another matter, as it depends on accurate calculations of the functions F and ρ of eq. 2.50. It cannot be guaranteed that there are no effects which have been overlooked in chapter 2 and which may significantly affect these calculations. Since some of the small effects considered in chapter 2 affect the excitation probability by $\sim 0.5\%$, I feel that any neglected effects will probably have a comparable or smaller effect.

3.1.2 Experimental Strategy

It was shown in the previous subsection that at least two measurements with different values of the sensitivity parameter ρ (eqs. 2.49 and 2.50) are required, and one would like to choose conditions with as widely differing values of ρ as possible. One may seek to do this by varying the bombarding energy, the scattering angle or the charge and mass of the exciting nucleus.

The sensitivity parameter depends on bombarding energy both directly and through the adiabaticity ξ. Although this dependence is strong, the useful energy range is very limited. As the bombarding energy is reduced, the excitation probability falls rapidly thus imposing a lower limit. At the high end, the onset of Coulomb-nuclear interference (subsection 2.5.1) provides an upper limit. In general, ρ varies by less than 10% between these two limits.

The variation of ρ with scattering angle is the same as that of $\Pi_{E2}^{E2E2}(\Theta,\xi,1)$ (fig. 2.4). The values range from zero at $\Theta = 0$ to a

maximum at $\Theta = 180°$. One could choose two widely spaced scattering angles for the measurements although the rapid decline in excitation probability as $\Theta \to 0$ (fig. 2.1) places a lower limit on the scattering angle. In practice one can use scattering angles where ρ is $\sim$ 25% of its value at $\Theta = 180°$. However, there are four reasons for wishing to use angles near 180° as much as possible. Firstly, excitation probabilities are largest at $\Theta = 180°$; secondly, the variation of the excitation probability with angle is slow near $\Theta = 180°$ so that the effect of uncertainties in the scattering angle is reduced; thirdly, peaks due to inelastic scattering are well away from peaks due to elastic scattering from likely target contaminants (e.g. Fe, Cu) and fourthly, annular detectors may be used thus maximizing the solid angle of the detector for a given range $\Delta\Theta$ of scattering angles. Thus, while the variation of ρ with angle could be used, the third possibility warrants investigation.

The effect of varying the charge and mass of the exciting nucleus can best be gauged from the first line of eq. 2.49. The useful range of bombarding energies for any projectile is such that the parameters u and a are approximately the same for all projectiles, so that ρ depends mainly on the charge Z_1 of the exciting nucleus and the adiabaticity. For these bombarding energies, the adiabaticity varies in the approximate range [Al75, p.280]

$$0.35\ E_{x[\mathrm{MeV}]} \lesssim \xi \lesssim 0.5\ E_{x[\mathrm{MeV}]}\ , \tag{3.1}$$

where E_x is the excitation energy. For a given target, ξ is least for light projectiles, but for a given projectile (with $Z \lesssim 20$), ξ is least for a heavy target. This means that, for a given target, the change in ξ as one increases the projectile charge reinforces the direct dependence of ρ on Z_1. For example, in the case of ^{198}Hg, ρ changes by a factor of four in going from ^{4}He to ^{16}O. (It seems that the increase in ξ is just balancing the slow increase in the parameter a with projectile mass.) For these reasons, the method of a fixed scattering angle of $\sim$ 180° and different projectiles was chosen for the target excitation experiments.

For a given projectile, ξ decreases as the target charge

increases, so that, for the case of ^{24}Mg, changing the target from ^{90}Zr to ^{208}Pb only changes ρ by a factor of 1.4. Also, light targets are disadvantageous because of the relatively broad range of energies of the scattered particles over the finite acceptance angles of the detector. Thus the method of varying the scattering angle was chosen for the projectile excitation experiments.

3.1.3 A Reorienteer's Checklist

Because of the level of precision required in these measurements, there are many effects, subtle and otherwise, which the experimenter must investigate and, if necessary, allow for. These are listed below. Neglect of any of them would cast doubt on the reliability of the inferred value of the quadrupole moment.

(i) The beam energy

From the plots of the various excitation functions in the previous chapter, it can be seen that they are all strong functions of energy through the adiabaticity ξ. In addition, from eq. 2.22

$$\chi^{E\lambda} \propto E^{\lambda-\frac{1}{2}} . \tag{3.2}$$

Thus it is found that for $\xi = 1$, the fractional change with energy of the parameter F, which is defined in eq. 2.50 and is given by

$$F = \left|\chi^{E2}_{of}\right|^2 R^2_{E2}(\Theta,\xi_{of}) \Big/ B(E2;o\rightarrow f) , \tag{3.3}$$

is about five times the fractional change in the energy. In order then to determine the excitation probability to ±1%, the beam energy must be known to better than ±0.2%.

(ii) Scattering angle

For backscattering there is no problem, since, for example, the fractional change with angle of $R^2_{E2}(\Theta,\xi)$, and hence F, is about 0.1%

per degree near $\Theta = 180°$. So an uncertainty of a degree or so in the scattering angle is quite small enough.

However, away from 180°, things are different. For $\Theta = 90°$, the fractional change of F with angle is 2% per degree, requiring the determination of the scattering angle to ~ 0.5%. At smaller scattering angles, the variation with angle increases — it is 5% per degree at $\Theta = 60°$.

It should be noted that Θ is the centre of mass angle. The variation of Θ with the lab angle Φ is given by

$$\frac{d\Theta}{d\Phi} = 1 + \gamma' [1 - \gamma'^2 \sin^2 \Phi]^{-\frac{1}{2}} \cos \Phi , \qquad (3.4)$$

where

$$\gamma' = A_p [1 - (1 + A_p/A_t)\ E_x/E]^{-\frac{1}{2}}/A_t . \qquad (3.5)$$

For the case of largest γ' considered (^{24}Mg on ^{208}Pb), $d\Theta/d\Phi$ differs from unity by 10% at most.

(iii) The extraction of the peak area

In these experiments the peak in the spectrum due to elastically scattered particles may be as much as 1500 times larger than any inelastic peaks. Because of various effects (see section 3.2.5), the elastic peak has a low energy "tail" which extends down into the region of the inelastic peaks of interest. Thus, to determine the ratio of the areas of the elastic and inelastic peaks, the area of the "elastic tail" under the inelastic peak must be determined in a reliable and consistent manner.

A useful guide to the quality of the spectrum is the ratio of the height of the inelastic peak to the height of the valley between the elastic and inelastic peaks. In heavy ion scattering, this ratio is ~ 10, which corresponds to an elastic tail which accounts for 5% - 10% of the area of the inelastic peak. Thus the area of the tail must be determined to ±(10% - 20%) in order to provide sufficient accuracy in the net area of the inelastic peak. This is done by fitting a

functional form to the spectrum, and using it to estimate the magnitude of the elastic tail under the inelastic peak.

To increase one's confidence in the fitted lineshape, an attempt should be made to determine the lineshape experimentally by collecting spectra under conditions where the excitation probability is negligible thus revealing that part of the lineshape of the elastic peak which is underneath the inelastic peak. The ability of the functional form to fit these spectra gives confidence in its appropriateness and the application of such experimental lineshapes to the data will indicate the degree to which the inferred excitation probability depends on the details of the lineshape used.

(iv) The avoidance of nuclear effects

The necessity of taking data under conditions where nuclear effects are negligible has been pointed out in subsection 2.5.1. This will be considered in more detail in subsection 3.6.1, but the general conclusion is that reorientation-effect measurements should include experimental evidence that the data used for the determination of the quadrupole moment are negligibly influenced by the nuclear force.

(v) Absence of contaminant peaks

In addition to the elastic and inelastic peaks, the spectrum may also contain peaks due to elastic and inelastic scattering from target contaminants, nuclear reactions between the projectile and the target or reactions between the scattered particles and the silicon nuclei in the detector. The last case refers to events where part of the energy of the particle incident on the detector is converted by a nuclear interaction to gamma radiation which then escapes from the detector — it is the problem of determining the lineshape of the detector.

Clearly, if any of the above processes should contribute counts to the spectrum in the region of the inelastic peak of interest, then errors will occur. A reorientation experiment should, therefore, contain evidence that

(a) there are negligible levels of target impurities which could produce elastically or inelastically scattered particles of an energy similar to the inelastically scattered particles of interest.

(b) the cross section of any nuclear reaction which may produce products in the energy range of interest is negligibly small.

(c) the lineshape of the detector does not contain any significant peaks which may be hidden under the inelastic peak of interest.

3.2 GENERAL

3.2.1 Beam Handling

Beams of ^{12}C, $^{16,18}O$ and ^{24}Mg were obtained from the ANU 14 UD Pelletron accelerator and beams of ^{4}He from the ANU EN tandem Van der Graaff accelerator. Both accelerators have been described previously [Es76, Op74]. The beams of ^{24}Mg were produced as suggested by Middleton [Mi77]. This method consists of sputtering Mg from a Mg cone with low energy Cs in the presence of NH_3. The ion species $^{24}MgH^-$ and $^{24}MgH_3^-$ are the most abundant negative ions under these conditions.

The beam transport systems of both accelerators include a 90° analysing magnet for determining the beam energy and, downstream of that, a switch magnet to direct the now largely monoenergetic beam into the desired beam line. A circular tantalum aperture was placed at the entrance of the switch-magnet vacuum box on both accelerators to block beam scattered from the walls of the vacuum box of the analysing magnet. The path of the charge state of interest through the analysing magnet was defined by sets of object and image slits. On the EN tandem, these were periodically cleaned to remove the accumulated carbon layer. This was not necessary for the 14 UD because care is taken to exclude hydrocarbons from that machine's beam transport system.

After passing through the scattering chamber, the beam is stopped

by a beam stop which is located some 2.5 m from the chamber. The beam stop is made of material of low atomic weight (carbon in the EN and aluminium in the 14 UD) so that any backscattered particles which may happen to travel up the beam tube and reach the annular detector will be low in energy compared with those scattered from the ^{198}Hg and ^{208}Pb targets.

3.2.2 Accelerator Calibration

The magnet constant, k, of an analysing magnet is given by [Ri69]

$$k = \frac{AE}{q^2 B^2} [1 + E/2Ac^2] , \qquad (3.6)$$

where q and A are the charge and rest mass of the ion of kinetic energy E which is deflected through 90° by the magnetic induction B. The term in square brackets is a consequence of special relativity, and is correct to first order in E/Ac^2. The constant k has been previously determined for both the EN [Es76, Jo77] and the 14 UD [Jo77, Sp77] accelerators. A summary is presented below.

The EN tandem was calibrated by observing the threshold of the reaction $^{2}H(^{16}O,n)^{17}F$, the energy of which is well known [Fr76]. This was done for two different field strengths by using two different charge states of ^{16}O. Calibrations at other field strengths were obtained by comparing the energies of ^{4}He particles backscattered from ^{197}Au and ^{27}Al targets with the energies of ^{4}He particles emitted in the decay of the daughters of ^{228}Th [Ma68]. The mean value of the magnet constant is $k = 55.187 \pm 0.014$ keV u e^{-2} mT^{-2}.

The 14 UD accelerator was calibrated using the backscattered particle technique referred to above, and by the observation of the resonance in the $^{12}C + p$ reaction which corresponds to the lowest $T = 3/2$ state in ^{13}N [Go75]. The results, which are shown in fig. 3.1, display a scatter which is large compared with the error bars. This is attributed to the beam taking different trajectories in the analysing magnet. The adopted value is $k = 78.073 \pm 0.038$ MeV u e^{-2} T^{-2} where the uncertainty is the standard deviation of the values in fig. 3.1.

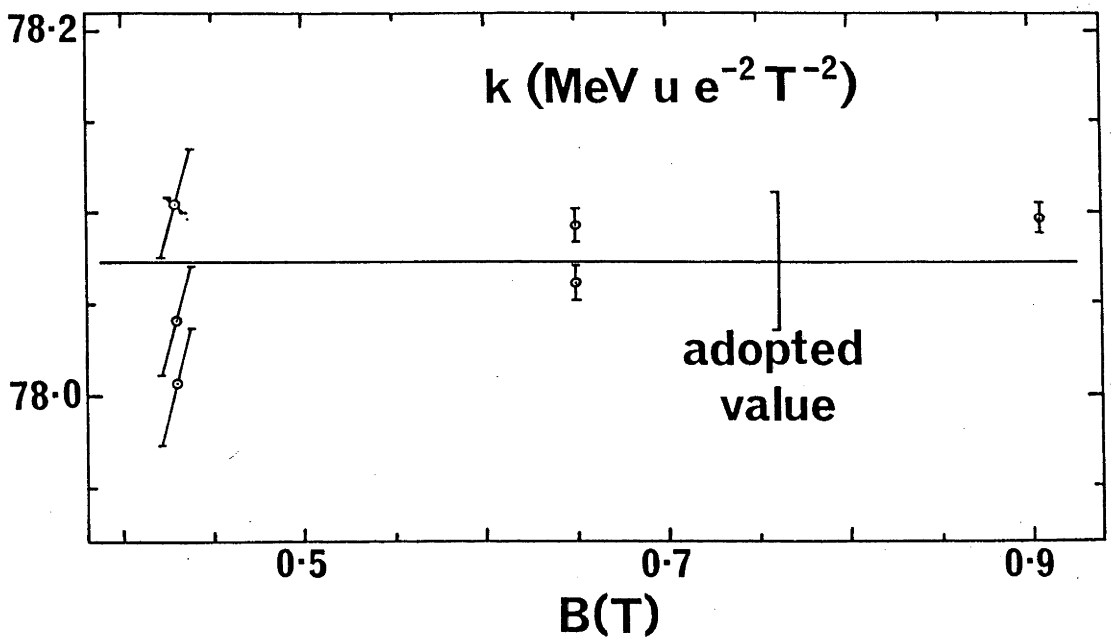

Fig. 3.1: The results of seven independent determinations of the magnet constant of the analysing magnet of the ANU 14 UD Pelletron accelerator.

3.2.3 Scattering Chamber Geometry

The apparatus for performing target excitation measurements, for example on ^{198}Hg, with the 14 UD accelerator is shown in fig. 3.2, which is drawn to scale. The backscattered particles are detected by an annular silicon surface barrier detector which is cooled to approximately -20 °C to reduce the leakage current and improve the noise characteristics. The tantalum defining slits for the detector had radii 5.1 mm and 7.6 mm, and the beam collimator at the entrance to the beam pipe was 4.6 mm in diameter. The 4.6 mm collimator and beam pipe were electrically insulated so that the focusing of the beam could be monitored. All of the defining edges of the various pieces of tantalum were highly polished to reduce slit-edge scattering. A 3 mm thick piece of tantalum was placed between the beam collimator and the detector to reduce the flux of X-rays at the detector.

For the target excitation experiments, the targets were placed perpendicular to the beam with the thin layer of target material toward the detector as shown in fig. 3.2. Electrons ejected from the

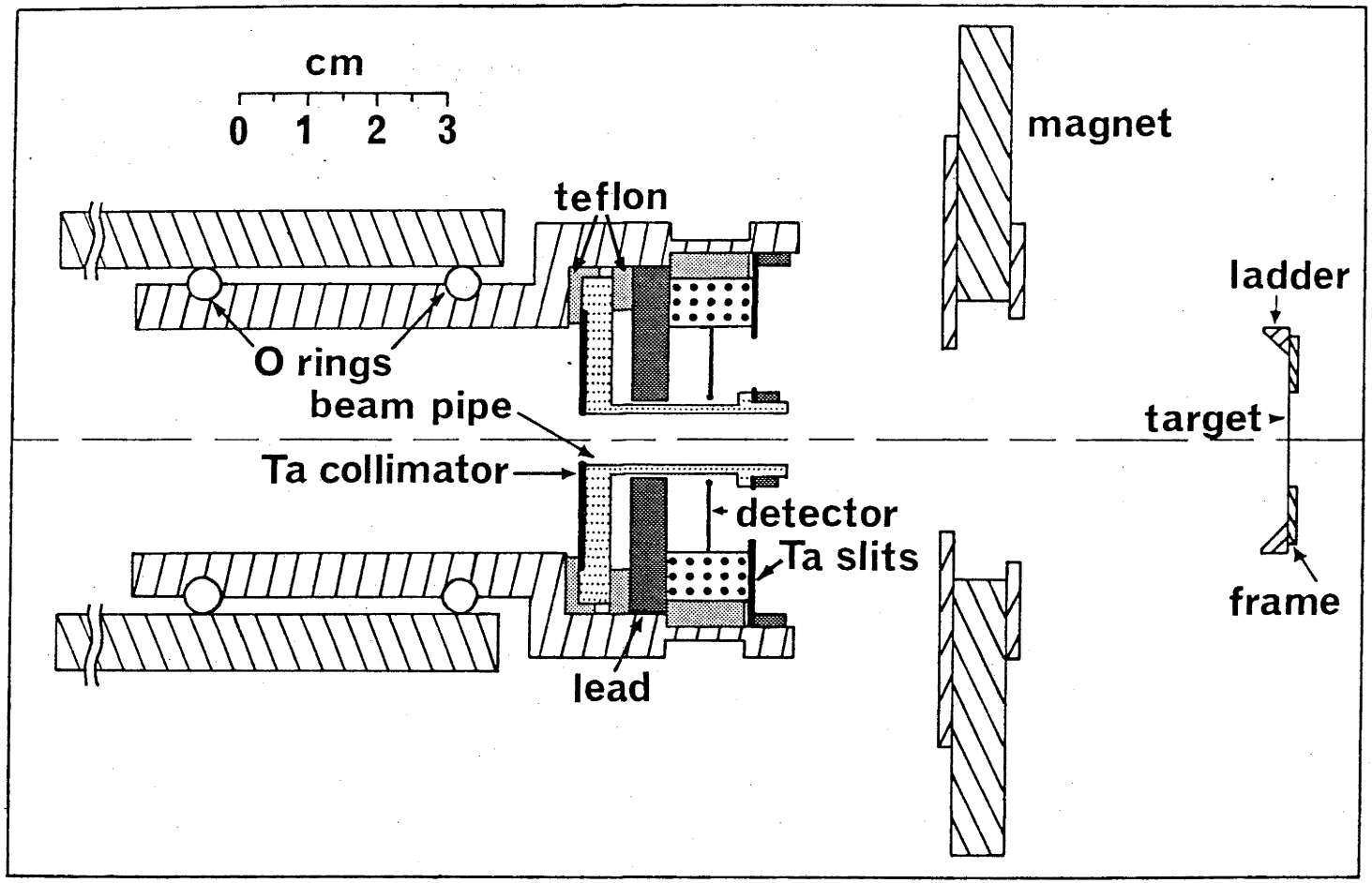

Fig. 3.2: A cross-sectional view of the apparatus for detecting backscattered projectiles with a silicon surface-barrier detector. The beam enters from the left. See the text for details.

target were prevented from entering the detector by a pair of bar magnets mounted between the target and the detector assembly. The distance between the detector and target was measured to an accuracy of ±3 mm, corresponding to an uncertainty in the scattering angle of ±0.5°. For the experiments with the 14 UD, distances between 48 mm and 70 mm were used. These correspond to mean scattering angles of 172.3° and 174.7° respectively. For the experiments on the EN tandem, the mean scattering angle was 171.6°.

The apparatus used when performing target excitation experiments with the EN tandem was identical to that described above but with the addition of a cold shroud maintained at liquid nitrogen temperature around the target ladder. This was to inhibit the deposition of hydrocarbon vapours on the target.

As discussed in subsection 3.1.2, the projectile excitation experiments required the detection of particles scattered through another angle in addition to $\theta \sim 180°$, and, as mentioned in subsection 3.1.3, this other angle must be accurately determined. There is considerable advantage in choosing this second angle to be 90°, as is shown below. A schematic diagram of the arrangement for making 90° measurements is shown in fig. 3.3. The nominal beam direction is defined as the central ray through the beam collimating apparatus. In the implementation of the ideas of fig. 3.3, beam collimation was provided by the annular detector mount (fig. 3.2). The nominal beam trajectory intersects the plane of the target at the point O. Detectors are placed on either side of the target as shown in fig. 3.3 and the points D and D' are the midpoints of the slits in front of these detectors. In the ideal situation, DOD' would be a straight line perpendicular to the nominal beam trajectory which would be the actual path of the beam. Consideration of the various possible deviations from this ideal situation reveal the advantages of this configuration.

If DOD' is indeed a straight line, then any error in setting DOD' perpendicular to the nominal beam trajectory will result in the scattering angle seen by one detector being greater than 90° by the same amount that that of the other detector is less than 90°. Now consider the quantity obtained by dividing the total number of

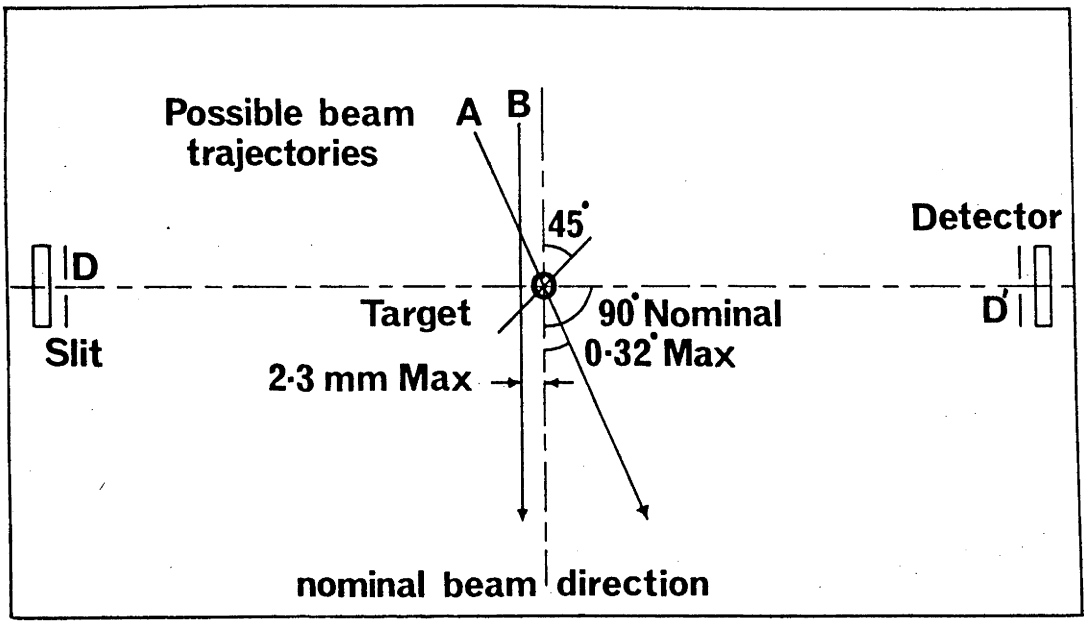

Fig. 3.3: A schematic diagram of the apparatus for detecting particles scattered through ±90°. The beam trajectories A and B represent the maximum possible deviations from the nominal beam direction.

inelastically scattered particles detected by the two detectors by the total number of elastically scattered particles similarly detected. I shall refer to this quantity as the averaged excitation probability although it is not the same as the average of the two excitation probabilities. If the solid angles subtended by the two slits at the point O are equal and if the Coulomb excitation functions F and ρ (eq. 2.50) are linear functions of the angle over the angular range involved, then the averaged excitation probability will correspond to a mean scattering angle of 90°. The detectors can easily be placed within ±2° and 90°, and figs. 2.1 and 2.4 show that the functions are reasonably linear over this angular range near $\Theta \sim 95°$ (which corresponds to $\Phi = 90°$).

The lines marked A and B in fig. 3.3 represent two beam trajectories which are the extreme deviations permitted by the beam collimating system from the nominal trajectory. Clearly, errors introduced by trajectory A will be cancelled in the averaged excitation probability for the same reason that the errors in setting

line DOD' perpendicular to the nominal beam trajectory are cancelled. The effect of trajectories of the type B can be eliminated by collecting half of the data with the target orientation shown in fig. 3.3 and half with the target perpendicular to the orientation shown in fig. 3.3. The cancellation of this particular error by rotating the target depends on the axis of rotation of the target passing through the point O.

As the above conclusions apply to any given ray of the beam, they are valid for beams of finite dimensions and divergences.

There are two sources of uncertainty in the scattering angle which are not cancelled in the averaged excitation probability. The first is due to the possibility of the beam striking the target above or below the point O. Using the maximum excursions from the nominal beam direction which are shown in fig. 3.3, the deviation due to the beam spot being high or low is less than 0.005°. The second and much more important source of uncertainty is due to the uncertainty in ensuring that the line DOD' is straight and that the axis of rotation of the target ladder passes through the point O. These uncertainties are considered below.

The apparatus to implement the above ideas is shown in fig. 3.4, which consists of a top view cut through in the plane corresponding to the plane of fig. 3.3. The target ladder, whose position and orientation were controlled from the lid of the scattering chamber, was constrained to move between four ball bearing races mounted in two pillars which were themselves mounted in a cylindrical collar. This permitted the whole assembly to be rotated about an axis perpendicular to the plane of fig. 3.4. The two detectors were mounted behind polished tantalum slits which defined a 2 mm × 15 mm aperture and were 180 mm from the target. As in the case of the annular detector, provision was made for cooling (not shown in fig. 3.4) and electron suppression.

The floor of the scattering chamber is grooved, which allowed the centre of the bar containing the target and detector assemblies to be placed within 0.1 mm of the centre of the chamber. The centre of the

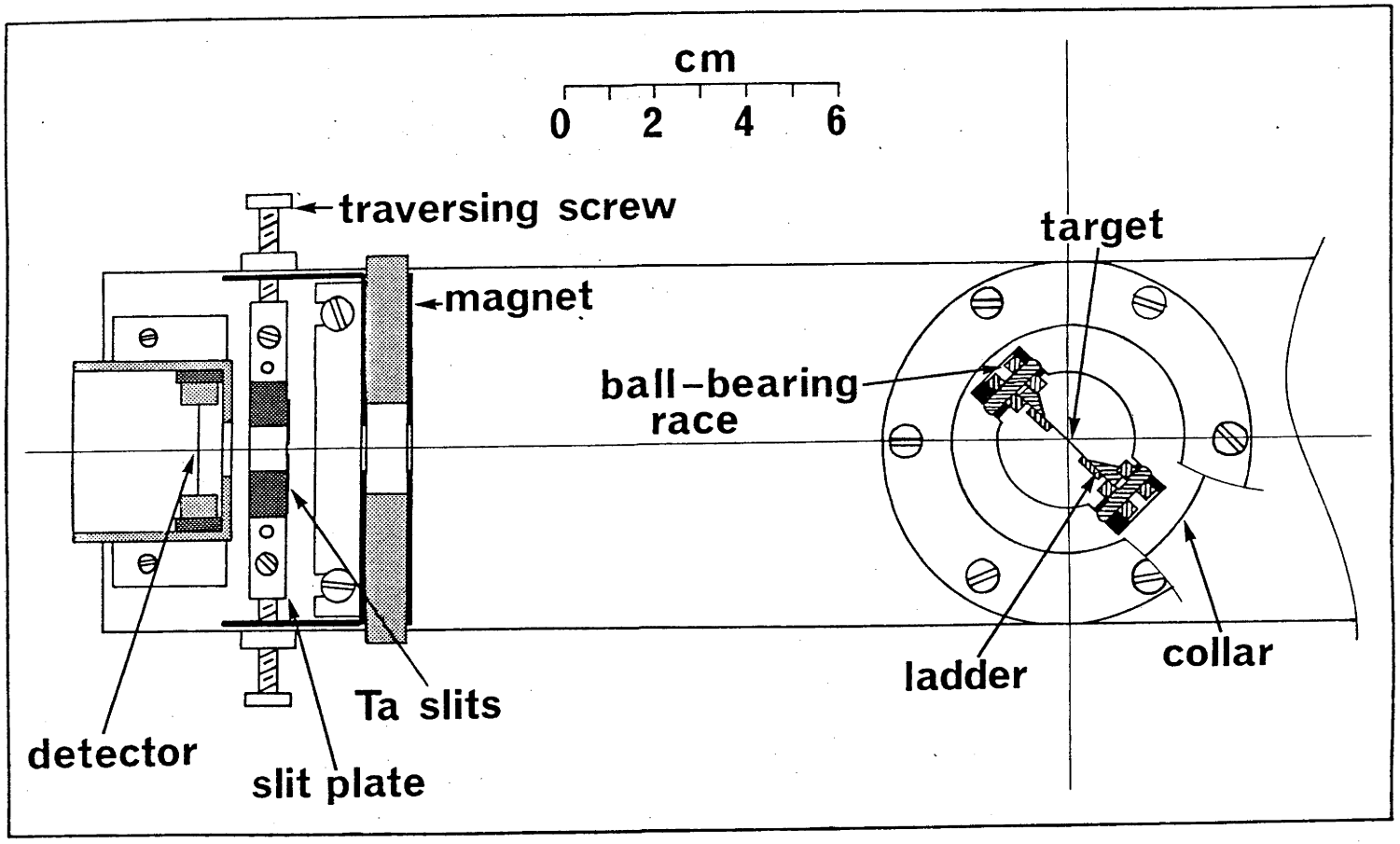

Fig. 3.4: A top view, cut through in the plane corresponding to the plane of fig. 3.3, of half of the apparatus for detecting particles scattered through ±90°. See the text for details.

target frame, which was directly above the centre of the bar, was taken to be the point O. Removal of the detectors allowed the alignment of the centre of the target frame and the slits with a theodolite. The standard error of the alignment was ±0.1 mm, where this number refers to the uncertainty in placing any one of the three elements on the line defined by the theodolite. Rotation of the central assembly did not produce any detectable displacement of the centre of the target frame, thus demonstrating that the axis of rotation of the target ladder was well within ±0.1 mm of the line defined by the theodolite.

The one remaining source of uncertainty was the movement of the thin targets relative to the target frame which had a 9.5 mm diameter hole. Inspection of the various targets used in this work showed that they could not bulge more than 2 mm perpendicular to the frame, and that most probably did not move by more than 1 mm. Consequently an uncertainty of ±1 mm was assigned to the position of the target. This gives an overall uncertainty in the scattering angle at 90° of ±0.3°.

A photograph of the chamber assembled to perform projectile excitation measurements is shown in fig. 3.5.

3.2.4 Targets

Care was taken during target manufacture to obtain targets of high uniformity and purity. Carbon foils, which provide the target backing, were prepared by depositing carbon on microscope slides coated in AR grade glucose. This seems to have a lower level of heavy contaminants than any other commonly used release agents. All pieces of equipment involved in the target making process were shot blasted (if they were metal) and cleaned with alcohol. Plastic gloves were worn whenever handling was required.

Target material was obtained from Oak Ridge National Laboratories. The lead was in the form of $^{208}Pb(NO_3)_2$ and the mercury in the form of

---

Fig. 3.5 (overleaf): A photograph of the scattering chamber assembled to perform projectile excitation measurements.

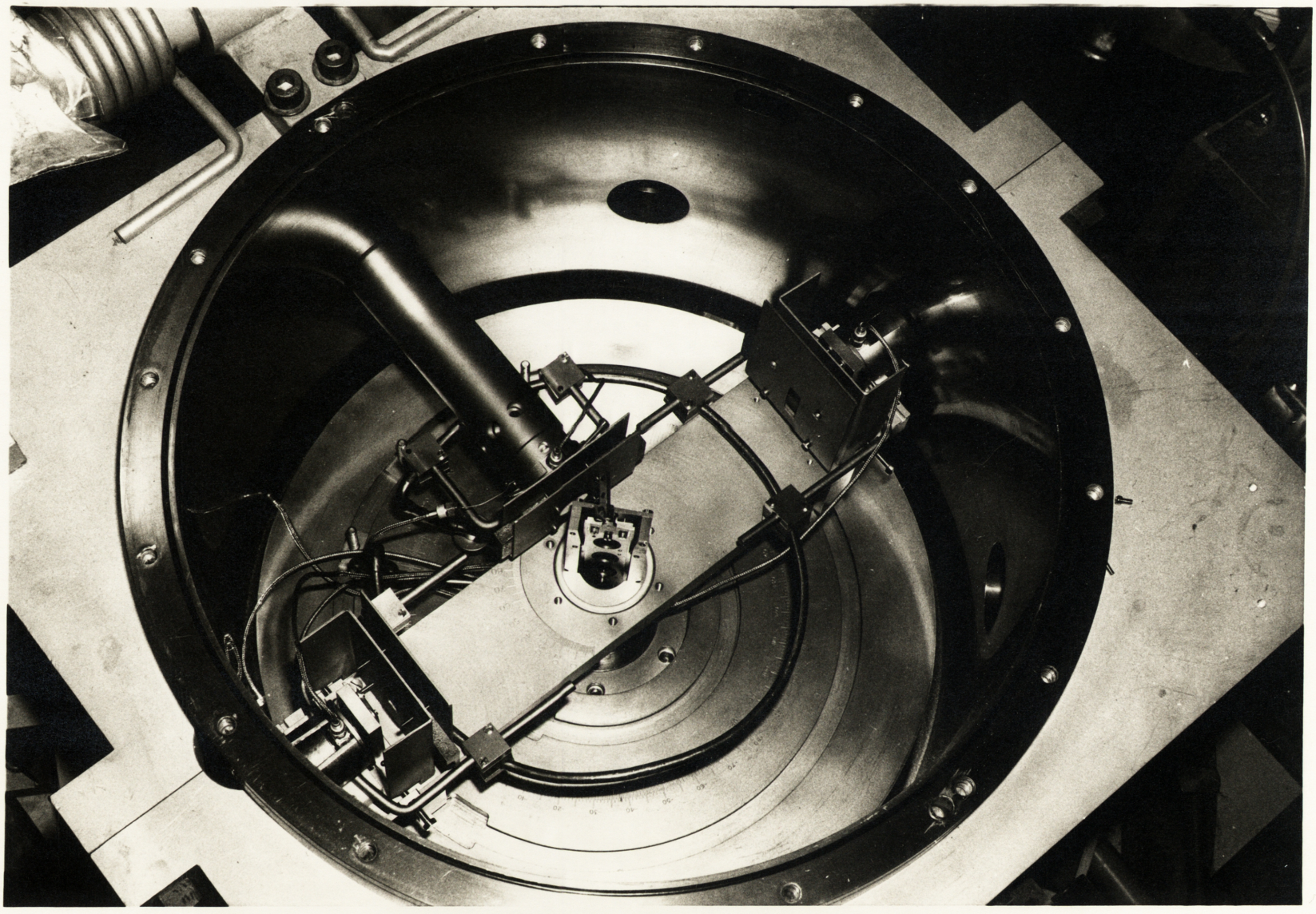

^{198}HgO. The isotopic composition of the target material is shown in table 3.1.

Table 3.1: Isotopic composition of

(a) Hg targets

Isotope	Concentration (%)
^{196}Hg	< 0.01
^{198}Hg	99.38 ± 0.03
^{199}Hg	0.31 ± 0.01
^{200}Hg	0.13 ± 0.01
^{201}Hg	0.07 ± 0.01
^{202}Hg	0.08 ± 0.01
^{204}Hg	0.02 ± 0.01

(b) Pb targets

Isotope	Concentration (%)
^{204}Pb	< 0.05
^{206}Pb	0.17 ± 0.05
^{207}Pb	0.69 ± 0.05
^{208}Pb	99.14 ± 0.10

Both $PbCl_2$ and PbS targets were prepared, but it was found that the sulphide targets were more stable under heavy-ion bombardment and these were used exclusively for the projectile excitation measurements. They were prepared by dissolving the nitrate in deionized water, and adding an aqueous solution of high purity H_2S. After drying, the PbS was evaporated under vacuum onto the previously prepared carbon foils. It was found that target stability under heavy-ion bombardment was considerably enhanced by the deposition of a layer of carbon over the PbS. An aluminium foil was included in the chamber during this deposition and, from the thickness of carbon deposited on it, the thickness of the carbon layer on the PbS targets was determined to be in the range 0.5 - 1.0 $\mu g.cm^{-2}$. The thickness of lead on the targets was kept low (< 10 $\mu g.cm^{-2}$) to reduce the target thickness component of the resolution.

The ^{198}Hg targets were prepared in the form of HgS by dissolving the oxide in high purity HCl before adding the H_2S solution. The important point in preparing HgS targets seems to be in preventing the HgS vapour from coming into contact with cool metal surfaces for it seems to condense on metals in preference to carbon. Accordingly, the

apparatus shown in fig. 3.6 was used. The whole target, including the carbon covering over the HgS, was prepared on the microscope slide before being mounted on a target frame. Targets produced by this method had partial thicknesses of mercury in the range 1 - 30 $\mu g.cm^{-2}$. Only targets thinner than 10 $\mu g.cm^{-2}$ were used. Further details on the manufacture of mercury targets can be found in ref. Es77.

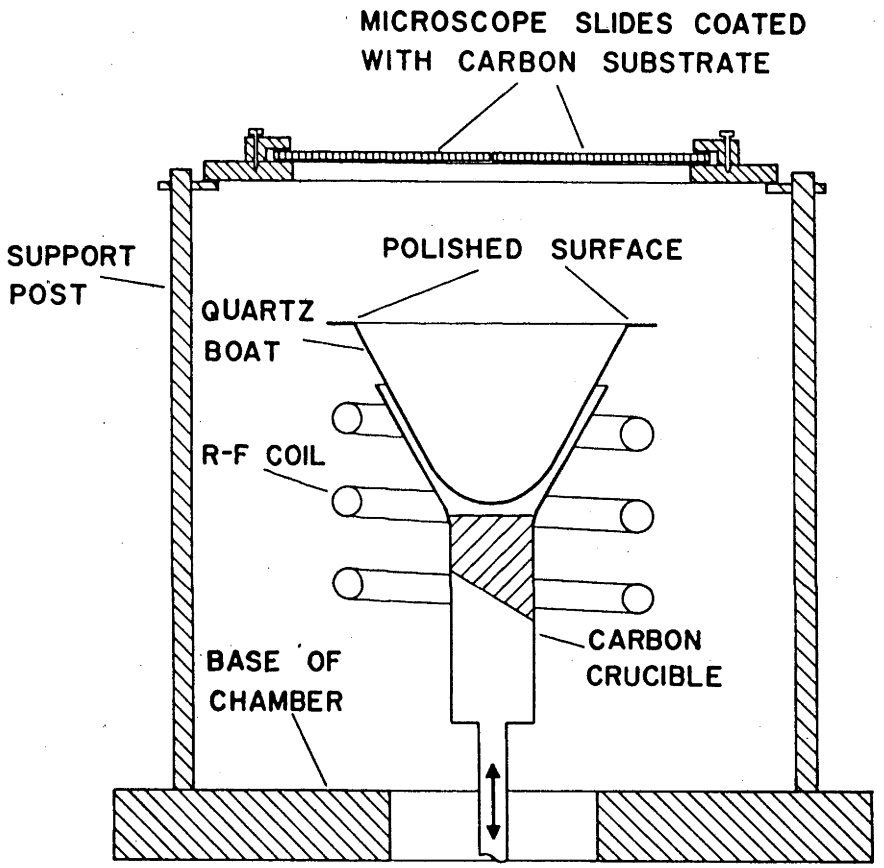

Fig. 3.6: The apparatus for the preparation of Hg targets. Before the evaporation, the boat is raised so that its polished surface is in contact with the microscope slides.

Because the bombarding energy must be known to ~ 0.1% (subsection 3.1.3), allowance must be made for the projectile's loss of energy in passing through the target and the carbon facing on the front of the target. Since the carbon layer is ~ 1 $\mu g.cm^{-2}$, the beam loses ~ 0.01% of its energy in passing through it. The correction for the energy loss in traversing the target itself (~ 0.4% of the incident energy)

is made by subtracting half of this energy loss from the incident energy. The stopping powers used in these calculations were obtained from Northcliffe and Schilling [No70].

3.2.5 Detectors and Electronics

Throughout these experiments, silicon surface-barrier detectors supplied by ORTEC Inc. were used. The response of silicon detectors to heavy ions has been extensively studied [e.g. Fi73, Se73, Ka74 and references therein]. It is observed that to obtain the same pulse height from the detector as is produced by an alpha particle, a heavy ion must have a higher energy than the alpha particle. This energy difference is referred to, somewhat confusedly, as the pulse height defect. Two obvious causes of energy loss, the energy loss in the gold layer on the front of the detector and the energy loss due to nuclear stopping, together account for about half of the observed pulse height defect [Wi71a]. The remainder is attributed to the increased recombination and trapping in the highly dense plasma produced by the heavy ion. Extrapolation from the data of Kassirov *et al.* [Ka74] suggests that the pulse height defect for 100 MeV ^{24}Mg ions is $\sim$ 1 MeV.

As well as producing the pulse height defect, all of the processes mentioned above contribute statistical fluctuations to the pulse height. Thus the resolution of these detectors worsens with increasing charge of the particle being detected. Further, this effect is not symmetric about the mean pulse height, but produces a low energy tail on the pulse height distribution. Nothing can be done about the contributions from the gold layer (except by making it as thin as possible) or nuclear stopping, but it might be hoped that recombination could be reduced by applying the highest possible electric field across the detector. For this reason, we requested that ORTEC supply us with annular detectors capable of withstanding fields of at least 1 Vμm^{-1}. For the 90° detectors, ORTEC "F" series detectors, which were rated at 1.4 Vμm^{-1} to 2.0 Vμm^{-1}, were used. Toward the end of this series of measurements, we requested from ORTEC an "F" series detector with an 8 mm hole drilled in it and received a

detector which could withstand 3.5 $V\mu m^{-1}$. The performance of this detector was not substantially better than that of the regular annular detectors. Perhaps this is evidence that the limit of what can be achieved by increasing the field has been reached, as suggested by England [En72]. One deleterious effect of a very high field was identified and this is shown in fig. 3.7. The spectra in fig. 3.7 were obtained by placing an "F" series detector in the focal plane of an ESP 90 magnetic spectrograph which was set to detect projectiles scattered through 15° from a ^{208}Pb target. A 0.8 mm slit was placed in front of the "F" series detector so that it was irradiated by a beam of essentially monoenergetic particles. The only difference between the two spectra in fig. 3.7 is the bias applied to the "F" series detector. It has been suggested that the broad peak on the high energy side of the elastic peak is due to charge multiplication in the detector [En77]. Its behaviour with bias supports this.

The pulses from the detectors were amplified by ORTEC model 125 preamplifiers and TENNELEC model 203BLR amplifiers and analysed by CANBERRA model 8060 analogue-to-digital converters.

3.3 ^{198}Hg DATA

The quadrupole moment of the first excited state of ^{198}Hg was determined by bombarding ^{198}HgS targets with various projectiles. It is usual in experiments of this type to use two projectiles only, e.g. ^{4}He and ^{16}O. However, as the energy of the first excited state is only 412 keV, peak-to-valley ratios for the ^{16}O spectra are low (~ 8), so, in order to improve the reliability of the result, ^{12}C projectiles were also used. These give spectra with peak-to-valley ratios of better than 12, but have the disadvantage that the reorientation sensitivity parameter ρ is $7 \times 10^{-4}\ e^{-1}\ fm^{-2}$ compared with $9 \times 10^{-4}\ e^{-1}\ fm^{-2}$ for ^{16}O.

The use of three projectiles also provides a check for systematic errors by testing the linearity of the ratio P/F with ρ (eq. 2.50).

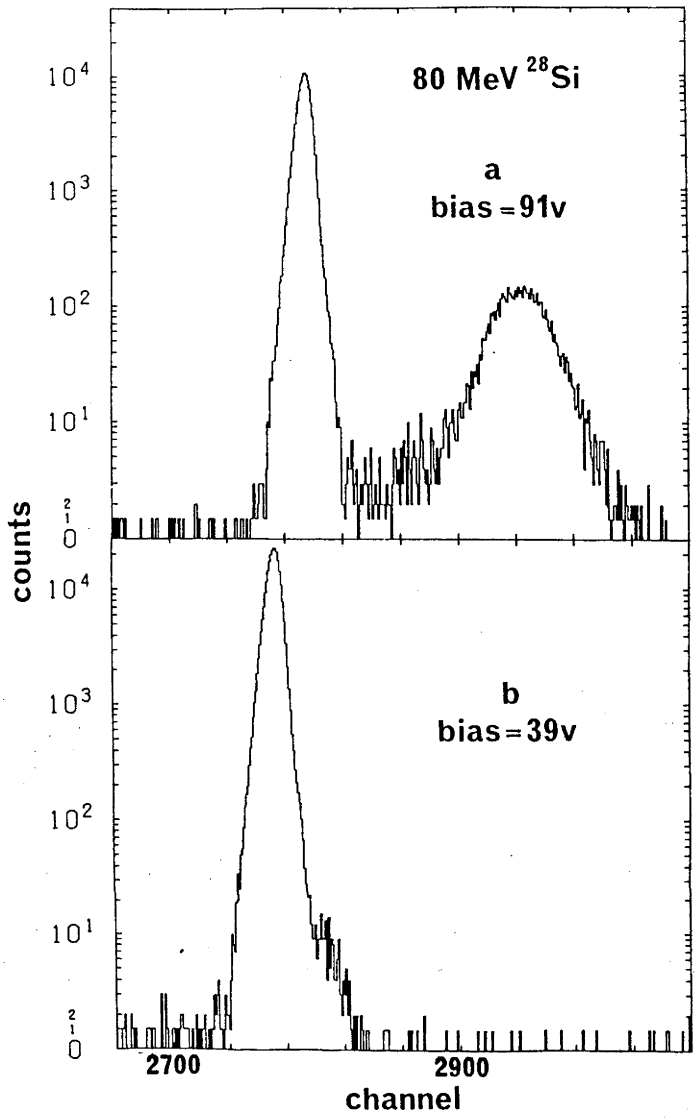

Fig. 3.7: The response of an ORTEC "F" series silicon surface-barrier detector to 80-MeV monoenergetic ^{28}Si ions. The two spectra were collected under identical conditions except for the bias across the detector. The broad peak on the high energy side of the full-energy peak in the top spectrum is attributed to the effect of charge multiplication in the detector.

3.3.1 ^{16}O and ^{12}C Data

^{16}O spectra were collected at bombarding energies ranging from 60 MeV to 80 MeV. The best peak-to-valley ratio obtained was a value of 9.6 for the 67 MeV data, and the worst was 6 for the 64 MeV data. These two spectra are shown in fig. 3.8. The full curves shown in

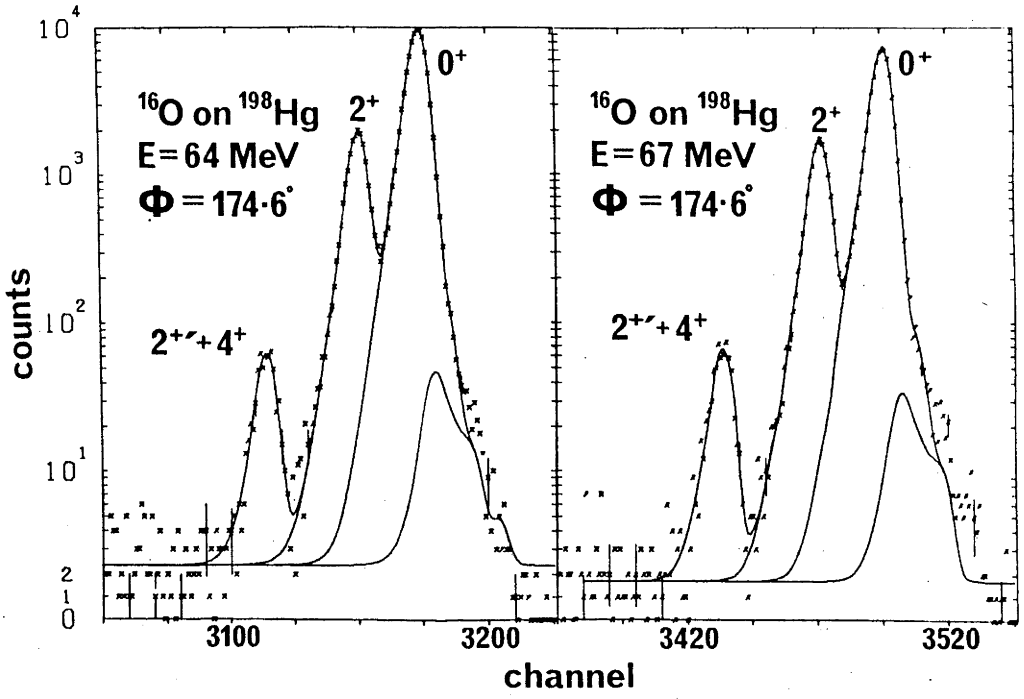

Fig. 3.8: Spectra of 64 MeV and 67 MeV ^{16}O ions scattered through 174.6° from ^{198}Hg. The peaks are labelled according to the angular momentum of the final state of ^{198}Hg, the peak labelled 0^+ being due to elastic scattering. The full lines show the results of fits to the spectra. See the text for details. The line underneath the elastic peak shows the area subtracted to allow for the other isotopes of Hg in the target.

fig. 3.8 are χ^2 fits of a mathematical function to the spectra. The function used was

$$f(z) = \begin{cases} H[\exp(-z^2/2\sigma_H^2) + f\exp(-(z-p)^2/2\sigma_H^2)] + B & (z \geqslant 0) \\ H[\exp(-z^2/2\sigma_L^2) + f\exp(-(z-p)^2/2\sigma_H^2) \\ \quad + A_s\exp(-b_s|z|)\{1-\exp(-z^2/2c_s\sigma_H^2)\}] + B & (z < 0)\,, \end{cases} \tag{3.7}$$

where $z = x - \bar{x}$, $\bar{x}$ being the mode of the peak, and B is a flat background. The parameters H, σ_H, f, p, σ_L, A_s, b_s and c_s were adjusted to obtain the lowest χ^2. The features of this lineshape are —

(a) It is a skewed Gaussian, that is σ_H and σ_L may be different.

(b) It has a shoulder on the high energy side of the peak. This

shoulder is a detector artifact which is present in all heavy ion backscattering spectra, including those taken with a ^{208}Pb target. It is fitted with a Gaussian positioned about σ_H above the mode and whose relative height f increases with the charge of the detected ion, varying from $\sim$ 1% for ^{12}C to $\sim$ 8% for ^{24}Mg. The actual value of f varies from detector to detector and tends to increase with the radiation received by the detector.

(c) It has a low energy tail which is zero at $x = \bar{x}$, rises to a maximum at about $x = \bar{x} - 2$ and falls exponentially with decreasing x thereafter.

In fitting the ^{16}O data, it was assumed that the elastic and inelastic peaks have the same lineshape parameters apart from position and height. The structure under the elastic peak is due to the other isotopes of Hg in the target. Their intensities were calculated using the assay shown in table 3.1 (p.127).

The area of the inelastic peak was determined by summing the data and subtracting the elastic tail as predicted by the lineshape. The uncertainty in the fit to the elastic tail was determined by varying the height of the tail (parameters A_s and B of eq. 3.7) and visually judging the effect on the fit. For example, fig. 3.9 shows the same spectrum as fig. 3.8a, but the height of the tail has been altered by ±20%. From this it is concluded that ±20% is a reasonable estimate of the relative uncertainty in the determination of the area of the elastic tail under the inelastic peak. As this area is about 4% of the gross area of the peak, it contributes about ±1% to the uncertainty in the net area — a contribution which is of the same order of magnitude as that due to statistics.

The procedure described above for unfolding the elastic and inelastic peaks makes some assumptions about the shape of the elastic tail where it is hidden underneath the inelastic peak. To verify these assumptions, a spectrum of 65 MeV ^{16}O ions backscattered from a ^{208}Pb target was collected. This allowed that portion of the lineshape which is under the inelastic peak in the ^{198}Hg spectra to be seen, as the first excited state of ^{208}Pb is at 2.615 MeV. Fig. 3.10a

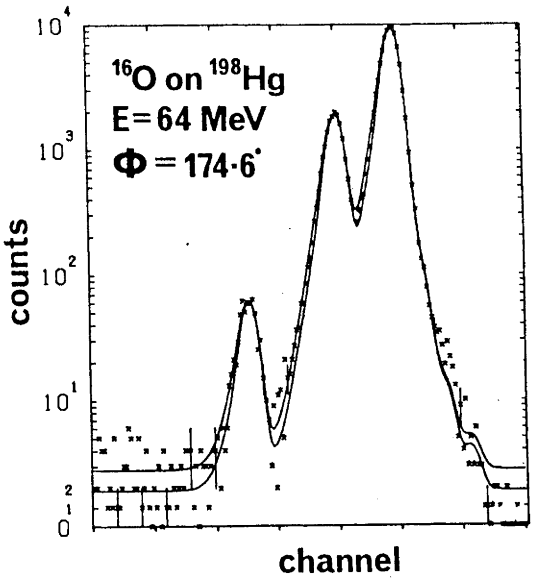

Fig. 3.9: The effect of varying the height of the background and the low-energy tail by ±20%.

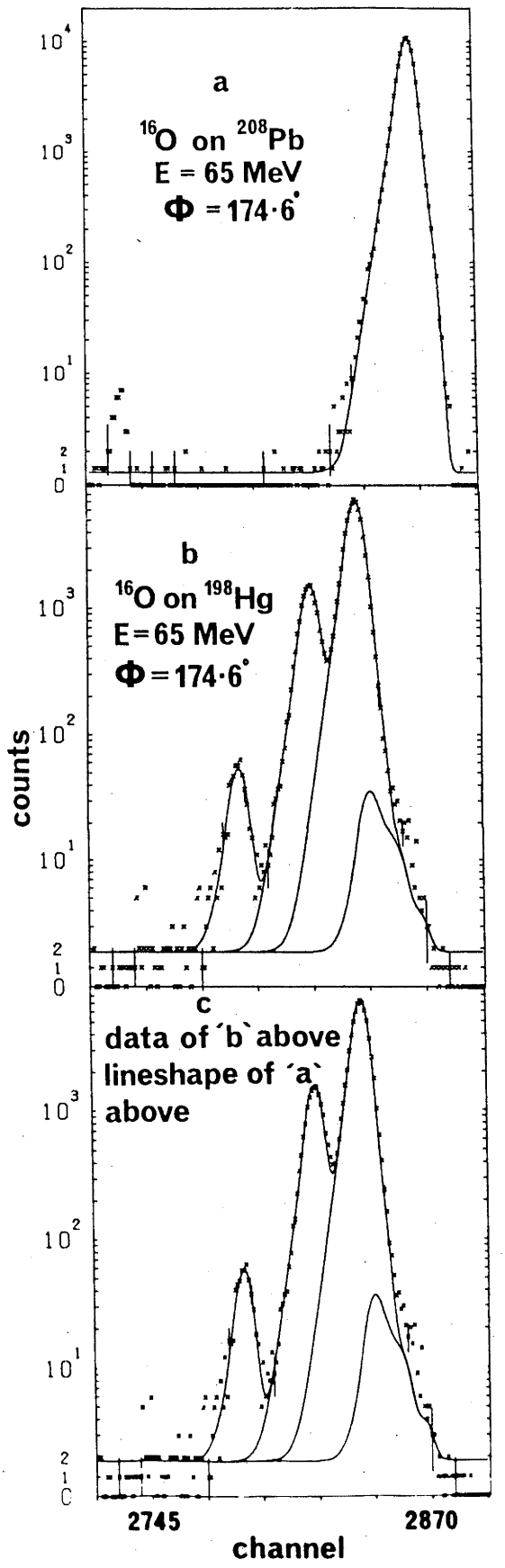

Fig. 3.10: Spectra of 65 MeV ^{16}O ions backscattered from (a) ^{208}Pb and (b) ^{198}Hg. The full lines on these two spectra show the results of fits to the data. Part c shows the result of fitting the data of part b using lineshape parameters derived from the data of part a.

shows the fit to this ^{208}Pb spectrum. Clearly the lineshape of eq. 3.7 is quite adequate. The dispersion in fig. 3.10a is the same as in figs. 3.10b and 3.10c which show the same spectrum — that of 65 MeV ^{16}O ions backscattered from ^{198}Hg — but with two different fits. The full line in fig. 3.10b was obtained by allowing all parameters to vary while that of fig. 3.10c is the same lineshape as in fig. 3.10a. The difference in the values of the excitation probability P_{exp}, defined as

$$P_{exp} = \frac{\text{inelastic peak area}}{\text{sum of elastic and inelastic peak areas}}, \qquad (3.8)$$

given by these two different lineshapes is 0.6%. This can be compared with the statistical uncertainties of ~ 1%.

Spectra of ^{12}C ions were collected at bombarding energies ranging from 43 MeV to 54 MeV. The spectra with the best and worst peak-to-valley ratios are shown in fig. 3.11, where the fits are also indicated. These spectra differ from those above by requiring an additional "long range" component in the low energy tail. This is provided by adding the term

$$A_L \exp(- b_L|z|)\{1 - \exp(- z^2/2c_L\sigma_L^2)\} \qquad (3.9)$$

to the terms in square brackets for the case $z < 0$ in eq. 3.7. The quantities A_L, b_L and c_L are three additional adjustable parameters. Again, the relative error in the determination of the area of the elastic tail under the inelastic peak was taken as ±20%, this area being less than 2% of the gross area in all cases.

To check this lineshape, a spectrum of 46 MeV ^{12}C ions backscattered from ^{208}Pb was collected. Fig. 3.12 shows this spectrum with its fit and fits to the 46 MeV ^{198}Hg data obtained by allowing all lineshape parameters to vary and by using the "^{208}Pb" lineshape of fig. 3.12a. The difference in the inferred excitation probability is 0.8%, which is again less than the statistical uncertainties.

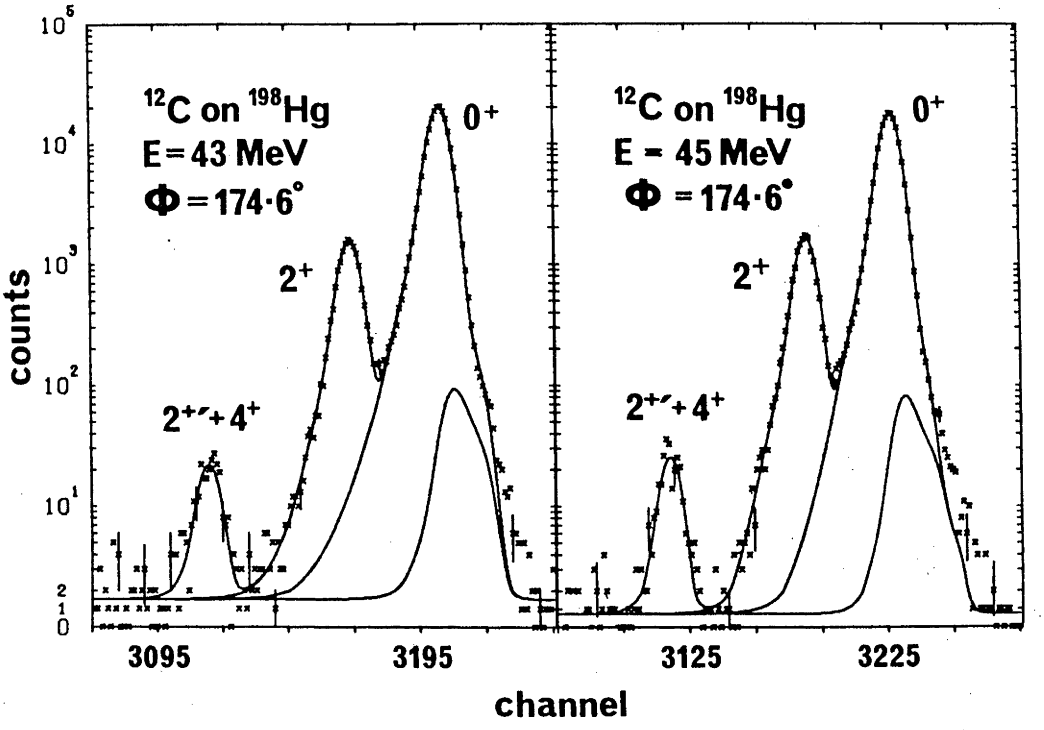

Fig. 3.11: Spectra of 43 MeV and 45 MeV ^{12}C ions scattered through 174.6° from ^{198}Hg. The peaks are labelled according to the angular momentum of the final state of ^{198}Hg, the peak labelled 0^+ being due to elastic scattering. The full lines show the results of fits to the spectra. The line underneath the elastic peak shows the area subtracted to allow for the other isotopes of Hg in the target.

3.3.2 ^{4}He Data

Spectra of ^{4}He backscattered from ^{198}Hg were collected with bombarding energies in the range 14.1 MeV to 18.0 MeV. The spectrum obtained at 14.1 MeV is shown in fig. 3.13. The peak-to-valley ratios were better than 100 for the low energy spectra, rising to about 300 at higher bombarding energies. The elastic tail is flat enough in the region of the inelastic peak for linear background subtraction to be sufficient. This was checked by fitting some of the spectra with the function of eq. 3.7 including the long range tail of eq. 3.9 but without the high-energy shoulder. One of the fitted spectra is shown in fig. 3.14. In all cases the value of the excitation probability inferred from the fit differed by less than 1% from the result obtained by linear background subtraction, this deviation being

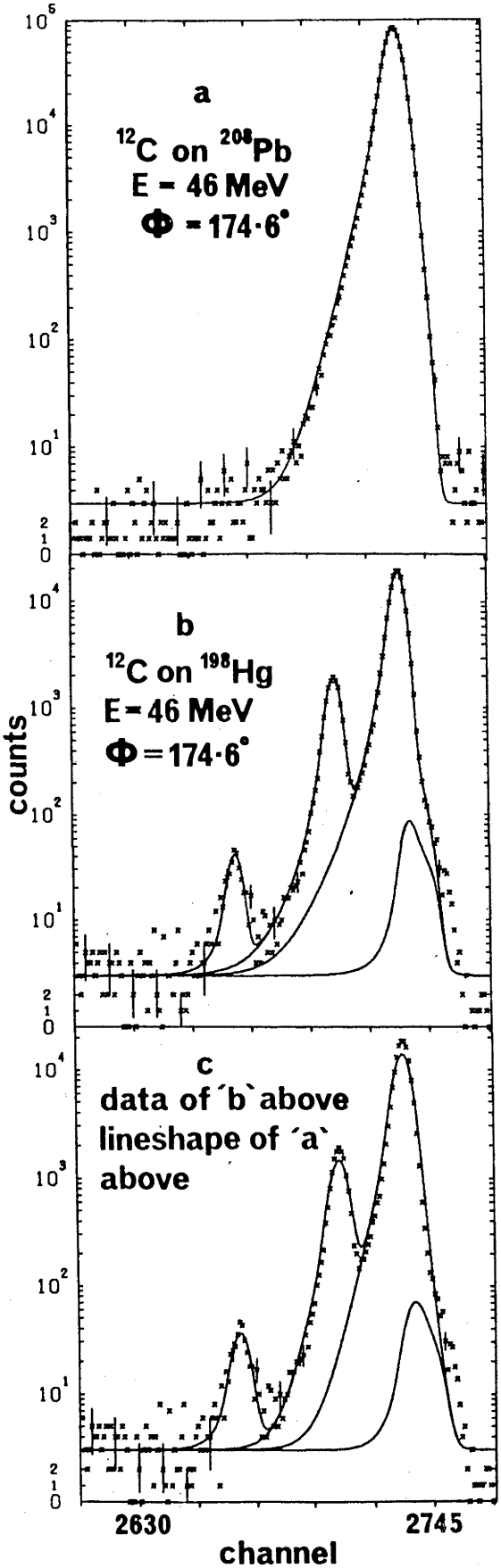

Fig. 3.12: Spectra of 46 MeV ^{12}C ions backscattered from (a) ^{208}Pb and (b) ^{198}Hg. The full lines on these two spectra show the results of fits to the data. Part c shows the result fitting the data of part b using lineshape parameters derived from part a.

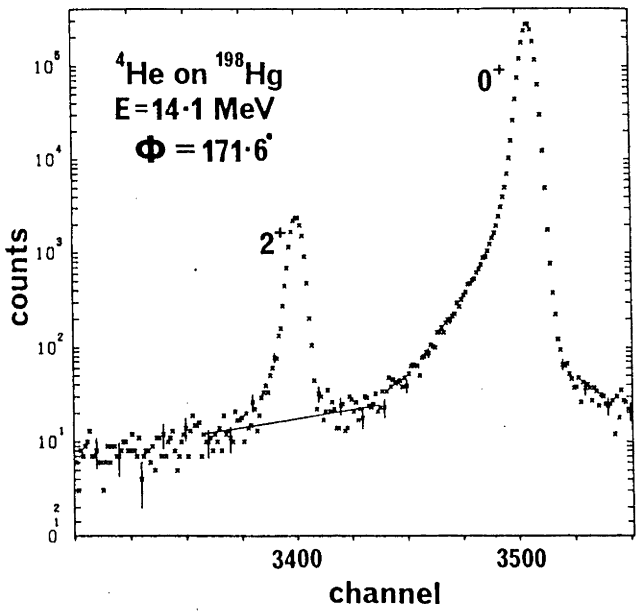

Fig. 3.13: A spectrum of 14.1 MeV ^{4}He ions scattered through 171.6° from ^{198}Hg. The peaks are labelled according to the angular momentum of the final state of ^{198}Hg. The full line shows the linear background area subtracted from the inelastic peak.

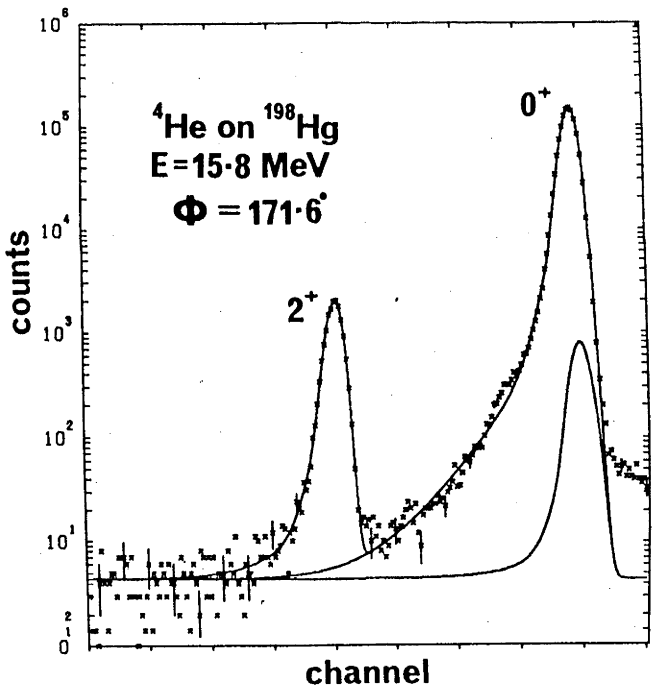

Fig. 3.14: A spectrum of 15.8 MeV ^{4}He ions backscattered from ^{198}Hg. The full curves show the fit to the data which was used to check the linear-background subtraction procedure.

comparable with the statistical uncertainties.

It has been suggested [Vo77] that measurements of this kind using surface-barrier detectors may contain systematic errors due to nuclear reactions between the incident particles and the silicon in the detector. That this is not so in this experiment can be seen from

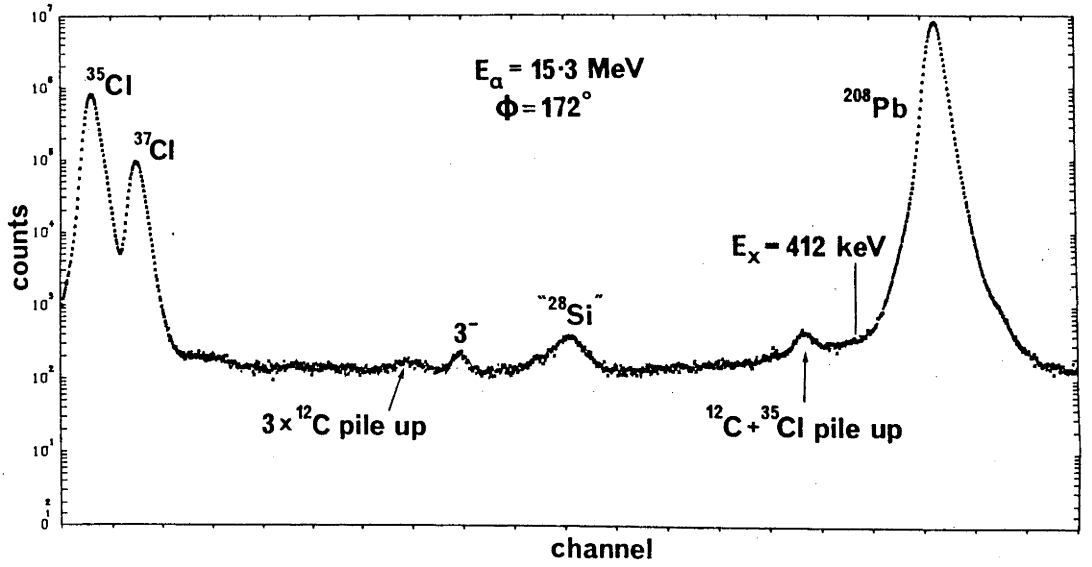

Fig. 3.15: A spectrum of 15.3 MeV ^{4}He ions backscattered from a $^{208}PbCl_2$ target on a carbon backing. Six of the peaks are due to elastic scattering from ^{208}Pb, ^{35}Cl and ^{37}Cl, to the excitation of the 3_1^- state of ^{208}Pb and to various pulse pile-up events. The seventh peak, labelled "^{28}Si" is a detector artifact and is discussed in the text. The position where an inelastic peak would have been had the target been ^{198}Hg is also shown.

figs. 3.10a and 3.12a in the case of heavy ion scattering and fig. 3.15 for ^{4}He scattering. Fig. 3.15 does indeed contain a detector effect — the peak labelled "^{28}Si" is due to the excitation of the first excited state of ^{28}Si and the subsequent escape of the de-excitation gamma ray — but this peak is clearly well away from the region where the inelastic peak would have been had the target been ^{198}Hg. It is possible that there are some very weak peaks due to other ^{4}He + ^{28}Si reactions in the region of interest but that these are obscured by the background. The general method used to obtain an upper limit on the magnitude of such peaks is as follows. A region of the spectrum centred at the position of interest and with a width equal to the FWHM of the elastic peak is summed. The required upper limit is taken as twice the square root of the sum. I shall refer to this procedure as taking twice the standard deviation of the background. With this method, upper limits of 0.3%, 0.08% and 0.02% can be placed on the contribution of possible peaks in the lineshape to the inferred excitation probability in the ^{4}He, ^{12}C and ^{16}O data respectively.

3.3.3 Checks for the Presence of Contaminant Peaks

The three effects which are considered in this section are elastic scattering from lighter mass contaminants, inelastic scattering from Hg isotopes other than ^{198}Hg and nuclear reactions.

Target contaminants which could produce elastic scattering peaks underneath the ^{198}Hg inelastic peak are isotopes with masses in the ranges A = 137 to A = 147 for the ^{4}He data, A = 174 to A = 186 for the ^{12}C data and A = 190 to A = 195 for the ^{16}O data. Upper limits on the concentrations of the two lighter mass groups can be obtained from an examination of the ^{16}O spectrum taken at 69 MeV bombarding energy. This is shown in fig. 3.16. Taking two standard deviations of the background, the concentration in the target of those impurities which would affect the data is < 70 ppm for the ^{4}He data and < 200 ppm for the ^{12}C data. This corresponds to effects on the excitation probability of < 0.8% and < 0.3% respectively. Because the excitation probability is ~ 0.15 in the ^{16}O data, contaminants of Os, Ir and Pt would have to be present in large concentrations (above 1500 ppm) to affect the data by 1%. Targets of Cd and Pb have been made using materials and methods similar to those used in making these Hg targets, and contaminations of these elements have never been observed; nor have those contaminants which are observed (e.g. Fe, Cu) ever been seen in concentrations as large as 1500 ppm.

The most abundant of the isotopic impurities is ^{199}Hg which accounts for 0.31% of all the Hg in the target. At these low concentrations, the effect of inelastic scattering from these impurities is negligible.

The most likely reactions at these energies are single nucleon transfer reactions, but all four such reactions for each of the three target-projectile combinations have Q values which are sufficiently negative to remove the reaction peaks from the regions of interest in the spectra.

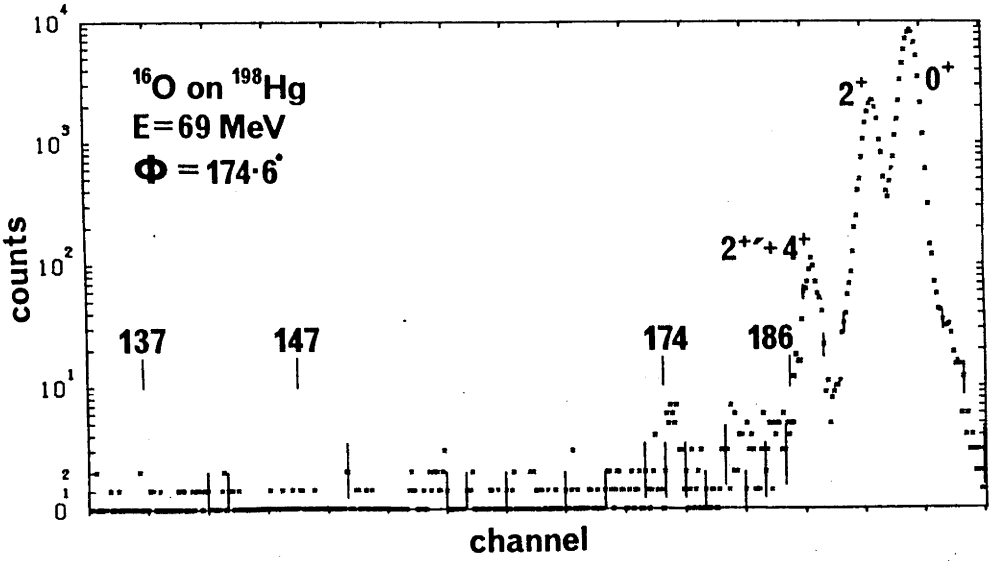

Fig. 3.16: A spectrum of 69 MeV ^{16}O ions backscattered from ^{198}Hg. The positions where peaks due to elastic scattering from target contaminants of mass 137, 147, 174 and 186 would be are shown.

3.3.4 Safe Bombarding Energies

In order to determine the bombarding energies at which the effects of the nuclear force become significant, the dependence of the ratio P_{exp}/P_{coul} on bombarding energy is examined. Here P_{exp} is the measured excitation probability (eq. 3.8) and P_{coul} is the excitation probability computed with the assumption of a purely Coulomb interaction using the de Boer-Winther computer program (section 2.1.2). The matrix elements used in this calculation are given in subsection 4.2.1.

Fig. 3.17 presents plots of the ratio referred to above. The abscissa of fig. 3.17 is linear in the distance of closest approach of the nuclear surfaces, s, which is conventionally defined by

$$s := a[1+\mathrm{cosec}(\Theta/2)] - R_0(\sqrt[3]{A_p}+\sqrt[3]{A_t}) , \qquad (3.10)$$

whence

$$s_{[fm]} = 0.7200\, Z_p Z_t (1+A_p/A_t)[1+\mathrm{cosec}(\Theta/2)]/E_{[MeV]} - 1.25(\sqrt[3]{A_p}+\sqrt[3]{A_t}) , \qquad (3.11)$$

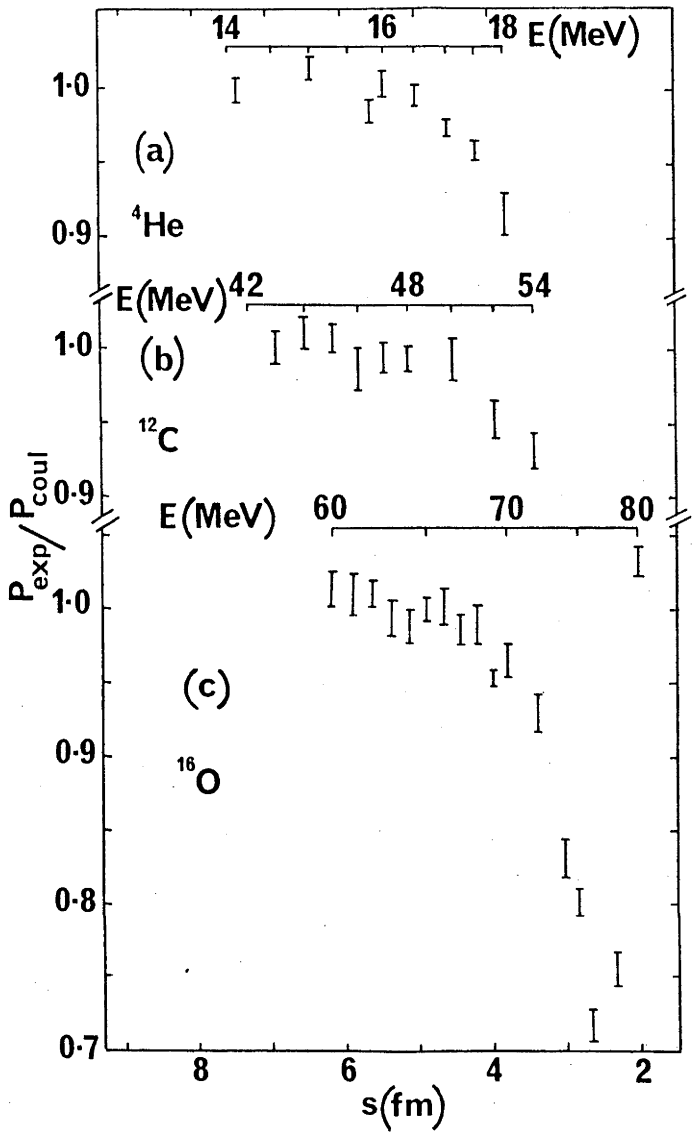

Fig. 3.17: The variation of the double ratio P_{exp}/P_{coul} with bombarding energy E and minimum separation s of the nuclear surfaces for the backscattering of (a) ^{4}He, (b) ^{12}C and (c) ^{16}O from ^{198}Hg.

the usual value of the nuclear radius parameter R_0 of 1.25 fm having been chosen. This method of plotting allows comparisons between the three projectiles to be made.

From consideration of fig. 3.17, it is seen that energies which maintain $s \geqslant 4.6$ fm have a contribution from the nuclear force which is negligible compared with the experimental errors. Thus, data taken with bombarding energies of 16.5 MeV (^{4}He), 48 MeV (^{12}C) and 66 MeV

(^{16}O) or less are used to determine the quadrupole moment.

3.4 ^{24}Mg DATA

3.4.1 Backscattering Data

Spectra of ^{24}Mg ions backscattered from ^{208}Pb targets were obtained at bombarding energies ranging from 80 MeV to 110 MeV. It was immediately clear that the lineshapes had different low-energy tails than those of the ^{12}C or ^{16}O spectra above. To determine the shape of the low energy tail, spectra were collected at bombarding energies ranging from 50 MeV to 62.5 MeV. At these energies, the excitation probability is less than 1% of its value at 80 MeV and the inelastic peak is lost in the background. Fig. 3.18 shows one of these low energy spectra. It is fitted with a lineshape which consists of the function of eq. 3.7 with the addition of a long-range, low energy tail of the form

$$A_L \exp(- b_L|z| - d_L|z|^{e_L})\{1 - \exp(- z^2/2c_L\sigma_L^2)\}\,, \qquad (3.12)$$

A_L, b_L, c_L, d_L and e_L being adjustable parameters.

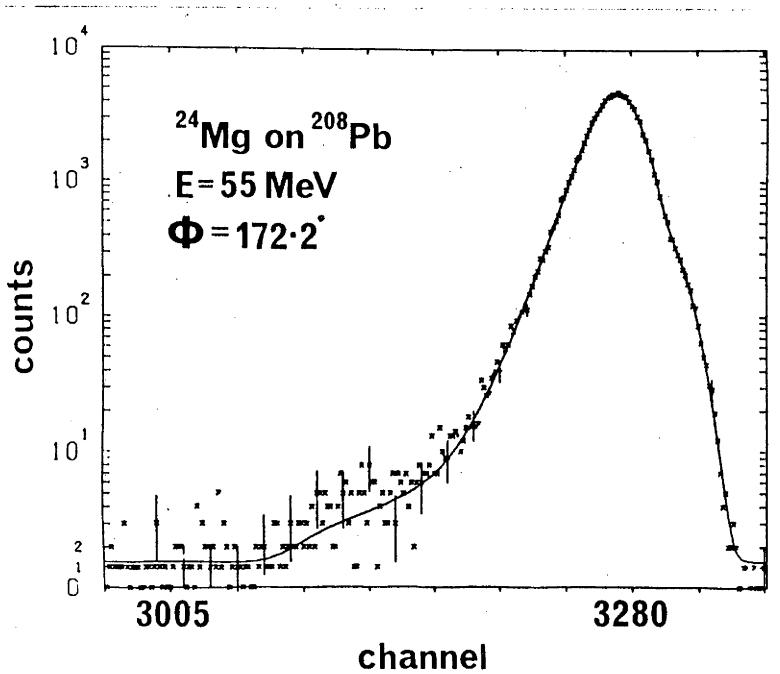

Fig. 3.18: A spectrum of 55 MeV ^{24}Mg ions backscattered from ^{208}Pb. The full line shows the result of a fit to the data. See the text for details.

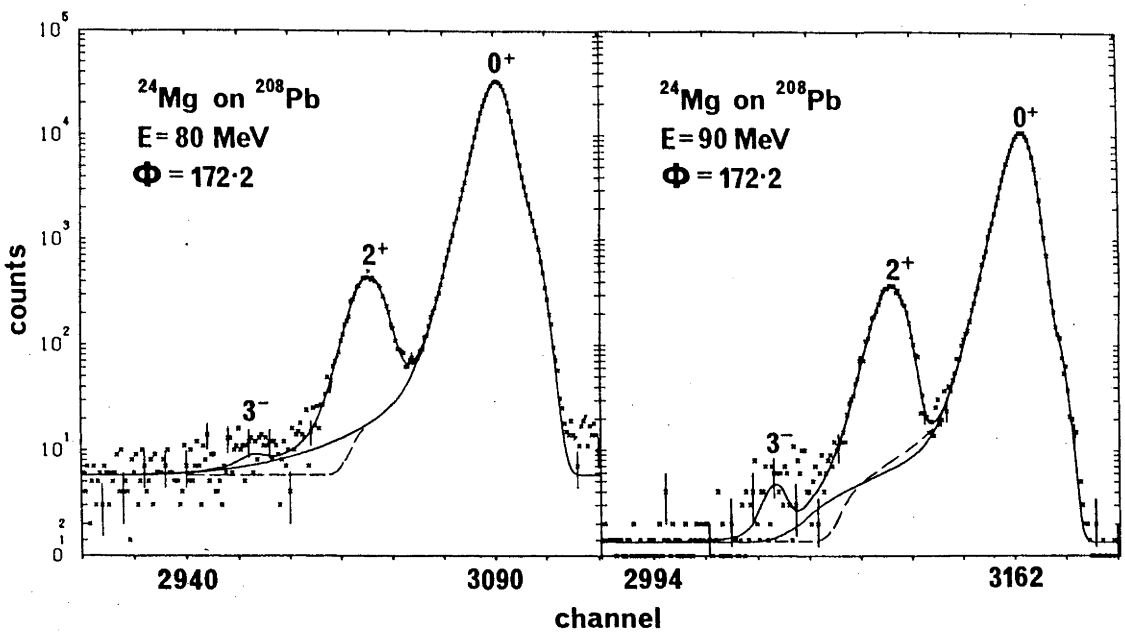

Fig. 3.19: Spectra of 80 MeV and 90 MeV ^{24}Mg ions backscattered from ^{208}Pb. The peaks labelled 0^+ are due to elastic scattering, those labelled 2^+ to excitation of the 2_1^+ state of ^{24}Mg and those labelled 3^- to the excitation of the 3_1^- state of ^{208}Pb. The significance of the full and broken curves is explained in the text.

This lineshape was then applied to the high energy data, and small adjustments made to the parameters to obtain a fit. Fig. 3.19 shows the fit obtained for two of the spectra before (full lines) and after (broken lines) the adjustment of the parameters. The change in inferred excitation probability due to this adjustment of the parameters was never greater than 4%, and was typically less than half of that value. In projectile excitation data, the inelastic peak is broader than the elastic peak because the excited projectiles suffer a recoil when they gamma decay, which most do long before reaching the detector. This gives the ^{24}Mg inelastic peak a complex shape, but it was found that good fits could be obtained by using the sum of two elastic-peak lineshapes. The peak due to the excitation of the first excited state of the target was not fitted, rather its position and height were computed using the known properties [Jo77a] of the level.

The uncertainty in the fit to the elastic tail was determined in the same manner as in the case of the ^{198}Hg data (subsection 3.3.1).

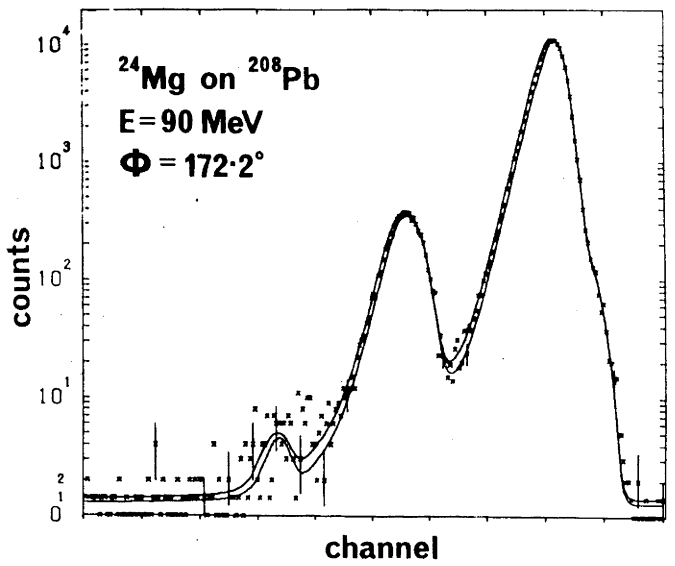

Fig. 3.20: The effect of varying the height of the background and low energy tails by ±15%.

Fig. 3.20 shows the same spectrum as fig. 3.19b but with a ±15% variation applied to the low-energy tail of the lineshape. The relative uncertainty in the area of the elastic tail under the inelastic peak was therefore taken as ±15%.

Fig. 3.18 shows no evidence of peaks in the lineshape. Two standard deviations of the background in the region where the inelastic peaks would be gives an upper limit of 2% on the contribution of peaks in the lineshape to the measured excitation probability.

3.4.2 90° Data

Spectra of ^{24}Mg ions scattered from ^{208}Pb through 90° were collected simultaneously with the backscattering data. These spectra show a similar lineshape to the ^{12}C spectra of subsection 3.3.1, that is, the function of eq. 3.7 with the long range tail of eq. 3.9. However, these spectra have no shoulder on the high energy side of the peak. That this is so was confirmed by placing one of the 90° detectors at 30° and collecting spectra of 80 - 82 MeV ^{24}Mg ions scattered from the same ^{208}Pb targets that were used in collecting the higher energy data. Fig. 3.21 shows one of these spectra fitted with the lineshape referred to above and fig. 3.22 shows this lineshape

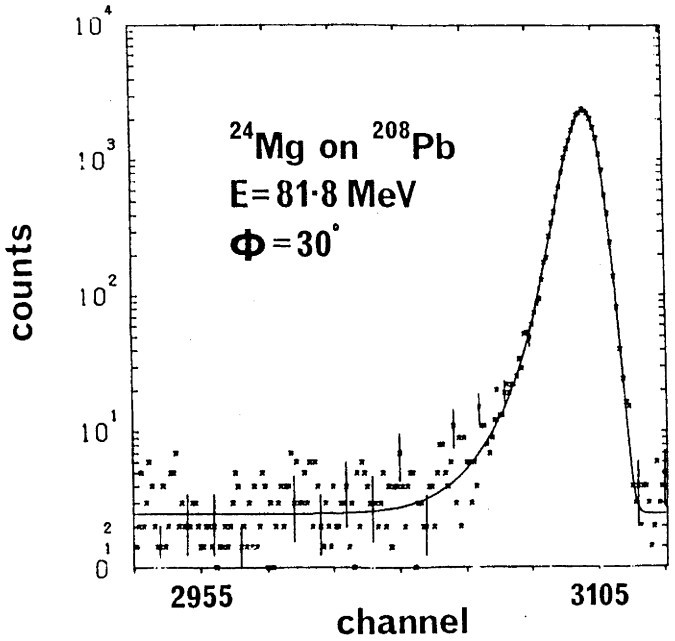

Fig. 3.21: A spectrum of 81.8 MeV ^{24}Mg ions scattered through 30° from ^{208}Pb. The full line shows the result of a fit to the data.

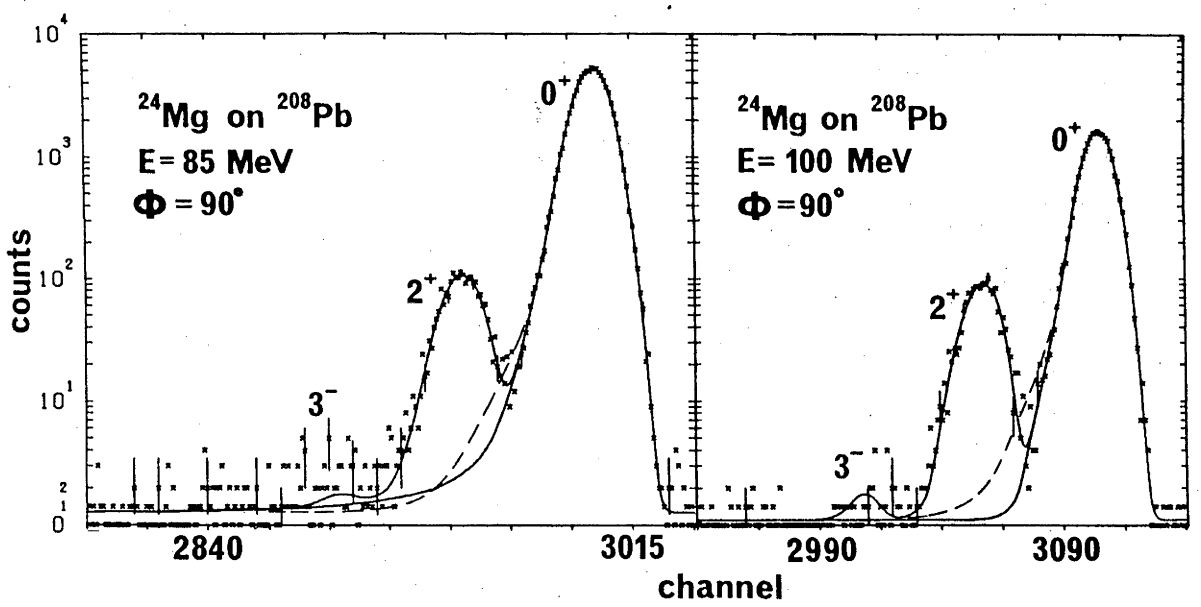

Fig. 3.22: Spectra of 85 MeV and 100 MeV ^{24}Mg ions scattered through 90° from ^{208}Pb. The peaks labelled 0^+ are due to elastic scattering, those labelled 2^+ to excitation of the 2^+_1 state of ^{24}Mg and those labelled 3^- to excitation of the 3^-_1 state of ^{208}Pb. The significance of the full and broken curves is explained in the text.

applied to two of the higher energy spectra (broken lines) as well as the fits obtained after adjustment of the lineshape parameters (full lines). In no case was the inferred value of the excitation

probability changed by more than 3% by the adjustment of the lineshape parameters. As in the case of the ^{24}Mg backscattered data, the ^{24}Mg inelastic peak is fitted by the sum of two lineshapes and a relative standard deviation of ±15% is attributed to the area of the elastic tail. Also, the position and magnitude of the ^{200}Pb inelastic peak were computed rather than being fitted.

The possibility of peaks in the lineshape can be investigated by inspection of the 30° spectra. The usual two standard deviations of the background again gives an upper limit of 2% on the contribution of such effects to the inferred excitation probabilities.

3.4.3 Checks for Contaminant Peaks

Elastic scattering from impurities in the target in the mass ranges A = 189 to A = 198 and A = 196 to A = 201 could contribute peaks to the spectrum for 90° and 172° scattering respectively. The possible presence of such impurities was investigated by examining a 55 MeV backscattering spectrum. This spectrum is shown in fig. 3.23, where the regions of interest are indicated. There is no evidence of peaks in these regions. Taking two standard deviations of the background, an upper limit of 0.2% can be placed on contributions to the inelastic peak from target impurities.

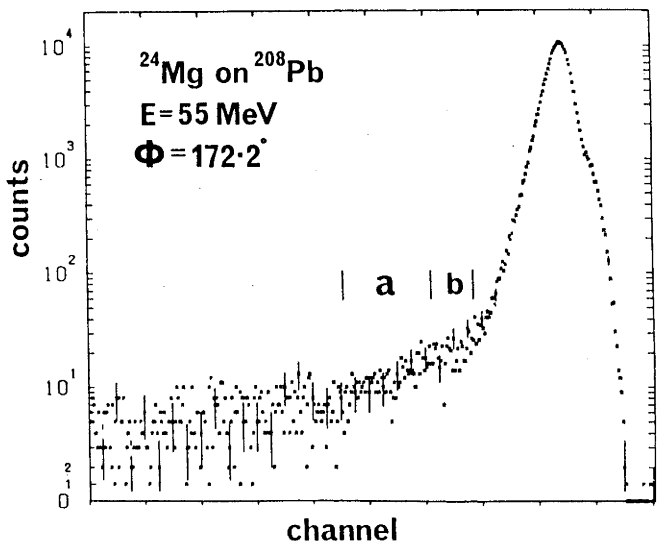

Fig. 3.23: A spectrum of 55 MeV ^{24}Mg ions backscattered from ^{208}Pb. The regions marked a and b indicate the regions where target contaminant peaks which would affect the 90° and backscattering data respectively would be.

The peak due to inelastic scattering from ^{208}Pb has obviously been taken into account in fitting the spectra shown above. The major isotopic contaminant in the target is ^{207}Pb which, with an isotopic concentration of 0.69% and a mass differing from that of ^{208}Pb by less than 0.5%, has a negligible effect.

The only single nucleon transfer reaction which is kinematically able to contribute to the region of the inelastic peak is the ^{208}Pb(^{24}Mg,^{25}Mg)^{207}Pb reaction. There is no evidence of peaks from this reaction elsewhere in any of the spectra collected. Fig. 3.24 shows a spectrum of 100 MeV backscattered ^{24}Mg ions and indicates the positions where the neutron pickup peaks would occur. Also shown in fig. 3.24 are the positions where peaks from the reaction ^{208}Pb(^{24}Mg,^{23}Na)^{209}Bi would come. The Q value of this reaction is such that the systematics of transfer reactions below the Coulomb barrier suggest that it should occur with an intensity similar to that of the neutron pickup reaction [Bu71]. If it is assumed that these intensities are in fact equal then an upper limit of 0.05% can be placed on the contribution of transfer reactions to the inferred excitation probability.

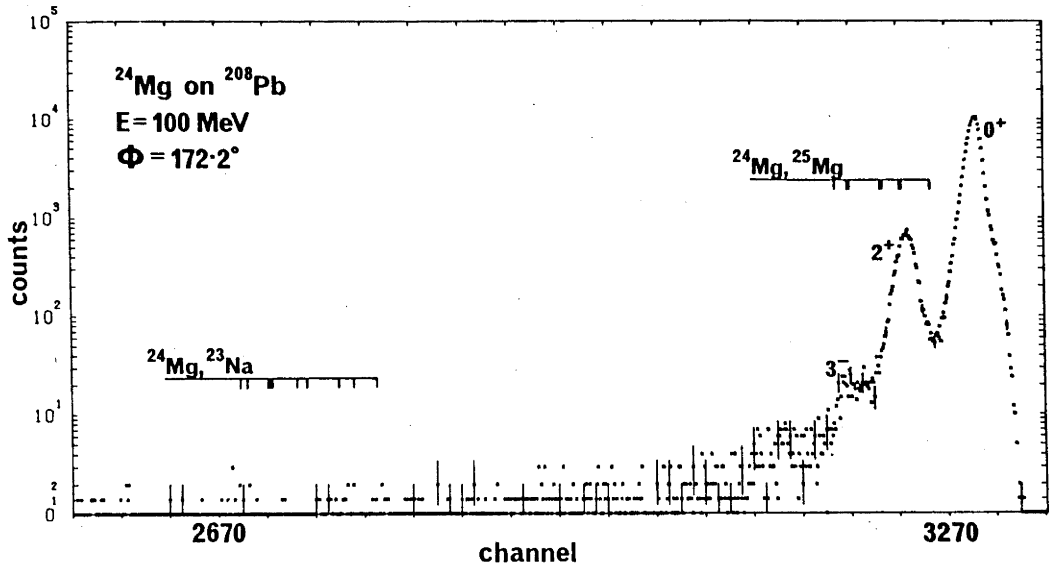

Fig. 3.24: A spectrum of 100 MeV ^{24}Mg ions backscattered from ^{208}Pb. The positions where peaks due to two transfer reactions would be are indicated. The significance of these two reactions is explained in the text.

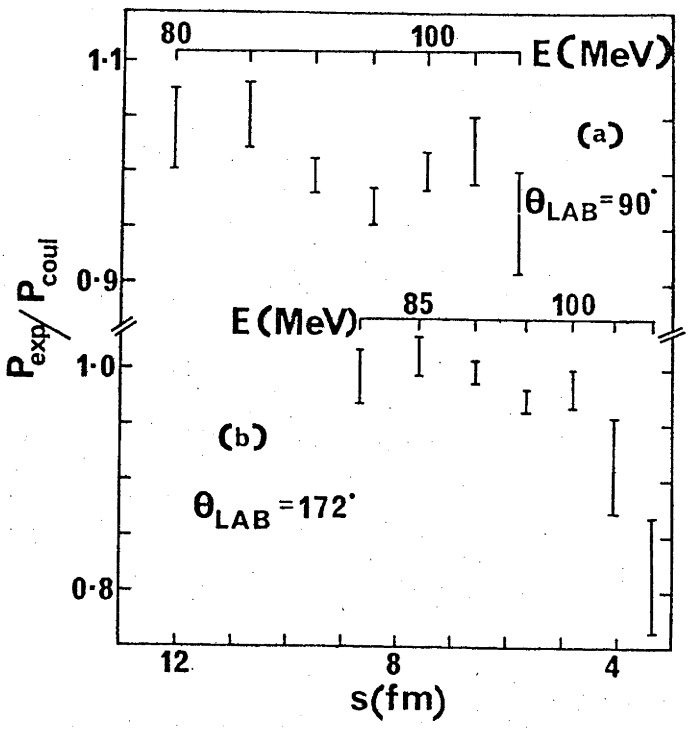

Fig. 3.25: The variation of the double ratio P_{exp}/P_{coul} with bombarding energy E and minimum separation s of the nuclear surfaces for the scattering of ^{24}Mg through (a) 90° and (b) 172° from ^{208}Pb.

3.4.4 Safe Bombarding Energies

Fig. 3.25 shows the energy dependence of the ratio P_{exp}/P_{coul} for ^{24}Mg. The matrix elements used to compute P_{coul} are given in subsection 4.3.1. There is no evidence that, at the bombarding energies used, the effect of the nuclear force on the 90° data is significant compared with the experimental errors. However, it would appear that this is not the case for the backscattering data at bombarding energies of 95 MeV and above. Therefore these data were not used in the determination of the quadrupole moment.

3.5 ^{18}O DATA

3.5.1 Backscattering and 90° Data

Spectra of ^{18}O projectiles scattered from ^{208}Pb targets were obtained at bombarding energies and scattering angles in the ranges E = 57 - 86 MeV, Φ = 172° - 175° and E = 59 - 86 MeV, Φ = 90°. Some of the backscattering data were taken simultaneously with the 90° data and some were taken separately so that the target could be placed

perpendicular to the beam. This always improved the peak-to-valley ratio.

The analysis of these data was more difficult than those of the other two experiments because the low excitation probability and relatively large recoil broadening in this experiment result in spectra with low peak-to-valley ratios. In addition, because of the relatively high excitation energy of the ^{18}O 2_1^+ state, the inelastic peak sits on a relatively flat part of the elastic tail so that, for a given peak-to-valley ratio, a relatively large fraction of the area under the inelastic peak is due to the elastic tail. For example, in a $^{198}Hg + ^{16}O$ spectrum with a peak-to-valley ratio of 6, the elastic tail accounts for $\sim$ 4% of the gross area of the inelastic peak; in an ^{18}O spectrum with the same peak-to-valley ratio, the corresponding figure is $\sim$ 20%. This means that the inferred excitation probabilities are correspondingly more sensitive to any systematic over- or under-estimation of the area of elastic tail underneath the inelastic peak. Evidence which suggests that a systematic over-estimation of the excitation probabilities may exist in the analysis of low energy 90° spectra will be presented in subsection 3.5.3. But first the fits to the experimental spectra and, in the next subsection, arguments against the existence of contaminant peaks will be presented.

Representative spectra are shown in fig. 3.26. The fits use a function consisting of a skewed Gaussian plus two exponential tails (eqs. 3.7 and 3.9). As in the case of ^{24}Mg, ±15% was found to be a reasonable estimate of the relative uncertainty in the area of the elastic tail underneath the ^{18}O inelastic peak provided that this area contained sufficient counts. In spectra such as that shown in fig. 3.26e, the statistical uncertainty in this area approached ±15%, requiring the relative uncertainty in the tail area to be increased. It was taken to be ±40% in the case of fig. 3.26e. As in the case of ^{24}Mg, the sum of two elastic peak lineshapes was used to fit the inelastic peak. Due to the greater recoil broadening in this case as compared to that of ^{24}Mg, the fitted lineshape often underestimated somewhat in the centre of the ^{18}O inelastic peak although the wings are well fitted. This is not a problem, since the gross area of the

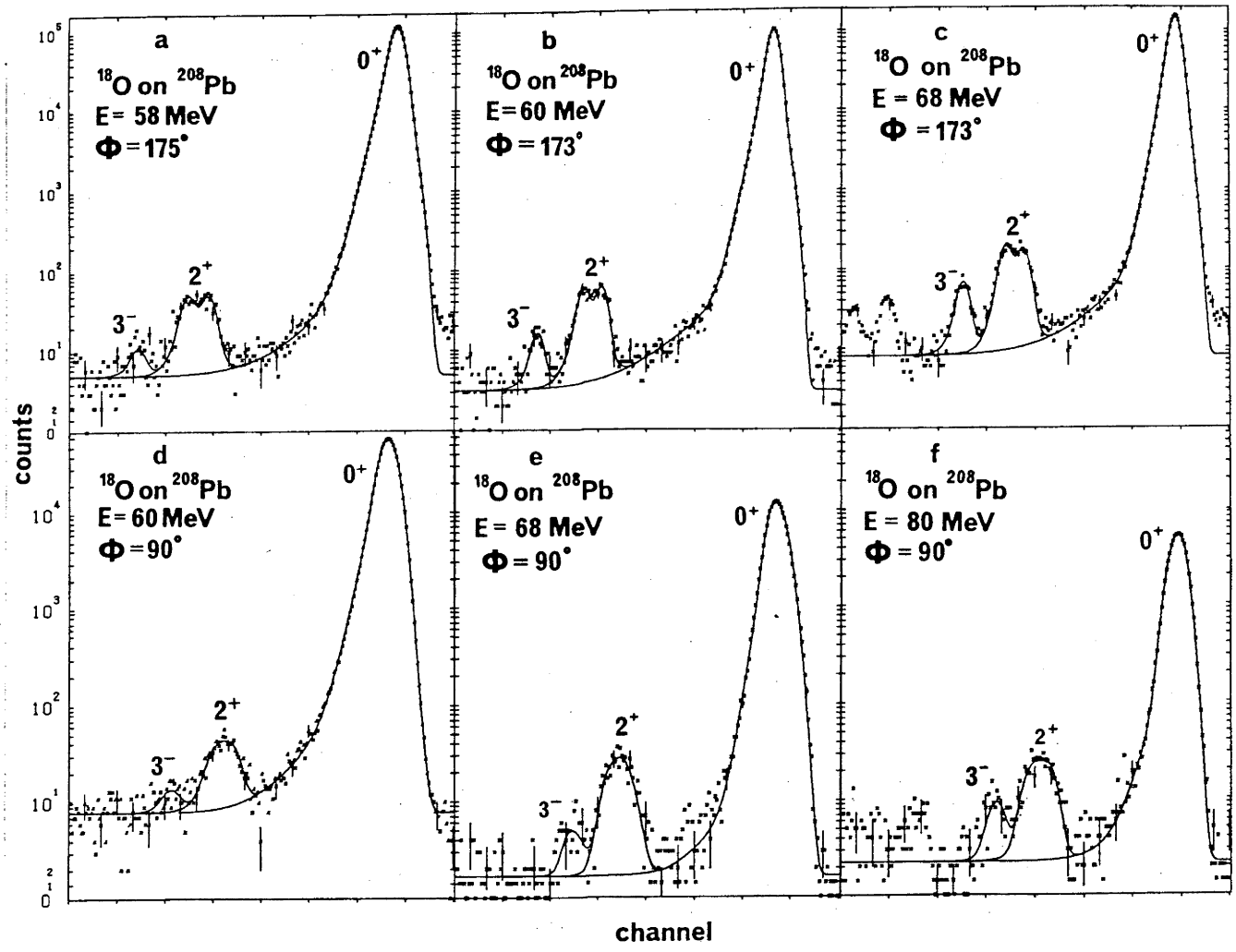

Fig. 3.26: Spectra of ^{18}O ions scattered from ^{208}Pb. The bombarding energies and scattering angles are indicated. The peaks labelled 0^+ are due to elastic scattering, those labelled 2^+ to excitation of the 2_1^+ state of ^{18}O and those labelled 3^- to excitation of the 3_1^- state of ^{208}Pb. The full lines show the results of fits to the data.

^{18}O inelastic peak was determined by summing the data. The only reason for fitting the inelastic peaks is to determine the region where the ^{18}O and ^{208}Pb inelastic peaks overlap. In this region, where the fit is good, the data were not summed, but the fit was used to estimate the magnitude of the ^{18}O inelastic tail underneath the ^{208}Pb inelastic peak. Having determined the gross area of the ^{18}O inelastic peak in this manner, the fit to the elastic peak was used to estimate the area of the elastic tail underneath the ^{18}O inelastic peak.

To verify the shape of the elastic tail where it lies underneath the inelastic peak, the same ^{208}Pb targets that were used in data collection were bombarded with ^{16}O projectiles. The lineshapes of the spectra of backscattered ions were then used to extract excitation probabilities from the ^{18}O spectra. Fig. 3.27 shows some of the results. The two ^{18}O spectra in figs. 3.27c and 3.27d are the same as in figs. 3.26b and 3.26d. The excitation probabilities obtained by this procedure were all within 2% of those obtained by allowing all lineshape parameters to vary. This is less than $\frac{3}{4}$ of the statistical uncertainty.

3.5.2 Checks for Contaminant Peaks

Target contaminants in the mass range A = 183 to A = 188 and A = 168 to A = 179 would place peaks from elastic scattering under the ^{18}O inelastic peak in the backscattering and 90° spectra respectively. The level of such impurities was determined by scattering 40 MeV ^{18}O ions from the same targets that were used to collect the higher energy data. Fig. 3.28 shows one of the backscattering spectra. Upper limits of 35 ppm and 20 ppm respectively, corresponding to two standard deviations of the background areas shown in fig. 3.28, can be placed on the concentration of impurities in the mass ranges given above. This leads to upper limits of 1.3% and 0.8% on contribution of target impurities to the excitation probabilities at 180° and 90° respectively.

As in the case of ^{24}Mg, the effect of the ^{207}Pb in the target is negligible.

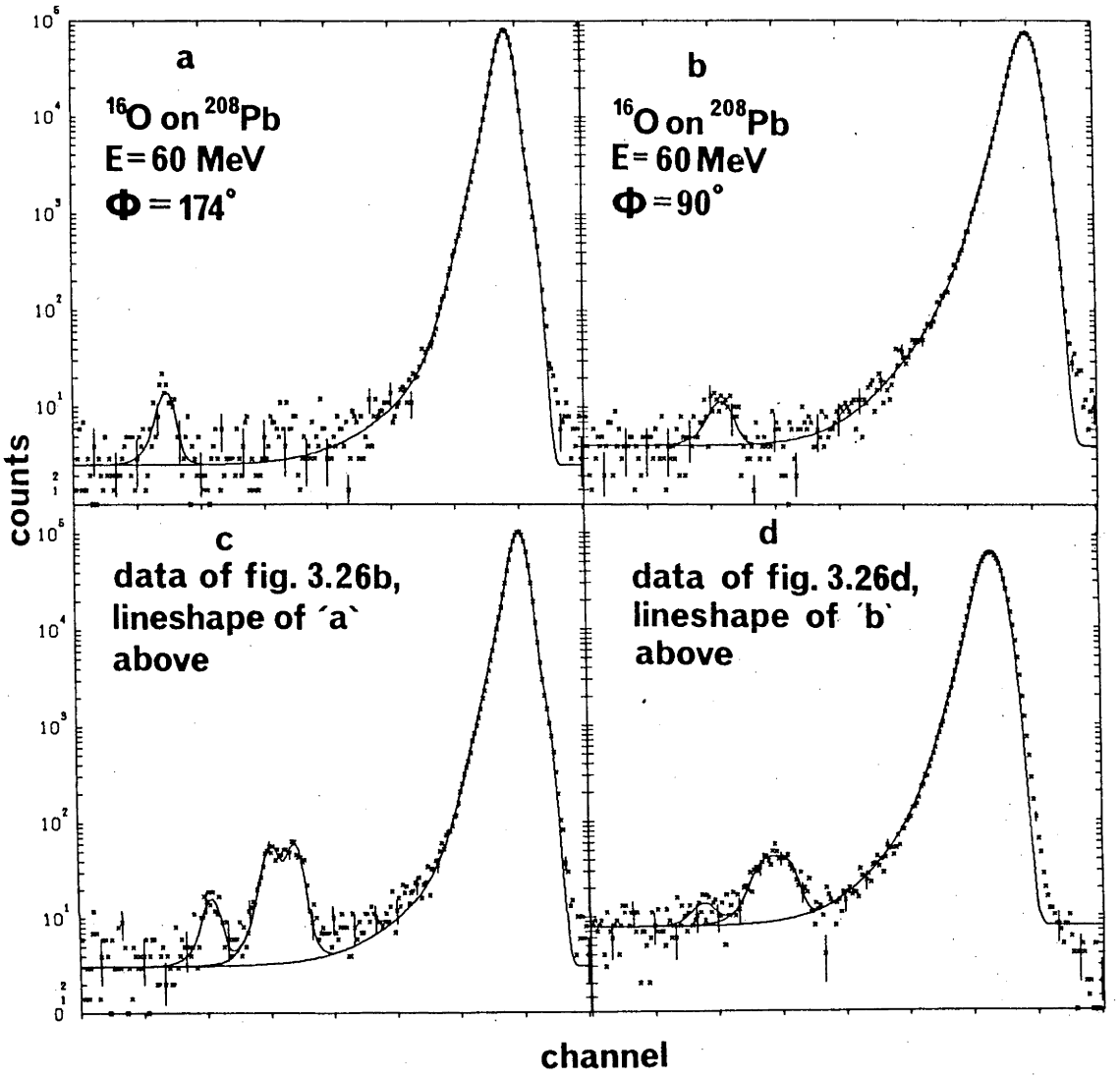

Fig. 3.27: Spectra of 60 MeV ^{16}O ions scattered through (a) 174° and (b) 90° from ^{208}Pb. Parts c and d show the results of fitting the data of figs. 3.26b and 3.26d respectively using lineshape parameters derived from the appropriate ^{16}O spectrum.

Peaks due to single neutron transfer reactions are clearly seen in both the backscattering and the 90° data at high bombarding energies (figs. 3.26c and 3.26f). However, the Q values of these reactions prevent them placing peaks in the region of the ^{18}O inelastic peak. No evidence for any other reactions, and, in particular, the ^{208}Pb(^{18}O,^{19}F)^{207}Tl reaction which could contribute peaks under the ^{18}O inelastic peak, is seen at any bombarding energy. In addition, the neutron transfer peaks become undetectable below

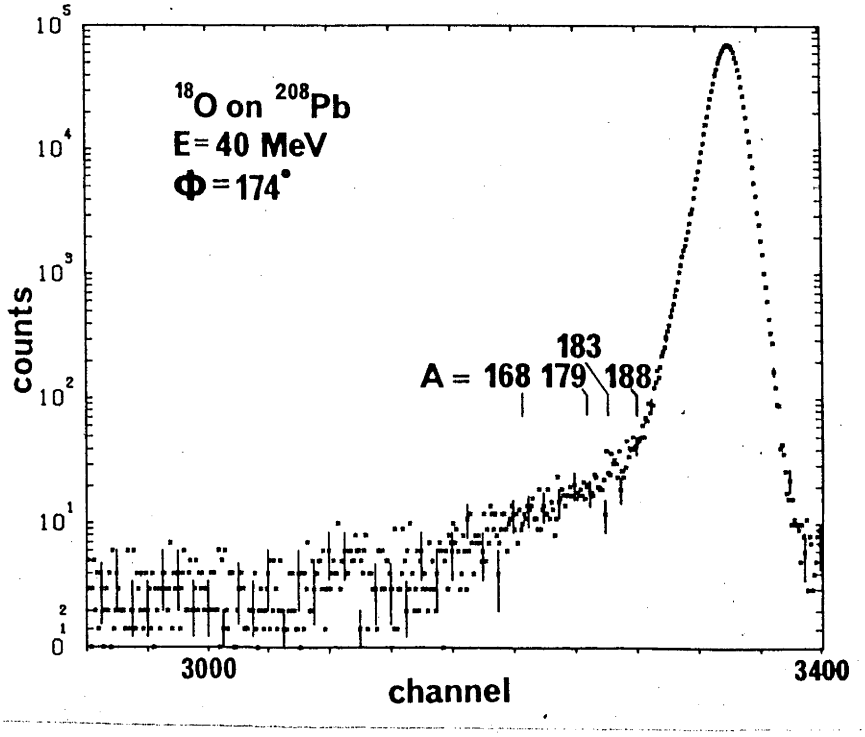

Fig. 3.28: A spectrum of 40 MeV ^{18}O ions backscattered from ^{208}Pb. The positions where peaks due to elastic scattering from target contaminants of mass 168, 179, 183 and 188 would come are shown.

bombarding energies of 76 MeV for the 90° data and 66 MeV for the backscattering data. The work of Buttle and Goldfarb [Bu71] suggests that the (^{18}O,^{19}F) reaction has a much lower cross section than the neutron transfer reactions, but if it is supposed that the intensities are the same, then an upper limit on the intensity of the proton transfer peaks in the low energy spectra can be obtained by taking two standard deviations of the background in the region where the neutron transfer peaks are expected. Considering only the backscattering spectra taken at 60 MeV and below, and 90° spectra taken at 72 MeV and below (the significance of these energies will become apparent in the next subsection), the upper limit obtained is 4% and 2% of the inelastic peak area for the 90° and backscattering data respectively.

The possibility of reactions between the scattered ^{18}O ions and the silicon in the detector has been raised many times [e.g. Vo77], and we felt that it was time to lay this bogey to rest. We followed a suggestion by LeVine [Le78] and placed an ORTEC "F" series detector in

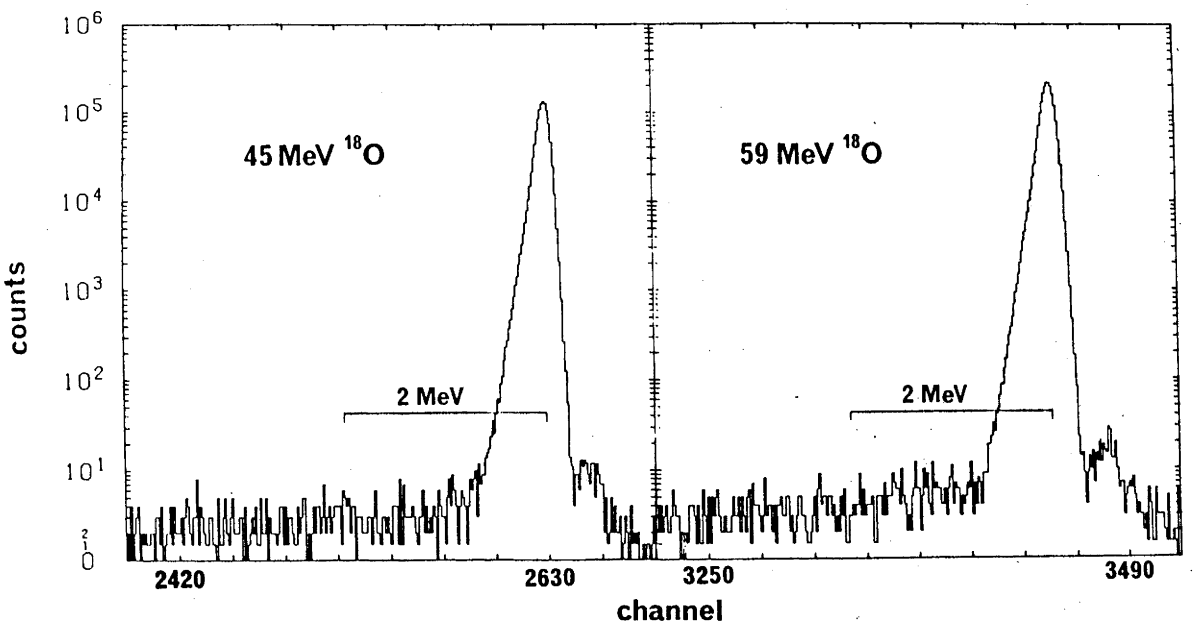

Fig. 3.29: The response of an ORTEC "F" series silicon surface-barrier detector to monoenergetic ^{18}O ions of the energies indicated. The origin of the small peak on the high energy side of the full-energy peak is not understood.

the focal plane of an ESP90 spectrometer in order to bombard it with a monoenergetic low-intensity beam of ^{18}O particles. The details of the arrangement have been given in subsection 3.2.5. Two spectra at different incident particle energies are shown in fig. 3.29. These two energies almost span the range of scattered energies obtained in the Coulomb excitation experiments. There is no evidence for reaction peaks 2 MeV below the full-energy peak; two standard deviations of the background in this region is < 15 ppm of the full-energy peak. There is a satellite peak at about 400 keV above the full-energy peak. Its area is ~ 90 ppm of the area of the full-energy peak and this fraction seems to be the same at all incident energies which suggests that it is not due to channelling. Also, it is too far above the main peak to be caused by a thin spot in the gold layer on the front of the detector. I have no other explanation for its presence, but its magnitude and position make it of no importance in this experiment.

3.5.3 Safe Bombarding Energies

Fig. 3.30 shows the variation of the ratio P_{exp}/P_{coul} with bombarding energy and minimum distance of closest approach s (eq. 3.11) for ^{18}O. It is clear that data with $s \gtrsim 6.2$ fm are negligibly influenced by the nuclear force. This separation corresponds to bombarding energies of 60 MeV for backscattering and 72 MeV for 90° scattering.

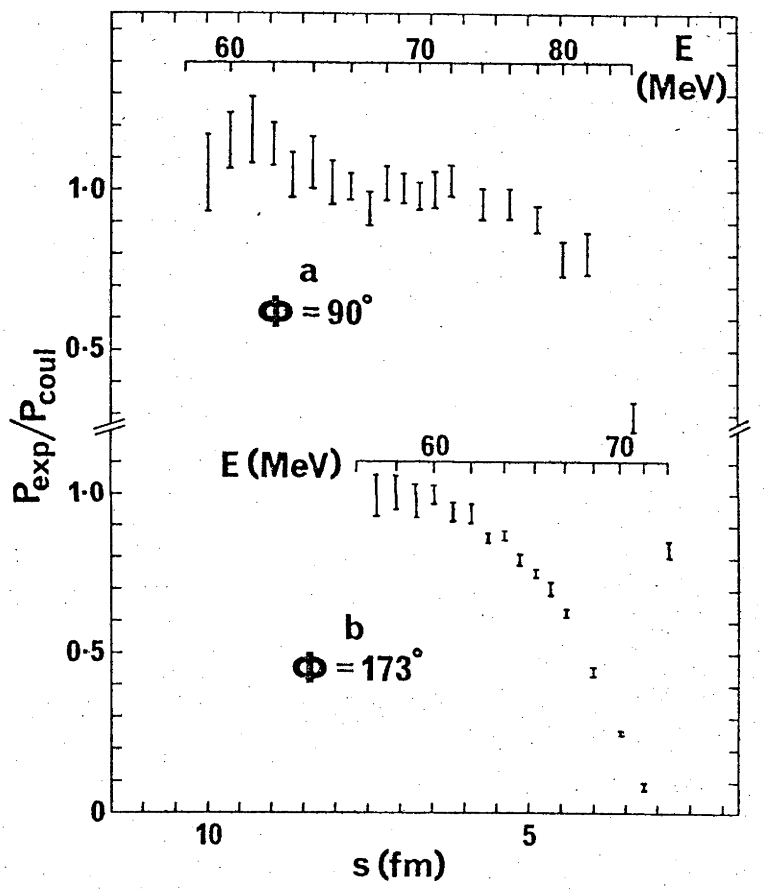

Fig. 3.30: The variation of the double ratio P_{exp}/P_{coul} with bombarding energy E and minimum separation s of the nuclear surfaces for the scattering of ^{18}O through (a) 90° and (b) 173° from ^{208}Pb.

The 90° data seem to show an unexpected rise below 65 MeV. The magnitude of this rise is greater than the upper limits placed on the contributions from contaminants and transfer reactions in the last subsection. However, between 65 MeV and 72 MeV the variation of P_{exp}

with energy is the same as that of P_{coul} suggesting that whatever is causing the problem below 65 MeV is negligible in this region. The data displayed in fig. 3.30a are quite reproducible. They were collected over a period of ~ 11 months in an almost random order of bombarding energies. Many different targets and four different detectors were used.

Because of the low excitation probabilities involved, it is almost impossible to pin down the cause or causes of this phenomenon. However, it may be noticed that the problem appears only in spectra with low peak-to-valley ratios. Also, the peak-to-valley ratio falls faster with decreasing bombarding energy than does the excitation probability, suggesting that the lineshape is worse in the data taken at lower energies. Because of the low peak-to-valley ratios, spectra taken below 65 MeV bombarding energy all have large elastic tails under the inelastic peak. The fraction of the gross area of the inelastic peak which is attributed to the elastic tail by the fitting procedure outlined above is 15-40% in the data taken below 65 MeV compared with 5-15% above. It is supposed therefore that our fitting procedure under-estimates the level of the elastic tail of the deteriorated lineshape which occurred in the low energy data. Consequently the analysis of the data below 65 MeV is considered to be unreliable.

There is no evidence in fig. 3.30b to suggest that the backscattering data suffer from the same problem as the 90° data. However, to be consistent, only those data obtained from spectra with peak-to-valley ratios greater than 7.5 are considered reliable. The figure 7.5 is greater than all of the peak-to-valley ratios of the 90° data below 65 MeV and less than all of those of the 90° data above 65 MeV. This removes the 57 MeV and 59 MeV data points from fig. 3.30b. It also disqualifies many of the backscattering spectra taken with the target at 45° to the beam direction. These last-named spectra have not been included in fig. 3.30b. Only two points, those at 58 MeV and 60 MeV, remain in the region below the Coulomb-nuclear interference anomaly in the backscattering data. It would clearly be pleasant to have more, but it would be very difficult, if not impossible, to obtain more with the current technique. It seems quite clear that

58 MeV and 60 MeV are safe energies for backscattering because they have the same values of P_{exp}/P_{coul} and because they have minimum distances of closest approach which are larger than that of the highest safe bombarding energy for 90° scattering.

3.6 SUMMARY OF EXPERIMENTAL RESULTS

3.6.1 Maximum Safe Bombarding Energies

A popular pursuit of writers of review articles on the reorientation effect has been the prediction of the maximum bombarding energy at which the effect of the nuclear force is negligible. This is almost invariably done by promulgating a minimum safe distance of closest approach and then using a formula similar to eq. 3.10 to connect this with a maximum safe energy. Over the years the suggested value of the minimum safe distance has steadily grown from 3 fm in 1968 [Bo68] to as much as 7.5 fm in 1977 [Cl77]. This indicates that the problem of unnoticed Coulomb-nuclear interference effects distorting the results of reorientation measurements has been widespread, and the number of instances recently brought to light (see for example section 5.1 and Jo77a) suggests that it remains so.

The data presented in previous sections highlight two separate problems in the determination of the maximum safe bombarding energy. The first is illustrated in fig. 3.31 which shows the Coulomb-nuclear interference curves for the systems $^{18}O^{*} - ^{208}Pb$, $^{16}O - ^{204}Pb^{*}$ and $^{16}O - ^{198}Hg^{*}$ where the asterisk indicates the excited nucleus. All of the data in fig. 3.31 are for backscattering. The data on $^{16}O - ^{204}Pb$ are from Jo77. These three systems have similar masses and charges so that, were there such a thing as a universal minimum safe distance, they should have similar maximum safe bombarding energies. A glance at fig. 3.31 shows that this is not so. The minimum safe distance of closest approach varies from 4.6 fm to 6.4 fm. It should be noted that the $^{18}O - ^{208}Pb$ data are not strictly comparable with the other two since the uncertainties in the ^{18}O data points are $\sim \pm 3\%$, while they are less than 1% for the target excitation data. It is clear that, should the measurements on ^{18}O be refined to the 1% level, then

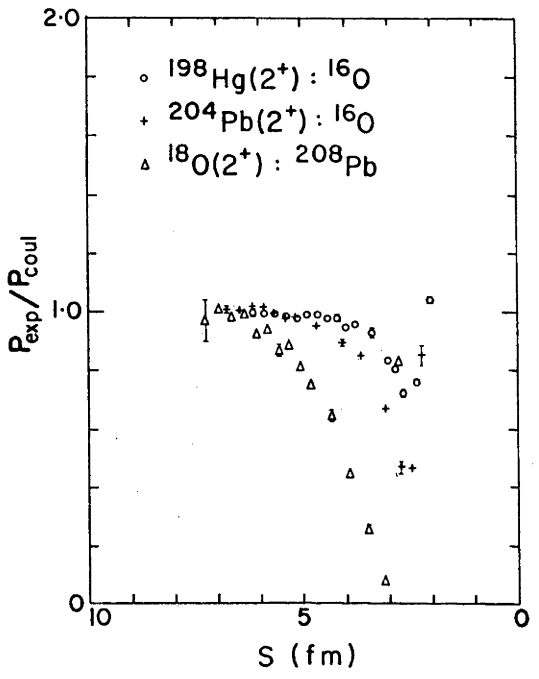

Fig. 3.31: A comparison of the size and position of the Coulomb-nuclear interference anomalies in the back-scattering of ^{16}O from $^{198}Hg^*$, ^{16}O from $^{204}Pb^*$ and $^{18}O^*$ from ^{208}Pb, the asterisk indicating the nucleus which is excited in each case.

the minimum safe distance would be even greater. This dependence of what is or is not "safe" on the accuracy of the data appears to have been largely overlooked in the literature, but may be part of the cause of the increase in the predicted safe distances over the years.

The second problem concerns the variation of the maximum safe bombarding energy with scattering angle. There seem to be few experimental data on this point. Some workers [e.g. Vo77] have implicitly assumed that the maximum safe energy is the same for all angles, but it is more usual to assume that it has a $1 + \mathrm{cosec}(\theta/2)$ dependence as given by eq. 3.10. Both the ^{24}Mg data (fig. 3.25) and the ^{18}O data (fig. 3.30) are consistent with this second assumption. However, in view of the problem which Coulomb-nuclear interference has caused in the past, one should be very careful about assumptions of its energy or angle dependence. For example, it should not be taken for granted that the $1 + \mathrm{cosec}(\theta/2)$ dependence of the maximum safe energy holds for forward scattering angles.

It may be reasonably argued that a bombarding energy which is safe for 180° scattering will be safe for all other scattering angles. So instead of going to the trouble of measuring the excitation

probability at a number of energies, one could choose a minimum distance of closest approach greater than ~ 6.5 fm for one's backscattering experiments, and collect forward angle data at bombarding energies which are no greater than those used for backscattering. Such a regimen would most likely ensure that the data are free from nuclear effects, but there are two problems. Firstly, the range of minimum safe distances in fig. 3.31 is so large that there would always be the worry that 6.5 fm was not large enough for the system under consideration. Secondly, and just as importantly, one is forgoing the opportunity of obtaining the best data, which are those at the maximum safe bombarding energy where peak-to-valley ratios are largest.

The conclusion is that there is currently no substitute for an experimental determination of the maximum safe bombarding energy and that, to obtain the best quality data, this determination should be carried out for every scattering angle used.

3.6.2 Tabulation of Measured Excitation Probabilities

For reference, all of the excitation probabilities measured in this work are collected into this section. Tables 3.2 to 3.4 present the excitation probabilities of the first excited states of ^{198}Hg, ^{24}Mg and ^{18}O respectively under the conditions indicated. Each table is divided by a horizontal line. Data above the line are negligibly influenced by nuclear effects and are used in the determination of the respective quadrupole moments. The italicized numbers in table 3.4 are unreliable (see subsection 3.5.3).

Table 3.2

Experimental values of the probability of exciting ^{198}Hg to its first excited state by the backscattering of

(a) ^{16}O

E (MeV)	$10^3 P_{exp}$
60	135.9 ± 1.6
61	143.4 ± 2.0
62	151.8 ± 1.4
63	158.1 ± 2.0
64	165.6 ± 1.9
65	176.5 ± 1.5
66	186.0 ± 2.2
67	192.4 ± 1.9
68	202.5 ± 2.7
69	204.5 ± 1.4
70	216.6 ± 2.6
72	227.4 ± 3.2
74	221.3 ± 3.6
75	221.8 ± 2.7
76	206.5 ± 3.3
78	233.7 ± 3.4
80	343.3 ± 3.4

(b) ^{12}C

E (MeV)	$10^3 P_{exp}$
43	71.4 ± 0.8
44	78.6 ± 0.7
45	85.0 ± 0.8
46	91.0 ± 1.3
47	98.1 ± 1.0
48	105.5 ± 0.9
50	121.4 ± 1.7
52	132.9 ± 1.8
54	147.0 ± 1.9

(c) ^{4}He

E (MeV)	$10^3 P_{exp}$
14.1	8.58 ± 0.07
15.0	11.06 ± 0.09
15.8	13.03 ± 0.11
16.0	13.92 ± 0.12
16.5	15.44 ± 0.11
17.0	16.82 ± 0.11
17.5	18.36 ± 0.15
18.0	19.35 ± 0.29

Table 3.3

Experimental values of the probability of exciting ^{24}Mg to its first excited state by scattering from ^{208}Pb through

(a) 90°

E (MeV)	$10^3 P_{exp}$
80	13.6 ± 0.6
85	22.0 ± 0.6
90	31.3 ± 0.7
95	43.6 ± 1.0
100	61.4 ± 1.1
105	82.5 ± 2.4
110	98.9 ± 4.7

(b) 172°

E (MeV)	$10^3 P_{exp}$
80	15.7 ± 0.4
85	25.7 ± 0.4
90	38.5 ± 0.4
95	53.4 ± 0.6
100	73.5 ± 1.4
105	89.4 ± 4.3
110	100.8 ± 6.4

Table 3.4

Experimental values of the probability of exciting ^{18}O to its first excited state by scattering from ^{208}Pb through

(a) 90°

E (MeV)	$10^3 P_{exp}$
59	*0.71 ± 0.08*
60	*0.93 ± 0.07*
61	*1.13 ± 0.10*
62	*1.28 ± 0.07*
63	*1.37 ± 0.09*
64	*1.64 ± 0.12*
65	1.79 ± 0.12
66	2.03 ± 0.08
67	2.16 ± 0.12
68	2.67 ± 0.14
69	2.97 ± 0.15
70	3.26 ± 0.14
71	3.74 ± 0.22
72	4.30 ± 0.21
74	4.95 ± 0.25
76	6.04 ± 0.30
78	6.90 ± 0.33
80	7.11 ± 0.50
82	8.57 ± 0.72
86	4.23 ± 0.69

(b) 173°

E (MeV)	$10^3 P_{exp}$
57	*0.629 ± 0.042*
58	0.774 ± 0.042
59	*0.913 ± 0.049*
60	1.117 ± 0.032
61	1.261 ± 0.030
62	1.493 ± 0.047
63	1.608 ± 0.029
64	1.883 ± 0.038
65	1.997 ± 0.045
66	2.200 ± 0.040
67	2.355 ± 0.069
68	2.422 ± 0.049
70	2.278 ± 0.068
72	1.599 ± 0.056
74	0.70 ± 0.09
76	8.03 ± 0.26
80	103.5 ± 3.0

Chapter 4

EXTRACTION OF QUADRUPOLE MOMENTS

The relationship between the excitation probability and the nuclear properties $B(E2;0^+ \to 2^+)$ and Q_{2^+} is given by equation 2.50. It is clear that, insofar as second order perturbation theory is a reasonable approximation, a graph of P_{exp}/F versus ρ will be linear with the intercept at $\rho = 0$ equalling $B(E2;0^+ \to 2^+)$ and the slope equalling the product of $B(E2;0^+ \to 2^+)$ and Q_{2^+}. Because the slope and intercept are not independent, the standard least-squares fitting equations require some modification. This is considered in the first section of this chapter.

The remainder of this chapter examines the magnitudes of the various effects considered in chapter 2 on the parameters F and ρ. The basis of this calculation is the modified de Boer-Winther computer program [Wi65] which integrates a symmetrized version of eq. 2.25. The input to this computer program includes all of the matrix elements between the nuclear states considered. This means that guesses of the true values of B(E2) and Q_{2^+} were used to determine F and ρ. Because eq. 2.50 is strictly correct to second order only, the values of F and ρ obtained by this procedure are weakly dependent on B(E2) and Q_{2^+}. If then, the guesses of B(E2) and Q_{2^+} differed significantly from the values extracted from the P_{exp}/F versus ρ plot, the procedure was repeated until consistency was obtained.

4.1 LEAST-SQUARES EQUATIONS

In the standard linear least-squares problem one seeks to minimize the quantity

$$\chi^2 := \sum_i (y_i - mx_i - c)^2/\sigma_i^2 , \qquad (4.1)$$

where the y_i have uncertainties σ_i and m and c are the slope and intercept respectively of the linear relationship between y_i and x_i. The x_i are assumed to have negligible uncertainty. By differentiating

χ^2 with respect to m and c, one finds that the minimum value of χ^2 is given by the following values of m and c:

$$m = \frac{jt - ks}{j\ell - k^2}, \tag{4.2}$$

$$c = \frac{\ell s - kt}{j\ell - k^2}, \tag{4.3}$$

where

$$j := \sum_i \sigma_i^{-2}, \quad k = \sum_i x_i \sigma_i^{-2}, \quad \ell = \sum_i x_i^2 \sigma_i^{-2},$$

$$s = \sum_i y_i \sigma_i^{-2}, \quad t = \sum_i x_i y_i \sigma_i^{-2}. \tag{4.4}$$

The uncertainties in m and c are given by [Be69]

$$(\Delta m)^2 = \sum_i \sigma_i^2 \left(\frac{\partial m}{\partial y_i}\right)^2, \quad (\Delta c)^2 = \sum_i \sigma_i^2 \left(\frac{\partial c}{\partial y_i}\right)^2. \tag{4.5}$$

Using eqs. 4.2 and 4.3, one finds that

$$(\Delta m)^2 = \frac{j}{j\ell - k^2}, \quad (\Delta c)^2 = \frac{\ell}{j\ell - k^2}. \tag{4.6}$$

If one identifies y_i with P_{exp}/F and x_i with ρ then one might conclude that

$$Q_{2+} = m/c$$

$$= \frac{jt - ks}{\ell s - kt} \tag{4.7}$$

and

$$(\Delta Q_{2+})^2 = \left(\frac{\Delta m}{c}\right)^2 + \left(\frac{m\Delta c}{c^2}\right)^2$$

$$= \frac{j\ell - k^2}{(\ell s - kt)^4} [j(\ell s - kt)^2 + \ell(jt - ks)^2]. \tag{4.8}$$

However, this neglects the interdependence of the slope and intercept. The correct approach is to rewrite eq. 4.1 as

$$\chi^2 := \sum_i [y_i - B(E2)\ Q_{2+} x_i - B(E2)]^2/\sigma_i^2 \tag{4.9}$$

and to differentiate χ^2 with respect to B(E2) and Q_{2^+}. This gives the equations

$$k\,B(E2) + \ell\,B(E2)\,Q_{2^+} = t$$

$$j\,B(E2) + 2k\,B(E2)\,Q_{2^+} + \ell\,B(E2)\,Q_{2^+}^2 = s + t\,Q_{2^+} \qquad (4.10)$$

which can be readily solved to show that the B(E2) is given by eq. 4.3 and that eq. 4.7 is correct. The uncertainties are given, analogously to eq. 4.5, by

$$[\Delta B(E2)]^2 = \sum_i \sigma_i^2 \left(\frac{\partial B(E2)}{\partial y_i}\right)^2 , \qquad (\Delta Q_{2^+})^2 = \sum_i \sigma_i^2 \left(\frac{\partial Q_{2^+}}{\partial y_i}\right)^2 . \qquad (4.11)$$

Using eqs. 4.3 and 4.7, one finds that $\Delta B(E2) = \Delta c$ but that

$$(\Delta Q_{2^+})^2 = \frac{j\ell - k^2}{(kt - \ell s)^4}\,[j(\ell s - kt)^2 + \ell(jt - ks)^2 + 2k(\ell s - kt)(jt - ks)] . \qquad (4.12)$$

The last term in eq. 4.12 accounts for the correlation between slope and intercept. For all cases considered below, eq. 4.12 differs from eq. 4.8 by $\sim 5\%$.

4.2 ^{198}Hg

4.2.1 Higher State Matrix Elements

A diagram of the low lying energy levels of ^{198}Hg is shown in fig. 4.1. Only the first three excited states were included in the calculations. The only previous information on the B(E2) values connecting the higher states is the ratio [Be73a]

$$\frac{B(E2;2_2^+ \to 0_1^+)}{B(E2;2_2^+ \to 2_1^+)} = 0.048 \pm 0.013 . \qquad (4.13)$$

To determine the value of these matrix elements, a spectrum of back-scattered 17.0 MeV ^{4}He ions was fitted, and the excitation probabilities of the 2_2^+ and 4_1^+ states determined. Fig. 4.2 shows this

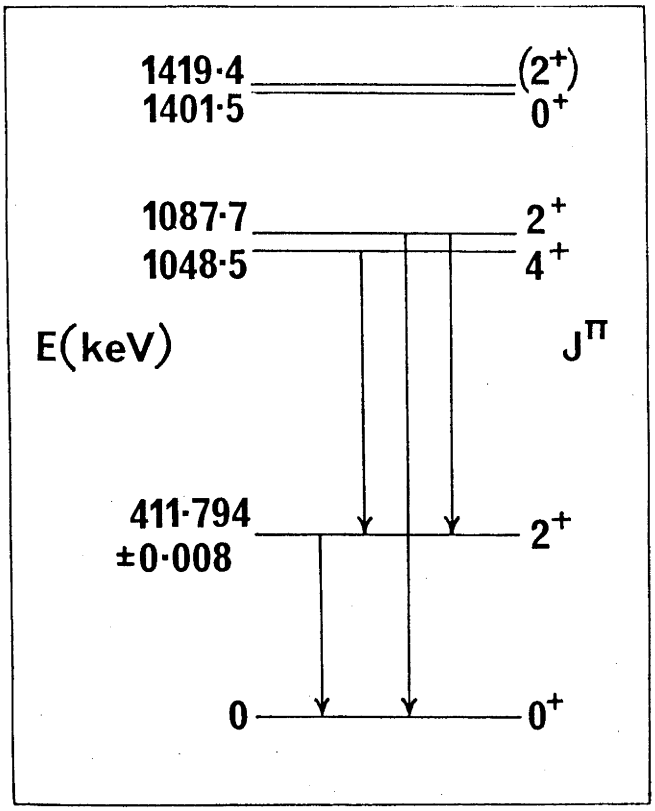

Fig. 4.1: The low-lying energy levels of ^{198}Hg. Data are from the compilation of Harmatz [Ha77a].

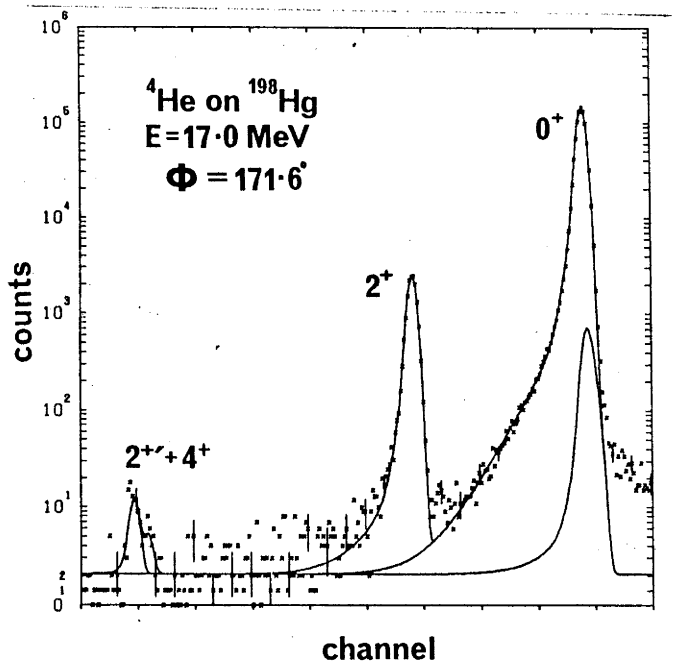

Fig. 4.2: A spectrum of 17.0 MeV ^{4}He ions back-scattered from ^{198}Hg. The peaks are labelled according to the angular momentum of the final state of ^{198}Hg. The full line shows the results of a fit to the spectrum.

spectrum. The shape of the 2_2^+ and 4_1^+ peaks was assumed to be the same as that of the 2_1^+ and 0^+ peaks. These results, together with eq. 4.13, imply $B(E2;0_1^+ \rightarrow 2_2^+) = 90 \pm 23$ e^2 fm^4 and $B(E2;2_1^+ \rightarrow 2_2^+) = 370 \pm 140$ e^2 fm^4.

An attempt was made to determine $B(E2;2_1^+ \rightarrow 4_1^+)$ and $B(E4;0_1^+ \rightarrow 4_1^+)$ by using the excitation probability determined above for the 4_1^+ state and the probability of exciting the same state by ^{12}C and ^{16}O scattering. This may be done in principle as the two-step excitation of the 4_1^+ state via the 2_1^+ state is less probable than direct E4 excitation in ^4He scattering, but much more probable in heavy-ion scattering. Because the peaks due to the excitation of the 2_2^+ and 4_1^+ states are unresolved in the heavy ion data (see figs. 3.8 and 3.11), the excitation probability of the 2_2^+ state was calculated using the B(E2) values quoted above. Fig. 4.3 shows the loci of values of $\langle 2_1^+ \| M(E2) \| 4_1^+ \rangle$ and $\langle 0_1^+ \| M(E4) \| 4_1^+ \rangle$ which are consistent with the ^4He, ^{12}C and ^{16}O data. From this, the value $|\langle 2_1^+ \| M(E2) \| 4_1^+ \rangle| = 150 \pm 30$ e fm^2, corresponding to $B(E2;2_1^+ \rightarrow 4_1^+) = 4500 \pm 1800$ e^2 fm^4, was adopted. Also, the value of $B(E4;0_1^+ \rightarrow 4_1^+)$ was taken to be less than 10^6 e^2 fm^8. It should be noted that this analysis assumes that $\langle 2_2^+ \| M(E2) \| 4_1^+ \rangle = 0$.

With no corrections other than for the effects of higher states and the use of the symmetrized theory (subsection 2.3.1), the values

$$\left.\begin{aligned} B(E2;0^+ \rightarrow 2^+) &= 9876 \pm 71 \text{ e}^2 \text{ fm}^4 \\ Q_{2^+} &= 73 \pm 12 \text{ e fm}^2 \end{aligned}\right\} p_4 < 0$$

and (4.14)

$$\left.\begin{aligned} B(E2;0^+ \rightarrow 2^+) &= 9883 \pm 71 \text{ e}^2 \text{ fm}^4 \\ Q_{2^+} &= 57 \pm 12 \text{ e fm}^2 \end{aligned}\right\} p_4 > 0$$

were obtained. In eq. 4.14, p_4 is the product of matrix elements given given by eq. 1.50. Its sign has not been experimentally determined, but most collective models predict it to be negative (section 1.2). The various contributions to the uncertainties in eq. 4.14 are shown in table 4.1. The uncertainty due to the uncertainty in the value of $B(E4;0_1^+ \rightarrow 4_1^+)$ has not been added to the other uncertainties as it is not independent of the uncertainty in $B(E2;2_1^+ \rightarrow 4_1^+)$. With the presently available information, the degree of dependence between these two uncertainties is not clear.

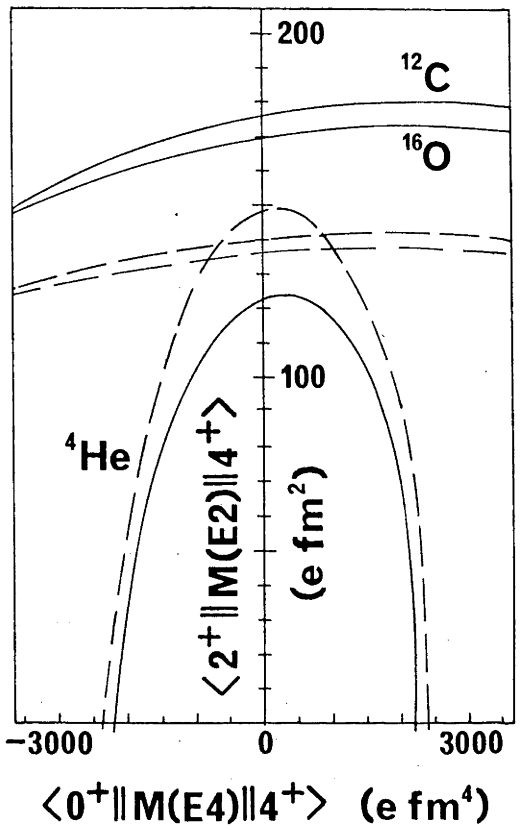

Fig. 4.3: Loci of values of the matrix elements $\langle 2^+ \| M(E2) \| 4^+ \rangle$ and $\langle 0^+ \| M(E4) \| 4^+ \rangle$ which are consistent with ^{4}He, ^{12}C and ^{16}O data. The broken lines show the magnitude of the statistical uncertainties.

Table 4.1

Sources of uncertainty in the analysis of the data on ^{198}Hg

Source of Uncertainty	$\Delta B(E2; 0^+ \to 2^+)$ (e^2 fm^4)	ΔQ_{2^+} (e fm^2)
Statistics	58	9
Beam energy	39	2
Scattering angle	0	0
Excitation energy	0	0
$\langle 2_2^+ \| M(E2) \| 0_1^+ \rangle$ $\langle 2_2^+ \| M(E2) \| 2_1^+ \rangle$	0	3
$\langle 2_1^+ \| M(E2) \| 4_1^+ \rangle$	11	7
Total	71	12
$\langle 0_1^+ \| M(E4) \| 4_1^+ \rangle$	0	8

4.2.2 Other Corrections

The other effects considered in chapter 2 affect the inferred values of Q_{2^+} and $B(E2;0^+ \to 2^+)$ to the extent shown in table 4.2. Each of these corrections is discussed below.

Table 4.2

Corrections to the ^{198}Hg analysis

Reason for Correction	Magnitude of Correction†	Change to $B(E2;0^+ \to 2^+)$ (e^2 fm^4)	Change to Q_{2^+} (e fm^2)
μ_{2^+}	1.1 μ_N/c‡	0	0
H_{2^+}	$\lvert H_{2^+}\rvert < 190$ e fm^4	0	±4
gdr	k = 1	0	10 ± 17
Structure of projectiles		0	0
Deviations from Coulomb potential and target thickness	$\frac{\Delta E}{E} \sim 10^{-4}$	8	0
Residual quantal correction	$\eta >$ 12 for ^{4}He, 38 for ^{12}C, 49 for ^{16}O	-32	-1
Special relativity	u/c < 9.5%	-153 ± 153	11 ± 11
Total		-177 ± 153	21 ± 20

† See text for discussion.

‡ Ha77a.

The magnetic dipole moment has no effect because the scattering angles used are close to 180°.

The value of H_{2^+} is not known. The upper limit shown in column 2 of table 4.2 was obtained by using eq. 1.24, the E4 analogue of eq. 1.61 and the upper limit on $B(E4;0^+ \to 4^+)$ obtained in the previous subsection.

The correction for the effect of the giant dipole resonance uses the Winther estimate of $S^{(11)2}_{0^+2^+}$ with the Levinger estimate of σ_{-2} (see

subsection 2.2.3). The uncertainty shown is due to the uncertainty ascribed in subsection 2.2.3 to the estimate of the parameter η_0.

The excited states of all three projectiles are at too high an excitation energy for them to have any noticeable effect on the excitation probability of the target.

The corrections for deviations from the Coulomb potential were made according to the prescription of section 2.4, those for residual quantal effects according to subsection 2.3.2 and those for the effects of special relativity according to section 2.6. In making these corrections, values of $\Delta E/E$, η and u/c were computed for each bombarding energy; representative magnitudes only are shown in table 4.2. The correction ΔE to the bombarding energy includes a correction for the energy lost in the target and in the carbon covering on the front of the target (subsection 3.2.4).

The adopted values of Q_{2^+} and $B(E2;0^+ \rightarrow 2^+)$ are therefore[†]

$$\left.\begin{aligned} B(E2;0^+ \rightarrow 2^+) &= 9700 \pm 170 \ e^2 \ fm^4 \\ Q_{2^+} &= \quad 94 \pm 24 \ e \ fm^2 \end{aligned}\right\} p_4 < 0$$

and (4.15)

$$\left.\begin{aligned} B(E2;0^+ \rightarrow 2^+) &= 9730 \pm 170 \ e^2 \ fm^4 \\ Q_{2^+} &= \quad 78 \pm 24 \ e \ fm^2 \end{aligned}\right\} p_4 > 0 \ .$$

Fig. 4.4 shows a plot of P_{exp}/F versus ρ for the case of destructive interference ($p_4 < 0$). This shows the degree of consistency between the three sets of data.

[†] It may be noted that the result differs from that given by Esat *et al.* [Es77a]. This is because the analysis in ref. Es77a omitted the effects of uncertainties in the beam energy and the gdr correction, and the corrections for H_{2^+} and relativistic effects.

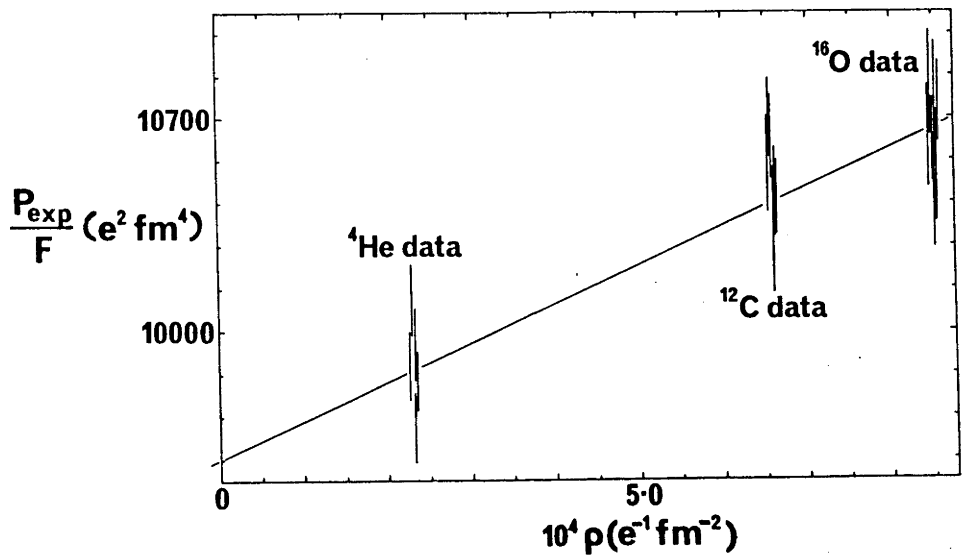

Fig. 4.4: The variation of P_{exp}/F with the sensitivity parameter ρ for ^{198}Hg.

4.3 ^{24}Mg

4.3.1 Higher State Matrix Elements

The lower part of the level scheme of ^{24}Mg is shown in fig. 4.5. Only the first three excited states were included in the analysis. The lifetimes of the pair of states near 4 MeV excitation energy have been measured a number of times, and the results show a scatter which is much larger than the uncertainties attached to them. The work up until 1973 is summarized by Endt and van der Leun [En73]. Since that review article, the lifetimes of these two states have been remeasured [Le73] with results similar to those adopted in ref. En73. I have adopted the arithmetic mean of these two sets of results with the uncertainties of ref. En73.

There is a much better agreement between the various measurements of the branching ratios of the levels concerned. The values in fig. 4.5 are weighted means of results quoted in refs. En73, Le73 and Br73. Finally, the mixing ratio of the $2_2^+ \rightarrow 2_1^+$ decay is from ref. En73. A recent measurement [Ki77] is in agreement with this, but has much larger errors.

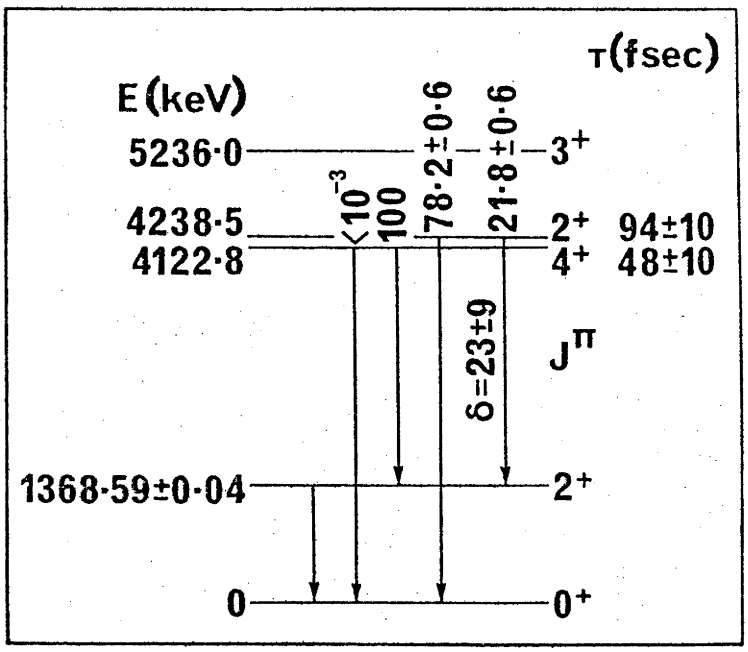

Fig. 4.5: The low lying energy levels of ^{24}Mg. The sources of the data are discussed in the text.

The data of fig. 4.5, together with the assumption that $\delta = 0$ for the $4_1^+ \to 2_1^+$ decay, give the reduced matrix elements shown in table 4.3. Although there are two interference terms, one involving $\langle 2_1^+ \| M(E2) \| 2_2^+ \rangle$ and the other $\langle 2_1^+ \| M(M1) \| 2_2^+ \rangle$, there is only one undetermined sign as the sign of the mixing ratio is the relative sign of these two matrix elements. This is indicated in table 4.3. In the following, p_4 remains as defined by eq. 1.50. Using these matrix elements, but taking $\langle 4_1^+ \| M(E4) \| 0_1^+ \rangle = 0$, one obtains

$$\left.\begin{aligned} B(E2;0^+ \to 2^+) &= 420 \pm 19 \ e^2 \ fm^4 \\ Q_{2^+} &= -18.8 \pm 1.3 \ e \ fm^2 \end{aligned}\right\} p_4 < 0$$

and (4.16)

$$\left.\begin{aligned} B(E2;0^+ \to 2^+) &= 422 \pm 19 \ e^2 \ fm^4 \\ Q_{2^+} &= -18.4 \pm 1.3 \ e \ fm^2 \end{aligned}\right\} p_4 > 0 \ .$$

It is seen that interference from higher states is negligible. This is mainly due to the large energy gap between the first and second excited states. The sources of the uncertainties in eq. 4.16 are shown in table 4.4.

The difficulty involving E4 transition moments, alluded to in

Table 4.3

Electromagnetic reduced matrix elements in ^{24}Mg

$\lvert\langle 4_1^+ \lVert M(E4) \rVert 0_1^+ \rangle\rvert$	<	6300	e fm^4
$\lvert\langle 4_1^+ \lVert M(E2) \rVert 2_1^+ \rangle\rvert$	=	31.1 ± 3.3	e fm^2
$\lvert\langle 2_2^+ \lVert M(E2) \rVert 0_1^+ \rangle\rvert$	=	4.98 ± 0.27	e fm^2
$\lvert\langle 2_2^+ \lVert M(E2) \rVert 2_1^+ \rangle\rvert^\dagger$	=	6.98 ± 0.39	e fm^2
$\lvert\langle 2_2^+ \lVert M(M1)/c \rVert 2_1^+ \rangle\rvert^\dagger$	=	0.007 ± 0.003	μ_N/c

† these two reduced matrix elements have the same sign.

Table 4.4

Sources of uncertainty in the analysis of the data on ^{24}Mg

Source of Uncertainty	$\Delta B(E2;0^+ \rightarrow 2^+)$ (e^2 fm^4)	ΔQ_{2^+} (e fm^2)
Statistics	8	1.2
Beam energy	17	0
Excitation energy	1	0
Scattering angles	3	0.5
Total	19	1.3

subsection 2.2.2, is well illustrated by this case. The very low upper limit placed on the branching ratio for the $4^+ \rightarrow 0^+$ decay implies the rather large upper limit on $\lvert\langle 4^+ \lVert M(E4) \rVert 0^+ \rangle\rvert$ shown in table 4.3. If this upper limit is included in the analysis, then the value of $B(E2;0^+ \rightarrow 2^+)$ would be changed by ±28 e^2 fm^4 and that of Q_{2^+} by ±6.1 e fm^2 where the sign depends on the phase of the E4 matrix element. However, an effect of this magnitude is highly improbable since the upper limit corresponds to an E4 transition strength of 10^6 W.u. The effect of the E4 transition on the quadrupole moment would be less than ±0.1 e fm^2 if the matrix element was less than 0.016 of the upper limit in table 4.3. This corresponds to an E4 transition strength of less than 300 W.u. which seems to be a reasonably safe upper limit for a 2sld-shell nucleus. Thus the effect of interference through the 4_1^+ level is taken to be negligible.

4.3.2 Other Corrections

The magnitudes of the other corrections are shown in table 4.5. The value of H_{2+} was obtained from the results of various inelastic scattering experiments. There have been many such measurements (see ref. Ee74 for a summary); table 4.6 lists the results of those where the analysis took account of the effects of hexadecapole deformations. The values $\beta_2 = 0.5$, $\beta_4 = 0.05$, $\langle r^2 \rangle = 8$ fm^2 and $\langle r^4 \rangle = 100$ fm^4 give $Q_{2+} = 93$ e fm^2 (eq. 1.12) and $H_{2+} = 14$ e fm^4 (eq. 1.13). If $\beta_4 = -0.05$, then $H_{2+} = 6$ e fm^4. These are the two values shown in table 4.5.

Table 4.5

Corrections to the ^{24}Mg analysis

Reason for Correction	Magnitude of Correction†	Change to $B(E2;0^+ \rightarrow 2^+)$ (e^2 fm^4)	Change to Q_{2+} (e fm^2)
μ_{2+}	$0.99 \pm 0.04\ \mu_N/c$ ‡	-2	0.1
H_{2+}	6 - 14 e fm^4	±1	0.2 ± 0.2
gdr	k = 1 §	24 ± 8	0.1
Structure of target	$B(E3;0^+ \rightarrow 3^-) = 0.67 \pm 0.04\ e^2\ b^3$ ¶	0	0
Deviations from Coulomb potential and target thickness	$\frac{\Delta E}{E} \sim 4.10^{-4}$	0	0.2
Residual quantal corrections	$\eta > 75$	1	0.4
Special relativity	$u/c < 10\%$	-15 ± 15	0.1 ± 0.1
Total		8 ± 17	1.1 ± 0.2

† see text for discussion.

‡ weighted mean of results from Eb74, Ho74, Ho75; sign of Eb74.

§ Ha73.

¶ Jo77a.

The correction for the structure of the target was made with the multipole-multipole version of the de Boer-Winther computer program. Only the first excited state of ^{208}Pb was included and the reorientation of that state was ignored.

Table 4.6

Deformation parameters for ^{24}Mg obtained from inelastic scattering

Projectile	β_2	β_4	$\langle r^2 \rangle$ (fm^2)	$\langle r^4 \rangle$ (fm^4)	ref.
17.5 MeV p	0.47	-0.05 ± 0.08			Sw69
17 MeV α	0.40	0.05			Eb71
104 MeV α	0.39 ± 0.01	-0.015 ± 0.015			Re72
183 MeV and 250 MeV e^-	0.47 ± 0.03	-0.03	8.2	104	Na72

The comments made in subsection 4.2.2 concerning the last three corrections in table 4.2 apply equally well to the last three corrections in table 4.5.

The final results are therefore

$$\left.\begin{aligned} B(E2;0^+ \to 2^+) &= 428 \pm 25 \ e^2 \ fm^4 \\ Q_{2^+} &= -17.7 \pm 1.3 \ e \ fm^2 \end{aligned}\right\} p_4 < 0$$

and (4.17)

$$\left.\begin{aligned} B(E2;0^+ \to 2^+) &= 430 \pm 25 \ e^2 \ fm^4 \\ Q_{2^+} &= -17.3 \pm 1.3 \ e \ fm^2 \end{aligned}\right\} p_4 > 0 .$$

A plot of P_{exp}/F versus ρ for the result with $p_4 < 0$ is shown in fig. 4.6.

4.4 ^{18}O

4.4.1 Higher-State Matrix Elements

Data on the energy levels of ^{18}O below 4.5 MeV excitation energy are shown in fig. 4.7. They have been taken from the compilations by Ajzenberg-Selove [Aj72, Aj78]. It is not clear from ref. Aj78 or from the sources which are quoted [Be73, Ol73] whether the mixing ratio for the $4_1^+ \to 2_1^+$ transition has been measured to be zero or whether this is

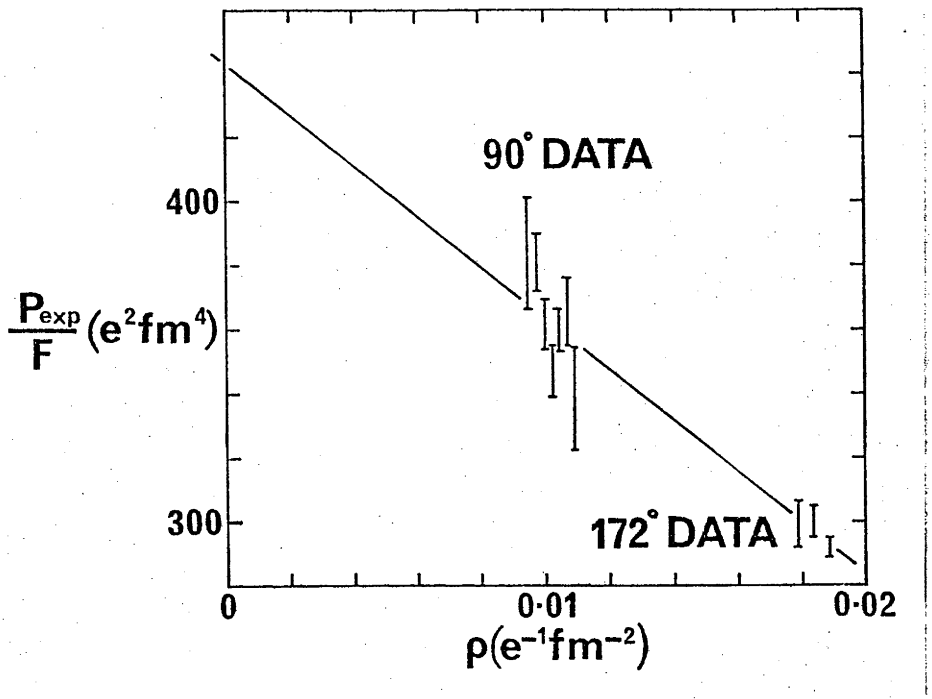

Fig. 4.6: The variation of P_{exp}/F with the sensitivity ρ for ^{24}Mg.

merely assumed to be the case. The matrix elements calculated by assuming that $\delta\ (4_1^+ \rightarrow 2_1^+) = 0$ are shown in table 4.7. The effect of the $J^\pi = 1^-$ state at 4.46 MeV was found to be negligible.

Using the symmetrized theory with the matrix elements of table 4.7, but with $\langle 4^+ \| M(E4) \| 0^+ \rangle = 0$, the values

$$\left.\begin{aligned} B(E2;0^+ \rightarrow 2^+) &= 35.2 \pm 1.8\ e^2\ fm^4 \\ Q_{2^+} &= -3.5 \pm 2.1\ e\ fm^2 \end{aligned}\right\} p_4 > 0$$

and (4.18)

$$\left.\begin{aligned} B(E2;0^+ \rightarrow 2^+) &= 33.3 \pm 1.8\ e^2\ fm^4 \\ Q_{2^+} &= -6.4 \pm 2.1\ e\ fm^2 \end{aligned}\right\} p_4 < 0\ .$$

are obtained. The sources of the uncertainties are shown in table 4.8. The result for $p_4 > 0$ is quoted first as this is the sign of p_4 predicted by the recent shell model calculations for ^{18}O [Er77, Mo78]. It should be noted that the results given in eq. 4.18 are for the selection of the data which was made in subsection 3.5.3. If all of

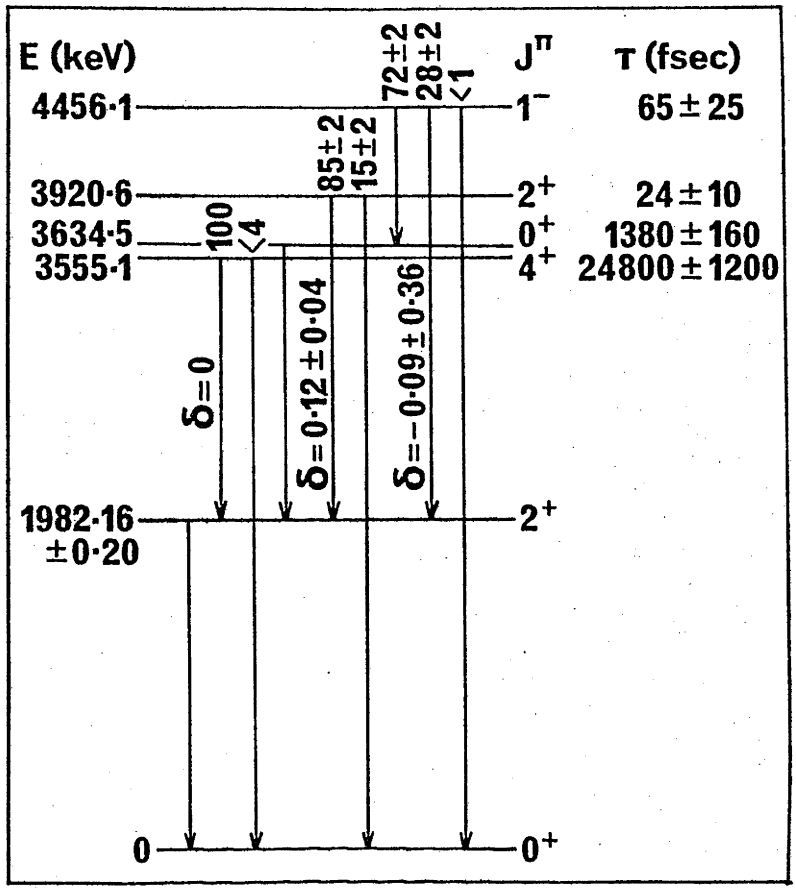

Fig. 4.7: The low lying energy levels of ^{18}O. Data are from compilations by Ajzenberg-Selove [Aj72, Aj78].

the data, including those which are clearly unreliable, were included in the analysis, then the inferred value of $|Q_{2^+}|$ would be increased by only 1.7 e fm^2 and that of $B(E2;0^+ \rightarrow 2^+)$ by 1.9 e^2 fm^4.

As in the case of ^{24}Mg, the upper limit on the value of $|\langle 0^+||M(E4)||4^+\rangle|$ obtained from gamma-ray spectroscopy is very large, again corresponding to an E4 transition strength of 10^6 W.u. To change the inferred value of Q_{2^+} by 0.1 e fm^2, the E4 transition strength would have to be 50 W.u. This again seems to be too large for an E4 transition in a 2s1d shell nucleus and so the effect of interference through the 4^+ state is ignored.

Table 4.7

Electromagnetic matrix elements in ^{18}O

$\lvert\langle 4_1^+ \lVert M(E4) \rVert 0_1^+\rangle\rvert$	<	3.10^4	e fm^4
$\lvert\langle 4_1^+ \lVert M(E2) \rVert 2_1^+\rangle\rvert$	=	5.56 ± 0.15	e fm^2
$\lvert\langle 0_2^+ \lVert M(E2) \rVert 2_1^+\rangle\rvert$	=	6.93 ± 0.40	e fm^2
$\lvert\langle 2_2^+ \lVert M(E2) \rVert 0_1^+\rangle\rvert$	=	5.2 ± 1.1	e fm^2
$\lvert\langle 2_2^+ \lVert M(M1)/c \rVert 2_1^+\rangle\rvert$ †	=	1.16 ± 0.21	μ_N/c
$\lvert\langle 2_2^+ \lVert M(E2) \rVert 2_1^+\rangle\rvert$ †	=	8.7 ± 3.2	e fm^2
$\lvert\langle 1_1^- \lVert M(E1) \rVert 0_1^+\rangle\rvert$	=	0.002	e fm
$\lvert\langle 1_1^- \lVert M(E1) \rVert 0_2^+\rangle\rvert$	=	0.194 ± 0.024	e fm
$\lvert\langle 1_1^- \lVert M(E1) \rVert 2_1^+\rangle\rvert$ ‡	=	0.0230 ± 0.0030	e fm
$\lvert\langle 1_1^- \lVert M(M2)/c \rVert 2_1^+\rangle\rvert$ ‡	=	9^{+19}_{-9}	μ_N fm/c

† these reduced matrix elements have the same sign.

‡ these reduced matrix elements have opposite sign.

Table 4.8

Sources of uncertainty in the analysis of the data on ^{18}O

Source of Uncertainty	$\Delta B(E2; 0^+ \to 2^+)$ (e^2 fm^4)	ΔQ_{2^+} (e fm^2)
Statistics	1.7	2.0
Beam energy	0.1	0.2
Excitation energy	0	0
Scattering angle	0.1	0.4
$\langle 0_1^+ \lVert M(E2) \rVert 2_2^+\rangle \langle 2_2^+ \lVert M(E2) \rVert 2_1^+\rangle$	0.4	0.6
$\langle 0_2^+ \lVert M(E2) \rVert 2_1^+\rangle$	0	0.1
$\langle 4_1^+ \lVert M(E2) \rVert 2_1^+\rangle$	0	0
Total	1.8	2.1

4.3.2 Other Corrections

The magnitudes of the other corrections are shown in table 4.9. Comment is as for the other nuclei except for the correction for the effects of the hexadecapole moment and giant dipole resonance.

Table 4.9

Corrections to the ^{18}O analysis

Reason for Correction	Magnitude of Correction†	Change to $B(E2;0^+ \rightarrow 2^+)$ (e^2 fm^4)	Change to Q_{2^+} (e fm^2)
μ_{2^+}	-0.295 ± 0.014 μ_N/c‡	0.3	-0.3
H_{2^+}	< 46 e fm^4	0	< ±0.1
gdr	k = 1	2.7 ± 2.0	1.1 ± 0.8
Structure of projectile	$B(E3;0^+ \rightarrow 3^-) =$ 0.67 ± 0.04 e^2 b^3§	0.3	0
Deviations from Coulomb potential & target thickness	$\frac{\Delta E}{E} \sim 0.2\%$	0.5	0.2
Residual quantal corrections	$\eta > 52$	0	0.2
Special relativity	u/c < 9.3%	-1.2 ± 1.2	-0.4 ± 0.4
Total		2.6 ± 2.3	0.8 ± 0.9

† see text for discussion.

‡ weighted mean of results from Sp75, As76, sign of Fo75.

§ Jo77a.

There are no measurements of β_4 for ^{18}O. The value shown in table 4.9 for H_{2^+} is that value which would change Q_{2^+} by 0.1 e fm^2. It is a relatively large number for this mass region — measured values of H_{2^+} for the other 2sld-shell nuclei [Re72] range from 16 e fm^4 (^{20}Ne) to 4 e fm^4 (^{26}Mg). A value of H_{2^+} of 46 e fm^4 for ^{18}O implies the deformation parameters $\beta_2 = 0.01$, $\beta_4 = 0.53$. This is very different from the usual assumption of $\beta_4 \lesssim \beta_2$. An attempt at the construction of empirical formulae for the values of β_2 and β_4 of light nuclei has been made by Specht [Sp71]. His formulae suggest that ^{18}O has the largest value of β_4 of any 2sld-shell nucleus with $\beta_2 = 0.28$, $\beta_4 = 0.39$. These imply $Q_{2^+} = -19$ e fm^2 (!) and $H_{2^+} = 45$ e fm^4. From these considerations, it seems unlikely that the value of H_{2^+} of ^{18}O is large enough to have a significant effect on this analysis.

The value of k was estimated from recent measurements of the

$^{18}O(\gamma,p)$ [Be76a] and $^{18}O(\gamma,n)$, $^{18}O(\gamma,pn)$, $^{18}O(\gamma,2n)$ and $^{18}O(\gamma,2np)$ [Kn76] cross sections. These indicate that $k \sim 1$, although it may be as high as 1.5 depending on the behaviour of the total photoneutron cross section above 33 MeV, the highest energy used in ref. Kn76. I have taken $k = 1$ and added a ±50% relative uncertainty to the uncertainty in η_0.

Thus the final results for ^{18}O are

$$\left.\begin{aligned} B(E2;0^+ \rightarrow 2^+) &= 37.8 \pm 2.9 \ e^2 \ fm^4 \\ Q_{2^+} &= -2.7 \pm 2.3 \ e \ fm^2 \end{aligned}\right\} p_4 > 0$$

and (4.19)

$$\left.\begin{aligned} B(E2;0^+ \rightarrow 2^+) &= 35.9 \pm 2.9 \ e^2 \ fm^4 \\ Q_{2^+} &= -5.6 \pm 2.3 \ e \ fm^2 \end{aligned}\right\} p_4 < 0 \ .$$

A plot of P_{exp}/F versus ρ for the result with $p_4 > 0$ is shown in fig. 4.8.

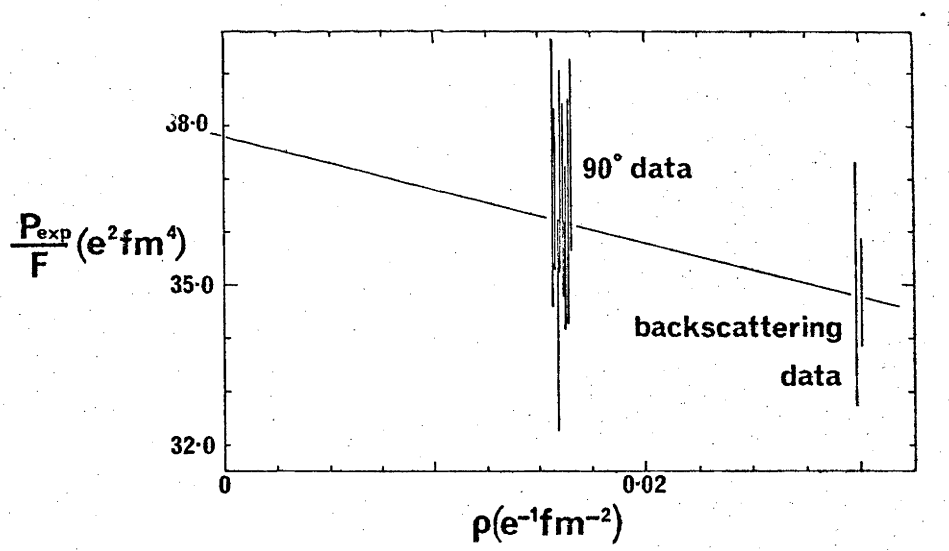

Fig. 4.8: The variation of P_{exp}/F with the sensitivity parameter ρ for ^{18}O.

Chapter 5

CONCLUSION

5.1 COMPARISON WITH PREVIOUS WORK

5.1.1 ^{198}Hg

Concurrently with this work, groups at the Universität zu Köln and the California Institute of Technology were also engaged in measurements of the quadrupole moment of the first excited state of ^{198}Hg. The Köln group used the reorientation effect while the Caltech group inferred Q_{2^+} from the X-ray spectrum of muonic ^{198}Hg. Their results are shown in table 5.1 along with the present results and the results of the $B(E2;0^+ \rightarrow 2^+)$ measurements listed in the most recent compilation on ^{198}Hg [Ha77a] (except for two measurements which were only reported by abstract).

Let us first consider the internal consistency of the various $B(E2;0^+ \rightarrow 2^+)$ measurements. With the exception of the work of Friedland and Lemmer [Fr63], there is very good agreement between our $B(E2;0^+ \rightarrow 2^+)$ value and those obtained before 1970. However, our result is two standard deviations away from that of the most recent lifetime measurement [Bu74]. Consideration of fig. 4.4 shows that, on the basis of our data, a $B(E2;0^+ \rightarrow 2^+)$ of 10900 e^2 fm^4 is most unlikely. This suggests that the uncertainties claimed by Burde *et al.* [Bu74] are probably optimistic. Nevertheless, their uncertainty was used for the purpose of obtaining the weighted mean but it was ignored in the determination of the uncertainty in the mean.

Turning to the quadrupole-moment measurements, there is reasonable agreement between the three published results. It should be noted that the Köln result [Bo78a] was not corrected for the effects of special relativity. If that correction is removed from our result (see table 4.2) then the two results become essentially identical. The Köln group have also reported [Bo77, Bo78] the results of a gamma-ray yields type of reorientation experiment (subsection 1.3.4 (iv)). This gave a quadrupole moment of -110 e fm^2, implying a prolate shape

Table 5.1

Results of previous and present measurements of Q_{2^+} and $B(E2;0^+ \rightarrow 2^+)$ of ^{198}Hg

Q_{2^+} (e fm^2)	$B(E2;0^+ \rightarrow 2^+)$ (e^2 fm^4)	Ref.	Method
	10900 ± 2500	Da53	resonance fluorescence
	10900 ± 1000	Me54	" "
	11400 ± 3800	Su58	β-γ delayed coincidences
	10000 ± 1200	Si61	β-ce " "
	7000 ± 400	Fr63	resonance fluorescence
	9600 ± 1900	Go66	β-γ delayed coincidences
	11900 ± 1800	Be67	" " "
	8800 ± 1000	Ra68	β-ce " "
	10900 ± 500	Bu74	" " "
	10500 ± 500		weighted mean†
94 ± 24 ‡ 78 ± 24 ‡	9700 ± 170	this work	reorientation, particle singles
52 ± 23§		Ha78	muonic X-rays
80 ± 18 ‡¶ 66 ± 18 ‡¶	9910 ± 60	Bo78a	reorientation, particle singles

† excluding result of ref. Fr63 and uncertainty of ref. Bu74, see text.

‡ first value for $p_4 < 0$, second for $p_4 > 0$ (see eq. 1.50).

§ insensitive to sign of p_4.

¶ not corrected for relativistic effects.

for ^{198}Hg. There has been no explanation of this error.

A comparison between the reorientation-effect measurements and the muonic-X-ray measurement suggests that, in contradiction to the predictions of most collective models, $p_4 > 0$, but the uncertainties are too large to be able to say definitely that this is so. Two experimental values are therefore considered for the purposes of comparison with theoretical predictions. These are shown in the first line of table 5.2. Because of the uncertainties in the gdr and relativistic corrections, it seems unreasonable to claim uncertainties

Table 5.2

A comparison of the theoretical predictions of Q_{2^+} and $B(E2;0^+ \rightarrow 2^+)$ of ^{198}Hg with the adopted experimental values

Q_{2^+} (e fm^2)	$B(E2;0^+ \rightarrow 2^+)$ (e^2 fm^4)	Ref.	Method
75 ± 24 65 ± 24 †	9870 ± 160	text	experiment
± 90 ‡		text	symmetric rigid rotor
-71 §		Co67	asymmetric rigid rotor
50	¶	Al66	particle-vibration coupling
75	¶	Co67	" " "
80.26	7848	Ku68	HFB, pairing + quadrupole
83		Lo75	particle-vibration coupling
69.9	¶	Ki76	boson expansion
4.5 ± 2 -22 ± 2 †		Ko78	energy-weighted sum rules

† first value for $p_3 < 0$, second for $p_3 > 0$ (eq. 1.49). The product p_3 is used here in place of p_4 because the two results of ref. Ko78 both have $p_4 < 0$.

‡ sign not predicted.

§ see text.

¶ model parameters chosen to reproduce a previous experimental $B(E2;0^+ \rightarrow 2^+)$ value of 10300 e^2 fm^4.

as small as those claimed by the Köln group. The experimental values of Q_{2^+} adopted in table 5.2 are therefore arithmetic means of the three measurements with uncertainties equal to those of the present measurement. The adopted $B(E2;0^+ \rightarrow 2^+)$ value is the weighted mean of the mean of the lifetime measurements as obtained above and the arithmetic mean of the reorientation-effect measurements.

The remainder of table 5.2 lists the various theoretical predictions of Q_{2^+} and $B(E2;0^+ \rightarrow 2^+)$. The symmetric rotational model value for Q_{2^+} was calculated from the experimental $B(E2;0^+ \rightarrow 2^+)$ value using eqs. 1.24 and 1.61. Since eq. 1.61 contains $(Q_0^{E2})^2$, the sign of the quadrupole moment cannot be obtained. In a concluding remark to a

paper reporting their particle-vibration-coupling calculations, Covello and Sartoris [Co67] observe that the asymmetric rotational model predicts $Q_{2^+} = -71$ e fm^2 as shown in table 5.2. It is not clear how they obtained the sign, since inspection of eqs. 1.67 and 1.71 shows that, in accord with the case of the symmetric rotational model, the expressions for the energies and reduced transition probabilities are unchanged if γ is replaced by $\pi/3 - \gamma$. In any case, the presence of a low-lying excited 0^+ state and more than two low-lying 2^+ states and the absence of obvious candidates for the 3_1^+ and 4_2^+ states suggests that the asymmetric rotational model is inappropriate.

The presence of the low lying 0^+ state indicates that the description of ^{198}Hg requires a model containing more degrees of freedom than rotation. The particle-vibration coupling calculations clearly do this, the different results being due to different parameter sets and to different assumptions about the nature of the coupling between the two proton holes. The Hartree-Fock-Bogoliubov calculations [Ku68] result in the parameters of the rotation-vibration model, and the spectra calculated by boson expansion [Ki76] remind one of the rotation-vibration spectrum of fig. 1.4. All of these models predict values of Q_{2^+} in substantial agreement with the experimental value quoted in table 5.2. It is a pity that the reports of these calculations do not allow one to extract the predicted sign of the products p_3 or p_4. This is a piece of information which must be readily available to those who performed the calculation and would be most useful in the comparison of calculations with reorientation-effect measurements.

The last line of table 5.2 lists the prediction of Q_{2^+} from a very recent calculation using energy-weighted sum rules [Ko78]. This method is model-independent in the sense that only very general assumptions are made about the nature of the nuclear interaction in the derivation of the value of sums of products of, for example, quadrupole matrix elements. Then, by inserting measured values of some matrix elements, others can be found. The calculations of quadrupole moments therefore depend on sufficiently many experimental B(E2) values of sufficient accuracy being available and hence are more

accurate for nuclei which have received a more complete experimental investigation than ^{198}Hg.

5.1.2 ^{24}Mg

The nucleus ^{24}Mg has been the subject of a very large amount of work. The most recent compilation [En73] lists twenty-two measurements of the lifetime of the first excited state using the five main techniques — inelastic electron scattering, resonance fluorescence, Coulomb excitation, Doppler shift attenuation and recoil distance. Since that compilation, eleven additional measurements (including the present one) have been reported. These are shown in table 5.3 along with the mean value quoted by Endt and van der Leun [En73]. The range of $B(E2;0^+ \rightarrow 2^+)$ values is very wide, even in the most recent measurements shown in table 5.3. In one attempt to unravel the situation, Biagi *et al.* [Bi75] rejected all data with uncertainties greater than 10%. I feel that this is a dangerous procedure as it tends to favour those workers who are over-optimistic about the level of uncertainty attached to their result. However, it is very difficult to suggest a better one. It might be noted, however, that all of the Coulomb excitation measurements are in good agreement with one another. The same cannot be said for any other group of measurements, except for those made by inelastic electron scattering. The weighted mean of the Coulomb excitation results is $B(E2;0^+ \rightarrow 2^+) = 425 \pm 9$ e^2 fm^4. This compares very well with the value of 428 ± 12 e^2 fm^4 adopted by Biagi *et al.* [Bi75] and with the value 429 ± 9 e^2 fm^4 which Endt and van der Leun propose to adopt in their next compilation [En78]. For the purposes of comparison with theory, I adopt this last value.

There is also a wide spread of reported values of Q_{2+}. It has been argued [Bi75] that this spread is not inconsistent with the uncertainties but, of the seven previous measurements, only two include the present result within their error bars and all but one are larger than the present result. The reasons for this are, in general, not clear. In the case of the first result listed in table 5.3, the analysis assumed that $B(E2;0^+ \rightarrow 2^+) = 504$ e^2 fm^4. From fig. 9 of ref. Pe69, the $B(E2;0^+ \rightarrow 2^+)$ value adopted above would give a Q_{2+} value of

Table 5.3

Results of previous and present measurements of Q_{2^+} and $B(E2;0^+ \rightarrow 2^+)$ of ^{24}Mg

Q_{2^+} [†] ($e\,fm^2$)	$B(E2;0^+ \rightarrow 2^+)$ ($e^2\,fm^4$)	Ref.	Method
-47 ± 19		Pe69	reorientation, γ yield
-38 ± 16		Pe69	" , γ angular distribution
-24.3 ± 3.5	425 ± 29	Ha70	reorientation, p-γ coincidence yield
-30.5 ± 6.4	420 ± 20	Vi71	reorientation, p-recoil coincidence yield
	486 ± 22	En73	compilation of 22 results[‡]
-16 ± 4	440 ± 30	Ha72a	reorientation, particle singles
-24 ± 6		Sc72a	" , γ lineshapes
	378 ± 15	Br73a	recoil distance (low recoil velocity)
	$425 \,^{+123}_{-78}$	Le73	Doppler shift attenuation (low recoil velocity)
	466 ± 36	Fo74	Doppler shift attenuation (high recoil velocity)
	420 ± 25	Jo74	inelastic electron scattering
-27 ± 5	440 ± 30	Bi75	reorientation, γ angular dist.; Coulomb excitation
	406 ± 25	Ho75	recoil distance (high recoil velocity)
	$679 \,^{+115}_{-85}$	Be76	Doppler-broadened lineshapes (low recoil velocity)
	442 ± 23	Sc77	Doppler shift attenuation (high recoil velocity)
	420 ± 14	Sc77	Coulomb excitation
-17.7 ± 1.3	428 ± 25	this work	reorientation, particle singles

[†] results for $p_4 < 0$, but values are insensitive to the sign of p_4.

[‡] including the results of refs. Ha70, Vi71.

-22 e fm^2. Thus there is, in fact, no discrepancy between our result and this work. It has been suggested [Bi75] that the work of Vitoux *et al.* was affected by the nuclear force. This suggestion was made on the basis of a private communication and implies that the Coulomb-nuclear interference curve presented in ref. Vi71 is somehow incorrect.

There is no obvious explanation of the other discrepancies. The present value is used for the purpose of comparison with theory. We feel that the relatively large effect of the quadrupole moment on the excitation probability (compared with its effect on, for example, the gamma-ray angular distribution) and the comparative simplicity of our method make our result more likely to be correct than the earlier results. An exception is the most recent result of Häusser *et al.* [Ha72a] which was obtained by a method similar to ours. However, over six years have elapsed since the appearance of this progress report and the authors have not seen fit to publish either spectra or details of the analysis. Only the briefest of descriptions of the experimental arrangement [Di71] has appeared. The time must surely be fast approaching when this result should be discarded on the basis of lack of supporting information.

^{24}Mg has been the subject of as much theoretical as experimental work and table 5.4 presents the numerous predictions of Q_{2^+} and $B(E2;0^+ \rightarrow 2^+)$. All of the calculations give approximately the experimental value of the quadrupole moment except for the configuration-mixing shell-model calculation of Krewald *et al.* [Kr74]. However, the shell-model calculations seem to underestimate the reduced transition probability. The Hartree-Fock calculations do much better but the results depend strongly on the size of the basis used. Mackintosh [Ma77a] has recently examined this point and the range of values shown in table 5.4 is the range of results obtained by considering from five to eleven oscillator shells. It may be noted that the rigid rotational model correctly predicts the relationship between Q_{2^+} and $B(E2;0^+ \rightarrow 2^+)$. This is, at first sight, surprising considering that there are only 24 nucleons but it is in agreement with the observed quasi-collective nature of many of the low-lying states of ^{24}Mg.

Table 5.4

A comparison of the theoretical predictions of Q_{2^+} and $B(E2;0^+ \rightarrow 2^+)$ of ^{24}Mg with experimental values

Q_{2^+} (e fm^2)	$B(E2;0^+ \rightarrow 2^+)$ (e^2 fm^4)	Ref.	Method
-17.7 ± 1.3	429 ± 9	text	experiment
± 18.7[†]		eq. 1.61	rigid rotational model
-15.0		Wi71	truncated shell model
-16	315	Mc71	" " "
-17.8	393	Gu71	Hartree-Fock
-17.5	174 to 191	Fo71	" "
-15	270	Ku72a	triaxial adiabatic model
-16 to -18	310 to 360	St72	SU(3) truncated shell model
-19.8	581	Ab72	Hartree-Fock
-16.0	392	Le73a	" "
-17.1	393	Cu73	" "
-15.8		Hi74	truncated shell model
-9.5	277	Kr74	shell model
-14.7	229	Kr74	Hartree-Fock
-17.4	353	Kh74	" "
	253 to 408	Ma77a	" "
-14.9		Ha77	folding model
-15.5 ± 0.7[‡]		Ko78	energy-weighted sum rules

[†] sign not predicted.

[‡] $p_3 > 0$, predicted value for $p_3 < 0$ is 8 ± 4 e fm^2.

5.1.3 ^{18}O

The quadrupole moment of the first excited state of ^{18}O has, like that of ^{24}Mg, received considerable attention, although much of this has been more recent than in the case of ^{24}Mg. The first measurement of Q_{2^+} of ^{18}O was performed by Häusser *et al.* [Ha71a, Ha72]. However, from fig. 3.30, it seems most likely that the data at three of the six scattering angles used was subject to Coulomb-nuclear interference. Consequently, I have ignored their results. The first published

measurement of Q_{2^+} appeared in 1975 [Kl75] and it was quickly pointed out [En76] that the value reported was inconsistent with previously accepted ideas of the structure of the 2^+ state of ^{18}O. This prompted a number of remeasurements of Q_{2^+} with results which are shown in table 5.5 together with the results of Kleinfeld *et al.* [Kl75] and of the many measurements of $B(E2;0^+ \rightarrow 2^+)$.

The various versions of the reorientation effect which were used are indicated in the last column of table 5.5, but some elaboration is desirable. All of the measurements used the excitation of ^{18}O projectiles by high-A targets and measured the excitation probability as a function of scattering angle. The targets were ^{196}Pt [Vo77], ^{197}Au [Fl77], ^{208}Pb [Vo77, De77 and this work] and ^{209}Bi [Kl75]. Vold *et al.* [Vo77] determined the excitation probability from particle-gamma coincidence yields while the other four measurements used the particle singles technique, Kleinfeld *et al.* and the present measurements using silicon surface-barrier detectors and the other two groups using magnetic spectrometers.

The range of reported Q_{2^+} values is disturbingly wide and clearly demands explanation. It might first be noted that the present work and that of Kleinfeld *et al.* are the only ones to investigate the onset of Coulomb-nuclear interference. Kleinfeld *et al.* report that there is no evidence of Coulomb-nuclear interference in the system $^{18}O + ^{209}Bi$ at bombarding energies up to and including 63 MeV. This corresponds to a minimum separation of surfaces of 5.8 fm and, when compared with our minimum safe separation of $\sim$ 6.2 fm for the $^{18}O + ^{208}Pb$ system, highlights the differences which can occur in the nuclear force between different pairs of nuclei with similar numbers of nucleons. It is certainly not reasonable therefore, for Vold *et al.* to assume that the Coulomb-nuclear interference effect is the same for $^{18}O + ^{196}Pt$ as for $^{18}O + ^{208}Pb$, nor for Flaum *et al.* [Fl77] to make a similar assumption about the $^{18}O + ^{197}Au$ system. Yet such assumptions are made. This point alone does not necessarily invalidate the work of these two groups, but it does attach some doubt to the reliability of their results.

In addition, the analysis used by Vold *et al.* explicitly assumes,

Table 5.5

Results of previous and present measurements of Q_{2^+} and $B(E2;0^+ \rightarrow 2^+)$ of ^{18}O

Q_{2^+} (e fm^2)	$B(E2;0^+ \rightarrow 2^+)$ (e^2 fm^4)	Ref.	Method
	$40\ ^{+34}_{-12}$	La61	inelastic electron scattering
	$36\ ^{+8}_{-4}$	Li63	Doppler shift attenuation (high recoil velocity)
	22 ± 10	Es64	Doppler shift attenuation (high recoil velocity)
	$32\ ^{+10}_{-8}$	Hi71	Doppler shift attenuation (low recoil velocity)
	46 ± 12	Ol73	Doppler shift attenuation (low recoil velocity)
	39.8 ± 2.3	Mc74	recoil distance (high recoil velocity)
	37.3 ± 1.9	Be74	recoil distance (low recoil velocity)
	47.8 ± 1.9	He75	Doppler shift attenuation (high recoil velocity)
-16 ± 2 -19 ± 2 †‡	48 ± 2 §	Kl75	reorientation, particle singles
	44.6 ± 1.8	As76	recoil distance (high recoil velocity)
	38.5 ± 6.0	Vo77	Coulomb excitation
2.0 ± 1.3 -1.0 ± 1.3 †	40.2 ± 1.4	Vo77	reorientation, p-γ coincidence yields
-4.5 ± 2.8 -7.3 ± 2.7 †	45.3 ± 2.6	Fl77	reorientation, particle singles
-7.6 ± 2.0 -10.7 ± 2.0 †	38 ± 4 §	De77	reorientation, particle singles
-2.7 ± 2.3 -5.6 ± 2.3	37.8 ± 2.9 35.9 ± 2.9 †¶	this work	reorientation, particle singles
	43.0 ± 2.6*	Li77	recoil distance (high recoil velocity)
	48 ± 3*	Fo78	Doppler shift attenuation (high recoil velocity)

† first value for $p_3 < 0$, second for $p_3 > 0$.

‡ not corrected for mutual excitation.

not only that the energy dependence of Coulomb-nuclear interference is the same for $^{18}O + ^{196}Pt$ as for $^{18}O + ^{208}Pb$, but also that the bombarding energy at which the interference effect becomes noticeable is the same for all angles. For their datum taken with a ^{208}Pb target, this is plainly and simply wrong, as a glance at fig. 3.30 shows. Calculations of the Coulomb-nuclear interference effect for $^{18}O + ^{196}Pt$ suggest that it is also incorrect for this system [Le78]. The net result of this error is that Vold *et al.* apply a substantial correction to data which are negligibly affected by Coulomb-nuclear interference. Removal of this correction gives, apart from their lowest energy point, Q_{2+} values in agreement with those of refs. Fl77 and De77 and with the present work.

Another point to be considered in the evaluation of the various measurements is the scattering angles used. The experiment becomes more difficult as the scattering angle is reduced because

(a) the excitation probability falls

(b) the fractional rate of change of the excitation probability with angle increases

(c) lighter-mass target contaminants move up into the region of the inelastic peak. (This is not a problem with the method used by Vold *et al.*).

Point (b) was emphasized in subsection 3.1.3 (i). In spite of its importance, only the present work and that of Kleinfeld *et al.* [see Bo76] detail special precautions taken to reliably determine the scattering angle. The most forward scattering angles used were 45° [Kl75, Fl77, De77], 65° [Vo77] and 90° [this work].

As well as the discrepancy in values of Q_{2+}, a wide variety of $B(E2;0^+ \rightarrow 2^+)$ values are listed in table 5.5, with the Coulomb excitation results disagreeing among themselves to the same degree as

---

§ not corrected for the effects of the gdr or deviations from the Coulomb potential or for quantal effects.

¶ corrected for effects of special relativity.

* preliminary result.

the lifetime measurements. Once again the result of Kleinfeld *et al.* stands out. It is the largest reported $B(E2;0^+ \rightarrow 2^+)$ value even without the gdr correction. Application of this correction would increase the $B(E2;0^+ \rightarrow 2^+)$ value by $\sim$ 10%. There seems to be a trend in the most recent $B(E2;0^+ \rightarrow 2^+)$ measurements toward lower values, in the 38 - 42 e^2 fm^4 range. An exception is that of Flaum *et al.* This result is difficult to understand because a relatively large reported $B(E2;0^+ \rightarrow 2^+)$ value is coupled with a relatively small Q_{2^+} value. On the other hand, the result of Kleinfeld *et al.* can be understood by supposing that their measurements of the excitation probability at forward angles err systematically on the high side. (It has been observed [La76, Fl77] that the backscattering data of Kleinfeld *et al.* are in agreement with lower magnitudes for both Q_{2^+} and $B(E2;0^+ \rightarrow 2^+)$.

Because of the above criticisms of the previous reorientation measurements and because of the wide spread in $B(E2;0^+ \rightarrow 2^+)$ values, it is difficult to suggest a weighting procedure for the purpose of obtaining adopted experimental values. The results of the present experiment are therefore used in the comparison with the theoretical predictions, which are listed in table 5.6. It is clear that all of the shell model calculations predict values of Q_{2^+} which are much smaller than the value of Kleinfeld *et al.* Lawson *et al.* [La76] found that a Q_{2^+} value of -16 e fm^2 could not be obtained while at the same time obtaining correct values for the magnetic dipole moment of the 2_1^+ state, the $2_2^+ \rightarrow 0_1^+$ and $2_3^+ \rightarrow 0_1^+$ branching ratios and the mixing ratio of the $2_2^+ \rightarrow 2_1^+$ transition. All of the most recent theoretical papers remark that the result of Kleinfeld *et al.* is quite inconsistent with the current theoretical interpretation. The present result clearly removes that problem.

5.2 NUCLEAR SHAPES

5.2.1 The Nuclei ^{198}Hg, ^{24}Mg and ^{18}O

The formalism of subsection 1.1.3 may be used to infer the shapes of the nuclei ^{198}Hg, ^{24}Mg and ^{18}O in both their ground and first-excited states. Table 5.7 lists the states used in the determination

Table 5.6

A comparison of theoretical predictions of Q_{2^+}, $B(E2;0^+ \to 2^+)$ and sgn p_3 of ^{18}O with experimental values

Q_{2^+} (e fm^2)	$B(E2;0^+ \to 2^+)$ (e^2 fm^4)	sgn p_3†	Ref.	Method
-2.7 ± 2.3	37.8 ± 2.9	−	this work	present experimental value
-5.6 ± 2.3	35.9 ± 2.9	+	this work	present experimental value
-2.0			Wi71	shell model
-3.4	24.5	−	En76	" "
-5.0 to -3.9	35.2 to 36.2		La76	" "
-5.9 to -5.2	46.6 to 60.5	−	Er77	" " ($e_n = 0.5$)
$\geqslant -5$			Kl77	SU(3) truncated shell model
-5.1	32	−	Mo78	shell model
8 ± 4		−	Ko78	energy-weighted sum rules
-13 ± 4		+	Ko78	energy-weighted sum rules

† a blank indicates that the sign was not reported.

Table 5.7

Excited states included in the determination of the n-body quadrupole moments of the ground and first-excited states of ^{198}Hg, ^{24}Mg and ^{18}O

Nucleus	States Included (MeV)	Sources of Matrix Elements
^{198}Hg	0 (0^+), 0.411 (2^+), 1.049 (4^+), 1.088 (2^+)	subsect. 4.2.1
^{24}Mg	0 (0^+), 1.369 (2^+), 4.123 (4^+), 4.239 (2^+), 5.236 (3^+), 6.010 (4^+), 6.432 (0^+), 7.348 (2^+), 7.747 (1^+), 8.436 (4^+), 8.654 (2^+), 9.002 (2^+)	subsect. 4.3.1, En73, Le73, En74, Jo74
^{18}O	0 (0^+), 1.982 (2^+), 3.555 (4^+), 3.635 (0^+), 3.921 (2^+), 5.260 (2^+), 5.336 (0^+)	subsect. 4.4.1, Aj78

of the 2-body and 3-body quadrupole moments of the 0_1^+ and 2_1^+ states of each nucleus. From the expressions for $Q_{J^\pi}^{E2(2)}$ and $Q_{J^\pi}^{E2(3)}$ (eqs. 1.31 and 1.32), it is clear that only $J^\pi = 2^+$ states can contribute to

Table 5.8

Values of the 2-body and 3-body quadrupole moments of the ground and first-excited states of ^{198}Hg, ^{24}Mg, and ^{18}O

Nucleus	Energy Level (MeV)	J^π	sgn p_4	$Q^{E2(2)}$ (e^2 fm^4)	$Q^{E2(3)}$ (e^3 fm^6)	% from Q_{2^+} and $B(E2;0^+\to 2^+)$	
						$Q^{E2(2)}$	$Q^{E2(3)}$
^{198}Hg	0	0^+	−	9790 ± 170	(5.0 ± 1.1) × 10^5	99	108
			+	9820 ± 170	(4.8 ± 1.3) × 10^5	99	93
	0.411	2^+	−	9900 ± 2300	(3.1 ± 1.9) × 10^5	51	58
			+	8900 ± 2200	(2.8 ± 1.7) × 10^5	46	57
^{24}Mg	0	0^+	−	464 ± 10	−4000 ± 400	92	115
			+	464 ± 10	−5300 ± 400	92	87
	1.369	2^+	−	440 ± 50	−2850 ± 340	46	56
			+	440 ± 50	−2940 ± 340	46	55
^{18}O	0	0^+	+	65 ± 10	−310 ± 110	59	26
			−	65 ± 10	130 ± 110	59	400
	1.982	2^+	+	43 ± 10	−130 ± 90	28	21
			−	50 ± 13	−90 ± 40	42	38

$Q_{0^+}^{E2(2)}$ and $Q_{0^+}^{E2(3)}$ and only positive parity states with $J \leqslant 4$ can contribute to $Q_{2^+}^{E2(n)}$. Table 5.8 shows the results of the calculations of the n-body quadrupole moments. In general, there are many terms in the expressions for $Q_{J^\pi}^{E2(3)}$ which have unknown signs. Values are shown for the different signs of p_4 (eq. 1.50), and the other terms, which are much smaller in magnitude, are incorporated into the uncertainty. Apart from these terms of unknown sign, the uncertainties are derived entirely from the uncertainties in the matrix elements — no allowance has been made for any possible "missing strength". To provide some indication of the magnitude of the various terms in the sums, the fraction of each sum which is contributed by the matrix elements $\langle 2_1^+ \| M(E2) \| 0_1^+ \rangle$ and $\langle 2_1^+ \| M(E2) \| 2_1^+ \rangle$ is also shown in table 5.8. It is interesting that a substantial contribution to $Q_{0^+}^{E2(3)}$ for ^{18}O is made by the term involving the product p_3. Indeed, since $Q_{J^\pi}^{E2(3)} < 0$ implies a prolate shape and $Q_{J^\pi}^{E2(3)} > 0$ an oblate shape (eq. 1.37), the inferred shape of ^{18}O in the ground state depends upon the sign of this product.

Table 5.9
Shape parameters for ^{198}Hg, ^{24}Mg and ^{18}O

Nucleus	State	$p_4 < 0$		$p_4 > 0$	
		B	Γ	B	Γ
^{198}Hg	0_1^+	0.0971 ± 0.0008	$55^{\circ}{}^{+\ 5^{\circ}}_{-\ 9^{\circ}}$	0.0972 ± 0.0008	$55^{\circ} \pm 8^{\circ}$
	2_1^+	0.10 ± 0.03	$42^{\circ}{}^{+18^{\circ}}_{-\ 9^{\circ}}$	0.09 ± 0.03	$43^{\circ}{}^{+17^{\circ}}_{-\ 9^{\circ}}$
^{24}Mg	0_1^+	0.524 ± 0.004	$14^{\circ}{}^{+\ 2^{\circ}}_{-\ 3^{\circ}}$	0.524 ± 0.004	$2^{\circ}{}^{+\ 6^{\circ}}_{-\ 2^{\circ}}$
	2_1^+	0.507 ± 0.020	$18^{\circ} \pm 3^{\circ}$	0.507 ± 0.020	$18^{\circ} \pm 3^{\circ}$
^{18}O	0_1^+	0.370 ± 0.032	$39^{\circ}{}^{+11^{\circ}}_{-\ 8^{\circ}}$	0.370 ± 0.032	$0^{\circ}{}^{+18^{\circ}}_{-\ 0^{\circ}}$
	2_1^+	0.330 ± 0.040	$21^{\circ}{}^{+\ 6^{\circ}}_{-\ 8^{\circ}}$	0.309 ± 0.031	$10^{\circ}{}^{+16^{\circ}}_{-10^{\circ}}$

This adds some weight to the shell model prediction $p_4 > 0$ (and, hence, $p_3 < 0$) [En76, Er77, Mo78] as one usually expects nuclei with a small number of particles outside of a closed shell to be prolate rather than oblate.

The inference of shape from n-body multipole moments requires the assumption of a model. If the equivalent-ellipsoid formalism of Kumar (subsection 1.1.3) is used, then the values of the deformation parameters B and Γ (eqs. 1.34 and 1.35) which are shown in table 5.9 are obtained. It should again be emphasized that the parameters B,Γ are not the same as deformation parameters β,γ of eq. 1.14. Rosensteel and Ihrig [Ro78] show that $1 - B/\beta$ and $\sin(\Gamma - \gamma)$ approach zero as $\beta \to 0$. For example, from their equations, one obtains $\beta = 0.1004$, $\gamma = 54^{\circ}$ for the ground state of ^{198}Hg ($p_4 < 0$) but $\beta = 0.450$, $\gamma = 10^{\circ}$ for the ground state of ^{24}Mg ($p_4 < 0$).

Table 5.10

Values of 2-body and 3-body quadrupole moments of the ground states of stable even-even nuclei in the mass range $184 \leqslant A \leqslant 206$

Nucleus	2^+ States Included	Sources of Matrix Elements	$10^3\ Q_{0^+}^{E2}(2)$ (e^2 fm^4)	$10^5\ Q_{0^+}^{E2}(3)$ (e^3 fm^6)
^{184}Os	0.120	La72, Ma77c	32 ±6	-46 ±22
^{186}Os	0.137, 0.768	La72, Sc74, Ba76, Ru78	33.5 ±1.1	-25.9 ± 2.6
^{188}Os	0.155, 0.633	Sc73b, Ba76, Ru78	30.5 ±1.0	-18.7 ±1.8
^{190}Os	0.187, 0.558	Sc73a, Ba76, Ru78	26.1 ±0.6	-10.1 ±1.1
^{192}Os	0.206, 0.489	Sc73, Ba76, Ru78	22.4 ±0.6	-2.6 ±1.2
^{194}Pt	0.328, 0.622	Ba76a, Ba78	16.29 ±0.15	6.7 ±0.6
^{196}Pt	0.356	Sc72b	14.9 ±0.5	4.8 ±1.1
^{198}Pt	0.407	Ha77a	10.1 ±0.5	7 ±3
^{198}Hg	0.412, 1.088	subsection 5.2.1	9.79 ±0.17	5.0 ±1.1
^{200}Hg	0.368	Ha78	9.0 ±0.6	13 ±7
^{204}Hg	0.437	Ha78	3.5 ±0.2	0.2 ±3
^{204}Pb	0.899	Jo78	1.66 ±0.03	0.22 ±0.09
^{206}Pb	0.803	Jo78	1.03 ±0.02	0.3 ±0.6

5.2.2 Systematics in the Mass Ranges $186 \leqslant A \leqslant 208$ and $16 \leqslant A \leqslant 40$

It is interesting to consider the variation of nuclear shape with mass, particularly in those mass ranges, such as $186 \leqslant A \leqslant 208$ and $16 \leqslant A \leqslant 40$, where the excited-state quadrupole moments suggest that a shape transition is taking place as A is varied. Tables 5.10 and 5.11 give the values of the 2-body and 3-body quadrupole moments of the ground states of even-even nuclei in the above mass regions. Only those nuclei with known values of $Q_{2_1^+}$ have been considered. Where the matrix elements connecting the 2_2^+ state are known, the sign of the product p_4 is taken to be negative except in ^{18}O and ^{194}Pt where there are indications that $p_4 > 0$ [this work and Ba76a]. In the case of ^{40}Ar,

Table 5.11

Values of 2-body and 3-body quadrupole moments of the ground states of stable even-even nuclei in the mass range $18 \leqslant A \leqslant 40$

Nucleus	2^+ States Included	Sources of Matrix Elements†	$Q_{0^+}^{E2(2)}$ (e^2 fm^4)	$Q_{0^+}^{E2(3)}$ (e^3 fm^6)
^{18}O	1.982, 3.921, 5.260	subsection 5.2.1	65 ± 10	-310 ± 110
^{20}Ne	1.634, 7.421, 9.508, 10.272		361 ± 18	-4500 ± 500
^{22}Ne	1.275	Ol74, Br76, Fi76	222 ± 6	-2300 ± 300
^{24}Mg	1.369, 4.239, 7.348, 8.654, 9.002	subsection 5.2.1	464 ± 10	-4000 ± 400
^{26}Mg	1.809, 2.938, 4.332, 4.835, 5.291	Le74, Wa75	317 ± 10	-2100 ± 700
^{28}Si	1.779, 7.381, 7.417, 7.933, 8.259	Me75, Da78	353 ± 12	2900 ± 600
^{32}S	2.230, 4.282, 5.549	Ba78a	358 ± 18	-1500 ± 500
^{34}S	2.127, 3.304, 4.115	Gr74, He75	244 ± 16	800 ± 800
^{36}Ar	1.970, 4.440	Jo74a, Sa75, No76	410 ± 180	2700 ± 1900
^{40}Ar	1.461, 2.524, 3.511	So76, So76a	500 ± 70	1700 ± 1100

† in addition to refs. En73, En74, En74a, Sc77 and Aj78.

the sign of p_3 is not determined by the sign of p_4 since the experimental value of Q_{2^+} [En73] is consistent with zero. The result in table 5.11 corresponds to $p_3 > 0$; if $p_3 < 0$, then $Q_{0^+}^{E2(3)} = -1300 \pm 1100\ e^3\ fm^6$.

The corresponding values of B and Γ are shown in figs. 5.1 and 5.2. The well known prolate-to-oblate transition between masses 184 and 198 is clearly seen. After reaching $\sim 60°$ at about A = 198, Γ seems to decrease to about 30° as shell closure is approached. The variation of Γ across the 2s1d shell is more erratic. The nuclei ^{24,26}Mg, ^{32,34}S show a smooth prolate-to-oblate transition but ^{28}Si has remarkably large values of both B and Γ. It would be very

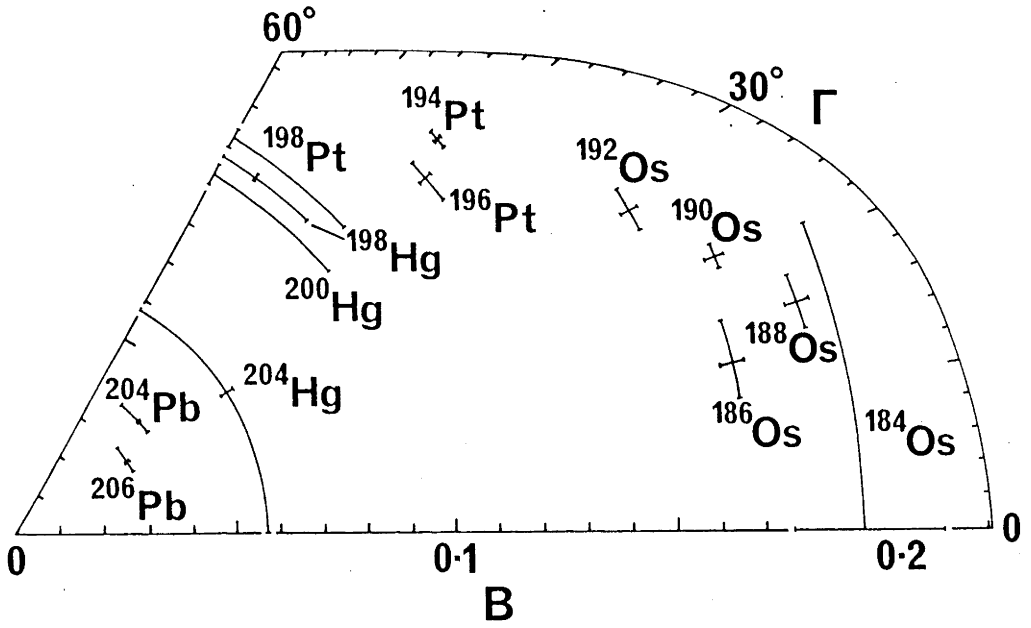

Fig. 5.1: Values of the shape parameters B and Γ of the ground states of some even-even nuclei in the mass range $186 \leqslant A \leqslant 206$.

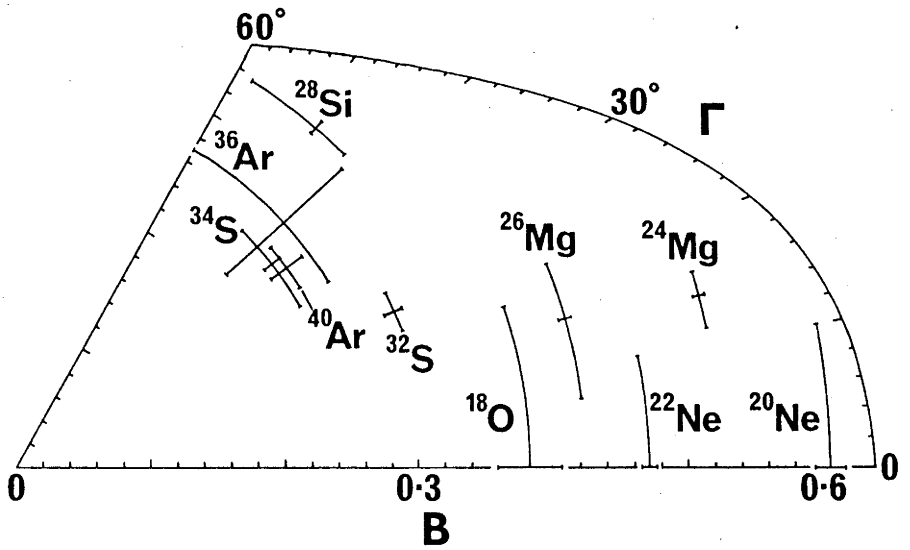

Fig. 5.2: Values of the shape parameters B and Γ of the ground states of some even-even nuclei in the mass range $18 \leqslant A \leqslant 40$.

interesting to know the quadrupole moment of ^{30}Si in order to place that nucleus in fig. 5.2. Information on ^{36}S and ^{38}Ar would also be interesting but the very low natural abundances of these isotopes makes quadrupole-moment measurements very difficult.

5.3 CONCLUSION

The measurements reported in this thesis establish values of the quadrupole moments of the first excited states of ^{198}Hg, ^{24}Mg and ^{18}O. In the cases of the two light nuclei, there were previous measurements which were in clear disagreement with the theoretical predictions. This work has removed these discrepancies. The measurement on ^{198}Hg was the first such measurement on any mercury isotope. It would be very interesting to extend this work to other isotopes as there is some disagreement in the predictions of Q_{2^+} for the heavier isotopes [cf. refs. Co67, Ku68]. That must, however, await a determination of the values of the higher state matrix elements of these nuclei.

In addition to the report of the experimental work, the theory used in the analysis of these experiments was examined in an attempt to locate possible sources of uncertainty in the analysis. Two such sources — the effects of virtual nucleon tunnelling and special relativity — were found. Estimates made of the relativistic effects showed that these are a significant source of uncertainty in the analysis of the ^{198}Hg experiment and further theoretical work on the relativistic theory of Coulomb excitation is warranted. While it was argued that virtual tunnelling is probably not a problem, one is nevertheless somewhat uneasy about neglecting it in cases such as ^{18}O where the electromagnetic excitation probability is very small. Some theoretical work on this phenomenon would clearly be desirable.

Appendix

For ease of comparison between this and other work, some relationships between the conventions used above and those used elsewhere are listed here.

(i) State Vectors and Electromagnetic Matrix Elements

The phase convention of Alder and Winther [Al75, p.317] for state vectors and matrix elements has been used. This means that

$$\langle J_1 \| M(\sigma\lambda) \| J_2 \rangle = (-)^{J_1-J_2} \langle J_2 \| M(\sigma\lambda) \| J_1 \rangle . \qquad (A.1)$$

Also, Q_{J^π} and $\langle J^\pi \| M(E2) \| J^\pi \rangle$ have the same sign in this convention. In another commonly used convention [Bo69] this is not so.

(ii) Units

The rationalized S.I. system [In78] of equations for electromagnetic quantities is used throughout. A detailed conversion table between this and the Gaussian system can be found in ref. In78. In particular, the nuclear magneton is defined by

$$\mu_N = \frac{e\hbar}{2m_p} , \qquad (A.2)$$

thus giving it the expected dimensions of current times area. This means that all magnetic moments in this work, except μ_{2^+} (see table 1.1), differ by a factor of the velocity of light from those which are commonly used. Thus, where Alder and Winther [Al75], using the Gaussian system, write

$$\chi^{M\lambda}_{fo} = \frac{\sqrt{16\pi}\, Z_1 e}{\hbar c} \frac{(\lambda-1)!}{(2\lambda+1)!!} \frac{\langle J_o \| M(M\lambda) \| J_f \rangle}{a^\lambda \sqrt{2J_o+1}} , \qquad (A.3)$$

I write

$$\chi_{of}^{M\lambda} = \frac{Z_1 e \mu_0}{\sqrt{\pi}\,\hbar} \frac{(\lambda-1)!}{(2\lambda+1)!!} \frac{\langle J_f \| M(M\lambda) \| J_o \rangle}{a^{\lambda}\sqrt{2J_o+1}}, \tag{A.4}$$

It is emphasized that the quantities $\chi^{M\lambda}$ defined by eqs. A.3 and A.4 have the same magnitude although they may differ in sign (see eq. A.5).

(iii) Other Differences

In general, the definitions used here coincide with those of Alder and Winther [Al75]. Those which are different are listed below, where the presuperscript A indicates that the quantity is as defined by Alder and Winther

$$^{A}\chi_{fo}^{\sigma\lambda} = (-)^{J_o-J_f}\chi_{of}^{\sigma\lambda} \tag{A.5}$$

$$^{A}Q_{\sigma\lambda\mu}(\varepsilon,w) = (-)^{\mu} Q_{\sigma\lambda\mu}(\varepsilon,w) \tag{A.6}$$

$$^{A}R_{(\lambda\lambda')k\kappa}(\theta,\xi_1,\xi_2) = (-)^{k}(2k+1)^{-\frac{1}{2}} R_{(E\lambda E\lambda')k\kappa}(\theta,\xi_1,\xi_2) \tag{A.7}$$

$$^{A}G_{(\lambda\lambda')k\kappa}(\theta,\xi_1,\xi_2) = (-)^{k}(2k+1)^{-\frac{1}{2}} G_{(E\lambda E\lambda')k\kappa}(\theta,\xi_1,\xi_2)\,. \tag{A.8}$$

References

Ab72 Y. Abgrall, B. Morand and E. Caurier. *Nucl. Phys.* A192 (1972), 372.

Ab73 M. Abramowitz and I.A. Stegun. *Handbook of Mathematical Functions* (Dover, N.Y., 1973).

Aj72 F. Ajzenberg-Selove. *Nucl. Phys.* A190 (1972), 1.

Aj78 F. Ajzenberg-Selove. *Nucl. Phys.* A300 (1978), 1.

Al56 K. Alder, A. Bohr, T. Huus, B. Mottelson and A. Winther. *Rev. Mod. Phys.* 28 (1956), 432 (reprinted with corrections in Al66a).

Al56a K. Alder and A. Winther. *Mat. Fys. Medd. Dan. Vid. Selsk.* 31 (1956), no. 1.

Al66 G. Alaga and G. Ialongo. *Phys. Lett.* 22 (1966), 619.

Al66a K. Alder and A. Winther. *Coulomb Excitation* (Academic Press, N.Y., 1966).

Al69 K. Alder and H.K.A. Pauli. *Nucl. Phys.* A128 (1969), 193.

Al72 K. Alder, F. Rösel and R. Morf. *Nucl. Phys.* A186 (1972), 449.

Al75 K. Alder and A. Winther. *Electromagnetic Excitation* (North-Holland, Amsterdam, 1975).

Al77 K. Alder, F. Rösel and R. Morf. *Nucl. Phys.* A284 (1977), 145.

An70 D.S. Andreyev, G.M. Gusinsky, K.I. Erokhina, M.F. Kudojarov, I.Kh. Lemberg and I.N. Chugunov. *Phys. Lett.* 32B (1970), 187.

An74 D.K. Anderson and D.A. Jenkins, in *Nuclear Spectroscopy and Reactions*, part B, ed. J. Cerny (Academic Press, N.Y., 1974), p.457.

As76 J. Asher, M.A. Grace, P.D. Johnson, J.W. Koen, P.M. Rowe and W.L. Randolph. *J. Phys. (Lond.)* G2 (1976), 477.

Ba76 F.T. Baker, T.H. Kruse, W. Hartwig, I.Y. Lee and J.X. Saladin. *Nucl. Phys.* A258 (1976), 43.

Ba76a F.T. Baker, A. Scott, T.H. Kruse, W. Hartwig, E. Ventura and W. Savin. *Nucl. Phys.* A266 (1976), 337.

Ba77 G. Bauer, F. Rösel and D. Trautmann. *Nucl. Phys.* A288 (1977), 113.

Ba78 C. Baktash, J.X. Saladin, J.J. O'Brien and J.G. Alessi. *Phys. Rev.* C18 (1978), 131.

Ba78a G.C. Ball, O. Häusser, T.K. Alexander, W.G. Davies, J.S. Forster and D. Horn. Chalk River Labs. Progress Report PR-P-117 (AECL-6177) 1978, p.13.

Be67 E.E. Verlovich and V.V. Lukashevich. *Izv. Akad. Nauk S.S.S.R. (ser. fiz.)* 31 (1967), 1603. English trans. *Bull. Acad. Sci. U.S.S.R. (phys. ser.)* 31 (1967), 1643.

Be69 P.R. Bevington. *Data Reduction and Error Analysis for the Physical Sciences* (McGraw-Hill, N.Y., 1969).

Be71 R. Beck and M. Kleber. *Z. Phys.* 246 (1971), 383.

Be73 J.A. Becker, L.F. Chase jr., D. Kohler and R.E. McDonald. *Phys. Rev.* C8 (1973), 2007.

Be73a R. Béraud. Thesis, Université Claude Bernard de Lyon, 1973 (unpublished).

Be74 Z. Berant, C. Broude, G. Engler and D.F.H. Start. *Nucl. Phys.* A225 (1974), 55.

Be75 B.L. Berman and S.C. Fultz. *Rev. Mod. Phys.* 47 (1975), 713.

Be76 R.B. Begzhanov, F.S. Akilov, A.Kh. Khalikov and M.S. Rakhmankulov. *Izv. Akad. Nauk Uzb. S.S.R. (Fiz.-Mat.)* 1976, no. 4, p.59.

Be76a B.L. Berman, D.D. Faul, R.A. Alvarez and P. Meyer. *Phys. Rev. Lett.* 36 (1976), 1441.

Be78 R. Beetz, F.W.N. de Boer, K. Fransson, J. Konijn, J.K. Panman, L. Tauscher and G. Tibel. *Nucl. Phys.* A300 (1978), 369.

Bi75 S.F. Biagi, W.R. Phillips and A.R. Barnett. *Nucl. Phys.* A242 (1975), 160.

Bl72 J. Blomqvist. *Nucl. Phys.* B48 (1972), 95.

Bo62 A.J.F. Boyle and H.E. Hall. *Rep. Prog. Phys.* 25 (1962), 441.

Bo68 J. de Boer and J. Eichler. *Advan. Nucl. Phys.* 1 (1968), 1.

Bo69 A. Bohr and B.R. Mottelson. *Nuclear Structure*, vol. 1 (Benjamin, N.Y., 1969).

Bo75 E. Bodenstadt, in *The Electromagnetic Interaction in Nuclear Spectroscopy*, ed. W.D. Hamilton (North-Holland, Amsterdam, 1975), p.735.

Bo75a A. Bohr and B.R. Mottelson. *Nuclear Structure*, vol. 2 (Benjamin, Reading Mass., 1975).

Bo76 A. Bockisch, P.-J. Dickers, W. Klein and A.M. Kleinfeld. *Nucl. Instr. Meth.* 135 (1976), 145.

Bo77 A. Bockisch. Thesis, Universität zu Köln, 1977 (unpublished).

Bo78 A. Bockisch, K. Baruth-Ram, A.M. Kleinfeld and K.P. Lieb. *Hyp. Int.* 4 (1978), 234.

Bo78a A. Bockisch, K. Baruth-Ram, A.M. Kleinfeld and K.P. Lieb. *Proc. Int. Conf. Dynamical Props. of Heavy-Ion Reactions*, vol. 1 (Atomic Energy Board of South Africa, Johannesburg, 1978), p.71.

Br59 G. Breit and R.L. Gluckstern, in *Handbuch der Physik*, vol. 41/1, ed. S. Flügge (Springer-Verlag, Berlin, 1959), p.496.

Br73 D. Branford. *Aust. J. Phys.* 26 (1973), 257.

Br73a C. Broude, F.A. Beck and P. Engelstein. *Nucl. Phys.* A216 (1973), 603.

Br76 C. Broude, W.G. Davies, J.S. Forster and G.C. Ball. *Phys. Rev.* C13 (1976), 953.

Bu71 P.J.A. Buttle and L.J.B. Goldfarb. *Nucl. Phys.* A176 (1971), 299.

Bu74 J. Burde, S. Eshhar, A. Ginsburg and E. Navon. *Nucl. Phys.* A229 (1974), 387.

Ca50 B.C. Carlson and G.S. Rushbrooke. *Proc. Camb. Phil. Soc.* 46 (1950), 626.

Cl72 D. Cline and C. Flaum. *Proc. Int. Conf. Nucl. Structure Studies using Electron Scattering and Photoreactions, Sendai*, 1972, p.61.

Cl73 D. Cline. *J. Phys. Soc. Jap.* 34 suppl. (1973), 377.

Cl77 D. Cline. University of Rochester report UR-NSRL-157 (1977).

Co67 A. Covello and G. Sartoris. *Nucl. Phys.* A104 (1967), 189.

Cu73 R.Y. Cusson and H.C. Lee. *Nucl. Phys.* A211 (1973), 429.

Da53 W.G. Davey and P.B. Moon. *Proc. Phys. Soc.* 66A (1953), 956.

Da58 A.S. Davydov and G.F. Filippov. *Nucl. Phys.* 8 (1958), 237.

Da59 A.S. Davydov and V.S. Rostovsky. *Nucl. Phys.* 12 (1959), 58.

Da60 A.S. Davydov and A.A. Chaban. *Nucl. Phys.* 20 (1960), 499.

Da68 J.P. Davidson. *Collective Models of the Nucleus* (Academic Press, N.Y., 1968).

Da78 J. Dalmas and G.Y. Petit. *Can. J. Phys.* 56 (1978), 917.

De69 S. Devons and I. Duerdoth. *Advan. Nucl. Phys.* 2 (1969), 295.

De77 D. Denhard, D.C. Palmer, D.J. Weber, R.J. Falkenberg, S. Kubono, J.L. Artz, T.K. Li and D. Ingham. John H. Williams Lab. of Nucl. Phys., University of Minnesota, Annual Report 1977 (COO-1265-190), p.75.

Di71 D.L. Disdier, O. Häusser and A.J. Ferguson. Chalk River Labs. Progress Report PR-P-89 (AECL-3912) 1971, p.13.

Do67 A.C. Douglas and N. McDonald. *Phys. Lett.* 24B (1967), 447.

Eb71 K.A. Eberhard and D. Robson. *Phys. Rev.* C3 (1971), 149.

Eb74 J.L. Eberhardt, R.E. Horstman, H.W. Heeman and G. van Middelkoop. *Nucl. Phys.* A229 (1974), 162.

Ee74 J. Eenmaa, R.K. Cole, C.N. Waddell, S.H. Sandhu and R.R. Dittman. *Nucl. Phys.* A218 (1974), 125.

Ei75 J.M. Eisenberg and W. Greiner. *Nuclear Models — Collective and Single-Particle Phenomena*, 2nd ed. (North-Holland, Amsterdam, 1975).

El70 P.J. Ellis and T. Engeland. *Nucl. Phys.* A144 (1970), 161.

En72 J.B.A. England. *Nucl. Instr. Meth.* 102 (1972), 365.

En73 P.M. Endt and C. van der Leun. *Nucl. Phys.* A214 (1973), 1.

En74 P.M. Endt and C. van der Leun. *At. and Nucl. Data Tables* 13 (1974), 67.

En74a P.M. Endt and C. van der Leun. *Nucl. Phys.* A235 (1974), 27.

En76 T. Engeland and P.J. Ellis. *Phys. Rev. Lett.* 36 (1976), 994, and T. Engeland (University of Oslo), private communication.

En77 J.B.A. England. (The University, Birmingham), private communication.

En78 P.M. Endt and C. van der Leun. Preprint — communicated by I.F. Wright (The University, Manchester).

Er77 T. Erikson and G.E. Brown. *Nucl. Phys.* A277 (1977), 1.

Es64 M.A. Eswaran and C. Broude. *Can. J. Phys.* 42 (1964), 1311.

Es76 M.T. Esat. Thesis, Australian National University, 1976 (unpublished).

Es76a M.T. Esat, D.C. Kean, R.H. Spear and A.M. Baxter. *Nucl. Phys.* A274 (1976), 237.

Es77 M.T. Esat, D.C. Kean and R.H. Spear. *Nucl. Instr. Meth.* 141 (1977), 405.

Es77a M.T. Esat, D.C. Kean, R.H. Spear, M.P. Fewell and A.M. Baxter. *Phys. Lett.* 72B (1977), 49.

Fa65 A. Faessler, W. Greiner and R.K. Sheline. *Nucl. Phys.* 70 (1965), 33.

Fe77 M.P. Fewell, D.C. Kean, R.H. Spear and A.M. Baxter. *J. Phys. (Lond.)* G3 (1977), L27.

Fi73 E.C. Finch. *Nucl. Instr. Meth.* 113 (1973), 41.

Fi76 L.K. Fifield, R.W. Zurmühle, D.P. Balamuth and S.L. Tabor. *Phys. Rev.* C13 (1976), 1515.

Fl77 C. Flaum, J. Barrette, M.J. LeVine and C.E. Thorn. *Phys. Rev. Lett.* 39 (1977), 446.

Fo51 L.L. Foldy. *Phys. Rev.* 83 (1951), 397.

Fo71 W.F. Ford, R.C. Braley and J. Bar-Touv. *Phys. Rev.* C4 (1971), 2099.

Fo74 J.S. Forster, D. Ward, G.J. Costa, G.C. Ball, W.G. Davies and I.V. Mitchell. *Phys. Lett.* 51B (1974), 133.

Fo75 M. Forterre, J. Gerber, J.P. Vivien, M.B. Goldberg and K.-H. Speidel. *Phys. Lett.* 55B (1975), 56.

Fo78 J.S. Forster, T.K. Alexander, G.C. Ball, W.G. Davies and I.V. Mitchell. Chalk River Labs. Progress Report PR-P-117 (AECL-6177) 1978, p.14.

Fr63 E. Friedland and H.R. Lemmer. *Z. Phys.* 174 (1963), 507.

Fr76 J.M. Freeman. *Nucl. Instr. Meth.* 134 (1976), 153.

Go66 S. Gorodetzky, N. Schulz, E. Bozek and A.C. Knipper. *Nucl. Phys.* 85 (1966), 529.

Go75 J.D. Goss, C.P. Browne, A.A. Rollefson and P.L. Jolivette. *Phys. Rev.* C11 (1975), 710.

Gr73 L. Grodzins. *J. Phys. Soc. Jap.* 34 suppl. (1973), 30.

Gr74 H. Grawe and R. König. *Z. Phys.* 266 (1974), 41.

Gu71 M.R. Gunye. *Phys. Lett.* 37B (1971), 125.

Ha64 D.W. Hafemeister, G. DePasquali and H. deWaard. *Phys. Rev.* 135 (1964), B1089.

Ha70 O. Häusser, B.W. Hooton, D. Pelte, T.K. Alexander and H.C. Evans. *Can. J. Phys.* 48 (1970), 35.

Ha71 R.C. Haight, J.X. Saladin and D. Vitoux. *Nucl. Instr. Meth.* 91 (1971), 445.

Ha71a O. Häusser, D.L. Disdier, A.J. Ferguson and T.K. Alexander. Chalk River Labs. Progress Report PR-P-91 (AECL-4068) 1971, p.12.

Ha72 O. Häusser, in *Dynamic Structure of Nuclear States* (Proc. Int. Summer School. Mont Tremblant, 1971), eds. D.J. Rowe, L.E.H. Trainor, S.S.M. Wong and T.W. Donnelly (University of Toronto Press, Toronto, 1972), p.465.

Ha72a O. Häusser, A.J. Ferguson and D.L. Disdier. Chalk River Labs. Progress Report PR-P-93 (AECL-4205) 1972, p.10.

Ha73 O. Häusser, A.B. McDonald, T.K. Alexander, A.J. Ferguson and R.E. Warner. *Nucl. Phys.* A212 (1973), 613.

Ha74 O. Häusser, in *Nuclear Spectroscopy and Reactions*, part C, ed. J. Cerny (Academic Press, N.Y., 1974), p.55.

Ha77 J.K. Hamilton and R.S. Mackintosh. *J. Phys. (Lond.)* G3 (1977), L19.

Ha77a B. Harmatz. *Nucl. Data Sheets* 21 (1977), 377.

Ha78 A.A. Hahn, J.P. Miller, R.J. Powers, A. Zehnder, A.M. Rushton, R.E. Welsh, A.R. Kunselman, P. Roberson and H.K. Walter. California Inst. of Technology Report CALT 63-299 (1978), to be published in *Nucl. Phys.*

He75 J.A.J. Hermans, G.A.P. Engelbertink, M.A. van Driel, H.H. Eggenhuisen and D. Bucurescu. *Nucl. Phys.* A255 (1975), 221.

Hi71 F. Hibou, P. Fintz, B. Rastegar and A. Gallmann. *Nucl. Phys.* A171 (1971), 603.

Hi74 J.F.A. van Hienen, P.W.M. Glaudemans and J. van Lidth de Jeude. *Nucl. Phys.* A225 (1974), 119.

Ho74 R.E. Horstman, J.L. Eberhardt, H.A. Doubt and G. van Middelkoop. *Phys. Lett.* 48B (1974), 31.

Ho75 R.E. Horstman, J.L. Eberhardt, H.A. Doubt, C.M.E. Otten and G. van Middelkoop. *Nucl. Phys.* A248 (1975), 291.

Hu76 K.-N. Huang. *Phys. Rev.* A14 (1976), 1311.

In78 International Union of Pure and Applied Physics, S.U.N. Commission. *Physica* 93A (1978), 1.

Is69 V.I. Isakov and I.Kh. Lemberg. *Pisma Zh. Eksp. Teor. Fiz.* 9 (1969), 698, English trans. *JETP Lett.* 9 (1969), 438.

Jo74 A. Johnson and T.E. Drake. *J. Phys. (Lond.)* A7 (1974), 898.

Jo74a P.M. Johnson, M.A. Meyer and D. Reitmann. *Nucl. Phys.* A218 (1974), 333.

Jo77 A.M.R. Joye. Thesis, Australian National University, 1977 (unpublished).

Jo77a A.M.R. Joye, A.M. Baxter, M.P. Fewell, D.C. Kean and R.H. Spear. *Phys. Rev. Lett.* 38 (1977), 807.

Jo78 A.M.R. Joye, A.M. Baxter, S. Hinds, D.C. Kean and R.H. Spear. *Phys. Lett.* 72B (1978), 307.

Ka74 S.A. Kassirov, G.G. Kovshevny, A.A. Kotov, V.R. Resnik, G.E. Solyakin and N.K. Terent'ev. *Nucl. Instr. Meth.* 119 (1974), 301.

Kh74 S.B. Khadkikar and D.R. Kulkarni. *Phys. Rev.* C10 (1974), 1189.

Ki72 T. Kishimoto and T. Tamura. *Nucl. Phys.* A192 (1972), 246.

Ki76 T. Kishimoto and T. Tamura. *Nucl. Phys.* A270 (1976), 317.

Ki77 H.T. King, M. Hass, R. Kaita and A.B. Robbins. *Phys. Rev.* C15 (1977), 829.

Kl75 A.M. Kleinfeld, K.P. Lieb, D. Werdecker and U. Smilansky. *Phys. Rev. Lett.* 35 (1975), 1329.

Kl77 K. Klingenbeck. *Phys. Rev.* C15 (1977), 831.

Kn76 U. Kneissl, K.H. Leister, H.O. Neidel and A. Weller. *Nucl. Phys.* A272 (1976), 125.

Ko78 W.K. Koo and L.J. Tassie. Submitted to *Nucl. Phys.*

Kr74 S. Krewald, K.W. Schmid, A. Faessler and J.B. McGrory. *Nucl. Phys.* A228 (1974), 524.

Ku68 K. Kumar and M. Baranger. *Nucl. Phys.* A110 (1968), 529.

Ku69 K. Kumar. *Phys. Lett.* 29B (1969), 25.

Ku72 K. Kumar. *Phys. Rev. Lett.* 28 (1972), 249.

Ku72a D. Kurath. *Phys. Rev.* C5 (1972), 768.

Ku75 K. Kumar, in *The Electromagnetic Interaction in Nuclear Spectroscopy*, ed. W.D. Hamilton (North-Holland, Amsterdam, 1975), p.55.

Ku75a K. Kumar, in *The Electromagnetic Interaction in Nuclear Spectroscopy*, ed. W.D. Hamilton (North-Holland, Amsterdam, 1975), p.119.

La61 F. Lacoste and G.R. Bishop. *Nucl. Phys.* 26 (1961), 511.

La69 L.D. Landau and E.M. Lifshitz. *Mechanics*, 2nd English ed. (Pergamon, Oxford, 1969).

La72 S.A. Lane and J.X. Saladin. *Phys. Rev.* C6 (1972), 613.

La75 L.D. Landau and E.M. Lifshitz. *The Classical Theory of Fields*, 4th English ed. (Pergamon, Oxford, 1975).

La76 R.D. Lawson, F.J.D. Serduke and H.T. Fortune. *Phys. Rev.* C14 (1976), 1245.

Le57 J.S. Levinger. *Phys. Rev.* 107 (1957), 554.

Le73 F. Leccia, M.M. Aléonard, D. Castéra, Ph. Hubert and P. Mennrath. *J. Phys. (Paris)* 34 (1973), 147.

Le73a H.-C. Lee. *J. Phys. Soc. Jap.* 34 suppl. (1973), 445.

Le74 E.W. Lees, A. Johnson, S.W. Brain, C.S. Curran, W.A. Gillespie and R.P. Singhal. *J. Phys. (Lond.)* A7 (1974), 936.

Le78 M.J. LeVine. (Brookhaven Nat. Lab.), private communication and *Bull. Amer. Phys. Soc.* 23 (1978), 42.

Li63 A.E. Litherland, M.J.L. Yates, B.M. Hinds and D. Eccleshall. *Nucl. Phys.* 44 (1963), 220.

Li74 E.M. Lifshitz and L.P. Pitaevskiĭ. *Relativistic Quantum Theory*, part 2, 1st English ed. (Pergamon, Oxford, 1974).

Li77 J.S. Lilley, A.R. Barnett, M. Franey, G. Kajrys, W.R. Phillips and H. Sharma. *Bull. Amer. Phys. Soc.* 22 (1977), 552.

Lo70 K.E.G. Löbner, M. Vetter and V. Hönig. *Nucl. Data Tables* A7 (1970), 495.

Lo70a P. Lorrain and D.R. Corson. *Electromagnetic Fields and Waves* (W.H. Freeman, San Francisco, 1970).

Lo75 V. Lopac. *Proc. Topical Conf. Problems of Vibrational Nuclei, Zagreb, 1974* (North-Holland, Amsterdam, 1975), p.396.

Ma55 M.G. Mayer and J.H.D. Jensen. *Elementary Theory of Nuclear Shell Structure* (Wiley, N.Y., 1955).

Ma65 J.F. Masso and L.D. Lin. *Phys. Rev.* 140 (1965), B1182.

Ma68 J.B. Marion and F.C. Young. *Nuclear Reaction Analysis* (North-Holland, Amsterdam, 1968).

Ma74 R.S. Mackintosh and L.J. Tassie. *Nucl. Phys.* A222 (1974), 187.

Ma77 R.S. Mackintosh. *Rep. Prog. Phys.* 40 (1977), 731.

Ma77a R.S. Mackintosh. *Nucl. Phys.* A280 (1977), 86.

Ma77b M. Maynard, D.C. Palmer, J.R. Cresswell, P.D. Forsyth, I. Hall and D.G.E. Martin. *J. Phys. (Lond.)* G3 (1977), 1735.

Ma77c M.J. Martin and P.H. Stelson. *Nucl. Data Sheets* 21 (1977), 1.

Mc64 N. McDonald. *Phys. Lett.* 10 (1964), 334.

Mc71 J.B. McGrory and B.H. Wildenthal. *Phys. Lett.* 34B (1971), 373.

Mc74 A.B. McDonald, T.K. Alexander, O. Häusser, G.J. Costa, J.S. Forster and A. Olin. *Can. J. Phys.* 52 (1974), 1381.

Me54 F.R. Metzger and W.B. Todd. *Phys. Rev.* 95 (1954), 853.

Me70 E. Merzbacher. *Quantum Mechanics*, 2nd ed. (Wiley Toppan, Tokyo, 1970).

Me75 M.A. Meyer, I. Venter and D. Reitmann. *Nucl. Phys.* A250 (1975), 235.

Mi45 A. Migdal. *Zh. Eksp. Teor. Fiz.* 15 (1945), 81.

Mi77 R. Middleton. *Nucl. Instr. Meth.* 141 (1977), 373.

Mo60 R.B. Moore and W. White. *Can. J. Phys.* 38 (1960), 1149.

Mo78 I. Morrison, R. Smith, P. Nesci and K. Amos. *Phys. Rev.* C17 (1978), 1485, and I. Morrison (University of Melbourne), private communication.

Mu76 B. Müller and W. Greiner. *Z. Naturf.* 31a (1976), 1.

Na72 A. Nakada and Y. Torizuka. *J. Phys. Soc. Jap.* 32 (1972), 1.

Ne67 H. Nebel and D.L. Lin. *Phys. Rev.* 156 (1967), 1133.

Ni78 K. Nishiyama and D. Riegel. *Hyp. Int.* 4 (1978), 490.

No70 L.C. Northcliffe and R.F. Schilling. *Nucl. Data Tables* A7 (1970), 233.

No76 P.J. Nolan, A.J. Brown, P.A. Butler, L.L. Green, A.N. James, C.J. Lister, J.D. MacArthur and J.F. Sharpey-Schafer. *J. Phys. (Lond.)* G2 (1976), 249.

Ol73 J.W. Olness, E.K. Warburton and J.A. Becker. *Phys. Rev.* C7 (1973), 2239.

Ol74 D.K. Olsen, A.R. Barnett, S.F. Biagi, N.H. Merrill and W.R. Phillips. *Nucl. Phys.* A220 (1974), 541.

Op74 T.R. Ophel, J.S. Harrison, J.O. Newton, R.H. Spear, E.W. Titterton and D.C. Weisser. *Nucl. Instr. Meth.* 122 (1974), 227.

Pe57 I. Perlman and J.O. Rasmussen, in *Handbuch der Physik*, vol. 42, ed. S. Flügge (Springer-Verlag, Berlin, 1957), p.109.

Pe69 D. Pelte, O. Häusser, T.K. Alexander and H.C. Evans. *Can. J. Phys.* 47 (1969), 1929.

Po78 R.J. Powers. *Hyp. Int.* 4 (1978), 123.

Ra68 B.V.N. Rao, K.M.M.S. Ayyangar and S. Jnanananda. *Ind. J. Pure Appl. Phys.* 6 (1968), 358.

Ra72 J. Rafelski, B. Müller and W. Greiner. *Lett. Nuovo Cim.* 4 (1972), 469.

Ra73 R.S. Raghavan, P. Raghavan and E.N. Kaufmann. *Phys. Rev. Lett.* 31 (1973), 111.

Ra76 J. Rafelski. *Phys. Rev.* C13 (1976), 2086.

Re72 H. Rebel, G.W. Schweimer, G. Schatz, J. Specht, R. Löhken, G. Hauser, D. Habs and H. Klewe-Nebenius. *Nucl. Phys.* A182 (1972), 145.

Ri69 W. Rindler. *Special Relativity* (Oliver & Boyd, Edinburgh, 1969).

Ro57 M.E. Rose. *Elementary Theory of Angular Momentum* (Wiley, N.Y., 1957).

Ro74 F. Rösel, J.X. Saladin and K. Alder. *Comp. Phys. Comm.* 8 (1974), 35.

Ro77 F. Rösel, K. Alder, R. Morf and J.X. Saladin. *J. Phys. (Lond.)* G3 (1977), 613.

Ro78 G. Rosensteel and E. Ihrig. *Phys. Rev.* C17 (1978), 1179.

Ru78 P. Russo, J.K. Sprinkle, D. Cline, P.B. Vold and R.P. Scharenberg, preprint, University of Rochester, submitted to *Nucl. Phys.*

Sa69 J.X. Saladin, J.E. Glenn and R.J. Pryor. *Phys. Rev.* 186 (1969), 1241.

Sa75 B.W. Sargent, W.G. Hanson, P.A. Puhach and D. Sinclair. *Nucl. Instr. Meth.* 124 (1975), 265.

Sc72 F. Scheck. *Nucl. Phys.* B42 (1972), 573.

Sc72a D. Schwalm, A. Bamberger, P.G. Bizzeti, B. Povh, G.A.P. Engelbertink, J.W. Olness and E.K. Warburton. *Nucl. Phys.* A192 (1972), 449.

Sc72b M.R. Schmorak. *Nucl. Data Sheets* B7 (1972), 395.

Sc73 M.R. Schmorak. *Nucl. Data Sheets* 9 (1973), 195.

Sc73a M.R. Schmorak. *Nucl. Data Sheets* 9 (1973), 401.

Sc73b M.R. Schmorak. *Nucl. Data Sheets* 10 (1973), 553.

Sc74 M.R. Schmorak. *Nucl. Data Sheets* 13 (1974), 267.

Sc77 D. Schwalm, E.K. Warburton and J.W. Olness. *Nucl. Phys.* A293 (1977), 425.

Se52 R. Serber and H.S. Snyder. *Phys. Rev.* 87 (1952), 152.

Se73 W. Seibt, K.E. Sundström and P.A. Tove. *Nucl. Instr. Meth.* 113 (1973), 317.

Sh63 A. de Shalit and I. Talmi. *Nuclear Shell Theory* (Academic Press, N.Y., 1963).

Si61 P.C. Simms, N. Benczer-Koller and C.S. Wu. *Phys. Rev.* 121 (1961), 1169.

Sl30 J.C. Slater. *Phys. Rev.* 36 (1930), 57.

Sm68 U. Smilansky. *Nucl. Phys.* A112 (1968), 185.

So76 J.R. Southon, L.K. Fifield and A.R. Poletti. *J. Phys. (Lond.)* G2 (1976), 117.

So76a J.R. Southon, A.R. Poletti and D.J. Beale. *Nucl. Phys.* A267 (1976), 263.

Sp71 J. Specht. *Lett. Nuovo Cim.* 2 (1971), 126.

Sp75 K.-H. Speidel, M.B. Goldberg, K. Hagemeyer, G.J. Kumbartzki, G. Goldring, Z. Shkedi, M. Schramm, G. Kraft and H.A. Doubt. *Phys. Lett.* 57B (1975), 143.

Sp77 R.H. Spear, D.C. Kean, M.T. Esat, A.M.R. Joye and M.P. Fewell. *Nucl. Instr. Meth.* 147 (1977), 455.

Sp77a R.H. Spear, J.P. Warner, A.M. Baxter, M.T. Esat, M.P. Fewell, S. Hinds, A.M.R. Joye and D.C. Kean. *Aust. J. Phys.* 30 (1977), 133.

St72 D. Strottman. *Phys. Lett.* 39B (1972), 457.

Su58 A.W. Sunyar. *Proc. 2nd U.N. Int. Conf. Peaceful Uses of Atomic Energy, Geneva, 1958*, vol. 14, p.347.

Sw69 R. de Swiniarski, C. Glashausser. D.L. Hendrie, J. Sherman, A.D. Bacher and E.A. McClatchie. *Phys. Rev. Lett.* 23 (1969), 317.

Te52 K.A. Ter-Martirosyan. *Zh. Eksp. Teor. Fiz.* 22 (1952), 284. English trans. ref. Al66a, p.15.

Th54 R.G. Thomas. *Prog. Theor. Phys.* 12 (1954), 253.

Vi71 D. Vitoux, R.C. Haight and J.X. Saladin. *Phys. Rev.* C3 (1971), 718.

Vo77 P.B. Vold, D. Cline, P. Russo, J.K. Sprinkle, R.P. Scharenberg and R.J. Mitchell. *Phys. Rev. Lett.* 39 (1977), 325.

Wa73 E.K. Warburton, P. Gorodetzky and J.A. Becker. *Phys. Rev.* C8 (1973), 418.

Wa75 P. Wagner, M.A. Ali, J.P. Coffin and A. Gallmann. *Phys. Rev.* C11 (1975), 1622.

Wi75 A. Winther and J. de Boer. California Institute of Technology, Technical Report, 18/11/1965. Reprinted in ref. Al66.

Wi71 B.H. Wildenthal, J.B. McGrory and P.W.M. Glaudemans. *Phys. Rev. Lett.* 26 (1971), 96.

Wi71a B.D. Wilkins, M.J. Fluss, S.B. Kaufman, C.E. Gross and E.P. Steinberg. *Nucl. Instr. Meth.* 92 (1971), 381.

Wi78 A. Winther and K. Alder. Preprint, Niels Bohr Institute.

Yo72 S. Yoshida and L. Zamick. *Ann. Rev. Nucl. Sci.* 22 (1972), 121.